Universität der Bundeswehr München

Advancement of the High-Enthalpy Free-Piston Reflected Shock Tunnel HELM for in situ Determination of Aerothermal Stagnation Conditions

Claudio Selcan

Full copy of the thesis approved by the
Department of Aerospace Engineering
of the Bundeswehr University Munich
for obtaining the doctoral degree
Doktor-Ingenieur (Dr.-Ing.)

Advisor:
1. Univ.-Prof. Dr.-Ing. Christian Mundt
2. Prof. Hideyuki Tanno

The doctoral thesis was submitted at the Bundeswehr University Munich on 30.07.2021 and accepted by the Department of Aerospace Engineering on 17.02.2022. The oral examination took place on 25.05.2022.

Abstract DE

Die experimentelle Bestimmung thermischer und kalorischer Zustandsgrößen des Testgases in bodengebundenen Hochenthalpie- und Hyperschall-Versuchsanlagen wird insbesondere durch die sehr hohen vorherrschenden Ruhedrücke, -temperaturen und die intermittierende Betriebsweise erschwert, welche Versuchszeiten im Millisekundenbereich diktiert. Um Daten der experimentellen Windkanal-Simulation mit numerischen Vorhersagen vergleichen zu können, ist eine genaue Bestimmung des thermischen Ruhezustands vor der Düsenexpansion jedoch unabdingbar. Zu diesem Zweck entwickelt die vorliegende Arbeit einen Ansatz der gezielten Kombination nicht-invasiver, lokal im Düsenreservoir sowie invasiver, in der freien Modellanströmung durchgeführter Messungen mit Methoden der numerischen Rückbildung, welche zu einer genaueren Bestimmung der thermischen Einlass- und Randbedingungen der Düsenströmung von Hyperschall-Kanälen beitragen soll. Lokale Messungen der nach Stoßreflektion im Düsenreservoir des Hochenthalpie-Stoßwellen-Kanals HELM erreichten Totaltemperatur werden mittels resonanter, laserinduzierter Gitter-spektroskopie (LIGS) durchgeführt. Hinter einfallenden Stoßwellen mit Machzahlen bis zu 3.6 in Luft als Testgas konnten erfolgreiche Messungen bei Ruheenthalpien bis 2,1 MJ/kg und -drücken bis 220 bar durchgeführt werden. Die notwendigen technischen Voraussetzungen werden im Detail erläutert. Um dieses Ziel zu erreichen, werden detaillierte und umfassende Betriebskonditionen des Stoßwellenkanals HELM über seinen gesamten Arbeitsbereich, mit nominellen Ruheenthalpien bis 25 MJ/kg und bis 1000 bar Berstdruck, erarbeitet. Die Betriebs-punkte folgen aus verschiedenen Ansätzen zur Beschreibung des angepassten Betriebs eines freien Kolbentreibers sowie einer angepassten Kontaktfläche. Um rechnerische Vorhersagen zu ergänzen und zu validieren, wird die momentane Beschleunigung des Verdichtungskolbens mittels eines mitbewegten Beschleunigungssensors aufgezeichnet und dessen zeitaufgelöste Trajektorie aus den Primärdaten rekonstruiert. Die über diskrete Wegpunkte im Treiberrohr korrigierte Messung erfasst Spitzenwerte von bis zu 30.000 m/s^2 Verzögerung. Eine systematische Vermessung der freien Modellanströmung des Stoßwellenkanals HELM wird im Rahmen dieser Arbeit erstmalig unter einer Kombination aus Freistrahlmessungen und numerischer Simulation durchgeführt, zwecks deren experimentell-numerische Rückbildungs-Routinen implementiert werden. Damit wird eine Bestimmung der kalorischen Ruhegrößen durch in situ und ex situ Messungen möglich, welche schlussendlich zu einer erhöhten Genauigkeit experimenteller Randbedingungen in Kurzzeit-, Hochenthalpie-Versuchsanlagen beiträgt.

Abstract EN

Experimental determination of test gas caloric quantities in high-enthalpy, hypersonic ground testing is impeded by excessive pressure and temperature levels as well as minimum test time scales of short-duration facilities. However, accurate knowledge of test gas conditions and stagnation enthalpy prior to nozzle expansion is vital to achieve a valid comparison of experimental data with numerical results. In order to facilitate a more accurate quantification of caloric nozzle inlet conditions in hypersonic shock tunnels, a deliberate combination of in situ non-intrusive measurements within the nozzle reservoir with ex situ intrusive free-stream measurements and numerical rebuilding is devised. For this purpose, in situ measurements of post-reflected shock stagnation temperature in the nozzle reservoir of the HELM facility (High-enthalpy laboratory Munich) are carried out by resonant, homodyne laser-induced grating spectroscopy (LIGS). For incident shock waves up to Mach 3.6, test conditions in air are advanced up to moderate stagnation enthalpies of 2.1 MJ/kg and stagnation pressures of 220 bar. Technical measures which were required to reach this goal are discussed in detail. In order to lay the foundation for this effort, detailed and comprehensive operation conditions for the HELM facility across the entire test envelope and up to the nominal range of 1000 bar burst pressure and 25 MJ/kg stagnation enthalpy are developed, according to different theories for tuned free-piston driver (FPD) and tailored contact surface operation for the first time. In order to complement and validate numerical predictions, continuous measurements of instantaneous piston acceleration by an on-board accelerometer facilitate to reconstruct and validate the time-resolved compression piston trajectory for a full-stroke and up to 30,000 m/s^2 peak deceleration. Measurements are corrected by and validated against localized waypoint markers. This work represents the first effort to systematically characterize the free-stream regime at the HELM nozzle exit by a deliberate combination of intrusive experimental measurements and numerical simulations - the use of experimental-numerical rebuilding routines, which are implemented for this purpose, will facilitate a deduction of caloric stagnation conditions from ex situ measurements and comparison to in situ measurements in the future, eventually contributing to a higher accuracy of boundary conditions in high-enthalpy, short-duration ground testing.

Declaration by the author

This thesis is composed of my original work and contains no material previously published or written by another person, except where due reference is made in the text. Where applicable, I have clearly stated the original contribution of others to co-authored work, significant technical procedures and any other original research work used or reported herein.

Parts of the work in this thesis have been published as original research articles under copyright of the author or under Creative Commons open access licence.

1. C. Selcan, T. Sander, P. Altenhoefer, F. Koroll, Ch. Mundt Stagnation Temperature Measurements in a Shock-Tunnel Facility Using Laser-Induced Grating Spectroscopy, AIAA Journal of Thermophysics and Heat Transfer, 32, 1, 2016, Doi: https://doi.org/10.2514/1.T5199

2. C. Selcan, T. Sander, Ch. Mundt In situ Nozzle Reservoir Thermometry by Laser-Induced Grating Spectroscopy in the HELM Free-Piston Reflected Shock Tunnel, Shock Waves, 2021, Doi: https://doi.org/10.1007/s00193-020-00982-9

I acknowledge that copyright of all material contained in my thesis resides with the copyright holder(s) of that material.

Claudio Selcan
Neubiberg, August 09, 2022

Acknowledgement

To my girlfriend and parents, for their enduring and neverending support along the arduous journey through the rocky valleys of misery and along splendid heights.

„Den lieb' ich, der Unmögliches begehrt."
Goethe, Faust II

Contents

List of Figures

List of Tables

Nomenclature

Abbreviations

ADC	Analog-digital converter
ALTP	Atomic layer thermopile
BL	Boundary Layer
CAD	Computer aided design
CARS	Coherent anti-Stokes Raman spectroscopy
CCD	Intensified charge coupled device
CEA	Chemical equilibrium with applications (computer program)
CFD	Computational fluid dynamics
CS	Contact surface
CT	Compression tube (driver)
CUBRC	Calspan-University of Buffalo Research Center
cw	Continuous wave
DFT	Discrete-Fourier-Transformation
DFWM	Degenerate four wave mixing
DIN	Deutsches Institut für Normung e.V.
DOF	Degrees of freedom
EOS	Equation of State
EQ	Equilibrium (thermo-chemical)
ESTCj	Equilibrium shock tube conditions, junior (computer program)
EXP	Experiment
FFT	Fast-Fourier-Transformation
FIT	Curve fit
FKM	Fluorcarbon rubber (Viton)
FPD	Free-piston driver
FPST	Free-piston shock tunnel
FS	Free-stream
FS	Full-scale (measurement uncertainty)
HEG	High-enthalpy shock tunnel Göttingen
HELM	High-enthalpy laboratory Munich
LENS	Large Energy National Shock Tunnel
LIF	Laser-induced fluorescence
LIGS	Laser-induced grating spectroscopy
LITA	Laser-induced thermal acoustics
L1d	Lagrangian 1D (Computer program)
MEMS	Micro-electro-mechanical-system
NASA	National Aeronautics and Space Administration
NEQ	Non-equilibrium
Nd:YAG	Neodymium-doped yttrium aluminum garnet

NS	Navier-Stokes
NSMB	Navier-Stokes multiblock (computer program)
PA	Polyamid (Nylatron)
PEEK	Polyetheretherketon
PLC	Programmable logic controller (SPS)
PLIF	Planar laser-induced fluorescence
PMT	Photomultiplier tube
ppm	Parts per million
PTFE	Polytetrafluorethylen (Teflon)
PUR	Polyurethane
RANS	Reynolds-averaged Navier-Stokes
RWTH	Rheinisch-Westfälische Technische Hochschule Aachen
SNR	Signal-to-noise-ratio
SP	Stagnation point
ST	Shock tube
TDLAS	Tunable diode laser absorption spectroscopy
TH2	Hypersonic shock tunnel at RWTH-Aachen
TI	Tailored interface (contact surface)
TUP	Tuned piston operation
VDI	Verein deutscher Ingenieure e.V.
JAXA	Japanese Aerospace Exploration Agency
1-D	One-dimensional
2-D	Two-dimensional
3-D	Three-dimensional

Symbols

a	[m/s]	Sound speed
a	[m/s^2]	Piston acceleration
A	[m^2]	Surface area
c	[-]	LIGS grating type constant
c_p	[J/kgK]	Specific heat (at constant pressure)
c_v	[J/kgK]	Specific heat (at constant volume)
Da	[-]	Damkoehler number
e	[J/kg]	Internal energy (specific)
E	[J]	Energy
Le	[-]	Lewis number
m	[kg]	Mass
M	[g/mol]	Molar mass
Ma	[-]	Mach number
n	[mol]	Amount of constituent
h	[J/kg]	Enthalpy (specific)
p	[Pa]	Pressure
P	[-]	Dimensionless driver coefficient (Hornung)
Pr	[-]	Prandtl number)
R_m	[J/molK]	Universal gas constant
R_N	[m]	Sphere radius (stagnation probe)
R	[J/kgK]	Specific gas constant
Re	[-]	Reynolds number
s	[J/kgK]	Entropy
t	[s]	Time
T	[K]	Temperature
u, v	[m/s]	Velocity
V	[m^3]	Volume
x	[-]	Mole fraction
y	[-]	Mass fraction

Vectors

$\vec{k}$	[-]	Pump beam wave vector
$\vec{q}$	[-]	Grating vector

Greek symbols

α	[-]	Degree of dissociation
α	[-]	Reformulation of isentropic exponent
λ	[nm]	Laser wavelength
λ	[-]	Piston driver volumetric compression ratio
Λ	[nm]	Interference grating constant
μ	[kg/ms]	Dynamic viscosity
ν	[m^2/s]	Kinematic viscosity
Θ	[deg]	Pump beam crossing angle
ρ	[kg/m^3]	Mass density
κ	[-]	Isentropic exponent (ratio of specific heats)
δ	[m]	Shock standoff distance (dimensional)
Δ	[-]	Shock standoff distance (non-dimensional)
Δ	[-]	Difference
φ	[deg]	Bragg angle
ω	[-]	Dimensionless driver coefficient (Itoh)
β	[-]	Piston over-drive parameter
σ	[N/mm^2]	Normal stress (mechanical)
μ_0	[kg/ms]	Sutherland reference viscosity
τ	[s]	Characteristic time scale
Γ	[-]	Non-dimensional similarity parameter (space)

Superscripts

$'$	Measured quantities
$''$	Predicted quantities
$*$	Critical state (choked flow)

Subscripts

a	Atomic (species)
abs	Absolute
ch	Chemical
e	Electrostriction
el	Electronic
eq	Equilibrium
kin	Kinetic
m	Molecular (species)
max	Maximum
neq	Non-equilibrium
p	Piston
$peak$	Peak (global maximum)
pot	Potential
$probe$	Probe beam
$pump$	Pump laser
r	Resonance
ref	Reference
rel	Relative
rot	Rotational
$rupt$	Diaphragm rupture
s	Shock
s	Species (atomic and molecular)
t	Thermalization
t	Total (stagnation condition)
vib	Vibrational
w	Wall
A	Buffer (secondary reservoir)
CT	Compression tube (driver)
D	Dissociation
R	Reaction rate
R	Recombination
ST	Shock tube
0	Initial value
0	Stagnation condition
1	Shock tube initial state
2	Post-incident shock state
3	Expanded driver gas state
4	Diaphragm burst state
40	Driver tube initial state
$4e$	Orifice exit state
5	Post-reflected shock state
$5e$	Post-reflected shock state (equilibrium)
7	State upstream of contact surface
8	State downstream of contact surface
∞	Free stream condition

1 Introduction and Relevance

1.1 Ground testing requirements

In order to circumvent and complement prohibitive free-flight testing of air-breathing propulsion or atmospheric re-entry vehicles, short duration test facilites worldwide aim to provide practical means for ground testing of generic and scaled configurations at flight-relevant flow regimes under controlled laboratory conditions. Specifically, fundamental scaling laws of relevant physical, non-dimensional parameters are being used to relate and extrapolate data from ground test experiments with scaled models to flight-scale configurations. The basic similarity parameters are Reynolds and Mach number. Whereas the former scales inertia to viscosity and hence affects lift, drag, surface pressure distribution and boundary layer transition, the latter scales compressibility effects, affecting shock wave shape and interaction, boundary layer growth, total pressure loss and entropy layer effects [1]. Depending on flight velocity and altitude, the requirements for a realistic duplication of dominant aerothermal parameters can be notably different and vary significantly along a vehicle's trajectory, as in the case of sub-orbital hypersonic flight, around Mach numbers ∼5-7 and altitudes ∼25-35 km, and a capsule's atmospheric re-entry at velocities u∼2-10 km/s and altitudes ∼20-80 km, see Fig 1.1.

In short-duration and continuous wind tunnels alike, flow velocity in the test section is provided by a strong expansion of the test gas to super- and hypersonic speeds in convergent-divergent nozzles. According to energy conservation, the highest achievable freestream velocity scales with the facility's total enthalpy:

$$h_0 \propto \frac{u_\infty^2}{2}.$$

(1.1)

1.1.1 Hypersonic ground testing

Up to flight velocities <2 km/s at sea level condition, the relevant flow regime is dominated by viscosity and compressiblility effects and thus can readily be duplicated in cold-gas hypersonic wind tunnels [3]. While high Mach numbers are easily obtained from strong expansion to low freestream static temperatures, particularly test flow density after nozzle expansion is of highest relevance in order to correctly duplicate the free-flight Reynolds number - dictating highest possible total pressure of such facilities. For such low-enthalpy flows, i.e. for stagnation temperatures below 2,000 K, air can be treated as a perfect gas. Here, variation of the isentropic exponent is either negligible or only affected by vibrational excitation and real gas effects are not of importance, rendering duplication of the absolute flight velocity of subordinate impor-
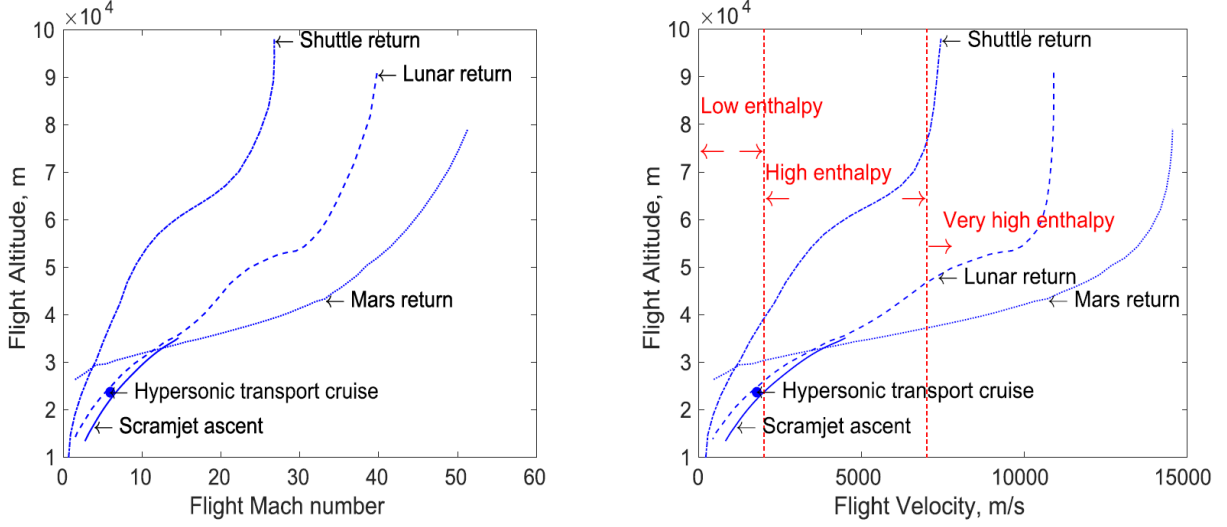
Figure 1.1: Representative (re-)entry trajectories of hypersonic flight vehicles, from [2].

tance. Yet, as the viscous and displacement boundary layer thickness in hypersonic flow grow strongly with Mach number and are further largely affected by the freestream-to-wall temperature ratio T_∞/T_w, as shown by recovery and reference temperature methods [4], the complete dimensional scaling is defined as follows:

$$\Gamma = \Gamma(Ma_\infty, Re_\infty, T_\infty/T_w). \tag{1.2}$$

According to Olivier [5], the freestream-wall temperature ratio is generally preserved for low-enthalpy flows in cold-gas hypersonic facilities due to low freestream temperature. In contrast, high-enthalpy flows with very high freestream temperatures behind strong shock waves will invalidate the equality of freestream-wall temperature ratio between free flight and wind tunnel test, requiring hot model techniques to ensure full scaling law validity.

1.1.2 Hypersonic nozzle flow

The basic principle of hypersonic ground testing is the expansion of a high-pressure, high-temperature relevant test gas to hypersonic Mach numbers Ma>5 and high velocities v>2 km/s by a convergent-divergent (de Laval) nozzle of large area ratio A/A*∼ $\mathcal{O}$(100-1000). Here, the energy equation, balancing kinetic and potential energy along a streamline,

$$h_0 = h + \frac{v^2}{2} = const \tag{1.3}$$

yields the relation for static and total gas temperature in depencence of local Mach number $Ma = u/a$:

$$\frac{T_0}{T} = 1 + \frac{\kappa - 1}{2}Ma^2 \tag{1.4}$$

, where enthalpy for a (calorically) perfect gas is written as $h(T) = c_p \cdot T$. The sound speed

$$a^2 = (\frac{\partial p}{\partial \rho})_s = \kappa \cdot R \cdot T \tag{1.5}$$

is written according to the ideal gas equation of state (EOS)

$$p = \rho \cdot R \cdot T. \tag{1.6}$$

The specific heat (at constant pressure) is written in dependence of the isentropic coefficient and specific gas constant $c_p = \frac{\kappa}{\kappa-1}R$. From the second law of thermodynamics

$$T ds = dh - v dp \tag{1.7}$$

$$\Delta s_{12} = c_p ln(\frac{T_2}{T_1}) - R ln(\frac{p_2}{p_1}) \tag{1.8}$$

the relations for isentropic, inviscid, supersonic flow of an ideal gas are derived as follows:

$$\frac{p_0}{p} = (\frac{T_0}{T})^{\frac{\kappa}{\kappa-1}} = (1 + \frac{\kappa-1}{2}Ma^2)^{\frac{\kappa}{\kappa-1}} \tag{1.9}$$

$$\frac{\rho_0}{\rho} = (\frac{T_0}{T})^{\frac{1}{\kappa-1}} = (1 + \frac{\kappa-1}{2}Ma^2)^{\frac{1}{\kappa-1}}. \tag{1.10}$$

Considering stationary, isentropic, adiabatic, inviscid, one-dimensional flow of an ideal gas, mass continuity along a streamline yields the relation for Mach number, static pressure through a nozzle of varying cross section area:

$$\frac{A}{A^*} = \frac{1}{Ma}[1 + \frac{\kappa-1}{2}Ma^2]^{\frac{\kappa+1}{2(\kappa-1)}} \tag{1.11}$$

$$Ma = \sqrt{\frac{2}{\kappa-1}[(\frac{p_0}{p})^{\frac{\kappa-1}{\kappa}}]}. \tag{1.12}$$

Critical conditions at the nozzle throat, where $Ma^* = 1$ are given according to Eq. 1.10 by:

$$\frac{T^*}{T_0} = \frac{2}{\kappa+1} \tag{1.13}$$

$$\frac{p^*}{p_0} = (\frac{2}{\kappa+1})^{\frac{\kappa}{\kappa-1}} \tag{1.14}$$

$$\frac{\rho^*}{\rho_0} = (\frac{2}{\kappa+1})^{\frac{1}{\kappa-1}} \tag{1.15}$$

$$\frac{u^*}{u_{max}} = \sqrt{\frac{\kappa-1}{\kappa+1}}. \tag{1.16}$$
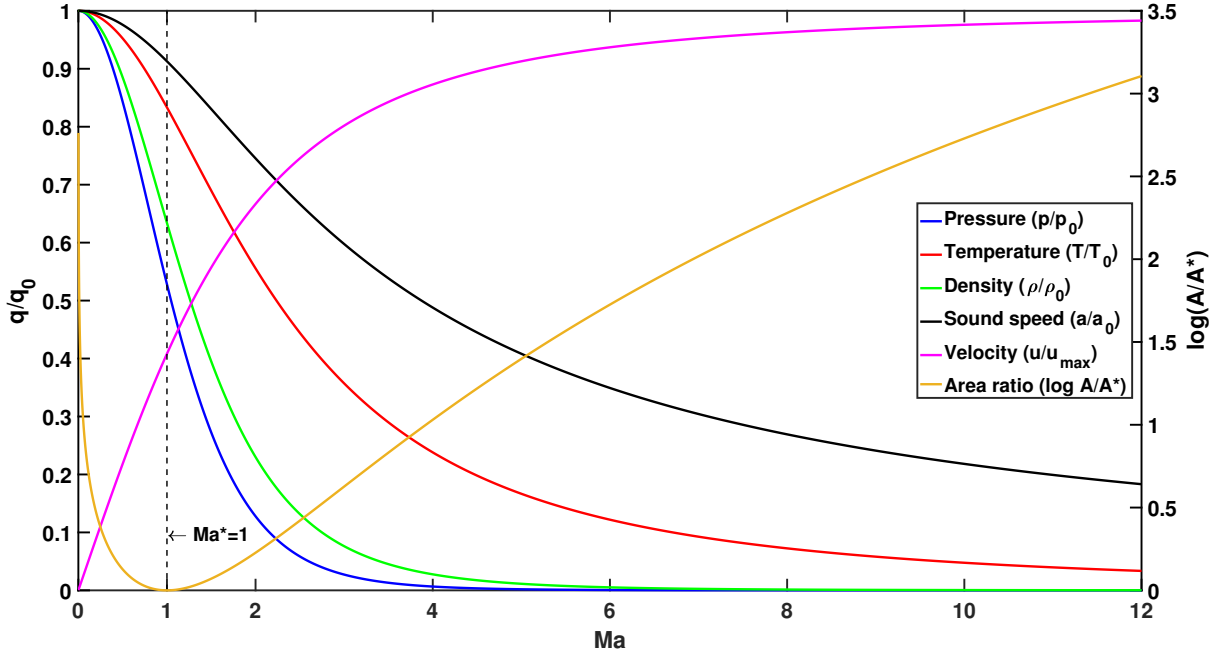
Figure 1.2: Mach number dependence of static pressure, temperature, density, sound speed, absolute velocity and area-ratio for one-dimesional, inviscid nozzle expansion of an ideal gas ($\kappa = 7/5$). Quantities are normalized by stagnation conditions and throat area, respectively.

From Eq. 1.12 it is observed that Mach number is primarily dictated by the expansion nozzle area ratio, whereas Eq. 1.3 indicates the absolute velocity of the expanded flow is written as:

$$u = \sqrt{2c_p(T_0 - T)}. \tag{1.17}$$

The limiting case of expansion into vacuum $p \rightarrow 0$ and neglection of the static energy component $T \rightarrow 0$ yields a maximum gas velocity which is quantified by the gas' total enthalpy or temperature, according to:

$$u_{max} = \sqrt{2h_0} = \sqrt{2c_pT_0}. \tag{1.18}$$

State quantities of the nozzle flow normalized by the total (stagnation) value are plotted over Mach number in Fig. 1.2. Considering the Reynolds number definition:

$$Re = \frac{\rho \cdot u \cdot L}{\mu} \tag{1.19}$$

where μ denotes dynamic viscosity and L represents the characteristic length scale, the former is seen to be linearly correlated to flow density which, according to Fig. 1.2, is observed to decrease by orders of magnitude in the process of nozzle expansion to hypersonic velocities. Accordingly, in order to duplicate flight-relevant Reynolds numbers on the order of Re$\sim \mathcal{O}(10^6)$ by the nozzle free-stream quantities, the test facility's stagnation pressure and density are to be maximized in order to simultaneously achieve physically relevant Reynolds numbers and flight Mach numbers Ma$\sim \mathcal{O}(10)$. Besides, high total enthalpy is required in order to correctly

duplicate the vehicle's absolute flight velocity u$\sim \mathcal{O}(2km/s)$.

1.1.3 High-temperature thermo-chemistry

At very high hypersonic Mach numbers $Ma \gg 10$, the non-dimensional flow field parameters become gradually independent from Mach number [6]. In contrast, similarity scaling for flow regimes along a re-entry trajectory, characterized by very high superorbital flight velocities $u \gg 2km$, mandates the duplication of the absolute velocity. According to Eq. 1.1, this directly corresponds to moderate and high-enthalpy test regimes of stagnation temperatures $\sim$2,000-10,000 K, substantially extending the set of non-dimensional parameters and chemical-physical phenomena to be accounted for.

Specifically, temperatures beyond 2,000 K will inevitably trigger thermodynamic real gas effects, i.e. gradual excitation of internal degrees of freedom (DOF) such as molecular vibration and rotation, and high-temperature chemistry, i.e. dissociation and ionization. In the case of an atmospheric re-entry capsule, the flow field ahead of the blunt body is governed by a detached bow shock wave of strong curvature. Gas along the stagnation point streamline is subjected to processing by a normal shock wave, inducing strong flow deceleration and conversion of kinetic to thermal energy. Resultant high gas temperatures typically exceed the specific dissociation energies of atmospherical flow species, i.e. oxygen and nitrogen in case of earth re-entry. High-temperature thermo-chemistry is triggered, where molecular dissociation and ionization limit the freestream temperature to approximately T<10,000 K. Such thermo-chemical (non-)equilibrium effects of shock-heated gas induce notable deviations from ideal gas behavior, e.g. shock standoff distances to be remarkably lower than for ideal gases [1].

Besides matching of the flow field physics by duplicating Mach and Reynolds number, free-flight relevant conditions to be reproduced by ground testing are further characterized by real-gas effects of high-temperature chemistry. Here, the stagnation enthalpy, Eq. 1.1, is typically higher than the specific dissociation energy of the test gas:

$$\frac{h_0}{h_D} > 1. \tag{1.20}$$

Relevant reactions pathways for high-temperature thermal dissociation and ionization of air,

i.e. nitrogen and oxygen, are listed according to Oertel [7]:

$$N_2 + M <=> N + N + M \tag{1.21}$$
$$N_2 <=> N_2^+ + e^- \tag{1.22}$$
$$N <=> N^+ + e^- \tag{1.23}$$
$$NO + M <=> N + O + M \tag{1.24}$$
$$O_2 + M <=> O + O + M \tag{1.25}$$
$$O_2 <=> O_2^+ + e^- \tag{1.26}$$
$$O <=> O^+ + e^- \tag{1.27}$$

$$NO <=> NO^+ + e^- \tag{1.28}$$
$$O^- <=> O + e^- \tag{1.29}$$
$$N_2 + O <=> NO + N \tag{1.30}$$
$$NO + O <=> N + O_2. \tag{1.31}$$
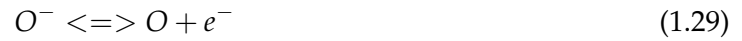
Characteristic ranges for high-temperature air chemical reactions are listed by Anderson [8]:

1. No chemical reactions: <2500 K

2. O_2 dissociation: ~2500-4000 K

3. N_2 dissociation: ~4000-9000 K

4. N, O ionization: >9000 K.

In addition to high-temperature chemistry, real gas effects at high temperatures pertain to the deviation from an ideal gas behaviour due to excitation of internal thermodynamic DOF such as inner-molecular vibration and rotation, interacting with the gas' translational modes and inducing a notable variation of the isentropic exponent, i.e. ratio of specific heats, see Fig. 1.3. In terms of internal thermodynamic DOF, the characteristic relaxation time τ determines the duration necessary for high shock-induced translational temperature to equilibrate with rotational and vibrational modes ($T_{trans} = T_{rot} = T_{vib}$). The latter differs for every internal DOF and depends on local particle density as the time to reach thermodynamic equilibrium is governed by the number of particle collisions, i.e. collisional frequency. Typical ranges of particle collisions are listed by Oertel [7]:

- Translational and rotational excitation: $\sim 1 - 10$

- Vibrational excitation: $\sim 10^2$

- Dissociation: $\sim 10^4 - 10^5$

- Ionization: $\sim 10^5 - 10^6$
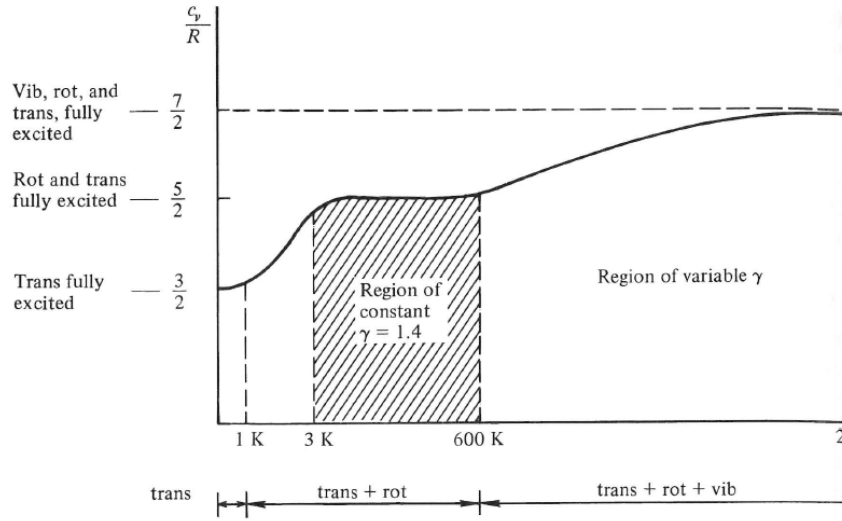
Figure 1.3: Variation of the isentropic exponent of a di-atomic molecule due to excitation of internal thermodynamic DOF, reproduced from [8].

Both, internal thermodynamic excitation and chemical reactions alike are triggered by high gas temperatures, becoming of growing importance for test gas properties at elevated temperatures and being the dominant parameter at high-enthalpy levels. Due to their endothermal character, the forward reactions of dissociation and ionization as well as internal thermodynamic excitation continuously draw on the thermal energy of the gas, gradually lowering the translational temperature of shock-heated flows. Hence, notable variations from ideal gas behavior include limited translational temperature as well as higher gas density, due to an increase in particle number density, even beyond the hypersonic limit of pressure, temperature and density:

$$\lim_{Ma_1 \to \infty} \frac{p_2}{p_1} = \infty \tag{1.32}$$

$$\lim_{Ma_1 \to \infty} \frac{T_2}{T_1} = \infty \tag{1.33}$$

$$\lim_{Ma_1 \to \infty} \frac{\rho_2}{\rho_1} = \frac{\kappa + 1}{\kappa - 1}. \tag{1.34}$$

The magnitude of deviations from ideal gas behaviour is illustrated in Fig. 1.4, where the change is state quantities across a normal shock wave is plotted over incident shock Mach number, comparing ideal gas behaviour to full thermo-chemical equilibrium according to CEA [9]. Evidently, where ideal gas an asymptotically approaches a hypersonic limit for density, dictated by the gas' isentropic exponent, and yields an unbounded increase is post-shock temperature and pressure, thermo-chemical equilibrium is characterized by a significantly lowered and limited static temperature as well as a notable decrease in density. Initial deviation from ideal gas behavior is observed to start around Ma=3 and to grow significantly with incident shock Mach number. The post-shock temperature T_2 is found to be limited to approximately ~10,000 K whereas, ideal gas law would predict post-shock temperatures beyond >23,000 K
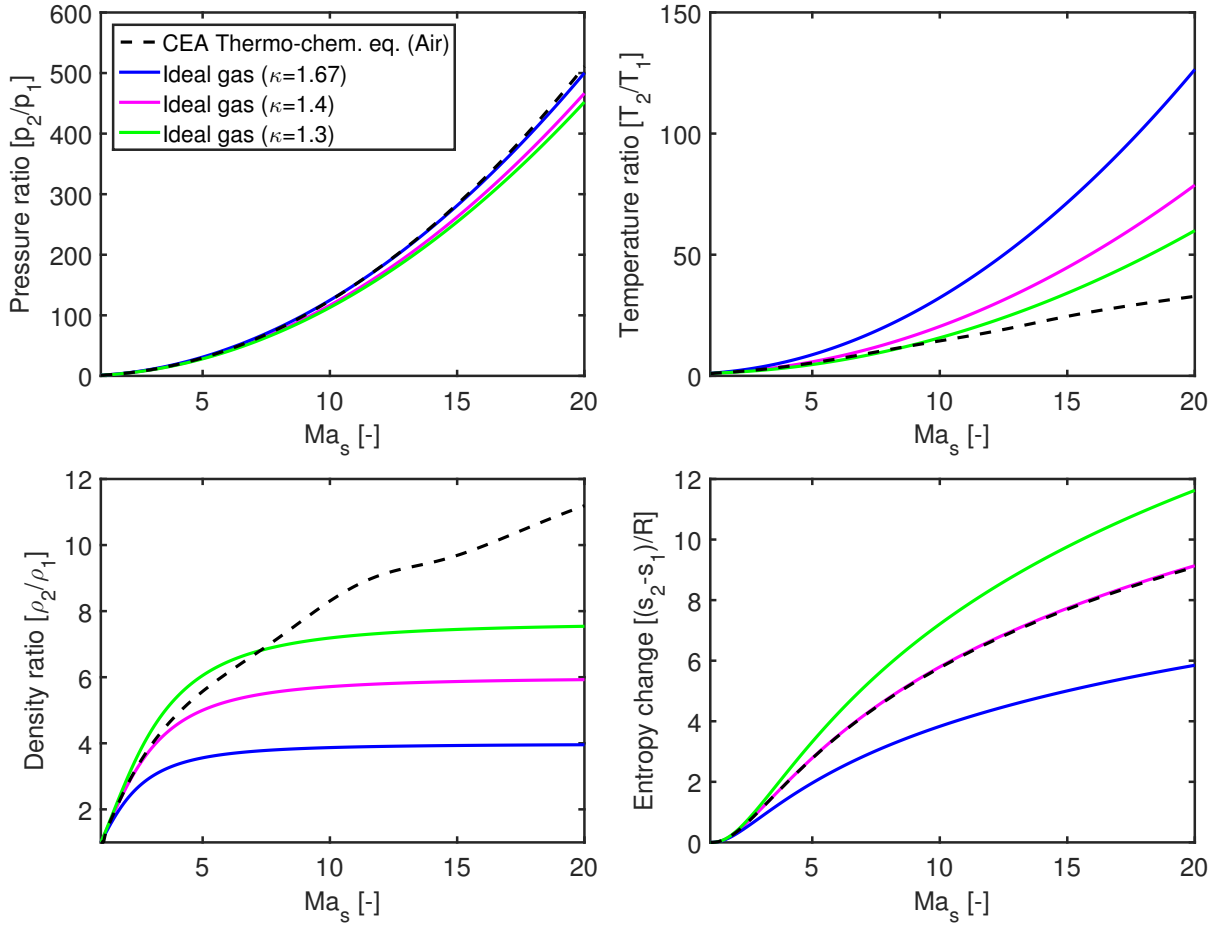
Figure 1.4: Change of state quantities (static pressure, temperature, density, entropy) across a normal shock wave of varying Mach number Ma_s. Curves are plotted for ideal gas behavior of mono- and di-atomic gases as well as equilibrium thermo-chemistry according to CEA, for dry air at T_1=293.15 K and p_1=1 bar.

for the case of Ma=20. Thus, while temperature shows a remarkably flattened slope, pressure is found to be the least sensitive quantity in terms of equilibrium deviations from the ideal gas law.

Thermo-chemical (non-)equilibrium

For a thermo-chemically reactive flow, the Damkoehler number becomes of importance, which relates characteristic flow residence time to the characteristic chemical time-scale and - considering characteristic fluid velocity $v = \frac{L}{\tau}$ -, can further be written in terms of flow characterstic length scale and chemical reaction length scale:

$$Da = \frac{\tau}{\tau_R} = \frac{L}{L_R}. \tag{1.35}$$

Whereas L is defined as characteristic length of the test body and thus yields residence time of the flow across the test configuration, reaction length scale is defined as the length over which

chemical reactions (i.e. transient change in chemical species concentration) occur to approach chemical equilibrium conditions. As such, it is defined according to the chemical relaxation time, governed by reaction pathway rate constants of dissociation and recombination. Accordingly, the non-dimensional Damkoehler number is being used to characterize the progress of time-dependent chemical reactions and thermodynamic excitation toward thermochemical equilibrium in reference to the flow time scale to determine the reacting gas state. In the first case of Da≪1 the characteristic flow residence time is much smaller than the time necessary for the gas to react. This case describes the case of a chemically frozen non-reacting gas with species concentration identical to the inlet conditions. The opposite case of Da≫1 in contrast determines flow residence time to outweigh necessary chemical reaction time scales such that the gas described has already fully approached equilibrium conditions. The intermediate case of Da~1 is thus characteristic for the non-equilibrium regime where where chemical reactions and internal molecular excitation still proceed such that species concentration and molecular excitation are subject to temporal change as the fluid flows over the body. In the case of blunt body flow, the shock standoff-distance is notably reduced in the case of chemically reacting flow in comparison to chemically frozen flow or ideal gas behaviour.

Different ranges in a re-entry vehicle trajectory are characterized by regimes of chemically and thermodynamically frozen, equilibrium and non-equilibrium flow, respectively, which are to be taken into account throughout ground testing. The high enthalpy levels of a reflected shock-tunnel facilitate to trigger and duplicate such conditions.

Recombination and nozzle flow freezing

Whereas translational temperature is largely reduced due to transfer to chemical energy by molecular dissoziation reactions, the opposite process of recombination again transfers chemical binding energy to translational, vibrational and rotational (temperature) states. Characteristic reactions for di-atomic gas molecule dissociation and recombination follow reaction equations:

$$O_2 + M <=> O + O + M \tag{1.36}$$

$$O + O + M <=> O_2 + M \tag{1.37}$$
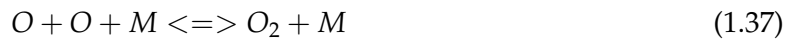
where M is representative of an anbitrary collisional partner. Both reactions occur simultaneously at any time with dissociation and recombination rate:

$$R_D = \rho T^\eta e^{-\frac{D_G}{kT}} \left(1 - \alpha\right) \tag{1.38}$$

$$R_R = \rho^2 T^\eta \frac{\alpha^2}{\rho_D} \tag{1.39}$$

where δ, T, α, ρ_D, k and η denote gas density and temperature, dissociated gas mass fraction, characteristic dissociation density, Boltzmann-constant and temperature exponent, respectively. The case of chemical equilibrium is a quasi-static equilibrium with both, dissoci-

ation and recombination, to occur at the same rate.

From Eq. 1.37 and 1.39 it becomes evident that dissociation and recombination require a different number of collisional partners: two and three particles, respectively. The dissociation reaction rate scales with $R_D \propto \rho$ whereas recombination rate scales with $R_R \propto \rho^2$, causing forward or backward reaction either to be preferred or inhibited, based on local particle density and molecular collision rates. This fundamental process dictates test gas at high density, such as present in the shock tunnel nozzle reservoir, to reach thermo-chemical equilibrium near instantaneously after incident shock reflection, whereas rapid and strong rarefaction in the expansion nozzle causes recombination to be largely inhibited by low test gas density. This process is known as nozzle flow (thermo-chemical) freezing and is a well known characteristic of reflected shock tunnels, the freestream conditions of which are prone to entail a certain percentage of dissociated and thermally excited species - hence deviating from thermo-chemical equilibrium or ideal gas behaviour, even at low static temperature. At elevated total enthalpy, deviations from an expected test flow behaviour around test bodies can become significant and induce largely different shock standoff distance in front of a blunt body as has been shown by Holden et al. [10]. In contrast, due to an acceleration of the test gas by an unsteady expansion, expansion tubes have been demonstrated to not be affected by nozzle flow freezing - yet, at the expense of a largely reduced test time [11].

High-enthalpy scaling

At high specific enthalpy, the dissociation degree of the freestream becomes an important chemical parameter for correct ground test duplication. Moreover, for a full duplication of the high-enthalpy test regime, test gas rarefaction and the different rate constants for forward- and backward two- and three-body (dissociation) reactions are to be taken into account, eq. 1.37. Precisely, such dissociation reactions dominate the non-equilibrium layer behind the detached bow shock wave in front of a blunt body and scale with the product of gas density and the model's characteristic length scale ρL [12]. The full similarity parameter space of high-enthalpy ground test experiments is thus defined as follows:

$$\Gamma = \Gamma(Re_\infty, Ma_\infty, Da_\infty, h_0/h_D, \alpha_\infty, \rho_\infty L, T_\infty/T_w). \tag{1.40}$$

As has been highlighted by Olivier and Gu [5], this relationship may further be extended to account for secondary parameters, such as intensity and frequency spectrum of freestream turbulence and acoustic noise as well as the ratio of surface roughness to boundary layer thickness. Such parameters are of particular importance when studying hypersonic boundary layer transition [13, 14].

1.2 Operation condition characterization

Hypersonic ground test facilities, geared to experimental testing of flight vehicles at high Mach numbers, are to provide for flight-relevant freestream conditions by virtue of high total enthalpy. As CFD has gained increasing importance in aerothermal design and experimental testing, understanding of nozzle flow fields and accurate knowledge on freestream properties in the test section become mandatory from two points of view: numerical code validation by comparison with experimental data and numerical rebuilding of high enthalpy experiments [15, 16]. In both cases, freestream conditions bridge the gap between numerical predictions and ground testing. If not accurately predicted, discrepancies in key design parameters such as surface heating rates and pressure levels are inevitable. Evidently, the computation of test section freestream properties itself, by correctly capturing physical and thermochemical phenomena of hypersonic nozzle expansion at high enthalpy, is dictated by the definition of nozzle inlet upstream boundary conditions. Therefore, incorrect reservoir values will, by definition, lead to incorrect freestream values and hence compromise ground test program accuracy [17]. In a discussion of generalized reference enthalpy formulations, Simeonides [18] highlighted the importance of hot freestream measurements (i.e. reproduction of total temperature/enthalpy) to provide for full similarity scaling, thus complete simulation of temperature-viscous effects in both laminar and turbulent flow. Determination of facility operation conditions and test gas thermochemical state in the nozzle supply region is, however, a challenging task. In particular, accurate quantification of nozzle reservoir enthalpy and stagnation temperature (i.e. caloric quantities) is not trivial [5, 19, 20].

1.2.1 Significance of nozzle reservoir conditions

Stagnation conditions in terms of total enthalpy and pressure are the facility parameters of central importance for the test flow provided at the downstream nozzle exit for model testing purposes. Quantification of the latter, either by numerical prediction which is the typical and practical approach in literature or by means of experimental determination is of utmost importance to provide correct upstream (i.e. inlet) boundary conditions for numerical simulations of the succeeding hypersonic expansion nozzle flow. In case the above inlet parameters are not accurately determined, comparison of experimental measurements and numerical predictions are prown to error and bound to diverge a priori as the free-stream conditions at the nozzle exit are not in satisfactory agreement. Furthermore, thermo-chemical non-equilibrium effects which occur throughout strong expansion largely depend on the inlet parameters in terms of thermo-chemical state of the test gas in the nozzle reservoir section. In a noteworthy experimental study by Holden et al. [10] in the CUBRC LENS I reflected shock tunnel facility with CO_2 test flow, pronounced differences in terms of blunt body shock standoff-distance in front of the NASA Mars Science Laboratory (MSL) capsule model were found to ensue from thermal freezing of large amount of internal energy in the molecular vibrational states. As this effect has not been adequately taken into account by the underlying thermo-chemical reaction model, nu-
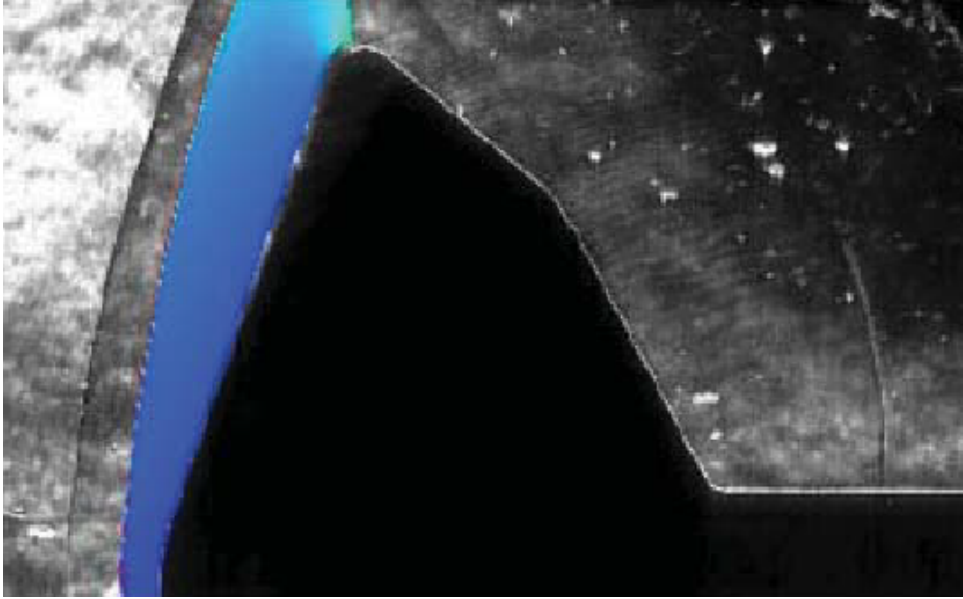
Figure 1.5: Comparison of CO_2 test flow bow-shock standoff-distance in front of the MSL capsule in LENS I facility by experimental Schlieren visualization and numerical prediction [10].

merical simulations came to underpredict the shock standoff-distance in the stagnation region by a factor of 2.5, see figure 1.5.

1.2.2 A priori numerical prediction

In reflected shock tunnel configurations, nozzle reservoir stagnation quantities are governed by shock relations and heated test gas reaction thereafter. Typically assuming thermochemical equilibrium from the nozzle supply to throat location, as is deduced from low relaxation times at high temperature and density [17], it is common practice to perform thermochemical equilibrium calculations by codes such as CEA [9] and others [21] to approximate reservoir conditions and thermodynamic transport properties. This includes equilibrium contributions of internal molecular degrees of freedom by rotational and vibrational excitation and electronic energy. In shock and expansion tube facilities, this is commonly implemented as part of complete facility operation simulations (i.e. including driver performance) by quasi one-dimensional codes such as L1d [22] or KASIMIR [23]. As post-reflected-shock wave stagnation pressure is known to be generally lower than numerically predicted, isentropic expansion assumption to measured pressure levels is employed to approximate less accessible, caloric quantities, such as temperature and enthalpy [21, 24]. Thereafter, inviscid tools like ESTCj [25] and NENZF [26] are used to predict quasi-steady, quasi one-dimensional nozzle exit (i.e. freestream) properties, based on measured incident shock speed, ST initial fill pressure and nozzle exit pitot pressure. Simulations of nozzle expansion from approximated thermochemical equilibrium reservoir state include gas chemistry, whereas vibration-dissociation coupling is typically not accounted for assuming vibrational excitation to be in thermodynamic equilibrium or frozen at the initial nozzle

supply state. Whereas performance of such one-dimensional, low computing-power method-ologies (absent of temporal and spatial gradients) at moderate enthalpy is good as compared to two-dimensional axisymmetric compressible RANS computations, with freestream prediction accuracy being within input data experimental uncertainty bounds [27], higher enthalpy test conditions demand for more intricate means of prediction [17]. 2-D nozzle codes specifically geared to this problem moreover provide for information on temporal and spatial (i.e. radial) gradients, thus freestream uniformity [28]. In the past, numerical tools capable of capturing the physics of hypersonic nozzle expansion struggled to predict the complicated thermochem-ical state, as characterized by shock-heated gas'multiple degrees of freedom, due to finite-rate chemical reactions and molecular excitation in the presence of turbulent flow. In modern CFD, intricate multiple-temperature models are being used to render this coupled problem tractable and to predict the test section state of the flow [29]. Accurate thermochemical modeling of re-laxation is important in prediction of freestream quantities such as static pressure, translational temperature and Mach number [20, 30]. Employing a compressible full NS-solver (DPLR) and chemical-vibrational non-equilibrium coupling to compute nozzle flow fields in the CUBRC LENS-I and LENS-II reflected shock tunnel facilities, MacLean et al. [17] highlighted the cor-rect determination of reservoir condition to be of upmost importance and of equal significance for nozzle flow computations and the duplication of flight-relevant freestream as turbulence modeling in the nozzle throat section. In the calculation of the nozzle supply state by a 1-D low computing-power code, based on normal shock relations and assuming vibrational-translational equilibrium, a non-ideal equation of state high density-correction [31] is argued, in order to correctly predict total enthalpy (i.e. flow velocity and Mach number). An evident case of mismatched (i.e. erroneous) nozzle freestream thermochemical boundary conditions is detailed in hypervelocity vehicle performance studies in CO_2 flow by Holden et al. [10] and MacLean and Holden [21]. It is reported on significant underpredictions (as large as 125%) of blunt body shock standoff distance and shape between experiments conducted in the LENS I reflected shock tunnel facility at total enthalpy 5-10 MJ/kg and DPLR-code computations. Based on equilibrium reservoir conditions, significant portions of vibrational and chemical dis-sociation energy, as induced by reflected shock-heating and test gas stagnation,were found to be frozen throughout strong nozzle expansion. In contrast to initial freestream conditions, which were numerically predicted close to full thermochemical equilibrium, experiments were accurately reproduced by assuming 42% of the freestream total energy to be frozen in CO_2 vi-bration modes [21]. The initial discrepancy is further demonstrated to ensue from unaccounted thermochemical freezing as an artifact of LENS I facility-inherent test gas stagnation, as respec-tive flowfield and shock structure in the LENS X expansion tube facility could be accurately predicted by initial freestream conditions, absent of vibrational and chemical energy freezing [10]. Most notably, predictions from a similar flow field for air at identical enthalpy of 5 and 10 MJ/kg were in close agreement with shock tunnel and expansion tube results, despite the presence of significant oxygen dissociation [10]. In this context, the same authors emphasized the importance of accurate thermochemical modeling and further suggested the use of suit-

able laser diagnostics for correct determination of non-equilibrium freestream properties [16]. Obviously, even the most refined numerical codes, with models apt to resolve intricate non-equilibrium processes within nozzle expansion, rely on accurate definition of thermochemical boundary conditions at the upstream nozzle inlet. If numerical inlet conditions deviate from ground test reservoir conditions, computational inaccuracies further downstream are a priori bound to occur. In this context, it is important to note that, according to the author's best knowledge, established numerical approaches, which calculate nominal facility operation parameters and total enthalpy from normal shock relations, depend on the central assumption of fully-tailored shock tube mode (i.e. single incident and reflected shock wave). In reality, however, this cannot be presupposed, as particularly at higher enthalpy, it is difficult to attain fully tailored and steady operation conditions. Hence, in cases where numerical tools for reservoir conditions prediction fall short in capturing the physics of over- and under-tailored operation, direct means of reservoir enthalpy determination are even more valuable.

1.2.3 Free-stream measurement based predictions

As direct measurement of upstream nozzle reservoir flow quantities by means of conservative techniques and reliable prediction has been challenging and affected by large inaccuracies [19], one resorted to indirect means to determine stagnation quantities. Those well established in the aerothermodynamic community concern semi-empirical correlations, relating test section stagnation heat transfer and pressure, as well as reservoir enthalpy: thereby allowing to deduce the latter from test body measurements. Most commonly, spherical heat transfer probes of defined nose radius are being used for this purpose: typically in the form of permanent probes to monitor facility operation. There exist empirical correlations which are widely accepted, based on flight experiments and ground tests, such as the Fay and Riddell equation [32], as well as a range of alternative formulations [33], some of them derived from computational investigations [20]. The accuracy of such methods is largely dictated by detailed knowledge on the freestream boundary layer chemical state (e.g. frozen, equilibrium) as well as surface catalycity, which, however, are not generally known a priori. Most notably, different formulations of first order influence factors, particularly of the (theoretically derived) stagnation point tangential velocity gradient, exist in literature [19]. In a formulation based on computational data by Verant [34], the velocity gradient is itself defined as a function of total flow enthalpy. Results and comparison of such methods are further described in Simeonides [18] and Walpot et al. [30] for reflected shock tunnel and hot-shot facilities. In the first case, numerical simulations, geared to reproduce high-enthalpy (15-20 MJ/kg) experimental conditions and freestream stagnation heat transfer in the HEG, indicated discrepancies in nozzle wall static pressure and heat transfer magnitude. A ∼50% overprediction of wall heat transfer was attributed to a deviating, lower than predicted stagnation enthalpy (on the order of ∼16 rather than 22 MJ/kg), as induced by conceivable conduction and radiation heat losses in the reservoir section [30]. In the second case of the Onera F4 arc-heated wind tunnel, Verant and Sagnier [20] demonstrated freestream, particularly stagnation heat transfer to be affected by particulate impact and reservoir gas con-

tamination, resulting in higher scatter and an overprediction of total enthalpy. As for probe geometry influence, spherical body and slender cone results, at high enthalpy condition of $\sim$20 MJ/kg, indicated a discrepancy of up to 30%. Semi-empirical correlations alternative to the Fay Riddell formulation with accuracies of 2-12% are presented. Reservoir total temperature overprediction due to unaccounted heat losses in the barrel of a hypersonic gun tunnel are similarly reported in freestream stagnation temperature measurements by Edney [35]. In the same facility, Buttsworth and Jones [36] used transient heat flux probes to measure freestream nozzle total temperatures of up to 700 K and reported on maximum possible bandwidths of up to 100 kHz. As such, mechanical probes are well suited for use in turbomachinery gas-path measurements where low to moderate total temperatures prevail. At higher temperatures and under more severe conditions, however, intrusive probes are strained to their structural, thermal and temporal limit as imposed by excessive gas temperature, abrasive particulate contamination and high degree of flow unsteadiness. Furthermore, particularly at moderate to higher velocities and Mach number, inaccuracies induced by (mostly conduction and radiation driven) limited temperature recovery pose the largest source of measurement error and mandate extensive broad-range calibration and data correction [37]. Therefore, as these detrimental effects become increasingly dominant at higher flow total temperature, the use of conventional probes for measurements in high-enthalpy environments is unfeasible, rendering non-intrusive optical diagnostics more attractive. More established optical techniques employed at the nozzle exit and test section, such as absorption spectroscopy, laser-induced fluorescence (LIF) and coherent anti-Stokes Raman scattering (CARS), are typically geared to freestream calibration and test time determination via probing primarily for velocity fields, species concentration and driver gas arrival [38, 39]. Considering fluid kinetic energy to be the primary contributor to total enthalpy of hypersonic flow, attempts to approximate nozzle reservoir enthalpy by direct measurement of kinetic energy ($h \sim v^2/2$) via test section laser velocimetry have been made to limited extent and varying success. An earlier work by Verant and Sagnier [20] measured freestream velocities of 5-6 km/s ($\sim$18 MJ/kg) in the Onera F4 tunnel via diode laser absorption spectroscopy (DLAS). Enthalpies rebuilt from velocimetry were however significantly lower than reference data from spherical stagnation heat transfer probes, which were deemed more reliable to deduce flow enthalpy. Similarly, DLAS measurements yielded no decisive information on the thermochemical state of the freestream flow (i.e. frozen or in equilibrium). In a more current work, Parker et al. [40] used tunable diode laser absorption spectroscopy (TDLAS) in the LENS I facility to measure freestream velocities of 2-5.4 km/s at the nozzle exit by Doppler velocimetry. Comparison with simple shock tube-code calculations of reservoir quantities indicated close agreement up to 11 MJ/kg. Beyond, as facility operation at higher enthalpies began to deviate from tailored interface mode, measurements increasingly deviated from calculations: at 14.2 MJ/kg, the total enthalpy was found to be $\sim$15% higher than predicted numerically, as induced by over-tailored operation not adequately captured by the shock tube-code. As deviations are expected to rise according to flow total enthalpy, direct measurement of freestream velocity was deduced to be a valuable tool to extend verified facility operation range to higher

enthalpies, where to attain full-tailored interface is difficult and where accuracy of established numerical tools of reservoir state prediction is increasingly compromised due to non-tailored conditions.

1.2.4 In situ quantification of reservoir conditions

Evidently, indirect approaches of reservoir state determination such as backward calculation from freestream convective heat transfer suffer from multiple sources of uncertainty, including experimental inaccuracies as entailed by surface heat transfer, data reduction and gauge calibration. Similarly, the intricate thermochemical relaxation process of hypersonic nozzle expansion compromises accuracy of indirect approaches to deduce reservoir quantities from optical diagnostics within and downstream of the nozzle. Even though related by nozzle flow calculations, in as much as measurement of freestream quantities is best achieved directly at the nozzle exit, reservoir quantities are most accurately determined locally at the nozzle supply section [39]. At the reservoir location, excessive pressure and density levels inhibit use of planar laser-induced fluorescence (PLIF) due to large collisional quenching rates. As for predissociation LIF, success rate is expected to be very low due to strong background radiation, in the form of heated test gas luminosity and particle radiation, which will outweigh weak signal amplitudes. With regard to robustness in the presence of harsh test environments, frequency-based techniques are clearly to be favoured over intensity (i.e. amplitude)-based methods. Above, in the light of a 1-D homogeneous shock tube flowfield, the straightforward use of laser-induced grating spectroscopy (LIGS) in combination with single-point calibration at ambient (i.e. initial) conditions is deemed more attractive than intricate PLIF setups, particularly as potential 2-D spatial resolution is not deemed to yield any additional information. As direct measurements in the nozzle supply by means of intrusive probes are impractical and prohibitive, nonintrusive means for in situ quantification of reservoir total enthalpy are rendered even more attractive [39]. To this end, in order to contribute to a more accurate determination of nozzle supply upstream (i.e. inlet) boundary conditions in hypersonic ground testing, laser-induced grating spectroscopy is proposed to provide for nonintrusive, time-accurate, high-accuracy, in situ measurements of nozzle reservoir stagnation temperature. In this context, the frequency dependence of temperature determination by LIGS is regarded particularly useful for harsh test environments, in as much as the frequency dependence of Doppler shift velocimetry proved to be more robust (including lower experimental uncertainty) than intensity-based measurements of temperature and species concentration by absorption spectroscopy in hypersonic flow [40]. Moreover, many optical methods and particularly absorption measurements are limited by line of sight integration, effectively probing any media they traverse, including the turbulent wall boundary layer, adding spurious background noise to measurements. In contrast, LIGS provides for accurate single-point measurements with high spatial resolution ($\sim$70 μm) in the core flow region of interest, thus unaffected by adverse side effects.

1.3 Motivation

This thesis details the work progress and outcome of my work as research assistant and doctoral student in the aerothermodynamics research group of Prof. Christian Mundt at the Institute for Thermodynamics, Department of Aerospace Engineering, at the University of the federal armed Forces Munich (Germany). The work has been carried out from February 2015 - March 2021 and focuses on the advancement of facility operation conditions and the determination of caloric stagnation conditions in the nozzle reservoir of the hypersonic free-piston reflected shock tunnel HELM (High-enthalpy laboratory Munich). By pursuing the groundwork of my predecessors, Katrin Schemperg and Philipp Altenhoefer, detailed operation conditions for the HELM facility for tuned driver and tailored interface operation across the entire operational envelope and up to the full-range of 110 MPa burst pressure and 25 MJ/kg stagnation enthalpy have been calculated for the first time.

1.3.1 Scope of the present work

Quantification of free-stream conditions at the test section and nozzle exit of a hypersonic shock tunnel mandates accurate knowledge of physical boundary conditions in the nozzle reservoir, i.e. upstream of the nozzle inlet. This is to provide dedicated CFD calculations of the expansion process with correct initial conditions and represents a prerequisite in order to achieve a valid comparison for experimental free-stream measurements, in turn serving to validate numerical models.

Whereas pressure of the stagnated test gas is readily measured, the thermo-physical properties and coloric quantities within the nozzle reservoir are not directly measureable or only with great effort and subject to high uncertainty. Typically, the latter are themselves determined by numerically modeling endwall-reflection of the incident shock, based on the shock velocity and readily assuming full thermo-chemical equilibrium in the post-reflected shock regime, based on physical reasoning. This argument is also employed by indirect approaches of numerical rebuilding of test flow conditions where stagnation enthalpy is deduced from ex situ measurements of absolute and pitot pressure and free-stream stagnation point heat transfer. However, in situ nozzle reservoir measurements, to substantiate or to disprove the equilibrium state hypothesis, have neither been carried out nor published as yet.

Against this background, non-invasive laser-diagnostic techniques such as LIGS (laser-induced grating spectroscopy) prove to be a valuable tool for the in situ determination of stagnation temperature in the highly-loaded nozzle reservoir. At the time of initiation of this work, LIGS had been priorly used to success for temperature measurements in the more benign test environments of quiescent test chambers and small conventional shock tubes. Thereafter, it was successfully applied to the HELM shock tunnel in 2015, measuring translational temperatures up to 1100 K (around 1.2 MJ/kg) in the post-reflected shock regime of a full-scale hypersonic test facilitiy for the first time - yet, at sub-optimal operation conditions, i.e. without tuned-piston operation and tailored contact surface. Accordingly, the success rate of single-shot mea-

surements was notably lowered due to the presence of secondary shock waves and pronounced pressure fluctuations.

Therefore, the objective of this work was to apply LIGS to stagnation temperature measurements in the HELM nozzle reservoir at elevated operation conditions, of increasing stagnation pressure and temperature, and at better behaved test conditions, allowing for a steadier pressure trend in the test volume. As suitable facility operation conditions, characterized by tuned piston and tailored interface behaviour, with noble gas driver and at diaphragm burst pressures beyond 300 bar were not yet determined at the onset of this work, the latter were to be developed based on established theory and to be empirically refined in the scope of this thesis. In order to successfully achieve the latter, a number of structural requirements of the HELM facility were rendered necessary, entailing a substantial mechanical revision and new design of some of the facility's core parts.

1.3.2 Starting point of this work

Fundamental development and mechanical design as well as the preliminary numerical prediction of operation conditions of the HELM facility are detailed in the work of Schemperg [41]. The facility is in operation since 2010 and was mainly operated until 2015 with a free-piston driver using air as driver gas and at maximum stagnation enthalpy, pressure and incident shock Mach number of $\sim$2 MJ/kg, 200 bar and 3.5, respectively. The highest burst pressure achieved so far was $\sim$400 bar. It was evident that the present operation conditions did not provide for a sufficiently long and quasi-steady test time at the nozzle exit, due to an off-tuned piston trajectory in the driver and an off-tailored contact surface in the driven section. Preliminary measurements with a full helium driver entailed moderate impact of the compression piston on the diaphragm station as the compression piston having been used so far did not feature a high-pressure piston seal to prevent noble gas leakage. In contrast, for the first time in an impulse facility worldwide, measurements of the time-resolved piston acceleration by an on-board sensor had been achieved by a prototype accelerometer device and for a single operation condition. Yet, complete reconstruction of the full-stroke piston trajectory was yet outstanding. In situ measurements of post-shock wave stagnation temperature in the nozzle reservoir have been conducted successfully and for the first time in a full-scale hypersonic test facility by Altenhoefer [42]. Measurements were however evident to be significantly limited by a low single-shot success rate and systematically inhibited due to particle loading of the test gas, recessed-mounted optical access windows to the nozzle reservoir and abrupt mechanical recoil and impact of the shock tunnel. Overcoming the latter three limitations represents the main challenge and effort of the present work. Once suitable driver and shock tube operation conditions were to be determined, the resulting free-stream conditions at the nozzle exit and hence performance of the HELM facility were to be quantified and characterized. This encompasses experimental measurements within the free-stream, numerical simulation of the test gas flow through the expansion nozzle and in the test section as well as the implementation and application of combined experimental-numerical rebuilding routines.

1.3.3 Structure of this work

According to the main objectives of this work, the thesis encompasses three fundamental chapters and details the relevant work progress. The first main thread focuses on the prediction and refinement of suitable tuned-piston and tailored-interface operation conditions of the HELM shock tunnel. Higher incident shock Mach numbers and stagnation enthalpies were to be achieved by implementation of a noble gas driver, which employs mixtures of helium and argon as driver gas. Simultaneously, the diaphragm burst pressure was to be systematically increased, in turn necessitating to achieve a soft-landing of the compression piston for safe facility operation. This objectives entailed fundamental mechanical redesign of the compression piston and integration of a wear-resistant high-pressure piston seal against high sound speed noble gas leakage. Moreover, ST orifice plates of varying area contraction were to be designed and used to limit driver gas mass flow and hence to achieve tuned-piston operation. Simultaneously, the piston trajectory predicted by different theories of tuned-operation was to be validated by experimental measurements of the instantaneous acceleration by an on-board mounted remote sensor. Measurements are compared against the 1-D point mass models of piston motion as well as predictions by the well-established L1d-code.

The second main thread details the application of LIGS to higher operation conditions, i.e. rising stagnation temperature and pressure, in the nozzle reservoir. Towards the start of this work it was evident that the successrate of single-shot measurements could only be improved by proving for a clean test gas and a minimized mechanical recoil and impact of the facility, such as to not deflect laser beams. Further, the level of temporal and spatial test gas perturbance within the nozzle reservoir at test time instant was to be systematically lowered at all cost. This entailed refurbishment and cleaning of the upstream buffer pressure vessel, design and construction of a heavy-duty hydraulic damping system as well as mechanical design of construction of flush-mounted optical access windows to the nozzle reservoir.

The third and last main thread describes the effort to systematically quantify free-stream conditions at the nozzle exit. This encompasses experimental measurements of pressure and stagnation point heat transfer in the test section, CFD predictions of the nozzle expansion process and within the test section and around intrusive probes, as well as a combination of both towards numerical-experimental rebuilding of test conditions and total enthalpy.

2 Free-Piston Shock Tunnel Operation Conditions

Besides real flight testing and numerical simulation, experimental simulation by ground testing constitues in short-duration facilities constitutes the third central pillar of aerothermodynamic analysis of high-enthalpy reentry and hypersonic airbreathing propulsion vehicles. Since the advent of the free-piston driver, shock tunnels represent the primary means for high-enthalpy ground testing as they are able to reproduce most of the relevant physical, chemical and thermal similarity parameters for duplication of an engine and trajectory relevant free-stream conditions - yet, only for a limited timescale of around t<10 ms.

2.1 Operation principle

2.1.1 Reflected shock processing

In reflected shock tunnels, high stagnation pressure and enthalpy of a relevant test gas are most effectively reached via strong compression and heating via two-fold shock processing by an incident and reflected shock wave within the shock tube. A schematic of a reflected shock tunnel is given in Fig. 2.1.

The incoming primary shock wave yields shock-compression and heating from state 1 to state 2. Incident shock pressure and temperature ratio are defined as follows:

$$p_{21} = \frac{p_2}{p_1} = 1 + \frac{2 \cdot \kappa}{\kappa + 1}(Ma_1^2 - 1). \tag{2.1}$$

When reformulating the isentropic exponent κ for the test and driver gas:

$$\alpha_1 = \frac{\kappa_1 + 1}{\kappa_1 - 1}, \quad \alpha_4 = \frac{\kappa_4 + 1}{\kappa_4 - 1}, \tag{2.2}$$

density and temperature ratio yield:

$$\rho_{21} = \frac{\rho_2}{\rho_1} = \frac{1 + \alpha_1 \cdot p_{21}}{\alpha_1 + p_{21}} \tag{2.3}$$

$$T_{21} = \frac{T_2}{T_1} = p_{21} \cdot \frac{\alpha_1 + p_{21}}{1 + \alpha_1 \cdot p_{21}}. \tag{2.4}$$
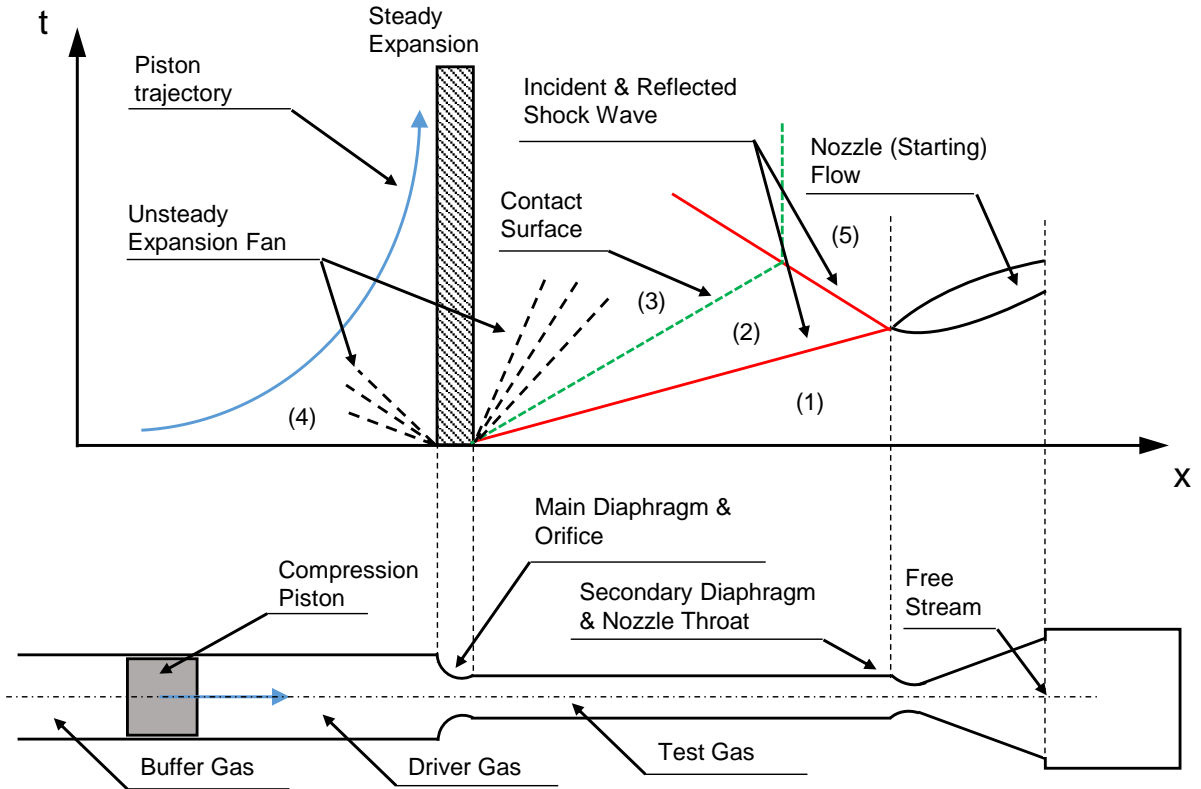
Figure 2.1: Schematic of a reflected shock tunnel with wave diagram.

Upon incident shock passage the test gas is accelerated by a velocity relative to the initial speed:

$$u_k = u_2 - u_1 = a_1 \cdot \frac{(\alpha_1 - 1)(p_{21} - 1)}{\sqrt{(1 + \alpha_1)(1 + \alpha_1 \cdot p_{21})}}. \tag{2.5}$$

Upon incident shock reflection off the plane shock tube endwall or the secondary diaphragm, the reflected shock again propagates upstream where the (re-)compression is characterized as follows:

$$p_{52} = \frac{p_5}{p_2} = \frac{p_{21} \cdot (\alpha_1 + 2) - 1}{\alpha_1 + p_{21}}. \tag{2.6}$$

Density and temperature ratio across the reflected shock wave are defined accordingly:

$$\rho_{52} = \frac{\rho_5}{\rho_2} = \frac{1 + \alpha_1 \cdot p_{52}}{\alpha_1 + p_{52}}. \tag{2.7}$$

Considering the test gas within the shock tube to be initially at rest, $u_1 = 0$, equation 2.5 is rewritten as follows:

$$u_2 = a_1 \cdot \frac{(\alpha_1 - 1)(p_{21} - 1)}{\sqrt{(1 + \alpha_1)(1 + \alpha_1 \cdot p_{21})}} = a_2 \cdot \frac{(\alpha_1 - 1)(p_{52} - 1)}{\sqrt{(1 + \alpha_1)(1 + \alpha_1 \cdot p_{52})}} \tag{2.8}$$

$$T_{52} = \frac{T_5}{T_2} = p_{52} \cdot \frac{\alpha_1 + p_{52}}{1 + \alpha_1 \cdot p_{52}}. \tag{2.9}$$

With respect to the upstream driver conditions, change from state 4 to state 3 is governed by isentropic expansion of the driver gas from compression-tube conditions to the state behind the contact surface:

$$\frac{p_4}{p_3} = \left(\frac{a_4}{a_3}\right)^{\frac{2 \cdot \kappa_4}{\kappa_4 - 1}}. \tag{2.10}$$

Considering an unsteady expansion wave, the velocity of state 3 is characterized as follows:

$$u_4 + \frac{2}{\kappa_4 - 1} \cdot a_4 = u_3 + \frac{2}{\kappa_3 - 1} \cdot a_3 \tag{2.11}$$

which simplifies due to $u_4 = 0$. The incident shock Mach number, as resulting from unsteady driver gas expansion is thus defined according the the compression and shock tube pressure ratio across the main diaphragm:

$$\frac{p_4}{p_1} = \left[1 + \frac{2\kappa_1}{\kappa_1 + 1}(Ma_1^2 - 1)\right] \cdot \left[\frac{1}{1 - \frac{\kappa_4 - 1}{\kappa_1 + 1}\frac{a_1}{a_4}(Ma_1 - \frac{1}{Ma_1})}\right]^{\frac{2\kappa_4}{\kappa_4 - 1}}. \tag{2.12}$$

Here, the isentropic definition of the speed of sound for an ideal gas is used to write:

$$\frac{a_4}{a_1} = \sqrt{\frac{\kappa_4 R_4 T_4}{\kappa_1 R_1 T_1}}. \tag{2.13}$$

2.1.2 Tailored-interface operation

In order to yield engine representative test conditions which duplicate free-flight regimes as close as possible, operation and test conditions of short duration facilities are specifically geared to cover a certain Reynolds- and Mach-number regime of a predefined vehicle trajectory. Besides providing for an accurate match of relevant non-dimensional similarity variables, the quality of test conditons is defined by the degree of temporal continuity of flow quantities and the available test time interval. In terms of a reflected shock-tunnel such as the HELM facility, the latter is dictated by dynamics of the contact surface (CS) between driver and test gas within the shock tube.

Reflected shock wave - contact surface interaction

The three characteristic reflected shock tunnel operation conditions (undertailored / overtailored / tailored) are classified upon reflected shock wave and contact surface interaction. Before proceeding to distinguish those three fundamental cases, the general equations which similarly govern all three states alike are established. For this purpose, Fig. 2.2 illustrates interac-
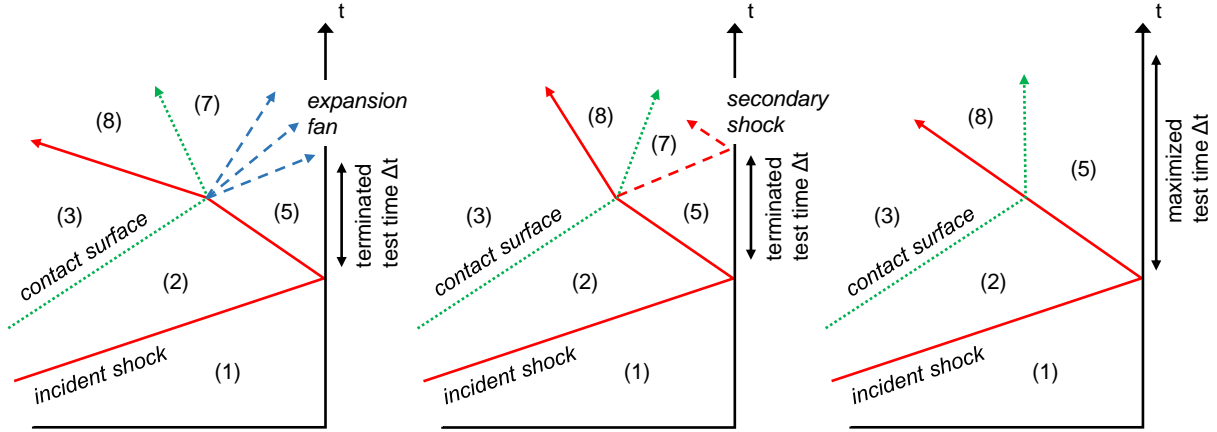
Figure 2.2: Wave diagram within the ST for undertailored (left), overtailored (middle) and tailored (right) contact surface, reproduced from [43].

tion of the contact surface and the reflected shock wave for the two non-ideal cases of over-/ and undertailored conditions and the ideal (tailored) case.

Considering continuity of velocity across the contact surface $u_3 = u_2$ as well as $u_8 = u_7$, driver gas velocity change across the reflected shock $u_8 - u_3$ for both non-ideal (under-/ overtailored) cases is seen to likewise describe test gas velocity change $u_7 - u_2$ and hence to write:

$$u_8 - u_3 = -a_3 \cdot \frac{(\alpha_4 - 1)(p_{83} - 1)}{\sqrt{(1 + \alpha_4)(1 + \alpha_4 p_{83})}} = u_7 - u_2. \tag{2.14}$$

Considering driver and test gas properties $\alpha_3 = \alpha_4$ as well as $\alpha_1 = \alpha_2$ to be maintained, respectively, one can write:

$$u_7 = a_1 \cdot \frac{(\alpha_1 - 1)(p_{21} - 1)}{\sqrt{(1 + \alpha_1)(1 + \alpha_1 p_{21})}} - a_3 \cdot \frac{(\alpha_4 - 1)(p_{83} - 1)}{\sqrt{(1 + \alpha_4)(1 + \alpha_4 p_{83})}}. \tag{2.15}$$

Undertailored operation

In the first non-ideal case of undertailored operation, the post-reflected shock pressure p_5 emerges to be too high with respect to the pressure upstream of the contact surface, such that the latter is not brought to rest upon interaction with the reflected shock but rather pushed back upstream. Here, the initial shock tube pressure p_1 has been set too high or the entailed incident shock Mach number was too low. In the undertailored case of an forward-facing CS, the reflected shock wave is convexly refracted upon contact surface penetration such that an additional expansion fan is formed, propagating toward the ST endwall. This entails a change of state from 5 to 7 for the test gas whereas the driver gas behind the contact surface is reflected shock-compressed to yield state 8 from state 3, see Fig. 2.2.

The unsteady expansion from state 7 to state 5 is described by:

$$u_7 - \frac{2}{\kappa_1 - 1} \cdot a_7 = u_5 - \frac{2}{\kappa_1 - 1} \cdot a_5 \tag{2.16}$$

with $u_5 = 0$. When assuming an isentropic relation between state 7 and 5, the former can be written by Eq. 2.16 as:

$$\frac{p_7}{p_5} = \left(\frac{a_7}{a_5}\right)^{\frac{2 \cdot \kappa_1}{\kappa_1 - 1}} = \left(1 + \frac{\kappa_1 - 1}{2} \frac{u_7}{a_5}\right)^{\frac{2 \cdot \kappa_1}{\kappa_1 - 1}}. \tag{2.17}$$

In order to yield a pressure decrease according to the expansion wave of $p_7 < p_5$, Eq. 2.17 dictates $u_7 < 0$. Here, the induced expansion wave is seen to prematurely terminate reflected-shock test gas state 5 in the nozzle reservoir by an ensuing pressure decrease. Evidently, undertailored operation is not desirable in order to attain a long duration, steady state test flow into the nozzle section.

Overtailored operation

In the second case of overtailored operation, the post-reflected shock pressure p_5 emerges to be too low in order to bring the contact surface to rest upon reflected shock interaction; instead, it is seen to still propagate downstream towards the ST endwall. Here, the initial shock tube pressure p_1 has been set too low or the entailed incident shock Mach number was too high. In the overtailored case of an backward-facing CS, the reflected shock wave is concavely refracted upon contact surface penetration such that an additional compression wave is formed, propagating toward the ST endwall. This entails a change of state from 5 to 7 for the test gas whereas the driver gas behind the contact surface is reflected shock-compressed to yield state 8 from state 3, see Fig. 2.2.
The velocity in region 7 is governed by the relation:

$$u_7 = a_5 \cdot \frac{(\alpha_1 - 1)(p_{75} - 1)}{\sqrt{(1 + \alpha_1)(1 + \alpha_1 p_{75})}}. \tag{2.18}$$

In order to yield a pressure increase according to the compression wave of $p_7 > p_5$ Eq. 2.18 dictates $u_7 > 0$. Here, the induced compression wave is seen to prematurely terminate reflected-shock test gas state 5 in the nozzle reservoir by an ensuing pressure increase. Evidently, overtailored operation is likewise undesirable in order to attain a long duration, steady state test flow into the nozzle section.

Tailored interface cnditions

As opposed to both preceding non-ideal cases, the ideal operation condition of a reflected shock tunnel is referred to as Tailored-Interface condition. The latter describes a well-matched combination of CT driver pressure p_4 and ST initial fill pressure p_1 which entail an incident shock

Mach number and post-reflected shock pressures, apt to bring the contact surface between driver and test gas to rest. As illustrated in Fig. 2.2, this ideal case indicates the longest-possible test time interval of a steady, unperturbed nozzle reservoir state 5. For Tailored Interface conditions, the test time interval is not terminated before the test gas is entirely entrained into the nozzle section.

In this case, neither a compression nor an expansion wave is formed upon reflected shock penetration of the halted contact surface such that intermediate state 7 is seen to coincide with post reflected-shock state 5. More in detail, considering pressure continuity $p_7 = p_5$, equation 2.21 and 2.22 are found to likewise reduce to $u_7 = u_5 = 0$.

When further considering conditions across the contact surface for pressures $p_7 = p_5 = p_8$ and $p_3 = p_2$ as well as pressure ratios $p_{83} = p_{52}$, the velocity continuity $u_3 = u_2$ left and right of the contact surface together with Eq. 2.14 yields:

$$u_2 = u_3 = a_3 \cdot \frac{(\alpha_4 - 1)(p_{52} - 1)}{\sqrt{(\alpha_4 + 1)(\alpha_4 p_{52} + 1)}} = a_1 \cdot \frac{(\alpha_1 - 1)(p_{21} - 1)}{\sqrt{(\alpha_1 + 1)(\alpha_1 p_{21} + 1)}} \qquad (2.19)$$

which is defined as the required and sufficient condition for Tailored Interface operation according to Nishida [43]. Eventually, for every sound speed ratio of driver and test gas a_4/a_1 there exists a specific ratio of burst pressure to initial test gas pressure p_4/p_1 to achieve tailored interface operation. When assuming an isentropic (adiabatic) driver gas compression with $\Delta s = 0$ according to Eq. 1.8, driver gas state quantities in a free-piston driver (FPD) at diaphragm rupture, p_4, T_4, ρ_4 and a_4, are found to be unambiguously determined by the volumetric compression ratio λ:

$$\lambda = \left(\frac{L_{40}}{L_4}\right) = \left(\frac{\rho_4}{\rho_{40}}\right) = \left(\frac{p_4}{p_{40}}\right)^{\frac{1}{\kappa}} = \left(\frac{T_4}{T_{40}}\right)^{\frac{1}{\kappa-1}} = \left(\frac{a_4}{a_{40}}\right)^{\frac{2}{\kappa-1}}. \qquad (2.20)$$

Considering test gas sound speed a_1 being fixed, the intial ST pressure p_1 is thus the single remaining quantity to be matched to yield tailored interface conditions after shock endwall-reflection. As has been shown by Esser [23], high shock Mach numbers necessitate for very high driver temperatures T_4, i.e. sound speeds a_4, which cannot be simply achieved by a conventional shock tube with heated driver section, but only by either a detonation or free-piston driver of high compression ratio $\lambda > 50$.

An alternative approach to determine conditions which yield a contact surface at rest is provided by Oertel [7], who defines tailored interface conditions according to acoustical theory. More precisely, in the case of tailored conditions, neither a shock wave nor an expansion wave is generated upon reflected shock penetration of the contact surface - which is found to coincide with the condition for reflection-free (i.e. anechoic) transmission of a sound wave upon transition between two media of different acoustical properties (namely driver and test gas, respectively). The condition from matched acoustic resistances or impedances is given by Oertel

as follows:

$$\frac{f_4(2+f_1)}{f_1(2+f_4)} < \frac{a_2}{a_3} < \frac{f_4}{f_1}\sqrt{\frac{2+f_1}{2+f_4}\frac{1+(1+f_1)(3+f_1)}{1+(1+f_4)(3+f_4)}} \qquad (2.21)$$

where f_1 and f_4 denote the internal degrees of freedom of the driver and test gas alike:

$$\kappa = \frac{f+2}{f}. \qquad (2.22)$$

In contrast to Nishida's theory which presents a closed system of equations and yields an unambiguous set of parameters for tailored interface, Örtel's theory merely yields a range of values and hence is not suitable for an accurate and unambiguous calculation of tailored interface conditions. Thus, in the scope of this work, tailored interface parameters are determined according to Nishida's theory whereas Örtel's equation is only employed as a secondary and optional criterion.

2.1.3 Tuned driver operation

Besides off-tailored ST operation, quasi-steadiness of test gas conditions in the nozzle reservoir as well as the free-stream, and hence the relevant test time interval, is significantly determined by driver gas pressure at the upstream ST inlet after diaphragm rupture. Precisely, strength of the incident shock wave, whose Mach number is initially determined according to Eq. 2.12, can decrease significantly as it propagates downstream the ST. This attenuation - besides losses due to viscous wall boundary layer friction [44, 45] - ensues from a premature drop of driver pressure in the time after diaphragm opening and applies primarily to free-piston drivers, where the two cases of a constant volume and a constant pressure driver are being distinguished.

In the first case, the piston has just enough kinetic energy to compress the driver gas for a specified diaphragm burst pressure to be reached and will rapidly decelerate and eventually come to rest shortly afterwards. Thereby, whereas the driver gas volume is considered near constant, driver gas outflow through the orifice plate and diaphragm station (where critical conditions due to a steady expansion are reached) induces a rapid decrease in driver pressure. In terms of wave dynamics, this pressure decrease manifests in the form of an expansion wave which moves upstream into the high sound speed driver gas and reflects off the low-velocity piston front. The formation of this reflected, unsteady expansion fan, the (u+a)-characteristic, has been described in detail by Gildfind [11], who reasoned the former to propagate downstream the ST at a velocity higher than the incident shock speed. Accordingly, the duration of quasi-steady test gas state (5) and hence test time will be significantly limited due to premature arrival of the expansion fan at the ST endwall. In effect, post-reflected shock pressure p_5 in the nozzle reservoir will continuously decrease shortly after incident shock endwall-reflection and hence significantly compromise test condition continuity. In the worst case the (u+a)-characteristic will overtake the incident shock wave and arrive at the ST enwall first, such that effectively no
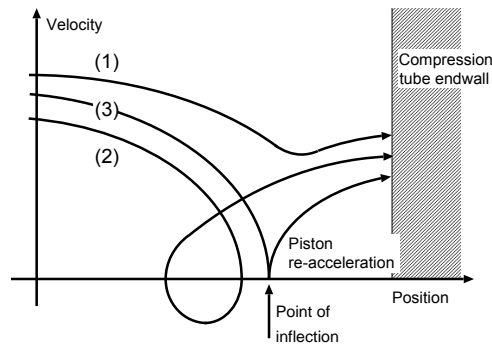
Figure 2.3: Characteristic piston motion in a FPD following diaphragm rupture: (1) direct impact, (2) rebound impact, (3) soft landing. Reproduced from [47].

quasi-steady conditions in the nozzle reservoir and no steady test time will be available at all. In contrast, the second case of a constant pressure driver describes the concept of compensating the driver gas outflow into the ST due to a finite, residual piston stroke at the moment as well as beyond time instant of diaphragm rupture. This aims at a sustained driver pressure in order to ensure quasi-steady expansion of the driver gas into the ST - as opposed to an unsteady expansion of compressed driver gas. Thereby, the (u+a)-characteristic is effectively suppressed and the detrimental attentuation of the incident shock wave is being alleviated [11]. This technique has been successfully applied to most facilities with FPD worldwide, shock tunnels and expansion tube alike [46–49], in order to increase the available test time interval. Yet, in as much as driver gas outflow compensation by finite piston stroke is effective, secure piston deceleration becomes increasingly difficult as driver gas speed of sound and volumetric compression ratio increase. Hence, safe facility operation - particularly at high-enthalpy - demands for an accurate design of FPD operation conditions.

2.1.4 Tuned piston operation and soft landing

Compression piston trajectory

A systematic analysis of the piston motion towards the end of the stroke was presented by Itoh [46], who identified three scenarios of piston motion at the top dead center, Fig. 2.3. In the first case of direct impact, the piston is not sufficiently decelerated to rest by the driver gas, striking into the CT endwall with a residual velocity. In the second case of rebound impact, the piston is overly decelerated beyond the point of rest and further pushed back upstream into the CT by high pressure driver gas. At a turning point and as driver gas vents into the ST, residual buffer pressure again accelerates the piston in downstream, potentially reaching high velocities over large relative distance and striking into the endwall uncontrolled. Both cases have in common to result from a mismatch of reservoir (buffer) pressure and initial driver pressure acting on the piston rear and front face, respectively, inducing an excessive or insufficient piston acceleration. Only the third case of soft landing ensures safe deceleration to near rest at the point of inflection, ensuring tolerable impact speed on the buffer thereafter.
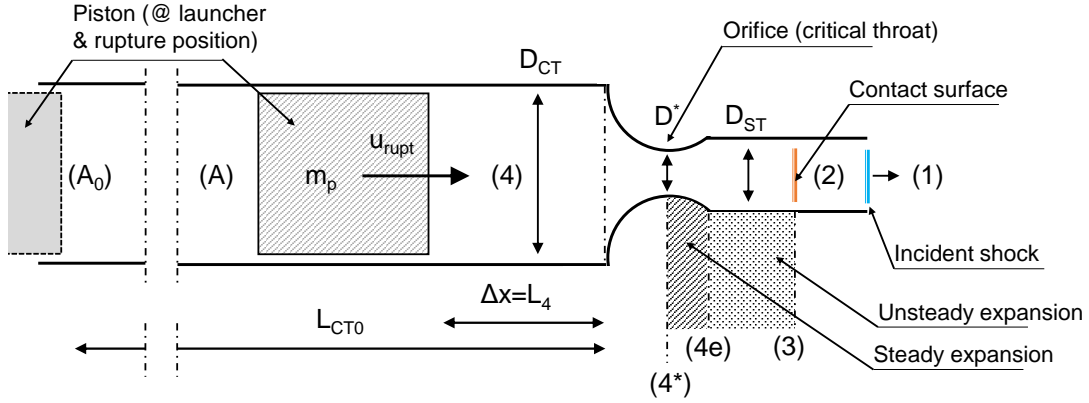
Figure 2.4: Schematic of tuned driver operation at diaphragm rupture.

Reference piston velocity

In order to determine suitable shock tunnel operation conditions - in terms of matched driver and shock tube as well as piston buffer (reservoir) initial fill pressure -, several alternative approaches of varying complexity exist in literature. These theories alike consider free piston dynamics in terms of a point mass, which is being accelerated and decelerated due to time-varying buffer and driver gas pressure.

At the moment of diaphragm rupture, compensation of driver gas for sustained driver pressure demands mass continuity between the residual piston stroke and critical conditions at the orifice throat:

$$\dot{m} = \rho_4 u_4 D^2 = \rho^* a^* D^{*^2}. \tag{2.23}$$

Considering index 4 to represent total (stagnation) driver gas conditions, isentropic equations for critical conditions $Ma^* = 1$ yield a constant critical mass flow rate of:

$$\frac{\rho^* a^*}{\rho_4 a_4} = \left(\frac{2}{\kappa + 1}\right)^{\frac{\kappa+1}{2(\kappa-1)}}. \tag{2.24}$$

Rewriting driver gas sound speed a_4 in terms of the volumetric compression ratio λ according to Eq. 2.20, the minimum piston speed required for compensation of driver gas outflow (i.e. gas displacement), defined as reference speed u_{ref}:

$$\frac{u_{ref}}{a_{40}} = \left(\frac{2}{\kappa + 1}\right)^{\frac{\kappa+1}{2(\kappa-1)}} \frac{A_{CT}}{A^*} \lambda^{\frac{\kappa-1}{2}}, \tag{2.25}$$

is found to be directly determined by the facility geometry (ratio of CT to ST/orifice diameter D_{CT}/D^*) and the compression ratio λ - the latter being the quantity of primary importance for operation condition characterization. The initial driver gas sound speed a_{40} is known a priori, where a mole fraction of $x_{He} = 1.0$ is typically taken as the reference case, for arbitrary mixtures of the mono-atomic noble gases helium and argon. The latter are almost exclusively used as driver gases due to the absence of low-energy inner thermodynamic DOF, such that the driver gas will neither undergo vibrational excitation nor dissociation and hence can be treated as a

perfect (ideal) gas of constant isentropic exponent $\kappa = 5/3$ up to very high temperatures and compression ratios. In case a di-atomic driver gas of isentropic exponent $\kappa = 7/5$ should be desirable, nitrogen is given preference over air, as dissociation for N_2 is effectively avoided up to relevant temperatures $T \sim 5,000K$. Eq. 2.25 is the starting point of any of the three alternative theories of varying complexity and different simplifications which have been proposed in literature to analytically/iteratively calculate operation parameters to reach the minimum condition required for tuned driver operation and simultaneously meet the condition of soft and secure piston landing at the CT endwall.

Tuned piston scaling argument

The simplest model abiding tuned operation and soft landing was proposed by Hornung and Bélanger [50], who introduced the assumption of steady piston deceleration, i.e. steady driver gas pressure p_4 after the moment of diaphragm rupture in order to make the problem of piston dynamics mathematically tractable, deriving a closed-form analytical formulation of suitable operation conditions. The energy balance of piston kinetic (point mass) to potential energy (due to driver gas pressure force of piston front area) yields:

$$E_{kin} = \frac{1}{2}m_p u_4^2 = E_{pot} = F \cdot L_4 = p_4 A_{CT} L_4 \tag{2.26}$$

such that, with piston reference speed Eq. 2.25, the non-dimensional (yet λ-dependent and hence variable) parameter P is introduced:

$$P = \frac{p_4 V_{CT}}{m_p a_{40}^2} = \left(\frac{2}{\kappa+1}\right)^{\frac{\kappa+1}{2(\kappa-1)}} \left(\frac{A_{CT}}{A^*}\right)^2 \lambda^\kappa, \tag{2.27}$$

where the CT volume $V_{CT} = A_{CT} L_{CT}$ is being used to express facility geometry. For means of comparison with alternative theories and fundamental scaling analysis, the constant formulation of P - normalized by compression ratio λ - is favourable:

$$\frac{P}{\lambda^\kappa} = \frac{p_{40} V_{CT}}{m_p \left(\frac{A^*}{A_{CT}}\right)^2 a_{40}^2} = \left(\frac{2}{\kappa+1}\right)^{\frac{\kappa+1}{(\kappa-1)}} = const. \tag{2.28}$$

It is worth to note that Eq. 2.28 is the non-dimensional balancing relationship of central importance for qualitative and quantitative scaling arguments of tuned driver operation conditions for any of the three competing theories. Already at this early point of the analysis, the following relationships and general conclusions can be derived for any tuned driver operation:

1. ($p_4 \uparrow \,\hat{=}\lambda \uparrow$ for $p_{40} \sim const$) With the initial driver gas pressure being maintained at aroung $p_{40} \sim 1bar$, higher burst pressures p_4 require for higher compression ratios λ.

2. ($L_{CT} \uparrow \,\hat{=}V_{CT}\hat{=}m_p \downarrow$) A longer CT allows for a heavier piston to be used for driver gas compression as there is enough residual distance from the diaphragm station $L_4 = \Delta x$ for the piston to be safely decelerated from its reference velocity u_{ref} to rest. Longer

CT are moreover favourable, as the longer distance renders moderate (relatively low) buffer (secondary reservoir) pressures p_{A0} sufficient for acceleration and deceleration. In contrast, this argument poses more difficulty to operation of facilities with shorter CT, necessitating for lightweight pistons to be accelerated by high buffer pressures over short distance. This is due to the fact that over the relatively short residual distance $L_4 = \Delta x$ only lightweight pistons can be securely brought to rest by pressure forces $F = p_4 A_{CT}$.

3. ($p_{40} \downarrow \; \widehat{=} \lambda \uparrow \; \widehat{=} m_p \downarrow$ for $L_{CT} = const$) For constant facility geometry, a more lightweigt piston is mandatory in order to yield higher compression ratios λ when aiming at a specified burst pressure p_4. As higher λ is required particularly for high-enthalpy conditions, the latter not only necessitate for lightweight piston operation but available driver pressure holding time τ will inevitably be smaller in this case due to a lower initial driver pressure p_{40} and hence a smaller driver gas mass to be expanded through to orifice into the ST after diaphragm rupture.

4. ($a_{40} \uparrow \; \widehat{=} (A^*/A_{CT}) \downarrow$) Higher helium-fractions y_{He} of the driver gas, required for high-enthalpy conditions, mandate to operate the facility with a smaller orifice diameter D^* (dictating critical mass flux density) in order to ensure safe deceleration of the piston and avoid premature driver gas venting. However, according to Itoh et al. [46] a smaller orifice diameter is generally undesirable, as it lowers the available driver pressure holding time τ, the pressure recovery factor between CT driver (burst) pressure and ST post-reflected shock pressure within the nozzle reservoir p_5/p_4 as well as the incident shock strength, and hence stagnation enthalpy [51].

5. ($a_{40} \uparrow \; \widehat{=} p_{40} \uparrow$ for L_{CT},(A^*/A_{CT}),$m_p = const$) At constant facility geometry, orifice diameter and piston mass, higher helium driver gas fractions induce higher initial driver pressures p_{40}. For specified burst pressure p_4 this is counterproductive, as it will inevitably reduce the compression ratio λ and hence incident shock Mach number Ma_s and stagnation enthalpy h_5.

Particularly with regard to driver pressure holding time τ, and in order to avoid a premature drop of driver pressure following diaphragm rupture and entailed incident shock attenuation, the theories of Stalker [52] and Itoh et al. [46] proposed the concept of piston over-driving, whereby the reference piston speed at diaphragm rupture u_{ref} is to be exceeded by the over-driving factor:

$$\beta = \frac{u_4}{u_{ref}} \sim 1.2 - 1.6. \tag{2.29}$$

By ensuring sustained driver gas pressure beyond the factual burst pressure, premature back-pressure drop behind the incident shock is effectively avoided, such that both, pressure holding time τ and pressure recovery factor p_5/p_4 are effectively raised. Stalker [52] was the first to propose the theory for calculation of soft-landing conditions, balancing piston residual kinetic energy and potential energy required to push remaining driver gas into the ST - effectively deriving the identical expression, 2.28, as Hornung and Bélanger [50], besides a safety factor being

introduced. The assumption of steady driver gas and piston rear pressure, p_4 and p_A, after diaphragm rupture represents the primary idealization of this theory. However, the temporal argument of Stalker's over-driving concept was only a tentative argument, finally explicitly formalized by Gildfind [48] to the condition of $\beta \sim 1.4$ in order to ensure enhanced pressure holding time $\tau \sim \Delta t = 0.8519\Delta x/U_{peak}$ within a $\pm 10\%$ margin of transient driver pressure around the net burst pressure p_4.

Based on the fundamental equations of piston motion formalized by Hornung [50], the first time-resolved, closed theory for a comprehensive and in-depth calculation of facility-specific tuned piston operation conditions with a minimum number of simplifications was presented by Itoh et al. [46]. Here, similar to Hornung's intial approach, isentropic, adiabatic compression of the driver gas and an isentropic, unsteady expansion of the buffer (secondary reservoir) gas driving the piston is assumed. As such, transient variation of driver gas pressure after diaphragm rupture and in the presence of residual piston (over-drive) motion as well as transient variation of expanded buffer gas, acting on the piston rear face, are not longer neglected as in former theoretical formulations. In search of conditions which fulfill the over-drive requirement and simultaneously grant soft piston landing, Itoh et al. [46] introduce an explicit condition, defining the latter as a point of inflection along the piston trajectory, where acceleration and velocity equal zero simultaneously. This point then defines the required length of the piston buffer stop from the diaphragm station for every single operation condition, such that the piston can securely come to rest with negligible impact velocity.

Similar to Stalker [52] and Hornung and Bélanger [50], the theory by Itoh et al. [46] introduces characteristic, non-dimensional parameters to formalize their theory, where the primary variable ω:

$$\omega^2 = 2(\kappa - 1)\left(\frac{2}{\kappa + 1}\right)^{\frac{\kappa+1}{(\kappa-1)}} \frac{p_{40} V_{CT}}{m_p \left(\frac{A^*}{A_{CT}}\right)^2 a_{40}^2} \tag{2.30}$$

reflects the identical scaling relationship expressed by Eq. 2.28 and characterizes a facility-specific driver operation point. For every over-driver parameter β there exists an unambiguous $\omega(\beta)$ to satisfy the piston soft-landing condition. A linearized closed-form solution to the full system of differential equations around the typical operation point $\omega_0 \sim 1.6$ was derived by the authors.

Buffer gas expansion

For all three theories alike, in order to determine the initial buffer pressure p_{A0} within the secondary reservoir, required to accelerate the mandated piston speed u_{rupt}, an unsteady (isentropic and adiabatic) expansion of the buffer gas is assumed. Time-dependent buffer pressure $p_A(t)$, acting on the piston rear face, is described as follows:

$$p_A(t) = p_{A0} \cdot \left[1 - \frac{\kappa_A - 1}{2}\left(\frac{u(t)}{a_{A0}}\right)\right]^{\frac{2\kappa_A}{\kappa_A - 1}} \tag{2.31}$$

where subscript A denotes buffer gas (typically di-atomic dry air at ambient temperature), with $\kappa_A = 7/5$, and $u(t)$ signifying the instantaneous piston speed throughout the transient compression process. Piston rear pressure $p_A(t)$ monotonically decreases throughout the initial acceleration phase and again increases throughout the subsequent deceleration phase towards diaphragm rupture. In his initial description of the equations of motion, governing piston point-mass dynamics, Hornung [53] advocated the idea of a transient shock wave to be provoced in the (low temperature and hence low sound speed) expanded buffer gas upon rapid (peak) piston deceleration due to increased pressure of the compressed driver gas, acting on the piston front face; this idea was however neither pursued by the author himself in subsequent publications, nor by any other author in literature (according to the current author's best knowledge). Thus, continuous processing of the buffer gas due to expansion and (limited) recompression is described exclusively by Eq. 2.31.

From a time-dependent pressure-force balance across the piston, instantaneous point-mass acceleration is expressed in terms of the transient buffer and driver gas pressures, acting on the piston rear and front face:

$$F(t) = \Delta p(t) \cdot A_{CT} = (p_A(t) - p_4(t)) \cdot A_{CT} = m_p \cdot a(t) \qquad (2.32)$$

$$a(t) = \frac{du}{dt} = \frac{A_{CT}}{m_p} \cdot [p_{A0}(1 - \frac{\kappa_A - 1}{2}(\frac{u(t)}{a_{A0}}))^{\frac{2\kappa_A}{\kappa_A - 1}} - p_{40}(\frac{L_{CT}}{x(4)})^{\kappa_4}]. \qquad (2.33)$$

Eq. 2.33 is henceforth employed to determine the initial buffer pressure p_{A0}, sufficient to accelerate the piston to a required speed at the instant of diaphragm rupture, to satisfy tuned FPD operation conditions.

Driver operation point considerations

From the over-driving concept, the following conclusion can be drawn, with regard to the choice of compression piston weight:

1. In general, a long CT and heavier piston are desirable, as moderate buffer pressure p_{A0} will suffice to accelerate the piston to relevant speed for tuned piston operation u_4, while the residual distance will be long enough to securely decelerate the piston to rest. Here, the time of near constant driver pressure will be extended due to higher mass inertia. Thereby, a heavier piston will be more effective to achieve a sustained driver pressure, even without the need for (strong) over-driving $\beta > 1$. In addition, since heavier pistons are suitable for low compression ratios, i.e. high inital driver gas pressure p_{40} for a specified burst pressure, the driver gas mass to be purged from the CT is relatively larger than for a lightweight piston, such that driver gas will be displaced into the ST for a longer duration which again contributes to a sustained driver pressure holding time.

2. Moreover, considering a fixed CT diameter, i.e. piston front face area, the dynamic mechanical load on the structure will be lower for a heavier piston, which - due to its higher mass - will be subjected to much smaller peak deceleration for identical burst pressure

than a lightweight piston. In accordance, mechanical design and structural stress analysis - particularly of very lightweight pistons - require much more effort than those of heavy compression pistons [48].

3. Lightweight compression pistons require relatively larger over-drive parameters $\beta \sim 1.4$ in order to ensure sufficiently high residual velocity in order to fulfill the tuned driver requirement of driver gas outflow compensation and sustained driver pressure holding time.

In order to maximize the stagnation enthalpy of a shock tunnel with FPD, the following considerationss are fundemantal:

1. High-enthalpy conditions, i.e. strong incident shock waves, firstly necessitate for high helium fractions in the driver gas, where the significantly increased sound speed $a_4 \uparrow$ after compression necessitates for very small orifice diameters $A^*/A_{CT} \downarrow$.

2. Besides operation with pure helium, large compression ratios of the driver gas $\lambda \uparrow$ are required, which dictates low inital driver gas pressure $p_{40} \downarrow$ for a specified or limited burst pressure.

3. As a detrimental side-effect, the driver pressure holding time $\tau_{hold} \downarrow$ and pressure recovery factor $p_5/p_4 \downarrow$ will inevitably decrease notably.

4. In order to meet the requirement of large compression ratios $\lambda \uparrow$, a lightweight piston $m_p \downarrow$ is required to be able to operate with low inital driver pressures $p_{40} \downarrow$.

5. To compensate the negative effects of a lightweight piston, a high over-drive parameter $\beta > 1$ is required in order to ensure sufficient driver gas holding time $\tau_{hold} \uparrow$ and pressure recovery factor $p_5/p_4 \uparrow$.

In contrast to high-enthalpy conditions, considerations for tuning a FPD for maximized test time and stagnation pressure follows different constraints:

1. High-stagnation pressure conditions do not require high compression ratios but are characterized by low-moderate $\lambda \downarrow$.

2. Low compression ratios dictate higher initial driver pressures $p_{40} \uparrow$, for which a heavier piston $m_p \uparrow$ is rendered more suitable.

3. Due to mass inertia, heavier pistons are not as rapidly decelerated as lightweight pistons and hence facilitate longer driver pressure holding times $\tau_{hold} \uparrow$ by definition.

4. Due to the latter argument, considerable over-driving - as in the case of lightweight pistons - is not required to maximize τ_{hold}, such that $\beta \sim 1.0 - 1.2$ will suffice for heavier pistons.

5. Due to generally lower compression ratios $\lambda \downarrow$ and helium fractions $x_{He} \downarrow$, driver gas (critical) sound speed will be lower $a_4^* \downarrow$, allowing for larger orifice diameters $A^*/A_{CT} \uparrow$ to be used.

6. The latter is beneficial to facilitate increased pressure recovery $p_5/p_4 \uparrow$.

Based on the aforementioned argument and scaling relationship, a holistic approach for the theoretical design of free-piston driver and shock tube operation conditions for the HELM shock tunnel was sought. With basic geometrical dimensions being fixed, suitable operation parameters were to be determined, which allow for a tuned-piston driver with soft landing condition, allowing for strong incident shock waves to be achieved after primary diaphragm rupture and with sustained driver pressure holding time. Here, in order to achieve a first systematic increase of the HELM facility's operation parameters to the maximum conditions of its operation envelope, i.e. by rising the burst pressure from 20 MPa to 1000 MPa as well as stagnation enthalpies from 2 MJ/kg to 25 MJ/kg, effective and safe operation conditions across the entire operation envelope were to be determined. Simultaneously, for suitable FPD compression ratios in the range $\lambda \sim 40 - 100$, suitable shock tube initial pressures p_1 were to be determined which satisfy TI conditions of the CS, in order to achieve maximized quasi-steadiness of stagnation conditions in the nozzle reservoir and hence maximized test time interval.

2.2 HELM Experimental test facility

The High-enthalpy laboratory Munich (HELM) is a medium size reflected shock tunnel at the University of the Federal Armed Forces Munich (UniBwM), which employs a high-performance free-piston driver configuration. The Stalker-type facility was comissioned in 2010 and provides means for hypersonic and hypervelocity ground testing. Rapid compression and heating of the driver gas within the compression tube (CT) facilitate high ratios of pressure and speed of sound of the driver and test gas, respectively. Resultant strong shock waves generated upon rupture of the primary diaphragm (steel) enable high stagnation enthalpies and pressure of > 20 MJ/kg and 200 MPa, respectively, upon incident shock wave reflection from the end wall of the driven section. Details on the facility operation envelope and upper design points are provided in Schemperg [41] and Schemperg and Mundt [54]. When operating in reflected shock-tunnel configuration, a thin secondary diaphragm (mylar) is employed as a solid end to reach post-shock stagnation conditions by re-compression heating. The diaphragm tears and melts thereafter, giving way to the downstream Laval and expansion nozzle, which accelerates the test gas toward the test chamber. A schematic of the HELM facility is provided in figure 2.5.

The facility has a total length of 39m, with a length of the CT and ST of 21 and 10 m, respectively. CT and ST feature an inner diameter of 286 mm and 95 mm, respectively. Until 2019, two compression pistons from aluminum and steel with 57.6 kg and 145.5 kg weight, respectively, have been used in the Stalker-type free-piston driver to reach diaphragm rupture pressures
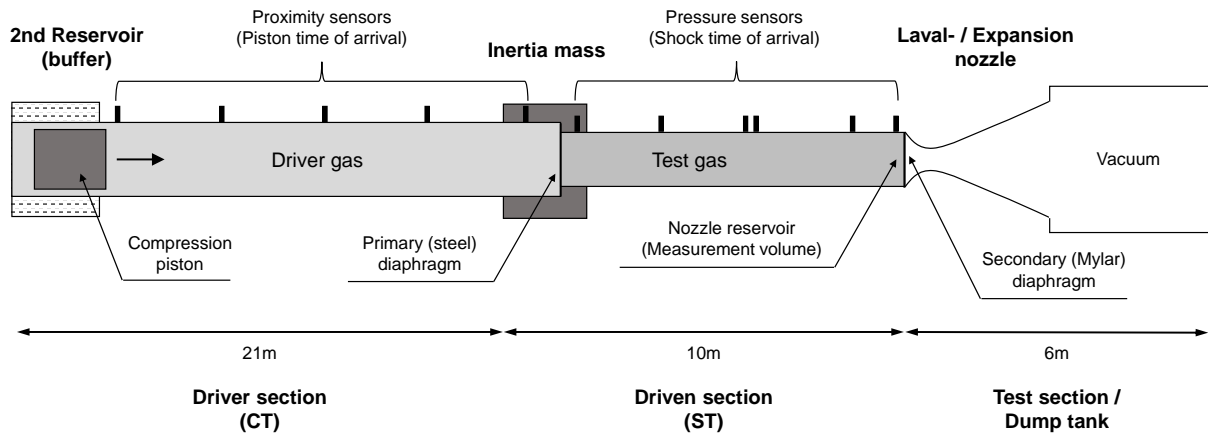
Figure 2.5: Schematic of the HELM high-enthalpy shock-tunnel facility.

throughout facility operation. The latter is varied by defining the thickness and grind depth of the primary diaphragm, which is designed to reach up to 100 MPa. Shock velocities within the ST and dynamics pressure traces within CT and ST were measured by high-pressure, fast-response piezoelectric pressure transducers (PCB Inc., type 111A22/111A23) flush mounted to the inner tube diameter and distributed along the driver and driven section. Sensors were thermally insulated against heat flux effects from shock-heated gases by a thin layer of high-temperature silicone and measure shock speeds by shock front time of arrival.

For discrete detection of the compression piston position, inductive proximity gauges are equally spaced along the CT.

2.3 HELM Facility advancement

2.3.1 Instrumentation

In the three-tier approach of this work, the first workload focussed on laser-spectroscopy measurements in the nozzle reservoir, which - at the current state of development - necessitates for experimental conditions at low stagnation enthalpy ($\sim$2 MJ/kg) and low burst pressure $\sim$20 MPa, with incident shock Mach numbers $\sim$3.5. For this range, the original dynamic pressure instrumentation - piezoelectric pressure sensors (PCB Inc., type 111A22/111A23) - was sufficient to withstand low-moderate stagnation pressures and heat loads behind the (reflected) shock wave, particularly within the nozzle reservoir. Evidently, the latter were found insufficient for the second workload of this thesis, which aimed at advancing operation parameters to the maximum design point, by predicting and validating high-pressure, high-enthalpy test conditions to cover the entire operation envelope of the HELM shock tunnel: precisely, up to 25 MJ/kg stagnation enthalpy, incident shock Mach numbers of 14.0 and diaphragm burst pressures of 110 MPa. In order to cope with expected high mechanical and thermal loads in the CT and ST, former instrumentation (intended for 'general purpose' applications according to the manufacturer) have been deliberately replaced in the course of this work by high-pressure

gauges (PCB Inc., type 109C11) since then - the latter being recommended for 'shock wave and detonation' applications by the manufacturer, with a maximum pressure ~500 MPa and an integral, ceramic diaphragm. The latter ensures sufficient thermal insulation against high heat fluxes even for the high temperatures behind strong shock waves and was found to behave superior to the typical approach of manually applying a layer of high-temperature silicone to an otherwise not thermally insulated (welded) front diaphragm surface.

In order to accurately validate and evaluate the usefulness of tuned FPD and TI conditions - being systematically predicted by theory in the following - by dedicated experiments, accuracy of the basic pressure instrumentation was to be improved. Since 2010, static pressures before the initiation of any experiment in the HELM facility were measured by static (absolute and differential) pressure gauges (WIKA GmbH, type A-10, 1% FS-accuracy) and measurement ranges of 4.0, 1.6 and 400 bar in the ST, CT and buffer (secondary reservoir), respectively. Including 1% FS-accuracy of the Siemens Simatic (PLC) ADC, maximum deviation thus amounted to 2%, inducing an uncertainty of $p_{ST} \pm 80 mbar$, $p_{CT} \pm 32 mbar$, $p_{A0} \pm 8 bar$. As such deviation was considered too large to run accurate experiments for development and tuning of new design points, the total uncertainty was henceforth reduced to 0.3% FS by deliberate replacement of former gauges by high-accuracy models (WIKA GmbH, type S-20, 0.25% FS-accuracy), closer adaption of the FS range for buffer pressure measurements p_{A0} ~100 bar, and a high-accuracy (16-bit) ADC: effectively reducing uncertainty of static pressure measurements by multiples, to $p_{ST} \pm 12$ mbar, $p_{CT} \pm 4.8$m bar, $p_{A0} \pm 0.3$ bar.

Data acquisition for high-frequency, dynamic pressure gauges and other short-duration instrumentation is accomplished by a transient recorder (MF-Instruments GmbH, type TransCom X-XL2) at sampling rates up to 5MHz and 14-bit ADC amplitude-discretization. Due to a shortage of test available test channels, this system was upgraded by a 40-channel stand-alone rack unit with 14-16 bit ADC-discretization and sampling rates up to 10MHz. Prior to digitization, differential signal amplifiers (MF-Instruments GmbH, type MFA-100) with 1 MHz full analog bandwidth (-3dB) and gain up to 1000 are used for analog signal processing.

2.3.2 Compression piston redesign

As the focus in this thesis' first step was on laser diagnostics at low-enthalpy within the nozzle reservoir, only low incident shock Mach numbers of up to ~3.5 were required, such that the first set of experiments in the HELM facility has been carried out with a di-atomic driver gas (air and/or nitrogen). For these measurement campaigns, FPD performance was of mere subordinate interest. Hence, until completion of laser diagnostic experiments, operation parameters of the driver were very low, with a maximum burst pressure of ~25 MPa and maximum buffer (secondary reservoir) pressure around ~4 MPa. No experience with higher conditions in the HELM facility was available at that time. These experiments were performed with the facility's former two compression pistons (57.6 and 145 kg weight), which have not yet been (required to be) equipped with a piston seal against driver gas leakage, but have been merely operated with two slide (wear) rings due to the original design, see Schemperg [41] and Altenhöfer [42].

Evidently, this design was not deemed suitable for high-pressure, high-enthalpy experiments with mixtures of helium-/argon as driver gas, as aspired in the second step of this work, but indeed prone to entail irreparable damage to the facility due to leakage of a low-density, high (critical) sound speed, mono-atomic driver gas and hence fatal piston impact on the diaphragm station. Thence, the piston design was to be revised fundamentally in order to ensure safe and reliable operation for tuned FPD operation with noble gas mixtures of high helium fraction. The new piston design was to fulfill the following requirements:

1. In order to ensure safe operation with a noble gas driver, effective sealing against high sound speed driver gas leakage at high pressures and compression ratios was to be accomplished by designing a suitable piston seal for the first time.

2. Prior wear (slide) rings were made from undoped (virginal white) PTFE (Teflon), which is characterized by a superiorly low friction factor but inferior mechanical resistance against abrasive wear. A suitable material was to be found in order to assure increased mechanical resistance to withstand effects of wear due to high friction shear force at increased piston velocities of up to $\sim$300 m/s.

3. Since a very early version of the old piston design incured mechanical failure of the frontal lock ring, which kept the front slide ring in place, the front part of the new piston was to be revised completely.

4. The new piston design was to ensure safe operation up to burst pressures of $\sim$1000 bar and hence was to be designed to withstand very high dynamic mechanical loads of up to 6.43 MN (normal pressure force acting on front face area).

High-pressure piston seal

In the process of devising a suitable piston seal against driver gas leakage, the technical concept suggested by Hornung [44] for the T5 shock tunnel piston was adopted. This idea is based on a wedge-shaped elastomer ring on the outer perimeter of the piston, which effectively seals against driver gas leakage by closing the gap to the CT wall by elastic deformation due to high contact pressure. In order to achieve a controlled sealing effect, which inevitably induces friction resistance to the piston, in proportion to the driving pressure, cavities by small through-hole bores in the piston front plate communicate acting pressure to the recessed wedge-shaped seal ring, effectively inducing a radial clamping force governed by the pressure to be sealed. This self-sealing concept was not only successfull in case of the T5 facility but has further been adopted in Australian FPD facilities, see [48]. In contrast, the HEG shock tunnel uses a C-shaped hollow ring of tungsten alloy, deforming under driver pressure load to achieve self-sealing by a low-friction copper band being pressed against the CT wall [55].

Choice of materials

Due to the high piston velocities and strong radial clamping forces of a pressurized piston seal, high friction forces on the circumferential surface of the seal ring are inevitable. In contrast, due to minimized mechanical contact, wear (slide) rings are much less affected by friction. Still, even at low piston velocities ~150 m/s previously encountered in the HELM shock tunnel and despite very low friction factor, undoped PTFE (virginal white) proofed too soft as the base material of future seal and slide rings, already inflicting strong abrasion and scratches in the past. After having tested different composite mixtures of PTFE doped with fibreglass, graphite and PEEK, which showed an evident increase in wear resistance with respect to virginal PTFE, these materials were however still not deemed sufficient. Finally, as suggested by Gildfind [48], PA (Nylatron) was found to be the material of choice for both seal and slide rings. By weighing the need for abrasive resistance to low friction factor, the seal ring is henceforth made from Nylatron NSM (which shows superior wear resistance) whereas the two slide rings are made from Nylatron 703 XL (granting even lower friction at a minimally reduced wear resistance). Seal and slide rings manufactured from these materials have since then been used for 170 experiments, reflecting superior performance without localized scratched but only minimum gradual and spatially homogeneous wear, even at piston speeds up to 300 m/s. Gardner [55] reported on the large-scale HEG shock tunnel to use wear rings from composite material (50% PTFE, 40% bronze and 10% graphite) with a pressure seal ring from copper coated tungsten alloy. Similarly, Gildfind [48] reported on the use of self-lubricating PA (Nylon 6 oil-filled cast) in the X2 facility for both, slide and seal rings.

As for the front plate, prior experience in the T5 facility [44] showed that use of a material with high resistance to transient heat flux is required in order to avoid or limit effects of ablation and melting at compressed driver gas temperatures up to 5,000 K, Eq. 4.21. Hence, in line with the suggestions of Hornung [44] and Gildfind [48], an aluminium-bronze-alloy with high temperature resistance, yet sufficient tensile strength, was deemed suitable. The current design thus uses a front plate from aluminium-bronze cast alloy (CC333G, 2.0975) with 5% ferritic content. This material grants superior resistance to high-temperature chemical corrosion at a melting point of ~1300 K and 650 MPa tensile strength. In case the relatively low yield strength of 280 MPa were found insufficient, a high-alloyed aluminium-bronze wrought alloy (CW308G, 2.0978) would grant significantly increased yield strength and tensile strength, yet at the expense of a reduced thermal conductivity [56]. Relevant thermo-mechanical material properties for a range of wrought and cast alloys are listed comprehensively by [56].

In regards to the piston main body and similar to the previous design [42], aluminium and steel were the materials of choice for the lightweight and heavy piston, respectively. In order to ensure high resistance to dynamic mechanical loads and increased lifetime, high-strength, highy yield stress materials have been chosen appropriate: aluminium cast alloy (EN AW 7075, 3.4365) and tempered steel (42CrMo4, 1.7225).

Mechanical screw joint

As the main body of the newly devised piston retains the primary dimensions and rear-geometry from the old design [42], is not geared to achieve a minimized weight by cut-outs, local material recess and narrowing at all cost (as in [48]), and is further manufactured from high-strength materials, the likelihood of the piston's main parts to fail mechanically due to stress overload was considered very low. Hence, the new piston was designed without the use of FEM methods. In contrast, particularly the bolted joints were identified as the weakest part of FPD piston designs: the latter typically making use of a (brass cast) lock ring at the front edge, keeping the front wear or seal ring in place while itself being fixed to the piston main body via a single, large-diameter thread, compare [44, 48]. Though having used a set of single bolts for fastening, the ring design was identified as a weak point in the HELM facility's piston design in the past, see [41, 42]. Precisely, if the inner main body and outer ring surface area are not matched suitably, strong axial mechanical load (tension) on the screw joint will inevitably result from a difference in pressure force, as the main body will generally experience stronger deceleration than the circumferential ring. This effect could only be averted by compensating axial surface area ratio with the mass ratio of both parts, which is however seldom the case:

$$F_1 = p \cdot A_1 = m_1 \cdot a_1, F_2 = p \cdot A_2 = m_2 \cdot a_2 \qquad (2.34)$$

$$a_2 = \frac{m_1}{m_2} \cdot \frac{A_2}{A_1} \cdot a_1, \qquad (2.35)$$

derived for spatially homogeneous driver pressure p, index 1 and 2 denoting either main body or circumferential ring. In order to deliberately avoid this weak point, a single solid front plate was devised, which is to keep the recessed seal and front slide ring in place, itself being fastened to the main body via a set of individual screws. In this case, any driver gas pressure acting on the front face will only exert a single axial compression force on the entire piston assembly, rather than exerting critical tension on the joints due to different compression forces (deceleration) on individual parts 1 and 2. Hence, with only axial compression forces acting on the piston rear and front face throughout both, acceleration and deceleration phase, respectively, this integral front plate design was regarded particularly advantageous. Furthermore, as relevant tension forces on the screw joint were deduced to be effectively avoided, the latter could be reduced to a minimum. The following design constraints were thus considered:

1. The maximum transient pressure force was determined to 6.4243 MN, from 1000 bar maximum nominal driver pressure and the CT area. This compression force was however not considered relevant for the screw joint, which can only fail due to tensile force.

2. From Eq. 2.35, due to the very low weight of individual steel screws (DIN 6912 flat-head and DIN EN ISO 898-1 regular head), for nominal thread dimension <M20, any driver pressure - acting on the screw head and piston front surface area - induces stronger deceleration of the screws than the piston body, by a factor of $a_2/a_1 \sim 4$. Hence, screws will be pushed in their seat by a compression force throughout the entire deceleration

phase, effectively avoiding possible failure of the screw heads due to mass inertia.

3. A moderately high steel grade 10.9 (tensile strength 1000 N/mm^2 at yield stress 900 N/mm^2 according to DIN EN ISO 898-1) for all screws was considered favourable over high steel grade 12.9 (tensile strength 1200 N/mm^2 at yield stress 1080 N/mm^2). According to the design rules for highly-stressed bolted joints (by German norm-standard VDI-2230-1-1), lower steel grades (ideally 8.8) are favoured for dynamic loads, due to the tradeoff between higher tensile strength at increased brittleness. Thus, steel grade 10.9 screws will most likely withstand a limited number of high-pressure experiments without failure, where loading beyond the yield stress will be noticed throughout maintenance due to loosening, ensuing from plastic deformation and elongation. Checking the tightening torque in intervals after a number of high-pressure experiments allows to timely notice plastic deformation and hence allows for all screws to be replaced before failure throughout succeeding experiments. In contrast, steel grade 12.9 screws will be more prone to immediately fail upon overload (potentially in the first experiment), tolerating less plastic deformation before failure.

4. Long threads - much higher then the otherwise-recommended factor of 1-2 between thread length and diameter for steel base material, required to achieve the maximum listed load limit - are recommended for dynamic loads, as they will allow for higher total (elastic and plastic) elongation before failure (VDI-2230-1-1).

Eventually, the first new piston design used a set of 12 M16x70mm (10.9) screws, where - due to assumed absence of relevant tension - DIN flat-head screws were deemed sufficient with total maximum permissable load of 1.565 MN, including a 80% reduced permissible load for flat-head screws (according to DIN 6912). Here, 6 screws each were placed over two pitch circles, see Fig. 2.6 A. Soon after the first high-pressure experiments (at maximum intermittent driver pressure of 1150 bar), this design was however found to have grossly neglected the relative pressure force between the front plate and piston main body. Precisely, the Chevron seal attains its self-sealing effect by deliberate communication of driver pressure to the recessed wedge-ring, via a number of circumferentially staggered, axial through-bores in the front plate on the outmost pitch circle, compare [44]. Further, driver pressure is only sealed effectively at the recessed Chevron seal, such that gas will reach over the outer cirumferential edge of the front plate (where driver gas leakage will be directly visible from local ablation, see Fig.A.14), and hence immediately fill the annular gap behind the front plate and seal ring. Unfortunately, this pressure was not sufficiently sealed from leaking through the tolerated radial clearance between main body and front plate, effectively reaching underneath the front plate. Hence, in the current design, the total driver pressure will thus not only effectively seal against leakage by pressurizing the wedged seal-ring, but also exert an axial force on the near total piston cross section area, resulting in a relative force of near 100% (6.4243 MN) between the front plate and the main body. This force acts as tension on the screw joint, which evidently exceeds the permissible load of 1.565 MN by multiples. Even though this worst-case consideration is some-
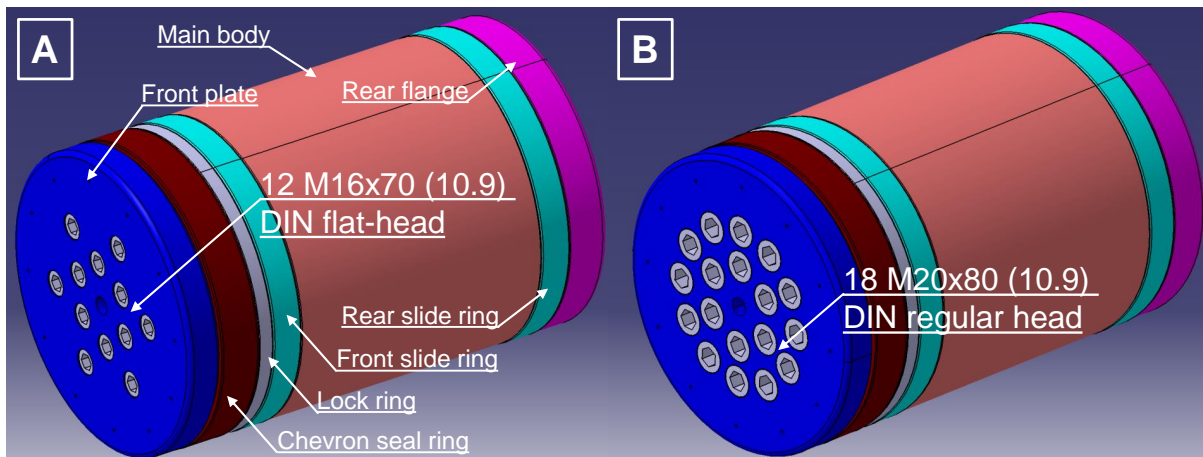
Figure 2.6: New HELM compression piston design. A: Initial version. B: First revision (final design).

what simplistic, the current screws nevertheless failed mechanically within 2-3 high-pressure (1000 bar) experiments by tearing of the screw heads, see Fig. A.15. This failure was however fortunate - flat-head screws being known to typically fail locally at the head rather than the thread (DIN 6912) - as no plastic deformation was induced in the threads, neither to the screw itself nor to the main body, such that the latter effectively incurred no damage at all, despite subsequent failing of 2 sets of screws in total. Since failure only happened in the last phase of a piston stroke, no damage to any component was inflicted and the piston assembly maintained almost perfectly attached, to be easily extracted from the CT.

Evidently, the design concept was to be revised in order to satisfy the permissable load limit of the screw joint. For this purpose, two additional radial thight-fitted o-ring seals are included within the radial gap, to seal the front plate rear area against high driver pressure, effectively reducing the relevant (wetted) surface area between main body and front plate, and hence the relative tension force on the screw joint, by 45% to 3.534 MN. This required permissable load is now achieved by increasing the number of screws from 12 to 18 (factor 1.5), increase of the thread dimension to M20x80mm and further using DIN regular head screws. Thereby, the dynamic load-appropriate steel grade 10.9 could be retained, in order to achieve permissable load with an effective safety factor of 1.3, compared to the expected maximum load of 3.534 MN. The finalized design (first revision) of the new piston is illustrated in Fig. 2.6 B.

It is pointed out that, within the above consideration, only static forces are assumed in the screw joint calculation, since a full dynamic load calculation by strictly following design rules (VDI-2230-1-1) would have required a number of 18 M36 (12.9) or 18 M39 (10.9) DIN regular head screws to achieve the total permissable load required, which was clearly deemed impractical, all the more considering the confined geometrical space. Further, an axial O-ring seal from high-temperature FKM rubber (Viton Sh75-80) was found to fail after around 10-20 experiments due to tear in the past. If a similar observation is made in the future, replacement by mechanically rigid seal rings from PTFE or copper is suggested.

2.3.3 ST Orifice plates

In the course of the present design study, the area contraction ratio from the CT to ST of A^*/A_4 ~0.11, for net tube diameters of D_{CT} =286 mm and d_{ST} =95 mm, was found to be too large in order to achieve FPD operation conditions in a realistic range of compression ratios λ ~40-100. Specifically, as the critical driver gas massflow rate is dictaced by the condition of choked driver gas at the CT-ST junction, i.e. critical diameter at the diaphragm station, the former was found to be comparatively large. In effect, the large driver gas outflow into the ST dictated very high residual piston speeds at the instant of diaphragm rupture of u_{rupt} >200 m/s in order to be able to compensate gas outflow by the piston stroke for tuned operation to be achieved. Further, impractically high buffer pressures in the secondary reservoir of 10-20 MPa resulted, which would have been required in order to accelerate the piston to such high velocities, significantly impeding safe FPD operation.

As a starting point and in order to determine a useful range of orifice diameters and CT-ST area contraction ratios for the HELM facility, the following dimensions and relevant operation parameters of other shock tunnel or expansion tube facilities, operated with a FPD worldwide, have been considered, see Table 2.1:

Table 2.1: Driver Operation Parameters of relevant shock tunnel and expansion tubes, operated worldwide with an FPD. (N/A - not available.)

Facility	-	HEG	T4	T5	HIEST	HEK	X2
Source	-	[57, 58]	[59, 60]	[44]	[61]	[46, 61]	[48]
D_{CT}	[mm]	550	229	300	600	210	257
d_{ST}	[mm]	150	76	90	180	72	85
d^*	[mm]	123-145	67	N/A	166-180	50-54	65
A_1/A_4	[-]	0.074	0.110	0.090	0.090	0.118	0.110
A^*/A_4	[-]	0.050-0.070	0.086	N/A	0.077-0.090	0.057	0.064
L_{CT}	[m]	34	26	30	42	16	4.37
L_{ST}	[m]	17	10/11	12	17	6.5	N/A
m_p	[kg]	280-700	90.4	120	220-780	30	10.5-35
p_{A0}	[bar]	23-115	24-125	15-50	52-83	40-63	11-69
p_4	[bar]	500-1000	360-750	100-500	520-900	640-740	155-360
λ	[-]	50-80	40-70	20-60	40-50	40-54	20-42.5
x_{He}	[%]	85-100	0-100	100	90-100	100	80-100
p_1	[bar]	0.24-1.24	0.3-2.5	0.1-0.95	N/A	N/A	N/A

Considering the primary dimensions of CT length, ST to CT area-ratio as well as piston speed, the following dimensions for orifice plates have been found suitable in order to gear the compression ratio of the HELM facility's FPD to a useful range of λ ~40-100 and simultaneously limit the buffer pressure to ~10 MPa, see table 2.2.

Orifice plates are manufactured from heat treatable steel with high tensile strength: 42CrMo4 (1.7225). In order to further limit plastic deformation at the surface due to the four diaphragm petals after rupture, the plates of ~35 kg weight are subjected to surface hardening treatment.

Table 2.2: Orifice plates at CT-ST junction, throat diameter and area ratio of the HELM facility.

No.	A^*/A_1	d^*	A^*	A^*/A_4
-	[-]	[mm]	[m^2]	[-]
1	1	95.0	0.0071	0.110
2	0.85	87.6	0.0060	0.094
3	0.75	82.3	0.0053	0.083
4	0.67	77.9	0.0047	0.074
5	0.50	67.2	0.0035	0.055

After machining of the basic shape by CNC milling, the parts are annealed for stress-relief before the detailed geometry and contour are manufactured. Eventually, the wear-resistance and top-layer hardness are improved by carbonitriding with moderate case-depth, in order to maintain non-hardened material underneath.

2.4 HELM Operation point design

In order to calculate detailed facility operation conditions for the HELM shock tunnel explicitly satisfying the tuned FPD and TI conditions for the first time, iterative calculation procedures outlined in the following have been implemented in MATLAB and coupled in the course of an upstream-downstream computation. This allows for seamless transfer of compressed driver gas' state quantities from tuned FPD design into the subsequent TI calculation by a computationally inexpensive and rapidly converging code.

2.4.1 Tuned piston calculation

Suitable parameters for tuned operation of the HELM's FPD while achieving soft landing condition have been calculated, based on the three established and alternative theories in relevant literature.

Hornung analysis

The analysis for tuned FPD operation by Hornung and Bélanger [50] is the simplest of the three available theories, as the closed formulation of parameter P, Eq. 2.27, facilitates direct relation of burst pressure p_4 and volumetric compression ratio λ_4. The detailed calculation procedure is outlined in the following:

1. Assign a range of desired burst pressures p_4 and specify initial driver gas by helium fraction x_{He} and thus initial sound speed a_{40} at ambient temperature $T_\infty = T_4 = T_1$.

2. For specified facility dimensions V_{CT} as well as piston mass m_p and orifice area contraction A^*/A_1, compression ratio λ_4 and initial driver pressure p_{40} are directly determined from Eq. 2.27.

3. By assuming isentropic (adiabatic) driver gas compression according to Eq. 2.20, relevant state quantities at diaphragm rupture (sound speed a_4, temperature T_4, compression ratio λ_4 and residual piston front-endwall distance $\Delta x_4 = L_4$) are directly known to calculate the reference u_{ref} and required piston speed u_{rupt}, for any assigned over-drive parameter β, from Eq. 2.26.

4. Finally, the only remaining unknown is the initial buffer (secondary reservoir) pressure p_A, which is iteratively determined from Eq. 2.31, assuming transient acceleration (and deceleration) due to time-dependent pressure forces acting on the piston front and rear face. The former is modeled by isentropic compression of the driver gas $p_4(t)$, while the latter $p_A(t)$ is modeled by an (isentropic) unsteady expansion of the low sound speed buffer gas from initial pressure p_{A0} as the piston accelerates: $p_A(u(t))$.

5. A point mass is considered for piston dynamics: $F = m_p \cdot a(t) = \Delta p \cdot A_{CT}$ and the full trajectory is explicitly computed by numerical integration via finite-differences, using either a 4th-order Runge-Kutta-scheme (2nd-order accuracy) or a 1st-order backward-Euler scheme (1st-order accuracy). Due to simplicity of the current problem, both schemes yield identical results with entirely negligible differences in time- and space-dependent variables. Convergence - for iteration of p_{A0} - is reached (and thus required p_{A0} being determined) as soon as the mandated piston speed $u(t_{rupt}) = u_{rupt}$ is reached at the required compression ratio λ_4, and hence residual piston-endwall distance $\Delta x_4 = L_4$ as the sufficient and required condition. Therein, the time between piston release $t = 0$ and diaphragm rupture t_{rupt}, required for driver gas compression, is further unambiguously determined.

Stalker analysis

The procedure for determining tuned FPD operation conditions following Stalker's [52] analysis in this work is implemented in a similar way to the approach outlined by Gildfind [48]:

1. Assign a range of desired burst pressures p_4 and specify initial driver gas by helium fraction x_{He} and thus initial sound speed a_{40} at ambient temperature $T_\infty = T_4 = T_1$. Further specify facility dimensions V_{CT} as well as piston mass m_p and orifice area contraction A^*/A_1.

2. For each assigned burst pressure p_4, start iteration with compression ratio λ as the independent variable and iterate through a plausible range of λ_4.

3. While iterating through λ, the latter unambiguously determines relevant state quantities at diaphragm rupture (sound speed a_4, temperature T_4, compression ratio λ_4 and residual piston front-endwall distance $\Delta x_4 = L_4$).

4. Thus, the reference piston speed u_{ref} and, for any assigned over-drive β, the required piston speed at diaphragm rupture $u_{rupt} = u_4$ will be determined, as well as the initial

driver pressure $p_{40} = p_4/\lambda^{\kappa_4}$.

5. Enforce the required condition - of piston kinetic to compressed driver gas potential energy balance - utilized by Stalker and Hornung according to Eq. 2.26, for assumed steady (time-independent) piston rear p_A and front p_4 pressure at the moment of as well as after diaphragm rupture.

6. Consider an arbitrary safety (scaling) factor of kinetic energy over-estimation (so as to tentatively compensate the simplification of assumed constant piston front and rear pressure - factor 2 suggested in primary literature) and deterministically calculate initial buffer pressure p_{A0} by inserting Eq. 2.26 into Eq. 2.31.

7. While aforementioned steps only satisfy the required condition, the sufficient (convergence) condition of mandated piston speed u_{rupt} at required position $x_4 = L_{CT} - \Delta x_4$ to be factually reached when utilizing the priorly projected buffer pressure p_{A0}, is to be tested by explicitly computing time-dependent piston trajectory via numerical integration of Eq. 2.33.

8. Convergence is reached as soon as an unambiguous compression ratio λ_4 and initial buffer pressure p_{A0} are determined for any assigned burst pressure p_4.

Itoh analysis

Itoh et al. [46] devised a linearization of the complete system of equations (of non-dimensionalized piston motion) around a typical operation point $\omega_0 \sim 1.6$ and presented a closed-form solution, where the parameter $\omega(\beta)$ characterizes different operation points in dependence of the over-drive parameter and facility dimensions. This linearized model is described by the non-dimensional parameters:

$$\omega^2 = \frac{1.788\beta}{1 + 0.156\beta - \epsilon[\phi - \frac{II_2}{J_\nu(\omega_0)}]} \tag{2.36}$$

where $J_\nu(\omega_0)$ denotes the Bessel function of scalar operation parameter ω, with:

$$\nu = (\kappa - 1)/2 \tag{2.37}$$

$$\alpha = (A^*/A_{CT}) * (a_{40}/a_{A0}) \tag{2.38}$$

$$\theta = \frac{\kappa_A - 1}{2} \left(\frac{2}{\kappa_4 + 1}\right)^{\frac{\kappa_4+1}{2(\kappa_4-1)}} \alpha \lambda^{\frac{\kappa_4-1}{2}} \tag{2.39}$$

and

$$z = (1 - e^{-0.075\lambda}) \cdot (0.48\beta + 0.684\omega + \frac{0.056\omega^2}{\beta}) \tag{2.40}$$

$$\epsilon = \frac{(1 - \lambda^{1-\kappa})\omega^2 + (\kappa - 1)^2\beta^2}{(\kappa - 1)(\lambda - 1)(1 - \theta z)^{\frac{2\kappa_A}{\kappa_A - 1}}\omega^2} \tag{2.41}$$

$$\phi = (1 - \theta\beta)^{\frac{2\kappa_A}{\kappa_A - 1}} \tag{2.42}$$

$$II_2 = -(0.8 + 0.004\lambda) \cdot (1.32 - 2.5\theta - (0.44 - 1.66\theta) \cdot (\beta - 0.8)^2). \tag{2.43}$$

Dimensional operation parameters are written as:

$$p_{A0} = \epsilon \cdot p_4 \tag{2.44}$$

$$\tau = (0.56 - 0.12\alpha - 1.3\alpha^2) \cdot (\beta - 1) \cdot (4 - \beta), \tag{2.45}$$

where τ [ms] denotes driver pressure holding time. In the current work, the deterministic calculation procedure is implemented as follows:

1. Solve Eq. 2.36-2.43 for $\omega(\lambda,\beta)$ in a relevant range of $\lambda =$10-100 and $\beta =$1.0-2.0.

2. Derive a relation for initial driver $p_{40}(\omega)$ and burst pressure $p_4(p_{40},\lambda)$ from Eq. 2.20 and Eq. 2.30.

3. Henceforth, determine sought compression ratio $\lambda(p_4)$ for assigned burst pressures $p_4 =$400-1000 bar and specified over-drive, e.g. $\beta = 1.4$.

4. Finally, calculate dimensional initial driver pressure p_{40}, buffer pressure p_{A0} and driver holding time τ_{hold} from Eq. 2.20 and Eq. 2.45, respectively.

2.4.2 Tailored interface calculation

Based on relevant driver gas conditions at diaphragm rupture, p_4 and $a_4(\lambda,x_{He})$, calculated by the three tuned-piston theories, ST parameters and primarily initial test gas pressure p_1 required to achieve a tailored CS are determined by iteratively solving the required and sufficient conditions defined according to Nishida's theory, Eq. 2.19. The procedure assumes a steady driver gas expansion from (total) state 4 at diaphragm rupture, considering choked flow 4* at the orifice throat A^*, and assuming a steady expansion to state 4e at the orifice exit and ST upstream inlet, Fig. 2.4. From there, an unsteady expansion of driver gas is assumed to state 3, giving rise to an incident shock wave of Mach number Ma_s, which processes the test gas from intial state 1 to post-incident and post-reflected states 2 and 5, respectively.
By limitation to noble gas mixtures of mono-atomic driver gases helium and argon, with $x_{Ar} = 1 - x_{He}$, the driver gas is modeled by ideal (perfect) gas behavior. In contrast, air as a mixture of di-atomic oxygen and nitrogen is assumed as the test gas, necessitating for considering departure from ideal gas EOS due to high-temperature thermo-chemistry for the shock-processed

states 2 and 5. As the mandatory TI-condition defined by Nishida applies to a kinematic (i.e. mechanical) velocity and pressure balance left and right of the CS, the discrepancy between different models of test gas processing were expected to be limited, nevertheless of relevant magnitude. Two procedures were implemented, firstly modeling the test gas by ideal gas EOS and secondly considering thermo-chemical equilibrium by coupling with NASA's CEA code [9]. After driver gas conditions 4 are determined - for all three TUP theories alike -, the TI-iteration for ideal and equilibrium gas differs in that the former is explicitly mathematically tractable and facilitates direct coupling between test gas states 2 and 5 and driver gas states 4e and 3 via the incident shock Mach number Ma_s as dependent variable for an assigned range of intial ST pressure p_1. For ideal gas EOS, the calculation procedure is as follows:

1. Assign state 4 quantities for an arbitrary tuned driver condition: p_4, $a_4(\lambda, x_{He})$.

2. Compute state 4e by assuming steady driver gas expansion through the orifice (nozzle) A^*/A_1 by solving Eq. 1.12 for Mach number Ma_{4e}.

3. Start iteration with incident shock Mach number Ma_s as independent variable to calculate normal shock relations, Eq. 2.1 and 2.6.

4. Solve Nishida's TI-criterion, Eq. 2.19, for u_2 and a_3; use the latter to calculate the driver gas state quantities Ma_3 and u_3 for an unsteady expansion due to Eq. 2.11.

5. Check required and sufficient condition $u_2 = u_3$ (kinematic continuity over CS) for convergence. Then impose $p_2 = p_3$ to calculate sought initial ST pressure p_1 from Eq. 2.1.

6. Calculate caloric post-shock quantities, T_2 and h_2 as well as T_5 and h_5, by assuming perfect gas behavior.

7. Check Örtel's criterion, Eq. 2.21, as a complementary indicator for completeness.

The second case of thermo-chemical equilibrium modeling by CEA, in contrast, does not allow for explicit (mathematical) coupling. Here, numerical implementation required an a priori definition of relevant test gas quantities for the post-indicent/-reflected states 2 and 5, respectively, via state surfaces of assigned incident shock Mach numbers Ma_s and initial test gas pressure p_1 for an arbitrary test gas of specified temperature T_1, formalized in the form:

$$p_{21}, p_{52}, T_2, T_5, u_2, h_2, h_5, \rho_2, \rho_5, a_2, a_5 = f(Ma_s, p_1, T_1) \tag{2.46}$$

Absolute state quantities and ratios across the normal (incident and reflected) shock are henceforth evaluated via the functional relationship of a surface fit, based on accurate cubic spline interpolation (with continuous derivative), which allows backward and forward interpolation, see Fig. A.1 in appendix. With Ma_s as iteration variable for a relevant range of p_1, the required and sufficient TI-condition defined by Nishida, Eq. 2.19, is likewise satisfied by convergence to yield equal kinematic states left and right of the moving contact surface: $u_2 = u_3$ and $p_2 = p_3$ such that the latter eventually comes to rest due to $u_5 = u_8 = 0$ and $p_5 = p_8$ after reflected

shock permeation. For identical assigned driver conditions and a predicted incident shock Mach number of similar magnitude, the initial ST pressures required to achieve TI-conditions by CEA were notably lower ($\sim$ 55%) than those ensuing from ideal gas EOS. Precisely, for high-enthalpy conditions of large incident shock Mach number Ma_s >12, intial ST pressures were predicted to be as low as p_1 <0.1 bar by CEA. In relation to relevant literature, Table 2.1, these predictions were regarded too low to be plausible and further to induce limited stagnation pressures p_5. Thus, preference was given to the larger values computed from ideal gas EOS in the following prediction of operation conditions. From experimental verification of both, the greater values of p_1 due to perfect gas behavior were found to result in under-tailored conditions by trend, whereas the lower values p_1 due to CEA were inclined to entail over-tailored conditions. Therefore, the values p_1 used within succeeding experiments were set somewhat lower than those predicted by ideal gas EOS.

In order to yield a realistic and physically relevant prediction of stagnated gas' state quantities within the ST nozzle reservoir, viscous losses are required to be considered. The latter encompass gradual attentuation of the incident shock wave as it propagates down the ST, ensuing wall boundary layer friction and inducing shock attenuation by up to 20-30% of the inviscid reference, [44]. Moreover, incident shock reflection off the ST-endwall is a non-uniform and explicitly dissipative process due to interaction of the bifurcated shock and the ST wall boundary layer, inducing a highly distorted shock front. Incured stagnation (total) pressure losses are known to range up to $\sim$30% [58]. Thus, considering ideal gas (Rankine-Hugoniot) relations as well as CEA to be inviscid by definition, i.e. assuming isentropic shock processing, incured losses are to be modeled by empirical loss factors. By evaluation of a range of $\sim$50 dedicated experiments in the HELM facility with different driver gas mixtures, orifice diameters and incident shock strengths, employing the lightweight compression piston, the following empirical loss factors for the incident shock and endwall reflection were determined:

Table 2.3: Empirical loss factors for incident shock attenuation and ST-endwall reflection in the HELM facility. Factors are determined based on measurements of incident shock velocity at the upstream ST inlet and closely upstream of the nozzle reservoir as well as post-reflected shock stagnation pressure in comparison to numerical prediction.

$\zeta_{Ma} = \dfrac{Ma_{s_{exp}}}{Ma_{s_{th}}}$	$\zeta_{21} = \dfrac{p_{21_{exp}}}{p_{21_{th}}}$	$\zeta_{52} = \dfrac{p_{52_{exp}}}{p_{52_{th}}}$
$[-]$	$[-]$	$[-]$
$\sim$0.8	1.0	0.84

Loss factors are defined by the ratio of experimentally determined values to those predicted by inviscid theory: $\zeta = q_{exp}/q_{th}$. From Table 2.3 it is observed that if incident shock attentuation ζ_{Ma} is considered, the pressure ratio across the incident shock wave will in allmost all cases reach 100% of its theoretical value p_{21} ($\zeta_{21} = 1$). Further, the empirical loss factor for shock-endwall reflection ζ_{52} is determined subsequently to shock attentuation and hence already incorporates the latter. Values listed in Table 2.3 have been found to yield good-excellent agreement with selective validation experiments and were hence deemed suitable to yield pre-

dictions of good accuracy in the following systematic calculation of TUP-TI conditions for the HELM facility's driver and shock tube section. Evidently, any such empirical loss factor is considered a representative average for a relevant test range, with a standard deviation of ~3-4% for the incident shock velocity being observed in the current work [62]. Krek and Eitelberg [58] reported on a similar standard deviation of ~3.5% for incident shock speed, and ~6% for stagnation enthalpy, respectively, for the HEG facility.

Whereas such an empirical correction of stagnation pressure from its theoretically predicted to an unambiguously measured value is evidently well justified due to physical reasoning (incured net total pressure losses for a sum of irreversible processes), an equally valid correction, i.e. adaption, of corresponding test gas temperature and enthalpy in the post-incident/-reflected shock regime is not that obvious. Due to lack of accurate knowledge and measurement data, the established approach in literature assumes an isentropic expansion of the stagnated test gas, adapting post-reflected shock temperature to experimentally measured, lower than predicted total pressures $p_{5e} < p_5$ and hence inducing an analagous, artificial decrease of stagnation temperature $T_{5e} < T_5$. Physical justification of this transfer of total pressure loss factors to total temperature is however contested by the author and hence not used herein. Instead, the present work applies empirical correction factors ζ_{exp} exclusively to kinematic quantities, precisely to model stagnation pressure loss Δp_t, whereas total temperature and enthalpy are calculated based on the inviscid ideal gas or equilibrium relation and not subjected to further correction. For brevity, the physical argument to substantiate this approach - based on the second law of thermodynamics - is postponed to the attachment, see A. Therefore, stagnation enthalpies calculated in the following are expected to range somewhat above those values stated in relevant literature for similar incident shock Mach numbers.

Alternative approaches for prediction of tailored interface operation have been presented by Gildfind [11] and Gardner [55].

2.5 Results

2.5.1 HELM Operation conditions

TUP-TI Hornung analysis

Results of the HELM operation point analysis due to tuned FPD operation by Hornung and Bélanger's analysis are plotted in Fig. 2.7, for an over-drive of $\beta = 1.40$ and the lightweight piston $m_p = 62.835$ kg. Corresponding tailored-interface conditions according to Nishida's theory are plotted in Fig. 2.8.

As is observed from Fig. 2.7, the driver analysis by Hornung and Bélanger yields FPD with notably high compression ratios of up to $\lambda \sim 125$ - in comparison to typical FPD values in Table 2.1. For identical helium fractions x_{He}, the general trend suggests larger compression ratios λ as the orifice diameter A^* decreases, which qualitatively balances the mass flow rate of driver gas through the critical area, see 2.25.

Hence, the smallest orifice diameter of A^*/A_1 =0.50 of all available, Table 2.2, has not been used herein, as compression ratios suggested by Hornung's analysis rose up to excessively high values of $\lambda \sim 155$, which are prohibitive and clearly impractical. Hence, for the reference case of x_{He} =100% driver gas, A^*/A_1 =0.67 represents the smallest possible orifice to yield useful compression ratios, with a maximum of $\lambda \sim 110$ at 1000 bar burst pressure. By use of the next larger orifice, A^*/A_1 =0.75, the compression ratio decreases to λ =55-95 for a pressure range p_4 =400-1000 bar. For driver gas helium fractions x_{He} =95%, only the next larger orifice A^*/A_1 =0.85 was found suitable to yield λ =59-102. For the same orifice, a further reduction to x_{He} =90% suggests λ =69-120, such that a non-constricted orifice of A^*/A_1 =1.00 is required to maintain $\lambda \leqslant 100$. Most notably, Hornung's theory proposes such high compression ratios, i.e. sound speed and hence critical conditions $a^*/a_4(\lambda)$, that even the full ST diameter A^*/A_1 =1.00, i.e. the basic facility dimensions of A_1/A_4, are not sufficient to achieve tuned operation for a driver gas of x_{He} =80%, suggesting excessively high λ =72-125. Further, the corresponding buffer pressure p_{A0} exceeds the 120 bar-margin.

In line with Hornung's basic scaling relationship, Eq. 2.28, tuned piston operation points achieve higher burst pressure p_4 by a monotonic increase in compression ratio λ, whereas the intial driver pressure p_{40} is left notably constant, see Fig. 2.7. Although variation of p_{40} with burst pressure is only minor, this is a difference to the TUP-theories of Stalker and Itoh, where initial driver pressure changes with burst pressure and compression ratio. For an enforced over-drive parameter of β =1.4, Hornung's theory is observed to predict very high piston speeds of up to $u_{rupt} \sim 300$ m/s at diaphragm rupture - the largest piston speeds reflecting a driver with greater helium fractions and larger orifice diameters. Here it is worth to note, that the over-driving concept is not part of Hornung's original theory, which merely enforced β =1.0 to achieve driver gas continuity - results of which are plotted in the appendix for sake of completeness. To facilitate a valid comparison with alternative theories - typically assuming an over-drive of $\beta \sim 1.4$ -, results in Fig. 2.7 are computed for β =1.4. It is to be pointed out that enforcing an over-drive parameter of β >1.0 yields elevated piston speed u_{rupt} and earlier diaphragm rupture t_{rupt}, which merely requires for greater buffer pressures p_{A0}, however does explicitly not achieve or induce changes in either compression ratio λ or initial driver pressure p_{40}. Hence, only the time-dependent variables of tuned FPD operation points - such as driver pressure holding time t_{hold} and stagnation pressure recovery p_5/p_4 are affected, which are however not explicitly modeled by Hornung's theory. Furthermore, - with the exception of p_5/p_4, which itself is affected by t_{hold} - the tailored-interface conditions in the downstream ST are not affected by β, as driver gas conditions at diaphragm rupture, p_4 and a_4, only depend on λ - compare TUP-TI conditions according to Hornung's theory for β =1.0 in the appendix. Hence, a potential gain due to increased over-drive β >1.0 can only be experimentally confirmed. Nevertheless, a tentative increase in buffer pressure p_{A0} will be required for any driver operation point as to overcome total pressure losses at the upstream buffer-CT junction. For the sake of completeness and comparison to alternative theories, tuned piston operation points for β =1.4 according to Hornung's theory are listed in the appendix.

Prior driver operation conditions - primarily compression ratio λ, burst pressure p_4 and sound speed a_4 - are henceforth used to compute suitable ST parameters, enforcing tailored-interface conditions according to Nishida's theory, see Fig. 2.8. It is observed that the greatest incident shock Mach numbers of $Ma_s \sim 15.1$ are achieved with the greatest helium fractions $x_{He} =$100% at maximum $\lambda =$109, even though helium fractions $x_{He} =$80% and $x_{He} =$95% reflect slightly larger compression ratios of up to $\lambda =$125. The inital ST pressure p_1 is observed to increase monotonically with incident shock Mach number, and changes from minimum $p_1 =$118-382 mbar to maximum $p_1 =$200-634 mbar for minimum and maximum burst pressures 400 bar and 1000 bar, respectively, for cases considered herein. Whereas near-linear increase in post-incident and post-reflected shock pressures p_2 and p_5 with burst pressure is observed, a non-linear increase of enthalpies h_2 and h_5 is evident. For cases considered herein, the two highest nozzle reservoir conditions achieved for a tuned piston driver according to Hornung's theory and tailored-interface operation according to Nishida correspond to a maximum post-reflected shock pressure of $p_5 =$465 bar, at the lowest enthalpy of $h_5 =$13.3 MJ/kg, and a maximum stagnation enthalpy of up to $h_5 \sim$30 MJ/kg the lowest pressure of $p_5 =$350 bar. Even though such an operation point of such high enthalpy in a RST is not likely to produce a sufficiently long driver holding time and ST test time interval, the large magnitude of incident shock number and stagnation enthalpy is plausible, considering Hornung's theory to suggest compression ratios λ and orifice diameters A^* which are notably higher than those values proposed according to the both other theories and which considerably increase incident shock strength.

As lower driver gas helium fractions require larger orifice diameters for tuned operation, only helium fractions within the range $x_{He} =$80-100% have been plotted - where tuned operation at $x_{He} =$80% already suggests a non-constricted orifice diameter of $A^*/A_1 =$1.00 according to Hornung's theory.

TUP-TI Stalker analysis

Results of the HELM operation point analysis due to tuned FPD operation by Stalker's analysis are plotted in Fig. 2.9, with corresponding tailored-interface conditions according to Nishida's theory plotted in Fig. 2.10. Results are based on an enforced over-drive parameter of $\beta =$1.40 for the lightweight piston $m_p =$62.835 kg.

As is observed from Fig. 2.9, tuned driver operation points computed according to Stalker's theory are characterized by a generally smaller compression ratio than suggested by Hornung, Fig. 2.7. For a range of relevant driver gas helium fractions $x_{He} =$80-100%, variation of the orifice diameter $A^*/A_1 =$0.5-1.0 achieves compression ratios of minimum $\lambda =$40-60 at low and maximum $\lambda =$70-105 at high burst pressures of $p_4 =$400 bar and 1000 bar, respectively. In contrast, tuned operation due to Hornung's theory at low helium fraction $x_{He} =$80% is only achieved by an excessive compression ratio of up to $\lambda =$125, further requiring a fully-opened orifice diameter $A^*/A_1 =$1.0. Similarly, Stalker's theory suggests the smallest orifice $A^*/A_1 =$0.5 to be suitable to limit the compression ratio to a maximum of $\lambda =$100 for the maximum helium fraction $x_{He} =$100% and burst pressure $p_4 =$1000 bar. Such a small ori-
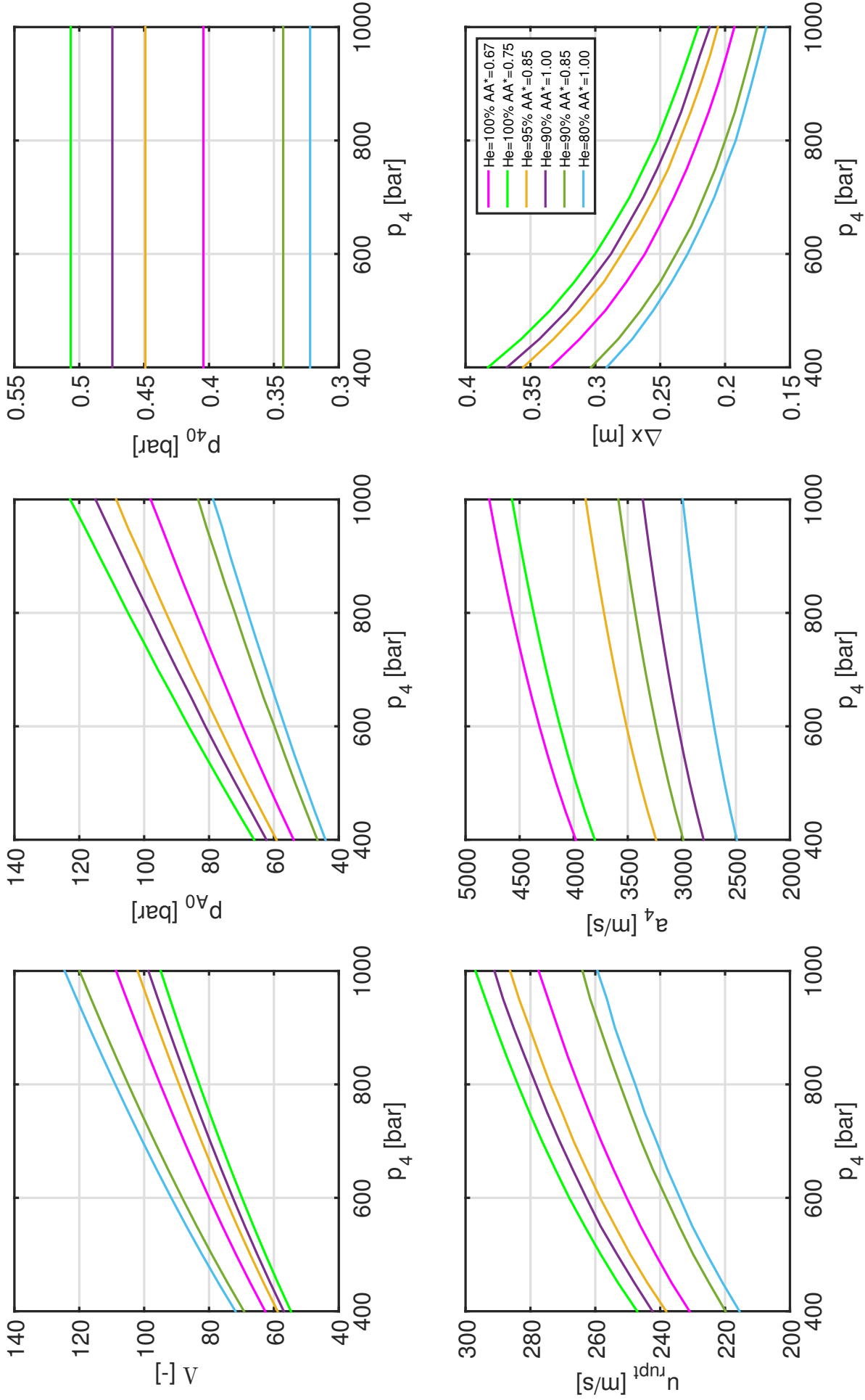
Figure 2.7: Parameters for tuned-piston driver according to Hornung and Bélanger theory. Values are calculated for an over-drive parameter of $\beta = 1.4$, lightweight piston $m_p = 62.835$ kg.
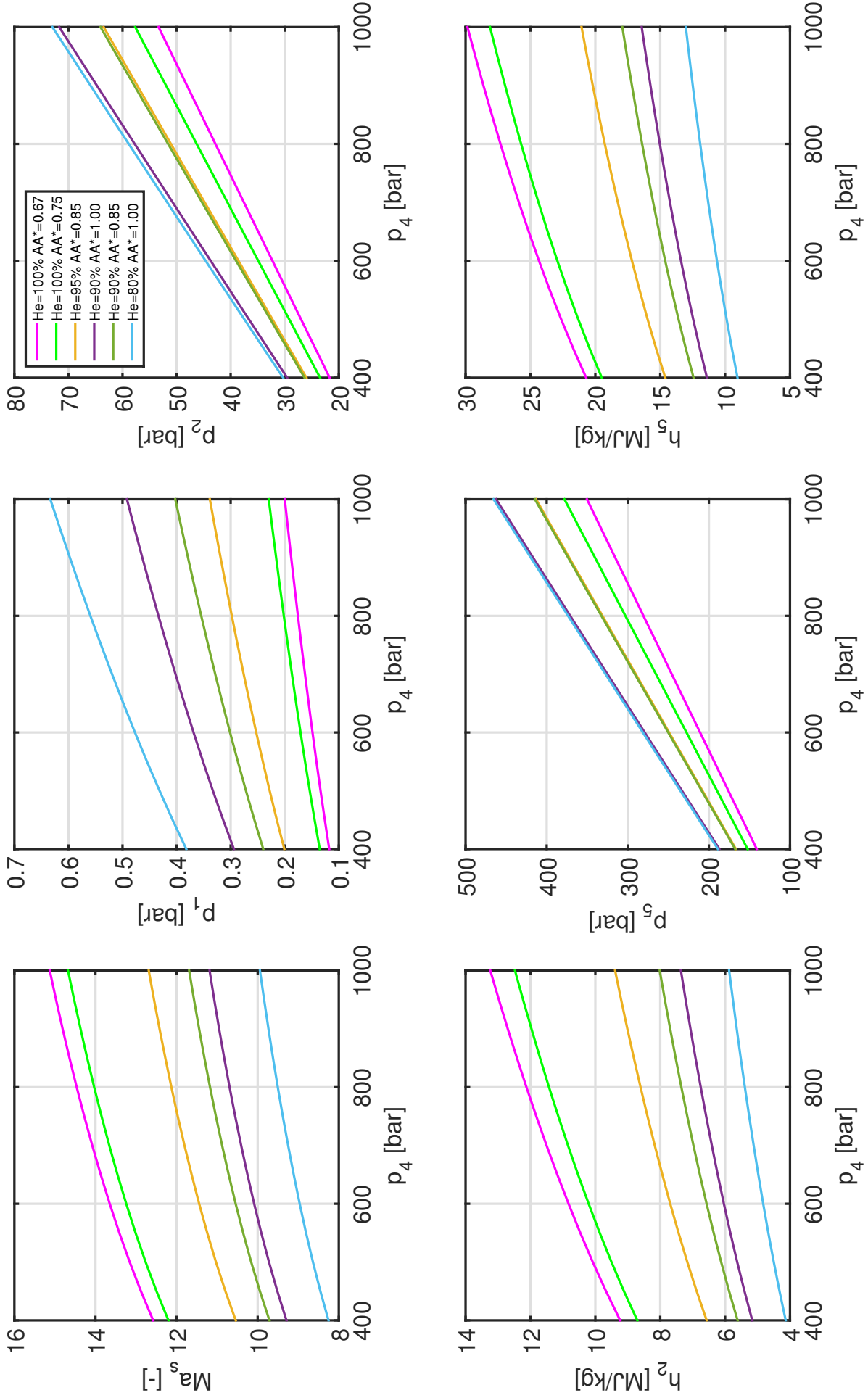
Figure 2.8: Parameters for tailored-interface operation according to Nishida's theory - driver values based on Hornung and Bélanger analysis for tuned-piston ($\beta = 1.4$).

fice suggested impractically high compression ratios of $\lambda \sim$155 due to Hornung's theory, Fig. 2.7. From Fig. 2.9 the highest buffer pressures of up to p_{A0} =113 bar are seen to result for cases of either large helium fractions x_{He} =95-100% or large orifice diameters A^*/A_1 =1.0, or a combination of both. Considering the fact that Hornung's theory predicts generally larger orifice diameters, buffer pressures p_{A0} for an identical over-drive parameter β =1.40 required according to Hornung's theory exceed those predicted by Stalker's analysis, compare Fig. 2.9 and appendix. Whereas intial driver pressure p_{40} according to Hornung does not change with burst pressure - but only with helium fraction and orifice area -, the former slightly varies in Stalker's analysis - yet, only by less then 3%, which renders both theories comparable. Still, due to notably elevated compression ratios in Hornung's analysis, p_{40} is found to be generally larger for Stalker's analysis, for an assigned range of burst presssures p_4 =400-1000 bar. Due to higher compression ratios λ and greater orifice diameters A^*/A_1 - primarily dictating reference piston speed compensation -, required piston speeds at diaphragm rupture up to u_{rupt} =297 m/s are notably higher for Hornung as compared to u_{rupt} =246 m/s for Stalker, for a given helium fraction x_{He} and burst pressure p_4 at over-drive β =1.4, compare Fig. 2.9. As for TI conditions in the downstream ST, Fig. 2.10, generally lower compression ratios λ entail slightly lower incident shock Mach numbers of up to $Ma_s \sim$14.1 for Stalker's theory, at similarly slightly higher initial ST pressures p_1 - required to meet TI-conditions. Accordingly, stagnation enthalpies of up to h_5 =26.1 MJ/kg are achieved by Stalker's tuned driver operation points - as opposed to higher enthalpies of up to $h_5 \sim$30 MJ/kg due to Hornung's conditions. While identical stagnation pressures of up to $p_5 \sim$470 bar are achieved in the low-enthalpy limiting case for both theories, the Hornung's high-enthalpy case achieves at higher predicted stagnation pressure of up to $p_5 \sim$350 bar, as opposed to $p_5 \sim$290 bar for Stalker's case.

TUP-TI Itoh analysis

Results of the HELM operation point analysis due to tuned FPD operation by the analysis of Itoh et al. [46] are plotted in Fig. 2.11, with corresponding tailored-interface conditions according to Nishida's analysis plotted in Fig. 2.12. Results are based on an enforced over-drive parameter of β =1.40 for the lightweight piston m_p =62.835 kg.

Interestingly, Itoh's analysis by trend suggests generally smaller orifice diameters to be suitable for limiting the compression ratio to $\lambda \sim$100 for elevated driver gas helium fractions than tuned FPD analysis by Stalker and Hornung. Here, in line with Stalker's theory, Itoh's analysis predicts the largest compression ratio of up to λ =107 at the smallest orifice A^*/A_1 =0.5 for a helium fraction of x_{He} =90% and not for a pure helium driver. Overall, the suggested compression ratio ranges between $\lambda \sim$70-110 for helium fractions x_{He} =70-100%. As such, only Itoh's theory predicts a tuned FPD condition for low helium fractions of x_{He} =70%, even without exploiting the full orifice area A^*/A_1 =0.85, to be achieved at a suitable compression ratio of λ =83. Both other theories predicted impractically high compression ratios of $\lambda \sim$150 in this case, hence being unable to yield practical FPD operation points for low helium fractions x_{He} <80%. In fact, with orifice area A^*/A_1 =1 and 0.85, Itoh's theory even
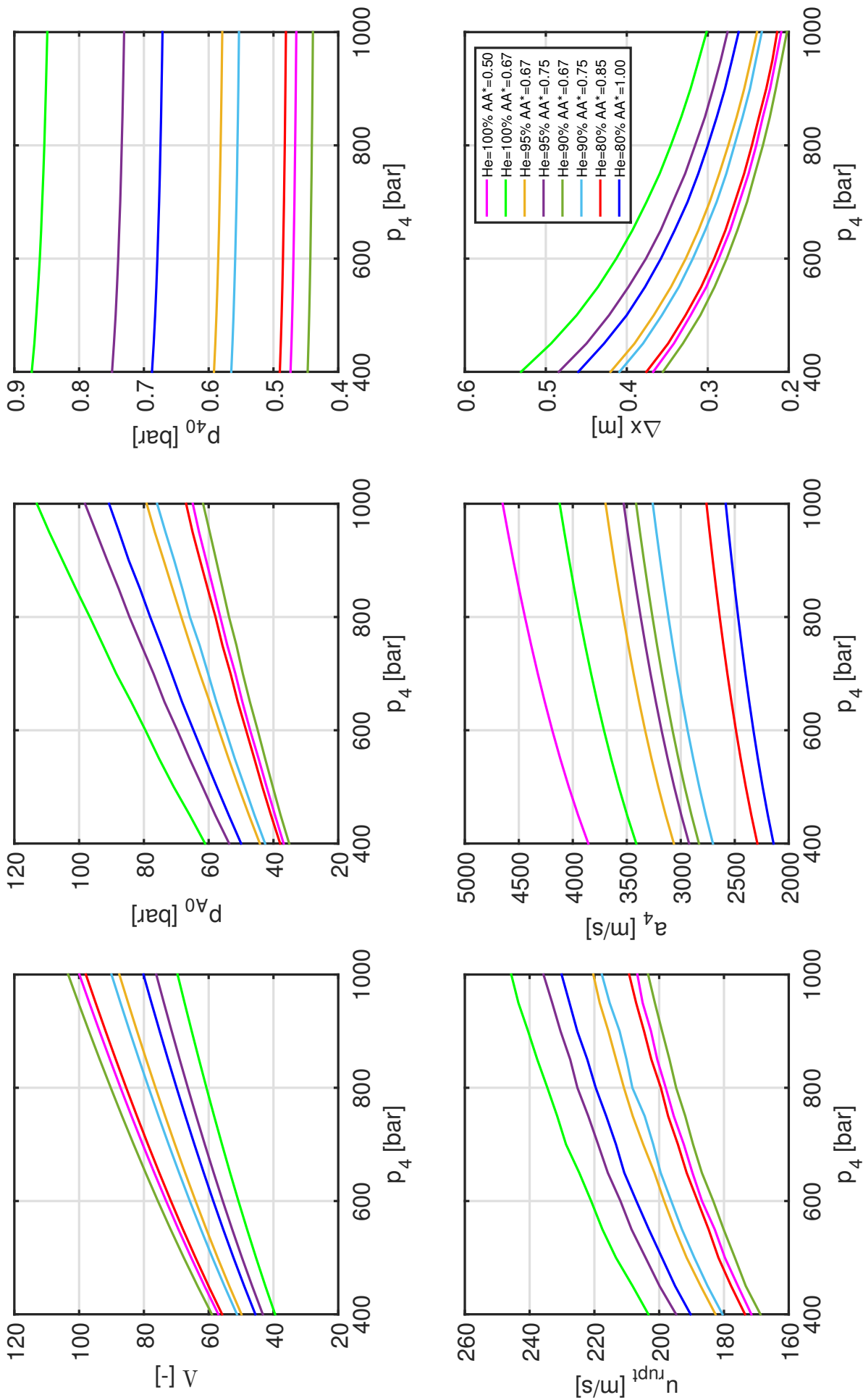
Figure 2.9: Parameters for tuned-piston driver according to Stalker's theory. Values are calculated for an over-drive parameter of $\beta = 1.4$, lightweight piston $m_p = 62.835$ kg.
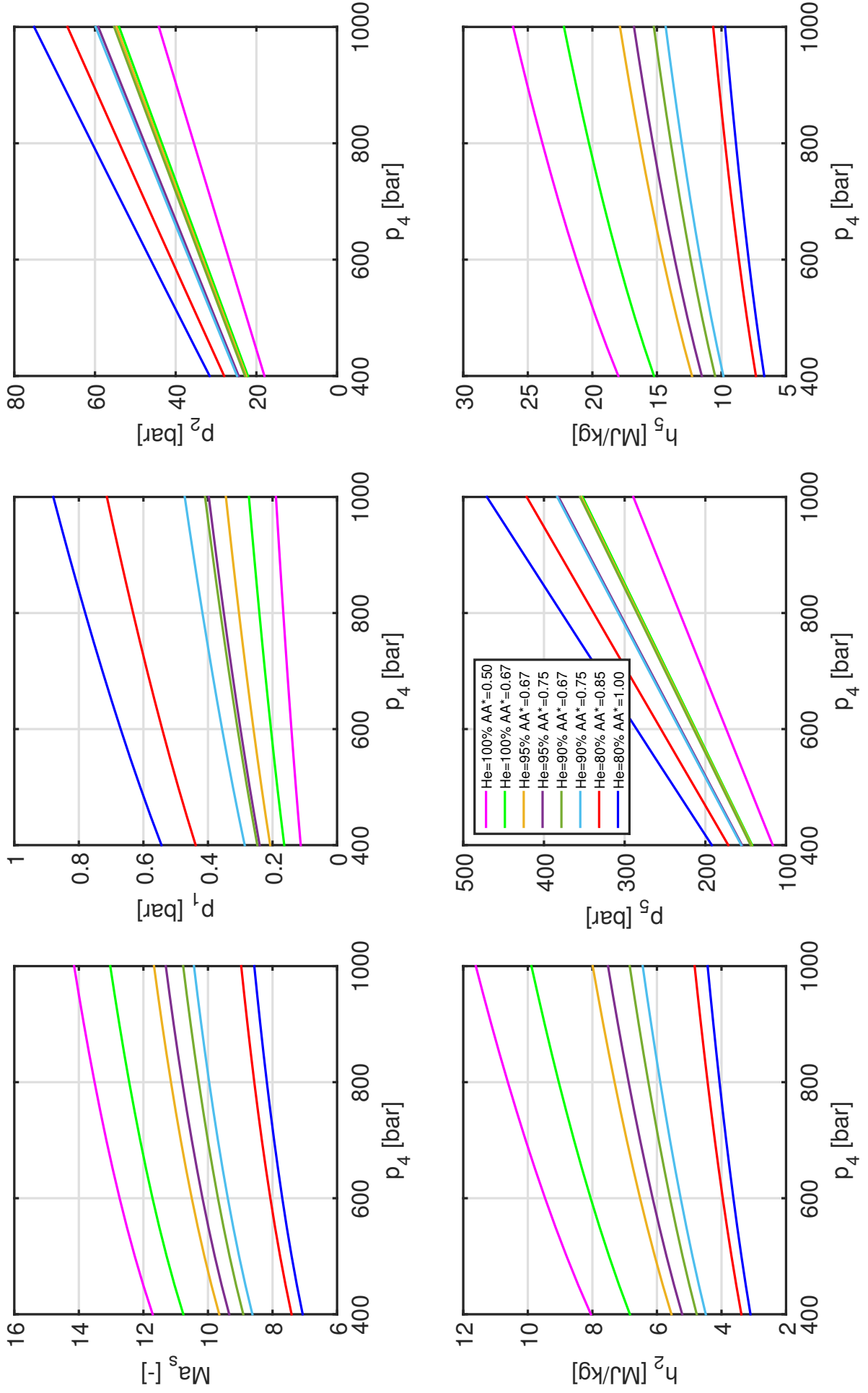
Figure 2.10: Parameters for tailored-interface operation according to Nishida's theory - driver values based on Stalker's analysis for tuned-piston ($\beta = 1.4$).

Legend:
- He=100% AA*=0.50
- He=100% AA*=0.67
- He=95% AA*=0.67
- He=95% AA*=0.75
- He=90% AA*=0.67
- He=90% AA*=0.75
- He=80% AA*=0.85
- He=80% AA*=1.00

facilitates to achieved tuned FPD operation for helium fractions as low as x_{He} =30-60%, while effectively limiting the compression ratio to maximum λ ~100 for the entire range of burst pressure p_4 =400-1000 bar considered. In this case, buffer pressures range as low as p_{A0} =27-45 bar, suggesting secure tuned FPD operation to stagnation enthalpies as low as h_5 =6 MJ/kg. These results are, yet, not incorporated herein for brevity. For the current high-enthalpy results with x_{He} =70-100% in Fig. 2.11, Itoh's theory limits the required buffer pressure to maximum p_{A0} <83 bar, in clear contrast to a maximum of 113 bar and 123 bar for Stalker's and Hornung's predictions, respectively. In comparison, variation of initial driver pressure with burst pressure p_4 up to 8.2% (rising with helium fraction) is found to be highest for Itoh's theory, as opposed to minor and total absence of variation for Stalker's and Hornung's analysis, respectively. Most notably, the required piston velocity at diaphragm rupture u_{rupt} for achieving an over-drive of β =1.4 is thus limited to maximum 180 m/s by Itoh's theory, in contrast to much larger values of 245 m/s and ~300 m/s according to Stalker and Hornung, respectively. In line with Stalker's operation points of λ =70~100, the risidual endwall distance ranges from Δx ~0.2-0.3 m. Yet, at maximum conditions ($p4$ =1000 bar and x_{He} =100%) Itoh predicts a lower compression ratio of λ =70, in contrast to the λ =100 by Stalker. Therefore, the maximum incident shock Mach number of Ma_s =12.54 is the overall lowest value, compared to a maximum Mach number of 15.13 and 14.15 predicted by Hornung and Stalker, respectively. Hence, the maximum stagnation enthalpy of h_5 ~21 MJ/kg achieved by Itoh is the overall lowest predicted enthalpy. Eventually, the highest stagnation pressure of p_5 =470 bar is predicted by Stalker at total enthalpy h_5 =9.72 MJ/kg.

2.5.2 Experimental validation

Based on the prior theoretical design of holistic operation conditions for the HELM facility, a representative range of exemplary conditions were tested in order to confirm or disprove their suitability. Whereas driver pressure holding time of tuned conditions for Itoh's theory is readily computed by the explicit Eq. 2.45, the latter is not clearly defined in Hornung's and Stalker's theories. In this case, τ_{hold} is deduced from the critical mass flow $\dot{m}^*$ through the orifice cross section A^* and estimated in reference to the driver gas mass m_{CT}:

$$\dot{m}^* = \left(\frac{2}{\kappa+1}\right)^{\frac{\kappa+1}{2(\kappa-1)}} \lambda^{\frac{\kappa+1}{2}} \rho_{40} a_{40} A^* \tag{2.47}$$

$$m_{CT} = \frac{p_{40}}{R_4 T_{40}} \tag{2.48}$$

$$\tau_{hold} \sim \frac{\dot{m}^*}{m_{CT}}. \tag{2.49}$$

In line with basic theory, estimated τ_{hold} for the heavier piston were found to range up to 100% above holding times for the lightweight piston for all three tuned driver theories. Further, according to the relatively large compression ratios λ and proposed orifice diameters A^*, operation points by the Hornung analysis yielded holding times up to 50% lower than those suggested by Stalker's analysis. Hence, to lower the likelihood of piston impact, operation points
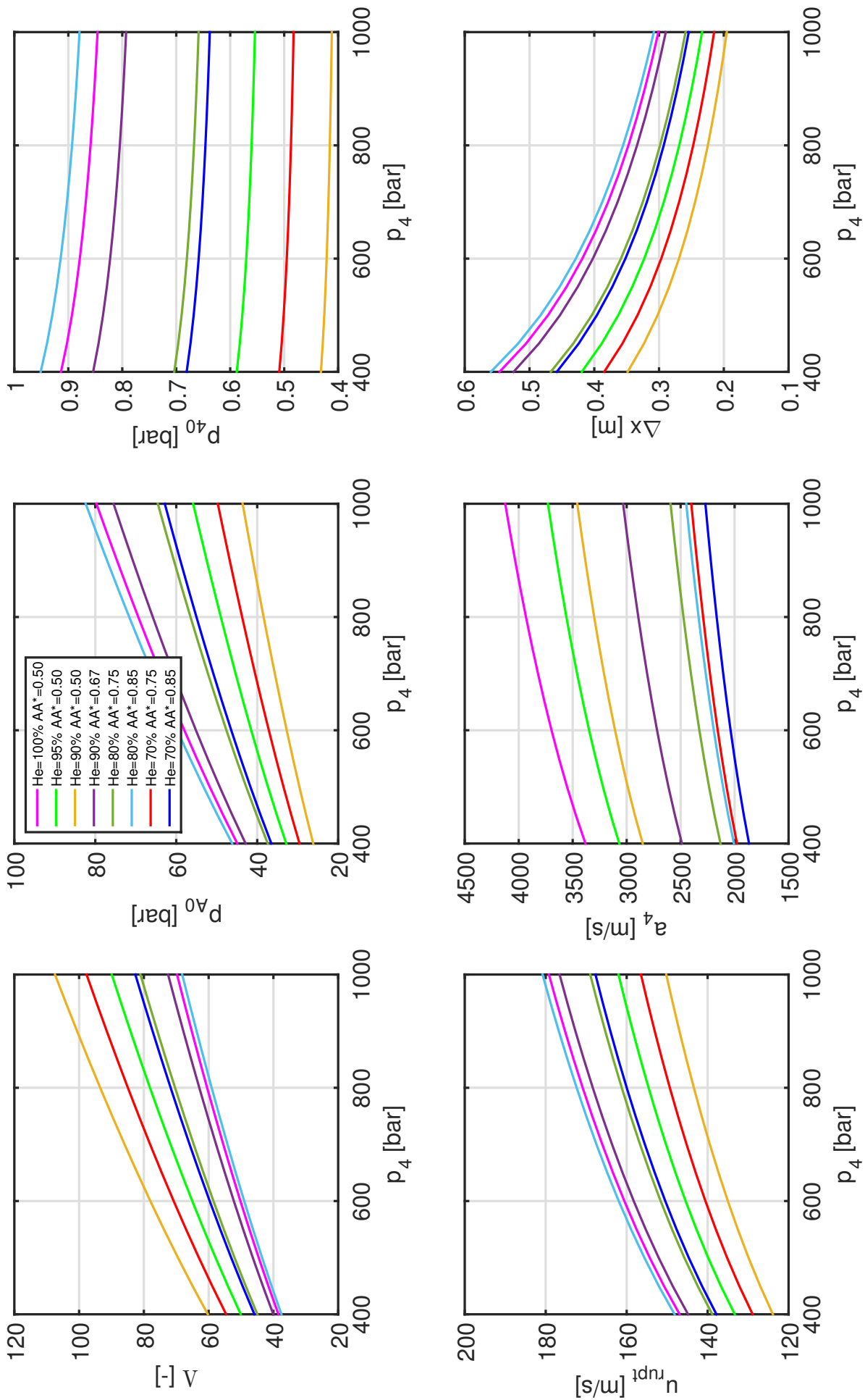
Figure 2.11: Parameters for tuned-piston driver according to Itoh's theory. Values are calculated for an over-drive parameter of $\beta = 1.4$, lightweight piston $m_p = 62.835$ kg.
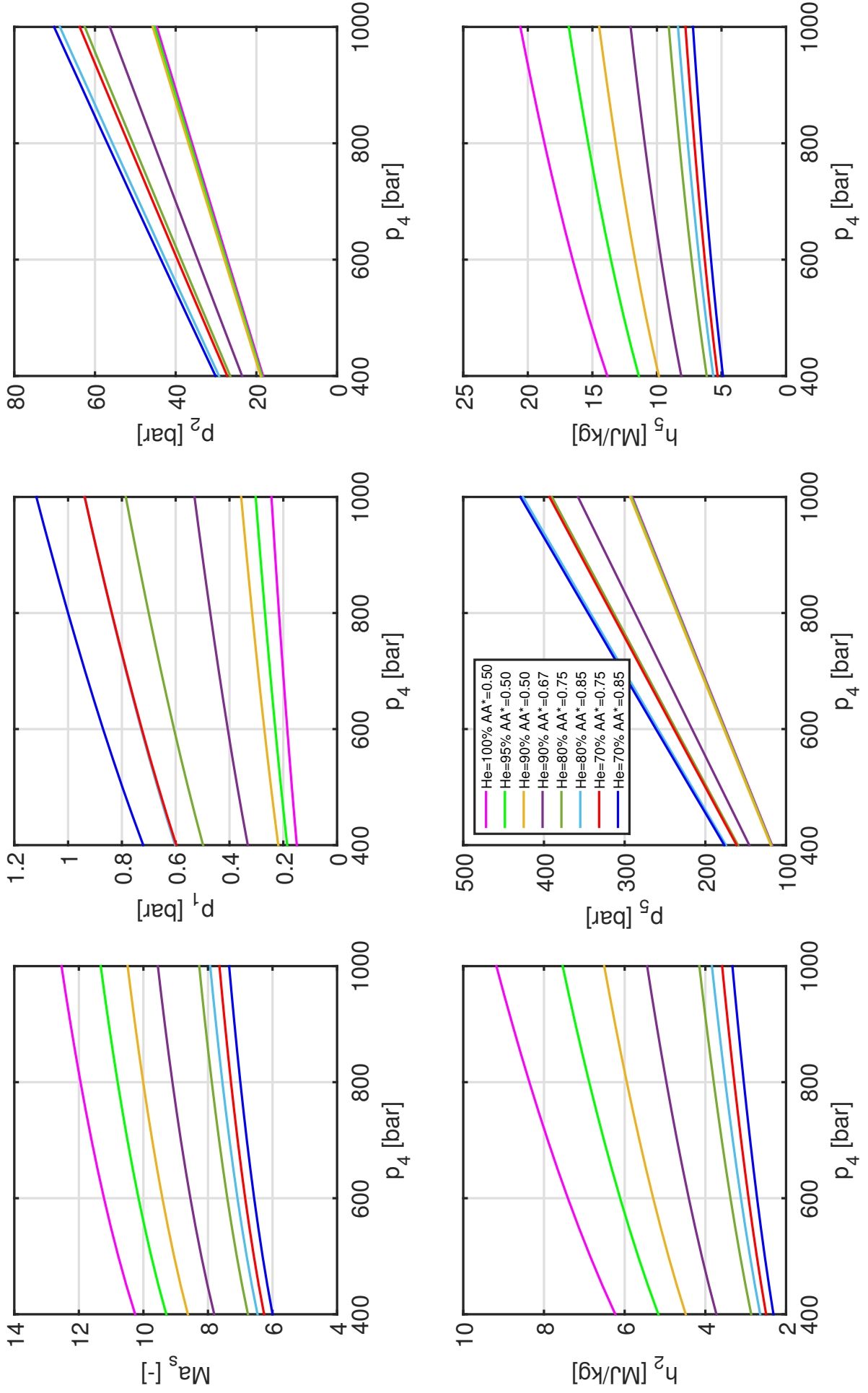
Figure 2.12: Parameters for tailored-interface operation according to Nishida's theory - driver values based on Itoh's analysis for tuned-piston ($\beta = 1.4$).

Legend:
- He=100% AA*=0.50
- He=95% AA*=0.50
- He=90% AA*=0.50
- He=90% AA*=0.67
- He=80% AA*=0.75
- He=80% AA*=0.85
- He=70% AA*=0.75
- He=70% AA*=0.85

of Stalker and Itoh were given preference in the experimental validation. According to the motivation of advancing operation conditions to the maximum design point, primarily in terms of stagnation enthalpy, experiments were carried out exclusively with the lightweight piston. For a set of 15 exemplary test conditions, summarized in Table 2.4, representative results - in terms of dynamic pressure traces in the CT and ST - are presented for three conditions each according to Itoh's and Stalker's theory, respectively, in Fig. 2.13 and 2.14. Pressure traces for additional experiments are listed in the appendix A for brevity.

Table 2.4: Experimental conditions run in the HELM facility according to prior driver and shock tube TUP-TI operation point design. Variations in burst pressure (due to diaphragm rupture) lead to departure from nominal burst pressure, scaled in increments of 100 bar. Stated burst pressure p_4 and compression ratio λ as measured in the experiment.

No.	Theory	y_{He}	A^*/A_1	β	p_4	λ	p_{A0}	p_{40}	p_1	v_s	Ma_s	p_2	p_5
-	-	[-]	[-]	[-]	[bar]	[-]	[bar]	[bar]	[bar]	[m/s]	[-]	[bar]	[bar]
1	Itoh	0.7	0.85	1.2	680	68.7	42.9	0.587	1.00	2303	6.77	55	247
2	Itoh	0.9	0.67	1.4	760	59.1	61.7	0.846	0.40	3271	9.62	42	277
3	Itoh	0.9	0.67	1.4	790	60.7	65.0	0.841	0.40	3432	10.09	40	300
4	Itoh	0.9	0.67	1.4	800	62.9	70.1	0.803	0.41	3536	10.31	56	348
5	Itoh	0.9	0.67	1.4	1000	71.9	75.0	0.804	0.44	3590	10.47	51	362
6	Itoh	0.9	0.67	1.4	860	65.7	75.0	0.803	0.43	3627	10.57	61	374
7	Itoh	1.0	0.50	1.4	840	62.2	73.0	0.864	0.19	4375	12.76	27	285
8	Itoh	1.0	0.50	1.4	950	67.3	77.7	0.851	0.20	4487	13.20	50	360
9	Itoh	1.0	0.50	1.4	1030	70.9	83.0	0.847	0.21	4667	13.61	32	330
10	Stalker	0.9	0.85	1.2	770	64.4	63.3	0.744	0.42	3500	10.29	46	348
11	Stalker	1.0	0.50	1.2	950	96.9	52.5	0.464	0.19	4795	14.01	60	350
12	Stalker	1.0	0.50	1.2	1040	102.5	57.0	0.463	0.25	4795	14.01	60	450
13	Stalker	0.9	0.67	1.2	870	95.0	46.0	0.439	0.30	3977	11.60	44	345
14	Stalker	0.9	0.67	1.2	880	95.6	50.0	0.438	0.26	4217	12.40	44	380
15	Stalker	0.9	0.67	1.2	1130	111.2	54.2	0.437	0.28	4375	12.76	43	380

Due to a certain amount of gas leakage in the driven section towards the end of this test campaign, initial ST pressures were difficult to accurately control such that set pressures p_1 eventually deviated from theoretical values by -15% on average. Accordingly, while measured burst pressure was in very good agreement with theory (to within ± 20 bar or 1-4%), the ratio of burst- to shock tube pressure p_4/p_1 induced an average deviation in incident shock Mach number, ranging from $< +1\%$ (run 1 and 11) up to $+14\%$ (run 6). Here, in agreement with theory, lower initial ST pressures p_1 consistently yield a higher shock Mach numbers, for every single experiment. Further in line with this trend, stagnation pressure p_5 is generally higher by up to $1 - 30\%$. Despite accurate agreement of theoretical and measured Mach number for runs 11 and 12, the mean stagnation pressure in the experiment was found to be higher by 27% and 55%, respectively. However, due to low time-steadiness and highly transient (i.e. fluctuating) pressure trace for Stalker conditions 10-15, accurate determination of the factual (representative) stagnation pressure is difficult and prone to error. For this reason, operation conditions

predicted by the Ito TUP-theory are generally favoured over operation points predicted by the Stalker theory. Maximum deviation occured for test run 14 (Stalker OP) with -32% lower than aspired pressure p_1, such that the resulting Mach number was by 17.6% higher than anticipated.

In summary, measured stagnation pressure is concluded to be in good agreement with theory, where generally higher pressures p_5 and shock Mach numbers in the experiment are evident to ensue from lower than anticipated initial ST pressures p_1. It is thus conclusive that in order to make experiments agree more closely with the numerically predicted OP, gas leakage in the ST is to be fixed, such that pressures p_1 can be accurately set to within required accuracy. A comparison of experimental and theoretical values is given in table 2.5.

Table 2.5: Comparison of measured values throughout experiments and anticipated values of predicted TUP-TI OP. Quantities of theoretical OP are stated as absolute values, discrepancy is stated as (percentual) relative deviation of measured from theoretical values.

No.	Theory	λ	$\Delta\lambda$	p_4	Δp_4	p_1	Δp_1	p_5	Δp_5	Ma_s	ΔMa_s
-	-	[-]	[%]	[bar]	[%]	[bar]	[%]	[bar]	[%]	[-]	[%]
1	Itoh	65.9	4.3	700	-2.9	0.937	6.7	303	-18.5	6.80	-0.4
2	Itoh	60.3	-2.0	750	1.3	0.456	-12.3	270	2.6	9.00	6.9
3	Itoh	62.9	-3.5	800	-1.3	0.471	-15.1	287	4.5	9.10	10.9
4	Itoh	62.9	0	800	0	0.471	-13.0	287	21.3	9.10	13.3
5	Itoh	72.5	-0.8	1000	0	0.530	-17.0	358	1.1	9.55	9.6
6	Itoh	65.4	0.5	850	1.2	0.487	-11.7	305	22.6	9.22	14.6
7	Itoh	62.9	-1.1	850	-1.2	0.223	-14.8	247	15.4	12.11	5.4
8	Itoh	67.5	-0.3	950	0	0.237	-15.6	276	30.5	12.40	6.5
9	Itoh	69.8	1.6	1000	3.0	0.244	-13.9	291	13.4	12.54	8.5
10	Stalker	-	-	-	-	-	-	-	-	-	-
11	Stalker	96.9	0	950	0	0.184	3.3	275	27.3	14.00	0.1
12	Stalker	99.9	2.6	1000	4.0	0.189	32.0	290	55.2	14.15	-1.0
13	Stalker	93.6	1.5	850	2.4	0.374	-19.8	303	13.9	10.41	11.4
14	Stalker	96.5	-0.9	900	-2.2	0.386	-32.6	320	18.8	10.54	17.6
15	Stalker	-	-	-	-	-	-	-	-	-	-

In addition, the process of shock formation upon diaphragm rupture and reflection off the ST endwall is obviously strongly dissipative (i.e. non-isentropic): the mechanisms of incident shock attenuation along propagation through the ST by the viscous wall BL, as well as shock-bifuration and total pressure loss due to 3D viscous phenomena upon shock-endwall reflection are well known. Hence, for a physically sound (i.e. meaningful) theoretical prediction of TUP and TI operation conditions, theory is to reflect viscous dissipation and total pressure loss in the CT and ST a priori; this is typically achieved by lumped correction (loss) factors, adapted to experimental measurements. Such a global loss factor has been determined for the run experiments and used within predicted operation points presented herein, 2.3. To further reduce observed deviation within experiments and theoretical OP, this loss factor is to be determined dependent on incident shock Mach number, itself being a dominant parameter for the a pri-

ori prediction of TI operation points and hence greatly affecting pressures p_1 suggested by theory. This is however an iterative process and requires a significant number of dedicated experiments, beyond the scope of this work, see [58]. Besides more evident losses in the down-stream ST, significant total pressure losses already affecting the initial shock strength (i.e. Mach number) occur upstream at the diaphragm station: here, viscous (friction) losses increase with decreasing orifice diameter due to stronger flow contraction and relatively stronger influence of flow perturbation from protruding metal petals of a non-perfectly opened diaphragm. This is in agreement with fundamental considerations of the TUP theory by Ito et al. [46] which predicts lower stagnation pressures p_5, i.e. lower pressure recovery p_5/p_4, for smaller ori-fice contractions A^*/A_4 at the diaphragm station, attirbuted to viscous losses. Furthermore, the attenuating influence of finite diaphragm opening times on shock strength is discussed by Rothkopf and Low [63].

2.6 Revised L1d model

Besides holistic prediction of suitable tuned FPD and TI operation conditions by an analytic model, single test conditions can be analyzed more in detail by Jacobs' [22] L1d-code, which is based on Lagrangian, quasi 1-D modeling, captures unsteady supersonic wave propagation by an approximate Riemann solver, including time-resolved prediction of the piston trajectory by points-mass modeling and using CEA to model thermo-chemical equilibrium gas behavior. L1d represents the well-established method for a priori prediction and design of new (specific) operation conditions in FPD short-duration facilities worldwide [64].

Starting from the status of Smith [65], the existing L1d-model for simulating operation of the HELM shock tunnel has been extensively revised in order to yield better agreement of numeri-cal predictions with experimental pressure measurements. In order to increase the accuracy, the number of geometrical points (variable gdata.n) was increased from initially 11,000 to 100,000 [66]. This variation was found to induce a lower driver pressure amplitude and to further decrease the incident shock velocity, eventually achieving a much closer agreement with the experiment, based on reduction in descrepancy of incident shock arrival at the ST endwall by up to 50% [67]. Moreover, viscous effects have been enabled in all three gas slugs: buffer, CT and ST alike. Finally, increase of cell count number and piston launcher geometry (updated local pressure loss region) were found to impart the greatest advantageous effect on correct burst pressure of 12% and 14%, respectively. In contrast, the time instant of shock arrival at the nozzle reservoir was favourably affected by the updated piston launcher geometry/losses to 3.5%, [67]. For a low Mach number test conditions with incident shock speed of $u_s =1273$ m/s, updating local loss regions in the ST and diaphragm station as well as piston launcher induced a favourable variation in predicted stagnation pressure amplitude p_5 of ∼12%, ∼46% and 104%, respectively. The number of cells for each gas slug was increased from 150, 200 and 200 to 1750, 1750 and 1000 for the buffer (secondary reservoir), CT and ST, respectively. The ge-ometry at the piston launcher (buffer-CT junction) was revised and more closely adapted to the
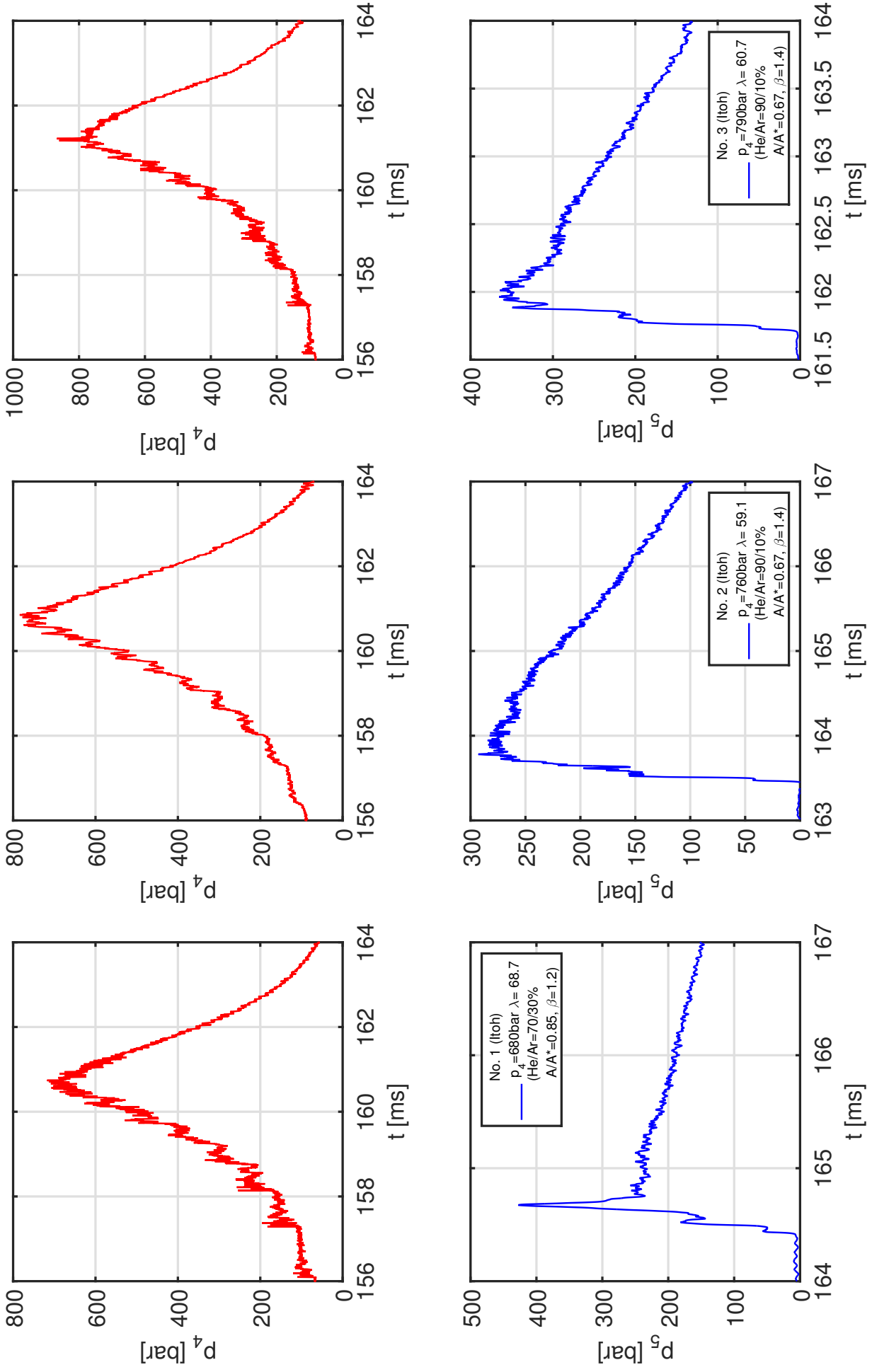
Figure 2.13: Driver and shock tube pressure traces for three representative conditions (No. 1-3) according to Itoh's tuned piston theory and for the lightweight piston m_p =62.835 kg. ST pressure p5 filtered by 30kHz LP-filter for means of illustration.

63
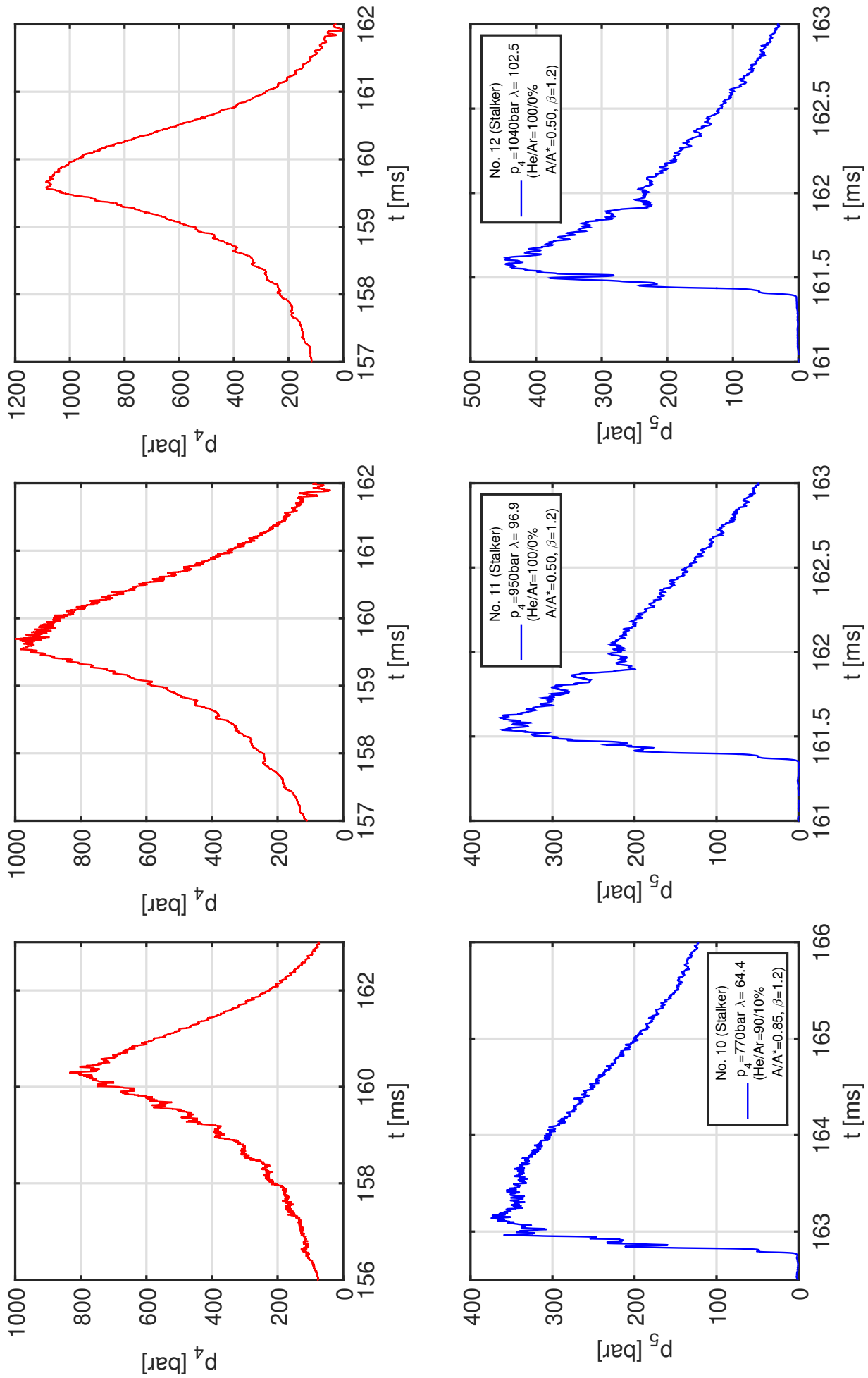
Figure 2.14: Driver and shock tube pressure traces for three representative conditions (No. 1-3) according to Stalker's tuned piston theory and for the lightweight piston m_p =62.835 kg. ST pressure p_5 filtered by 30kHz LP-filter for means of illustration.

No. 12 (Stalker)
p_4=1040bar λ= 102.5
(He/Ar=100/0%
A/A*=0.50, β=1.2)

No. 11 (Stalker)
p_4=950bar λ= 96.9
(He/Ar=100/0%
A/A*=0.50, β=1.2)

No. 10 (Stalker)
p_4= 770bar λ= 64.4
(He/Ar=90/10%
A/A*=0.85, β=1.2)
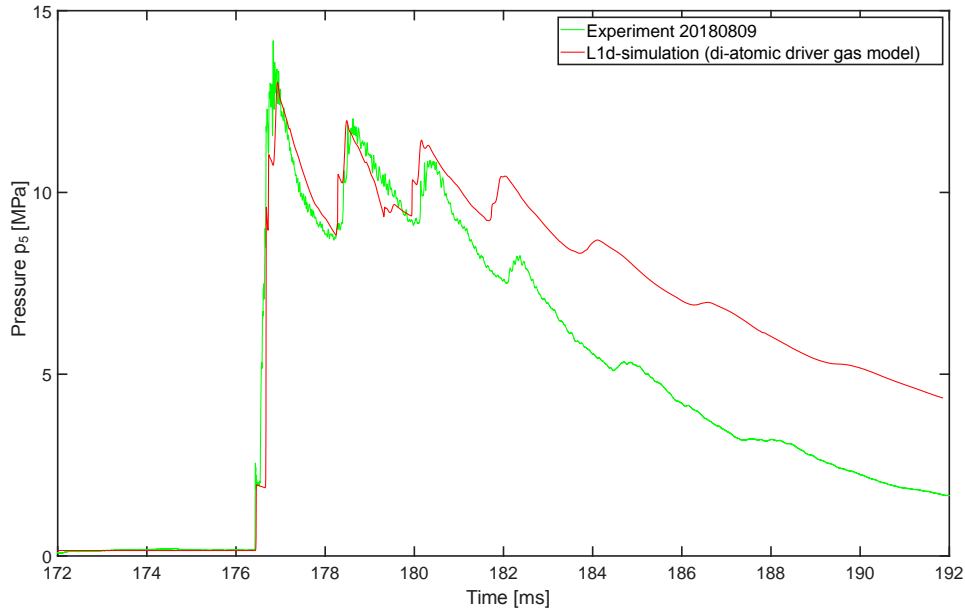
Figure 2.15: Parametervariation of the diaphragm holding time $\tau_{opening}$ in the revised L1d-model, refined for di-atomic driver gas. Strong incident pressure waves from the non-tuned FPD with low-sound speed di-atomic driver gas manifest in terms of strong discontinuities of the stagnation pressure p_5. Adopted from Häußlein [68] and van der Kruijssen [69].

factual geometry (based on CAD data), including a variation of the (total) pressure loss factor at the choked throat section. In reference to laser-distance measurements (± 1 mm accuracy), the axial location of two dynamic wall-pressure ports closest upstream of the nozzle reservoir (ST endwall) was corrected. Further, construction of the hydraulic damping systems required shortening of the ST by removal of a tube segment of 1m length, which was incorporated into the L1d geometry. By refining the diaphragm (opening) holding time, close qualitative and quantitative agreement (in terms of stagnation pressure and incident shock time of arrival at the ST endwall) between experiment and prediction could be achieved by the revised L1d-model for operation with a di-atomic driver gas, see Fig. 2.15.

Since prior experiments in the HELM shock tunnel (and predictions of those) have used a di-atomic driver gas, designing and evaluating high-enthalpy, high-pressure tuned FPD and TI conditions required the L1d-model to be adapted to a noble gas driver of helium-/argon-fractions. The model has been revised accordingly, with details provided by van der Kruijssen [69]. Whereas good agreement between predicted and measured driver pressure is reached at low helium fractions, see Fig. 2.16, accuracy of the model to predict stagnation pressure, particularly at larger helium fractions and stronger incident shocks $Ma_s \geq 10$ was found to be limited so far, according to van der Kruijssen [70], see Fig. 2.17. Thus, the L1d-model revised in the present work does not yet yield satisfactory agreement with experimental measurements for prediction of high-pressure, high-enthalpy test conditions in the HELM facility. Nevertheless, the primary influence parameters were unambiguously identified. Finally, further refinement is required and closer agreement with experiments is deduced be achievable in the future by
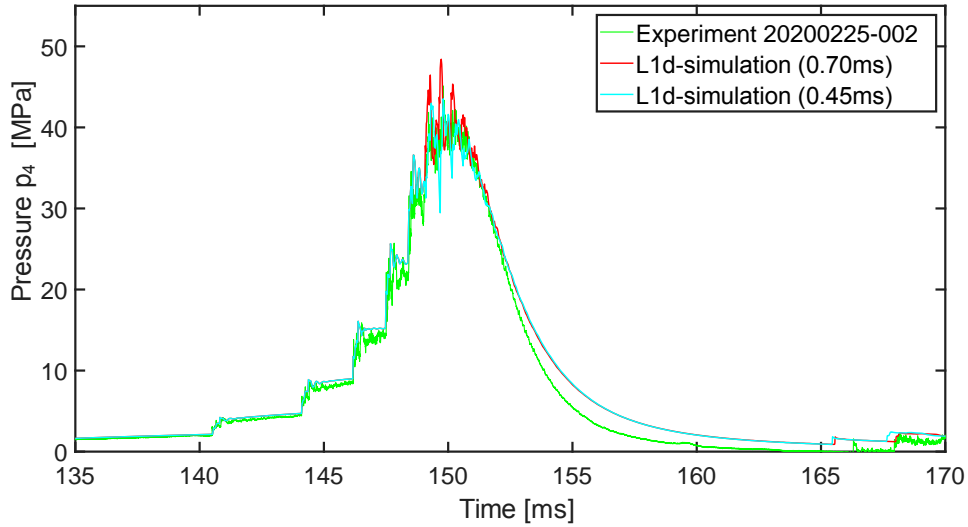
Figure 2.16: Influence of diaphragm holding time $\tau_{opening}$ on driver pressure predicted by the revised L1d-model, refined for mono-atomic driver gas. Experiment conducted at low 20% helium fraction (rest argon) and burst pressure p_4 =400 bar. Adopted from van der Kruijssen [69].

further adaptation of localized loss-factors for different orifice contractions. Due to a computational runtime of hours-days for a detailed L1d-simulation with a single combination of assigned operation parameters, this code is more suitable for fine-tuning test conditions, as a second step after initial prediction with computationally inexpensive analytical methods.

2.7 Time-resolved piston trajectory

2.7.1 Numerical predictions

Equations of piston motion

To cater to the need of accurate and time-resolved piston trajectory prediction, a fundamental model of transient piston motion within the CT, prior to as well as after the moment of diaphragm rupture, was firstly devised by Hornung [53]. In this Newtonian model, the piston is modeled as a point-mass, one-dimensional dynamic of which results from transient pressure (force) variation at the piston rear and front face, $p_{A0}(t)$ and $p_4(t)$, as entailed by continuous buffer and driver gas processing. Both, expanding buffer gas and compressed driver gas are described according to the ideal gas EOS, where time-resolved pressure variation is analytically modeled by an unsteady expansion of the buffer gas and steady compression of the driver gas. Both changes of state are assumed to be isentropic and adiabatic. Time-resolved acceleration of
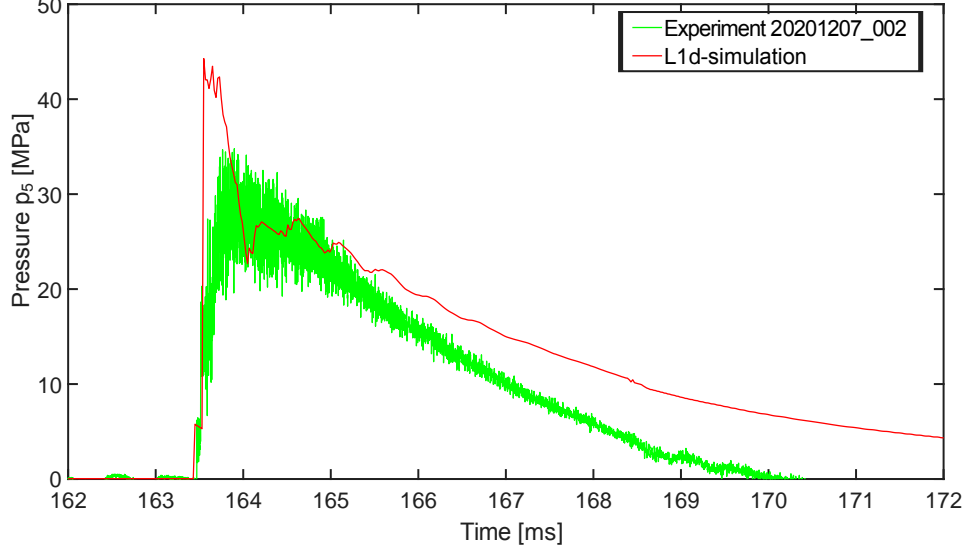
Figure 2.17: Measured and L1d-predicted stagnation pressure p_5 for high helium fraction x_{He} =90%, burst pressure p_4 =750 bar and incident shock Mach number Ma_s =9.62. Adopted from van der Kruijssen [69].

the piston mass for time instants before diaphragm rupture is thus described by:

$$F(t) = \Delta p(t) \cdot A_{CT} = (p_A(t) - p_4(t)) \cdot A_{CT} = m_p \cdot a(t) \qquad (2.50)$$

$$a(t) = \frac{du}{dt} = \frac{A_{CT}}{m_p} \cdot [p_{A0}(1 - \frac{\kappa_A - 1}{2}(\frac{u(t)}{a_{A0}}))^{\frac{2\kappa_A}{\kappa_A - 1}} - p_{40}(\frac{L_{CT}}{x(t)})^{\kappa_4}] \qquad (2.51)$$

where $x(t)$ denotes instantaneous piston position, in reference to the initial position at piston launcher $x(t = 0) = L_{CT}$ and decreasing over time. Thus, $u(t) = \dot{x}(t)$ and $a(t) = \ddot{x}(t)$ signify instantaneous velocity and acceleration, respectively. Here, the term $L_{CT}/x(t) = \lambda(t)$ represents the time-dependent volumetric compression ratio, governing pressure $p_4(t)$ at the piston front.

After the instant of diaphragm rupture, where $p_4(t_{rupt}) = p_{rupt}$, the priorly compressed driver gas will be purged from the CT to the downstream, low-pressure ST by steady expansion and acceleration through the diaphragm station, reaching critical (choked flow) conditions at the orifice throat. Hence, the time-dependent pressure $p_4(t)$ at the piston front will further decrease due to continuous driver gas outflow. Considering Eq. 1.8, the isentropic relation yields:

$$\frac{p}{\rho^\kappa} = const \qquad (2.52)$$

$$\rho_4(t) = \frac{m_4(t)}{x(t)} \cdot \frac{1}{A_{CT}} = \frac{m_4(t)}{V_4(t)} \qquad (2.53)$$

such that transient pressure variation at the piston front is written in reference to the instant of diaphragm rupture:

$$\frac{p_4(t)}{p_{rupt}} = (\frac{x_{rupt}}{m_{rupt}})^{\kappa_4} \cdot (\frac{m_4(t)}{x(t)})^{\kappa_4} \qquad (2.54)$$

where $m_{rupt} = m_{40}$ denotes driver gas mass (identical for all time instants until diaphragm rupture). After diaphragm rupture, the continuous decrease of driver gas mass in the CT over time, $m_4(t) = m_{CT}(t)$, is modeled by the instantaneous mass flow rate, assuming critical conditions at the orifice throat:

$$\dot{m}_{CT}(t) = \frac{d}{dt} m_{CT} = \rho_4^* \cdot a_4^* \cdot A^* \tag{2.55}$$

$$= -\left(\frac{2}{\kappa_4 + 1}\right)^{\frac{\kappa_4+1}{2(\kappa_4-1)}} \cdot A^* \cdot \sqrt{\kappa_4 p_4(t) \rho_4(t)} \tag{2.56}$$

where the time-varying (critical) sound speed of an ideal gas is written in reference to instantaneous total quantities as $a_4(t) = \sqrt{\kappa_4 R_4(t) T_4(t)} = \sqrt{\kappa_4 p_4(t)/\rho_4(t)}$. When considering the (expanded buffer gas) pressure at the piston rear face to maintain constant for moments after diaphragm rupture $p_A(t \geqslant t_{rupt}) = p_A(t_{rupt}) = const$, combining Eq. 2.54 and Eq. 2.51 yields the governing equations for time-varying piston acceleration after diaphragm rupture to:

$$a(t) = \frac{du}{dt} = \frac{A_{CT}}{m_p} \cdot \left[p_A(t_{rupt}) - p_{rupt} \left(\frac{x_{rupt}}{m_{CTrupt}}\right)^{\kappa_4} \cdot \left(\frac{m_{CT}(t)}{x(t)}\right)^{\kappa_4} \right] \tag{2.57}$$

$$\frac{d}{dt} m_{CT} = -\left(\frac{2}{\kappa_4+1}\right)^{\frac{\kappa_4+1}{2(\kappa_4-1)}} \cdot \kappa_4^{1/2} \cdot p_{rupt}^{1/2} \cdot \left(\frac{x_{rupt}}{m_{CTrupt}}\right)^{\frac{\kappa_4}{2}} \cdot \left(\frac{m_{CT}(t)}{x(t)}\right)^{\frac{\kappa_4+1}{2}} \cdot \frac{A^*}{\sqrt{A_{CT}}}. \tag{2.58}$$

Piston trajectory prior to as well as after the instant of diaphragm rupture is captured by considering choked driver gas outflow into the ST. This became the established model for simple yet valuable analysis of piston motion in various free-piston facilities worldwide [71–75]. Along these lines, Gardner [55] pointed out that in the process of designing new operation conditions, the FPD's low-enthalpy operation limit of a large-scale facility such as the HEG to have been limited by strong piston rebound in the past, predicted by the PaCT code [71], based on Hornung's model.

It is noted here that temporal variation of piston rear pressure $p_A(t)$ in the time resolved model is modeled by an unsteady expansion along the full piston stroke. Due to dominant dependence of the latter to instantaneous piston velocity, small velocities throughout the deceleration phase after diaphragm rupture will inevitably induce an instantaneous piston rear pressure which is evidently biased and explicitly non-physical. This shortcoming of the unsteady expansion model and over-predicted piston rear pressure is a problem well-known in literature; different authors have proposed alternative remedies, including modeling a normal shock wave induced in the cold, low sound speed (expanded) buffer gas due to near instantaneous piston deceleration [53] or an overall correction of the buffer gas' isentropic exponent κ_A to better match the time resolved piston trajectory $x(t)$ of an otherwise determined reference case [71]. However, to best knowledge of the author, assuming an unsteady buffer gas expansion along the full piston stroke produced the most accurate results published in relevant literature, compare [75].

Piston motion: wall friction and leakage

In the original model of piston motion, Hornung [53] assumed zero piston wall friction and driver gas leakage. In the current work, transient shear force resistance by mechanical friction between the piston (wear and seal rings) and the tube wall is modeled with respect to the instantaneous piston velocity, however are also set to zero for numerical results presented herein. This is in agreement with observations in relevant literature, which - attributed to the very low friction factor of abrasive material employed for wear and sealing rings (typically doted PTFE or PA) - found piston-tube wall friction to be insignificant for trajectory predictions [72]. In case of the quasi-1D (Langrangian) L1d-code [22], total pressure losses at the piston launcher (buffer-CT junction) and diaphragm (orifice) constriction were similarly found to outweigh effects of piston wall friction [76]. Interestingly, Byrne [59] deduced piston wall friction to be negligible even in the case of a dedicated piston brake in the T4 facility. Besides the T4 and X3 facilities, such a piston brake is also in use at the HEG shock tunnel, where the piston trajectory is predicted by L1d [55].

Moreover, the self-sealing Chevron ring is assumed to seal perfectly such that driver gas leakage throughout the compression process is deliberately set to zero herein. This assumption is justified, considering very high driver gas temperature and sound speed after the (adiabatic) compression process of up to $a_4 = 4650 m/s$ and $T_4 = 6250K$, respectively, compare Fig. 2.9. While the sealing wedge-force is deliberately designed to linearly rise with driver pressure (at the piston front), leakage of the compressed driver gas in terms of a steady leakage mass flow (at choked conditions $u^* = a^* \propto \sqrt{h_0/2}$ and $T^* \sim 3/4 T_4$ for mono-atomic driver gas $\kappa = 5/3$) through any arbitrary gap (within the piston or between piston perimeter and CT wall) will be directly visible from molten wetted surfaces or pressure communicating cavity, due to excessive convective heat load, compare [44]. In fact, whereas the current piston has been operated with identical seal and wear rings for around 100 moderate pressure experiments, abrasive wear on the seal ring increased for the high-pressure experiments presented herein. In this case, the CNC-machined (lathed) circumferential surface of the piston front plate (despite using transient heat flux resistant aluminum-bronze [44]) showed evident signs of ablation by melting due to high convective heat flux as an artifact of heated driver gas leakage past the piston seal and perimeter in the course of two successive experiments, compare Fig. A.14. After replacement of the sealing ring, no further signs of surface melting were noticed until abrasion of this second ring again induced leakage after another set of experiments. Hence, the assumption of negligible driver gas leakage in the numerical simulation is well justified.

Numerical solution

In order to compute the time-resolved piston trajectory along a full stroke, from initial launcher position up to the top dead center (i.e. piston buffer impact) at the downstream CT end, the governing equations defined by Hornung, Eq. 2.51 and Eq. 2.58, are solved for moments before and after diaphragm rupture, respectively, by numerical integration via finite-differences:

$u(t) = \int a(t)\,dt$ and $x(t) = \int u(t)\,dt$. A 4th-order Runge-Kutta-scheme (2nd-order accuracy) is implemented for this purpose, with seamless transfer of state variables at the moment of diaphragm rupture.

In line with the modeling assumptions of Mizoguchi and Aso [75], piston rear pressure for instants after diaphragm rupture is not maintained constant but further computed for an unsteady expansion $p_A(u(t))$. Representative, finite diaphragm opening times of $\tau_{opening} \sim \mathcal{O}(10 - 100\mu s)$ are used to explicitly model the time-resolved diaphragm cross-section opening $d(t)$ by the model of Outa et al. [77]:

$$\frac{A(t)}{A*} = \left(\frac{d(t)}{d^*}\right)^2 = 1 - cos\left(\frac{\pi}{2}\left[\frac{t - t_{rupt}}{\tau_{opening}}\right]^2\right) \qquad (2.59)$$

for $t_{rupt} \leqslant t \leqslant t_{rupt} + \tau_{opening}$, denoting instants of fully closed and fully opened cross-section. While in reality, a finite area contraction of the net orifice cross-section due to blockage from the bent diaphragm petals is expected, this effect is not considered in the present analysis. While variation of the buffer gas' isentropic exponent κ_A from its nominal value 7/5 of a diatomic gas (dry air) without relevant vibrational excitation is easily incorporated to gear the computed piston trajectory to a certain reference case, compare [71], dominant uncertainty is reasoned to be imparted by the simplification of an unsteady expansion, such that variation of the isentropic exponent due to buffer gas expansion is considered of subordinate impact only and hence neglected herein. The current model considers zero piston-wall friction and zero driver gas leakage; for brevity, details are given in the appendix. In this case, Mizoguchi [75] showed that diaphragm opening time can be accurately determined by parametric variation and comparison with the experimental driver pressure trace.

Results

As required piston velocity and buffer pressure rise with burst pressure and helium fraction, particularly high stagnation pressure/-enthalpy test conditions are prone to piston impact when striving for tuned FPD operation. Therefore, time-resolved piston trajectories at the highest nominal driver conditions considered herein, $x_{He} =100\%$ and $p_4 =1000$ bar with the lightweight piston $m_p =62.835$ kg and over-drive $\beta =1.4$, are computed according to the Hornung-Mizoguchi model for four exemplary tuned FPD operation conditions. Respective test conditions according to Itoh et al. ($A^*/A_1 =0.5$), Stalker ($A^*/A_1 =0.5$-0.67) and Hornung and Bélanger ($A^*/A_1 =0.75$) are plotted in Fig. 2.18, Fig. 2.19, Fig. 2.20 and Fig. 2.21, respectively. The piston trajectory is plotted until the time (position) of piston buffer impact (landing) at the CT endwall. Vertical dashed lines mark the time instant of diaphragm rupture and instantaneous piston position. Horizontal dashed lines mark CT endwall and assigned diaphragm burst pressure. Operation parameters are detailed in Table 2.6. For all four conditions computed by the time-resolved code, the latter is found to accurately reproduce assigned FPD operation parameters, over-drive β and compression ratio λ, to within 2.36% and 0.06%, respectively. In the case of Itoh's condition, the residual endwall distance (i.e. compression

Table 2.6: Operation parameters of tuned-FPD conditions (predicted for β =1.40) as input for time-resolved piston trajectory modeling. Diaphragm opening time: $\tau_{opening}$ = 100μs. Superscripts " denote quantities computed from the time-resolved model.

FPD	x_{He}	p_{rupt}	$\frac{A^*}{A_1}$	m_p	λ	p_{A0}	p_{A0}	β''	λ''	u''_{impact}
-	[%]	[bar]	[-]	[kg]	[-]	[bar]	[bar]	[-]	[-]	[m/s]
Itoh	100	1000	0.5	62.835	69.77	79.72	0.846	1.425	69.76	44.08
Stalker	100	1000	0.5	62.835	99.93	64.90	0.465	1.433	99.89	59.54
Stalker	100	1000	0.67	62.835	69.60	113.04	0.849	1.432	69.61	74.92
Hornung	100	1000	0.75	62.835	94.89	122.82	0.507	1.395	94.84	180.17

ratio) at diaphragm rupture predicted by the time-resolved code of Δx =0.3008 m (λ =69.81) is found to agree with values computed according to the FPD prediction to within 0.06%, reflecting remarkably good agreement for modeling of driver gas compression. Spatial variation of instantaneous piston velocity reflects an accurately predicted tuned FPD condition, where velocity reaches a maximum of u_{max} =305.84 m/s before decreasing to $u(t_{rupt})$ =182.38 m/s at the instant of diaphragm rupture and reaching an intermittent minimum of u_{min} =-5.82 m/s. Hence, despite minimum rebound character due to a negative instantaneous velocity, the piston position is only marginally affected, accurately marking the point of inflection, which is defined as the sought characteristic of a tuned FPD condition defined by Itoh et al. Even though temporarily coming to the desired halt at a residual endwall distance of Δx =0.14 m, the large piston rear pressure p_A induces re-acceleration of the piston thereafter, entailing a final impact velocity of up to 44.08m/s. As Itoh's tuned FPD analysis suggests capturing the piston by extending the piston buffer to the predicted point of inflection, such impact velocities by re-acceleration are not part of Itoh's linearized model and hence are not available for comparison. Nevertheless it is deduced from physical reasoning that the prominent rise of piston rear pressure after diaphragm rupture is evidently non-physical but an artifact of the simplifying unsteady buffer gas expansion model. Therefore, the factual piston rear pressure, re-acceleration and final impact velocity will be lower in the experiment. Eventually, in line with Itoh's analysis, the point of inflection, where u ~0 m/s, corresponds to a near vanishing instantaneous piston acceleration, which is similarly predicted by the time-resolved model. Thus, with experimental validation still outstanding, the time-resolved model of piston dynamics is nevertheless reasoned to accurately predict the time-resolved piston trajectory of established tuned FPD theory.

In the case of both Stalker's condition, varying the assigned orifice contraction A^*/A_1 from 0.5-0.67, gears the nominal compression ration λ from 99.93-69.60, necessitating for a near 50% higher buffer pressure p_{A0}. As is observed from Fig. 2.19, and Fig. 2.20, time-resolved computations for Stalker conditions predict a direct impact on the piston buffer (CT endwall) with an impact velocity of u_{impact} ~60-75 m/s for both cases. In comparison to Itoh's conditions, this ensues from either a very high nominal (and reached) compression ratio of λ ~100 (at a near 50% decreased initial driver pressure p_{40} for the former case or an above 40% increase in
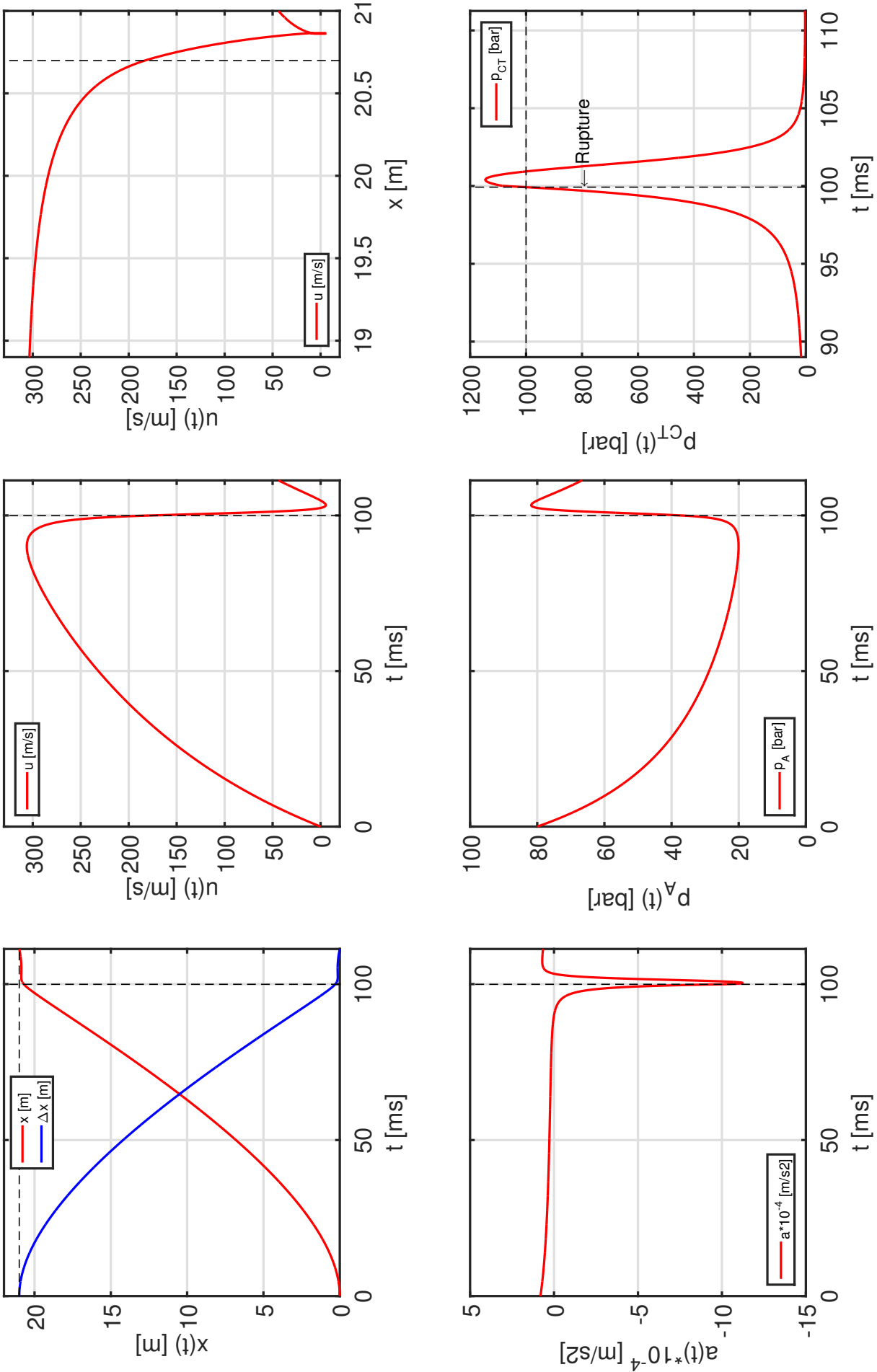
Figure 2.18: Full stroke piston trajectory according to Hornung and Mizoguchi model, for a tuned FPD condition according to Itoh: $x_{He} =100\%$, $A^*/A_1 =0.5$. Values are calculated for an over-drive parameter of $\beta =1.4$, lightweight piston $m_p =62.835$ kg.
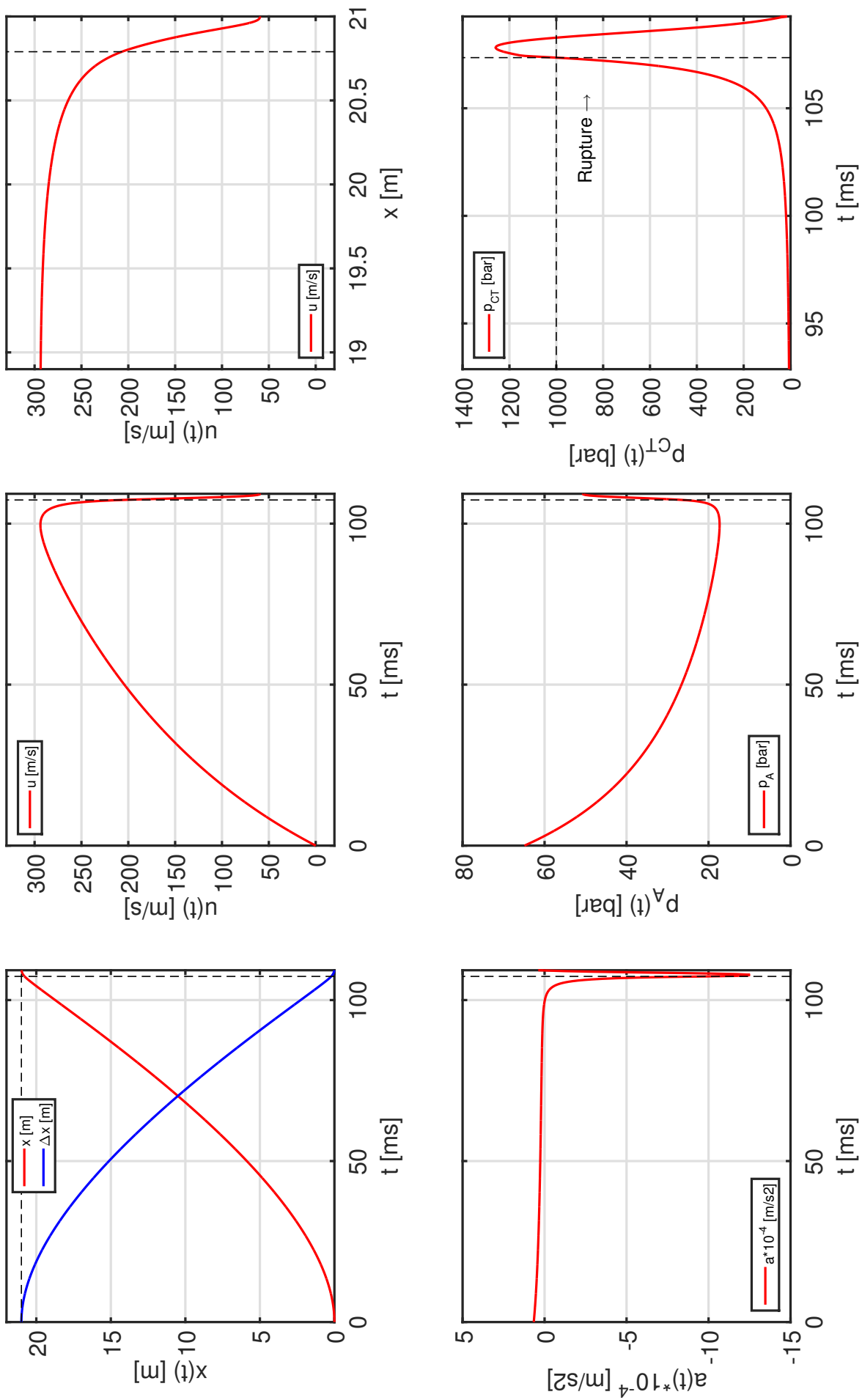
Figure 2.19: Full stroke piston trajectory according to Hornung and Mizoguchi model, for a tuned FPD condition according to Stalker: $x_{He} = 100\%$, $A^*/A_1 = 0.5$. Values are calculated for an over-drive parameter of $\beta = 1.4$, lightweight piston $m_p = 62.835$ kg.
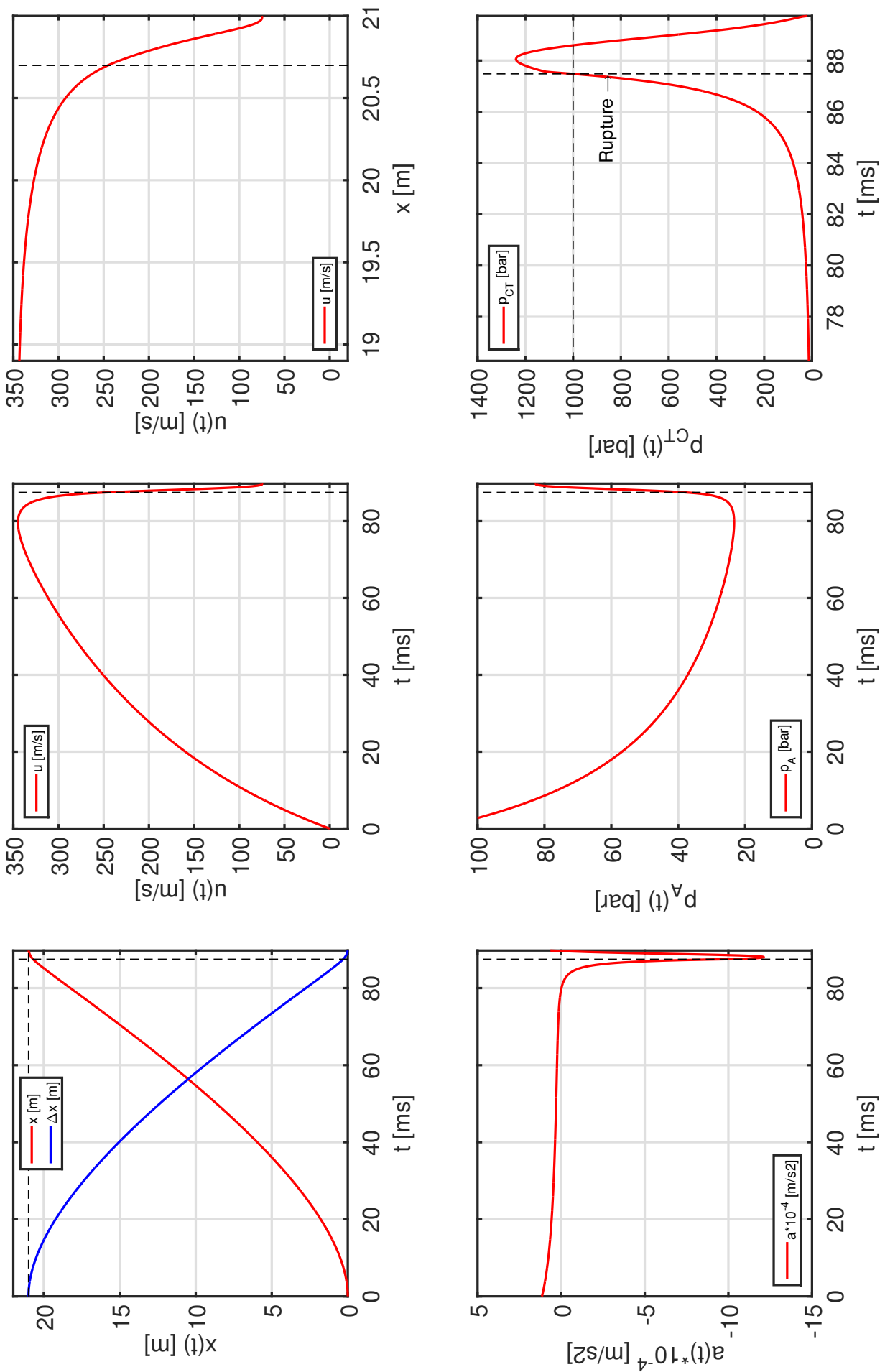
Figure 2.20: Full stroke piston trajectory according to Hornung and Mizoguchi model, for a tuned FPD condition according to Stalker: $x_{He} = 100\%$, $A^*/A_1 = 0.67$. Values are calculated for an over-drive parameter of $\beta = 1.4$, lightweight piston $m_p = 62.835$ kg.
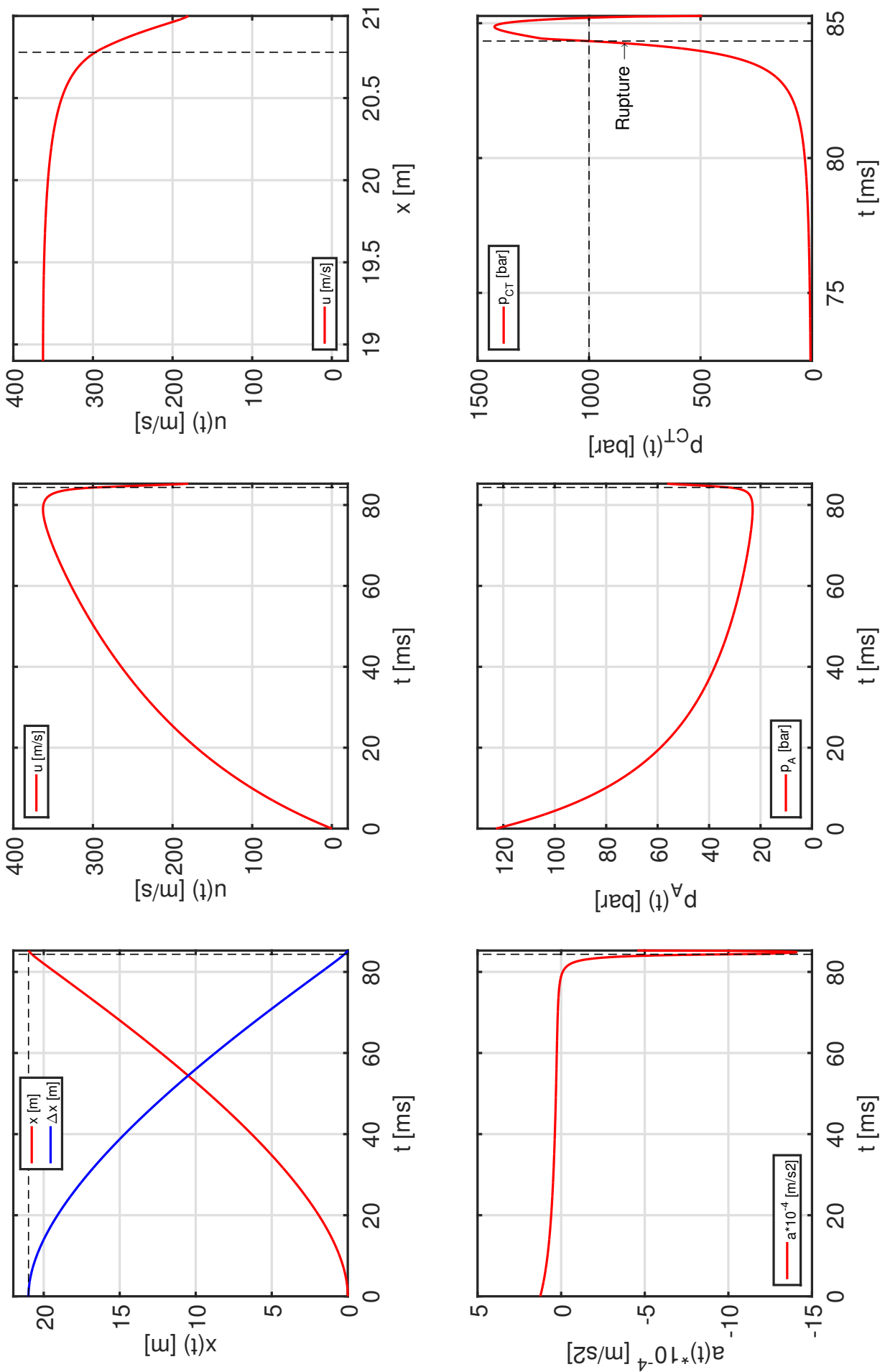
Figure 2.21: Full stroke piston trajectory according to Hornung and Mizoguchi model, for a tuned FPD condition according to Hornung: $x_{He} = 100\%$, $A^*/A_1 = 0.75$. Values are calculated for an over-drive parameter of $\beta = 1.4$, lightweight piston $m_p = 62.835$ kg.

buffer pressure p_{A0} at identical nominal (and reached) compression ratio of $\lambda \sim$70 is the latter case. Whereas Itoh's condition results in a temporary rise of CT-pressure of 15% over the nominal burst pressure p_{rupt} =1000 bar, both Stalker conditions induce a temporary pressure over-shoot of more than 20% - thus, all conditions, by trend, exceed the $\pm$10% margin for over-drive $\beta \sim$1.40 suggested in literature on tuned FPD, compare [11].

In the case of Hornung's condition, increasing the orifice area to A^*/A_1 =0.75 requires the overall highest piston speed at diaphragm rupture of $u_{rupt} \sim$300 m/s in order to compensate the largest predicted driver gas critical mass flow of $\dot{m}^* \sim$110 kg/s. Therefore, the suggested buffer pressure rises up to a maximum of p_{A0} =123 bar, as opposed to a remarkably low initial driver pressure p_{40} =0.507 bar. The resulting very high compression ratio $\lambda \sim$100 induces a severely limited residual endwall-distance $\Delta x(\lambda)$. In effect, piston deceleration takes place too late (i.e. too close to the diaphragm), entailing direct piston impact with a excessive impact velocity of u_{impact} =180 m/s on the piston buffer. Here, the driver pressure temporarily soars up to above $p_4 >$1400 bar, representing an intolerable pressure over-shoot beyond the nominal burst pressure.

Eventually, based on time-resolved prediction of the instantaneous piston trajectory, tuned FPD prediction by Itoh's analysis is clearly the most favourable operation condition for the HELM facility at the maximum nominal design point. An accurate tuned piston trajectory, with an intermittent inflection point at successfull over-drive $\beta \sim$1.4 and tolerable driver over-pressure, is predicted by the time-resolved model - though at mere moderate compression ratio of $\lambda \sim$70. In contrast, the first Stalker condition facilitates a significantly elevated compression ratio of $\lambda \sim$100, yet inflicts a direct piston impact due to insufficient piston deceleration over an accordingly very limited residual endwall-distance $\Delta x(\lambda) \sim$0.21 m. Direct piston impact is predicted to be even more severe for Stalker's second condition, whereas Hornung's condition is evidently restrictive and unfeasible due strong buffer pressure over-estimation at an overly large orifice area. It is to be pointed out that a decrease of the orifice area to A^*/A_1 =0.67 entailed a nominal compression ratio of $\lambda \sim$110 due to Hornung's analysis, which is clearly impractical, compare Fig. 2.7.

Despite good-excellent agreement of suitable operation points due to tuned FPD analyis and time-resolved modeling, factual experiments will vary from the latter due to artifacts of inaccurate physical modeling: precisely, total pressure losses inflicted at the buffer-CT junction are omitted herein, yet, will induce an inevitable reduction of piston rear pressure in the experiment. On the contrary, the insufficient model of an unsteady expansion strongly manifests in terms of piston rear pressure over-prediction throughout the piston deceleration phase to rest, i.e. particularly towards over distances between diaphragm rupture and buffer impact. In effect, theoretically predicted impact velocities, particularly for Itoh's condition, where the piston comes to an intermittent halt, will not be as severe in the experiment. Accordingly, accuracy and conclusion of numerical simulations of the time-resolved piston trajectory by Hornung's anlytical model are limited by definition [71, 78]. Hence, a range of tuned FPD conditions were run as validation experiments in the HELM facility, even though low-moderate piston impact

velocities were predicted and despite of large compression ratios $\lambda \sim 100$. Effort is made to measure instantaneous piston acceleration (and hence time-resolved full-stroke trajectory) by an on-board accelerometer in the following, eventually facilitating corrections and increased accuracy of analytical models and numerical predictions of piston motion.

2.7.2 Accelerometer measurements

Any simple or elaborate approach of a priori numerical prediction of the piston trajectory will be subject to uncertainty, based on its assumptions and idealizations. In the case of analytical models, uncertainty primarily arises from assuming an unsteadily expanding buffer gas, varying total pressure losses at the piston launcher, modeling of time-varying piston rear pressure at instants of strong deceleration to rest and insufficient knowledge of the accurate diaphragm opening time. In the case of more sophisticated (quasi 1-D) CFD modeling, the highest uncertainty is induced by empirical, localized loss factors, which are to be geared closely to different test ranges or even individual experiments [76]. This corresponds to a divergence of predicted piston position and velocity of up to 25%, reported in literature [72, 73].

Evidently, the unambiguous measurement of time-resolved piston trajectory is highly desirable, firstly to be able to validate existing, theoretically predicted FPD operation points and secondly to lower the risk of piston impact in the ongoing design of new, high and potentially critical operation conditions [48].

Piston trajectory measurement

Literature on direct measurement of piston position, velocity or acceleration is generally scarce. Effort is ongoing and in FPST facilities worldwide, this is typically achieved by (time-of-arrival) sensors mounted in the CT wall at discrete axial locations. Itoh et al. [46] demonstrated a tracking system of compression piston trajectory which employs 6 photoelectric sensors, consisting of laser- and photodiodes, mounted at discrete axial positions along the CT of the HEK shock tunnel. Here, aluminum piston lateral surface was marked with a discrete fringe pattern of low reflectance stripes with sharp edges and spatial pitch by anode oxidation. As the piston passes sensor locations, its' position at discrete time instants is deduced from a sequence of characteristic intensity peaks as light reflecting off the alternating high and low reflectance surface is detected. Information on instantaneous velocity in the vicinity of 6 sensors is obtained from numerical differentiation of a least-squares, polynomial curve fitted through discrete time-position data. The sensor located upstream of the diaphragm allowed direct measurement of instantaneous piston speed up to 220 m/s. This facilitated to demonstrate accurate prediction of piston stroke and velocity and thus a validation of Itoh's [46] method for calculating tuned piston operation. Although not presented by the authors, such time-resolved, high-quality data of piston displacement and velocity will enable derivation of instantaneous acceleration to calculate piston rear pressure around sensor locations. A similar measurement system has been reported for the HIEST shock tunnel [61]. Tanno et al. [47] further studied tuned pis-

ton operation in a FPD demonstrator NAL-CTA. Due to low-pressure operation, the facility was equipped with spacious optical access to the CT endwall via an acrylic window of 15cm length, allowing to visually track piston motion at the top dead center by a low shutter time CCD camera at 6 fps. By measuring velocities from 220 m/s down to rest, trajectory data clearly demonstrated tuned operation and enabled resolving a piston saddle point prior to buffer impact. Measurement accuracy due to image processing of ±2.4-5.0 m/s was reported. Zhixian et al. [74] described a similar tracking system of piston motion in the FD-21 shock tunnel which comprises of 8 stationary, photoelectric sensors distributed along the CT, employed to validate numerical predictions of piston trajectory, based on Hornung's analytical model, by reference discrete piston position data. Eitelberg et al. [24] and Atcitty and McIntyre [71] reported on a similar approach in the HEG shock tunnel.

Besides detecting piston passage at discrete locations along the CT, continuous measurements of instantaneous piston velocity and position by an on-board mounted sensor are regarded particularly advantageous. Along these lines, the first successful measurements of piston acceleration by an on-board mounted accelerometer were presented by Altenhöfer [42] and Mundt [64] in the HELM shock tunnel. The on-board, stand-alone device - which is a preceding version of the one used in the current work - was devised and assembled by staff from the French-German Research Institute Saint-Louis (ISL) and was rigidly mounted to the compression piston rear face. It comprised of an embedded data acquisition system (microcontroller, ADC converter, signal amplifier, RAM chip, USB communication port, batteries) and used a piezoresistive accelerometer (Endevco Inc., type 727-60K-5-120) for time-resolved measurement of instantaneous piston acceleration. For a small number of low-pressure experiments, a peak amplitude deceleration of up to -8,000 g was measured on a 57 kg piston, indicating the latter to be over-predicted by a L1d simulation of this operation condition; however, no velocity or displacement data was derived.

About the same time, Gardner [55] reported on preliminary tests on the use of a similar stand-alone accelerometer on a compression piston of 800 kg weight for a low-enthalpy condition in the HEG shock tunnel. However, due to damage to the accelerometer, no useful data was retrieved. To best knowledge, the only study in literature having successfully conducted direct, on-board, time-resolved measurements of piston acceleration and trajectory reconstruction along a full piston stroke in a FPD so far was presented recently by Gildfind et al. [78] for the X3R facility, reporting on the use of a similar device with piezoresistive accelerometer. The latter are well-known to be prone to error from sources such as integration drift and zero point offset [79] which becomes particularly relevant after mechanical piston impact [78]. Such spurious DC drift induces non-physical behavior as velocity and displacement are obtained by twofold numerical integration of acceleration data. After unsatisfactory calibration against a commercial, piezoelectric accelerometer of known sensitivity in a low amplitude -200 g drop-test, an approach to correct for non-linear response and deviations from net sensitivity was presented where trajectories predicted by numerical integration were fitted to optical waypoint-markers by a CCD camera. This method of accelerometer sensitivity correction was

then successfully adapted to measurements of piston acceleration in X3 expansion tube driver. In reference to the work of Itoh et al. [46], the concept of optical piston detection was reversed: the stand-alone device was equipped with an on-board laser diode to track changes in the reflectance off a circumferential fringe pattern applied to the CT diameter by aluminum foil. Temporal correlation facilitated unambiguous verification of piston position, enabling to correct accelerometer sensitivity in order to yield physical piston trajectory by a least-squares fit of the latter through discrete position data. For a low-pressure test condition in the X3 expansion tube driver, the stand-alone device was mounted to the front face of a 280 kg piston, measuring rigid body acceleration in a range (+200/-500 g) for a full piston stroke at 12-bit amplitude discretization and 28 kHz sampling rate. For piston velocities up to 100 m/s and 13.4m displacement, the authors quoted an uncertainty in waypoint position of ± 10 mm, stating factual error to be even lower. Comparison of measured piston trajectory to L1d predictions for a low-pressure oscillatory motion, i.e. without diaphragm rupture, showed good agreement in terms of peak displacement whereas piston rebound motion was not captured as accurately by the simulation. The studies of Altenhöfer [42] and Gildfind et al. [78] thus demonstrated proof-of-concept for in situ acceleration measurement and trajectory reconstruction along a full piston stroke in a FPD by an on-board, stand-alone accelerometer in open literature.

Accelerometer

The current work uses succeeding version of the device previously used by Altenhöfer [42], where electronic hardware components of the data acquisition system are improved for higher robustness to mechanical loads on behalf of ISL. A single-channel microcontroller samples analog voltage input in the range ±5 V at a sampling rate of 200 kHz after amplification with a gain of $\sim$50, allowing for measurement of $\pm$40,000 g in the full voltage range. Amplitude discretization with an 16-bit ADC facilitates to resolve increments of $<$2 g where an internal flash drive memory is read out via USB (universal serial bus). The housing is made from durable aluminum AW 7075-T6 alloy and is mechanically fastened to the piston rear face via a set of screws, see [42]. A picture of the new device is given in the appendix A.

Technical approach

The complete piston trajectory in terms of instantaneous velocity and position along a full stroke can be reconstructed by numerical integration of primary time-resolved acceleration data via the trapezoidal or Simpson rule, either one yielding identical results. It is remarkable to note that the qualitative piston motion accurately agrees with numerical predictions by Hornung's analytical model or L1d and reflects a physical behavior. In clear contrast, attributed to a combined effect of erroneous DC integration drift, zero-point offset and insufficiently accurate calibration by the manufacturer, quantitative data reflects unplausible behavior such as piston displacement beyond the length of the CT which is clearly unphysical. Hence, simply imposing the manufacturer stated sensitivity is unfeasible such that quantitative measurements require

for correction by an accurate reference. Therefore, similar to the work of Gildfind et al. [78], the current work makes deliberate use of discrete waypoint markers which are provided by five inductive proximity sensors (Baumer GmbH, type IFRP 12P1501/S14), near wall-flush mounted along the CT. As the HELM compression piston is assembled from different slices of materials (metals including aluminium being inductive, plastic seal and slide rings being non-inductive), geometrically defined sharp edges of individual components along the lateral surface induce a unique succession of rising and falling (digital) signal flanks upon axial passage which are used to detect time-discrete arrival and further facilitate time-averaged velocity measurements at every single sensor location. A representative digital signal data trace is provided in the appendix A. With a stated rise time of τ <50μs of current sensors, waypoint markers provide for a reference of instantaneous piston position of $\pm$10 mm and $\pm$15 mm at 200 and 300 m/s nominal velocity, respectively. Considering a minimum relative distance of sensor locations of 2.5 m, this uncertainty amounts to mere 0.6% at maximum, reflecting current waypoint markers to provide for an accurate reference of time- and space-discrete piston position. The available edge-to-edge distance on the piston and sensor rise time entails a maximum absolute uncertainty of $\pm$1.3-11.1 m/s, equivalent to $\pm$1.3-3.7% relative deviation (at nominal velocity 200-300 m/s), for measurements of time-averaged velocity, indicating the latter to be slightly less accurate and less suitable as a primary reference. Thus, as piston arrival at discrete waypoints serves as an accurate spatial reference, a non-linear least-squares routine is employed to fit the integrated piston trajectory through known reference locations and time instants by correcting the sensor sensitivity - assumed constant in the relevant frequency range - by up to 5% from the manufacturer stated value). Resulting corrected data traces are evident to reflect both, physical qualitative and quantitative behavior and hence to facilitate accurate measurements of the full stroke piston trajectory.

Results

For a single low-pressure operation condition LP1 (p_4 =200 bar, λ_{rupt} =44) in air as driver gas, measured and computed kinematic quantities of the piston trajectory are presented in Fig. 2.22. The maximum positive acceleration upon release valve switching amounts to 3000 m/s^2 whereafter the piston continuously accelerates to a maximum instantaneous velocity of 170 m/s at $\sim$16 m. Driver pressure increase and piston rear pressure decrease induce deceleration to zero after $\sim$ 223 ms, with the notable deceleration to a peak of $\sim$30,000 m/s^2 corresponding to the strong rise in driver pressure: beyond a diaphragm rupture pressure of p_4 =200 bar at λ_{rupt} =44. In effect, the velocity drops from it's maximum to a minimum value of <5 m/s over a distance of $\sim$2.6 m, coming to a near halt at a distance of 0.44 m from the endwall (λ =47.7). Thereafter the piston accelerates again to a limited instantaneous velocity of $\sim$24 m/s when impacting on the piston buffer at the CT endwall. As such, the full-stroke piston displacement represents a near ideal soft-landing trajectory as suggested by Tanno et al. [47], see Fig. 2.3. Further acceleration thereafter is seen to be caused by a sensed positive signal of the accleration sensor (beyond the level of zero-acceleration), which is, however, clearly non-physical and an

artifact of erroneous signal offset and numerical integration. The same behaviour was reported by Gildfind et al. [78] after impact on semi-rigid piston buffers for a piezoresistive accelerometer. Green markers in the time-position plot represent locations of unambiguous piston passage at the reference sensor position: the curve of integrated acceleration is observed to near perfectly coincide with the independent reference signal of sensors 1-4, exemplifying accuracy of the current approach and instantaneous piston acceleration measurements. Towards the CT-endwall (21 m), the curve reflects further piston movement beyond the fixed stop, which is - identical to the rising velocity - caused by erroneous acceleration signal offset. As the current L1d model is not apt to accurately capture the pressure trace and piston trajectory of higher test conditions with noble gas driver in the HELM facility, see Fig. 2.17, a meaningful comparison to the measured piston trajectory in Fig. 2.22 is unfeasible at current.
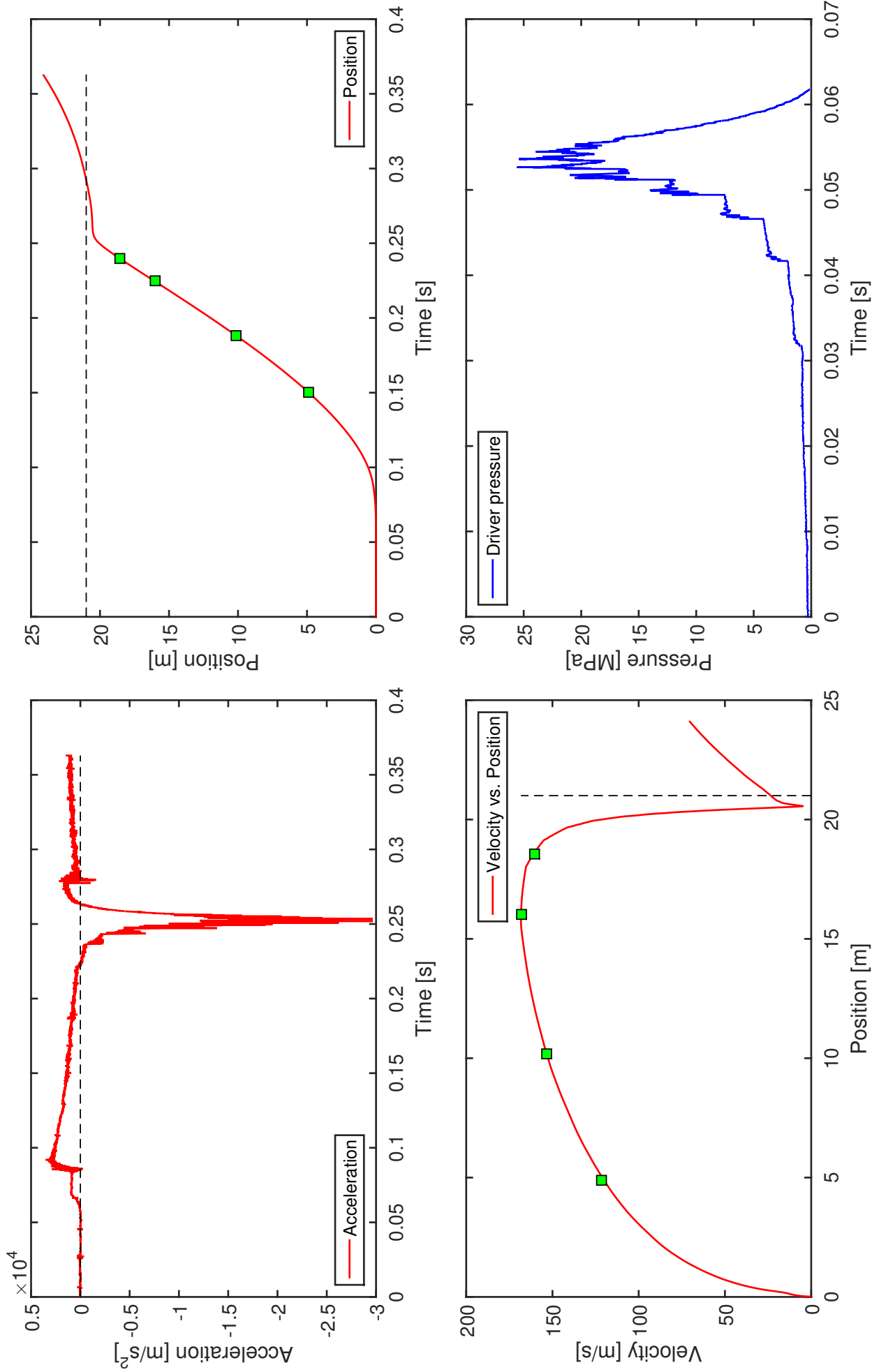
Figure 2.22: Piston trajectory quantities over a full piston stroke for low-pressure condition LP-1. Plotted are instantaneous acceleration and local position over time, velocity over position and driver pressure trace over time. Dashed horizontal and vertical lines mark zero-acceleration magnitude and driver tube length (21 m), respectively. Green markers indicate instantaneous piston position and time of arrival at distinct inductive proximity sensor locations 1-4.

3 LIGS in situ Nozzle Reservoir Thermometry

This chapter details the background and application of non-invasive optical diagnostics applied for in situ nozzle reservoir stagnation (translational) temperature measurements in the HELM shock tunnel. Starting from a background on relevant literature, the specific approach of LIGS application as a key aspect of the present work is detailed. Parts of this work have been priorly published in Selcan et al. [62, 80] and portions of the text herein have been adopted.

3.1 Review of suitable optical diagnostics

3.1.1 Fundamental requirements

Evaluation of experimental measurement data in high-enthalpy and high-speed ground test facilities requires knowledge of test gas thermodynamic properties in the nozzle reservoir, in order to accurately define nozzle flow upstream boundary conditions. Therefore, direct experimental acquisition of test gas temperature prior to nozzle expansion is most beneficial to determine the stagnation enthalpy of short duration facilities, such as reflected shock tunnels and expansion tubes. This allows for suitable numerical rebuilding of the nozzle expansion flow and thus contributes to an accurate definition of free-stream quantities at the nozzle exit. Yet, as much as knowledge of the nozzle reservoir test gas temperature is highly desirable, investigation of high-enthalpy flows by means of conventional probes is strongly restricted by thermal, mechanical and temporal limitations. Further adverse effects such as associated aerodynamic blockage and heat loss via thermal radiation are well known. Optical techniques in contrast, are in general well suited for measurements under severe conditions due to their non-intrusiveness and absence of mechanical and thermal restrictions. However, in light of the severely limited test time, excessive temperature and pressure levels as well as closely restricted optical access, the requirements for suitable optical diagnostics to application in ground testing facilities are closely defined and have been aptly summarized by Danehy et al. [81]:

1. Hypersonic impulse facilities with steady test time <10-100 ms necessitate for high repetition rate laser systems (kHz-MHz), such that a common laser operation rate of 10 Hz only allows for a single measurement per test run.

2. As many facilities operate merely once/few times per day, statistical averaging of a significant number of measurements is often times not possible, rendering single-shot capability desirable.

3. Many large facilities (particularly free-piston driven) face significant axial displacement due to mechanical recoil and reaction forces, making geometrical beam path alignment challenging and less stable. This becomes further important with increasing distance between laser and test section, resulting in long path lengths prone to misalignment.

4. Large facilities operating at very high pressures often have no or merely limited optical access - furthermore the windows material's spectral properties have to be suitable for the diagnostic technique to be used.

5. At high-enthalpy conditions, strong gas luminosity and spurious background radiation significantly complicate the detection of weak light signals, favoring the use of coherent techniques wherever possible.

3.1.2 Established optical diagnostics

Evidently, the strength of some established laser techniques for hypersonic flows is increasingly limited when to be applied to the highly loaded nozzle reservoir section of a free-piston shock tunnel. Spontaneous Raman spectroscopy is attractive due to a relatively simple optical setup of a single laser beam, fundamental single-pulse capability, absence of collisional quenching effects and restriction to resonant excitation, however, suffers from a severely weak signal intensity and incoherent signal scattering [82]. Despite relatively inexpensive spectral analysis, it is thus not suited to acquire single-shot measurements under harsh high temperature conditions, all the more in the presence of strong background luminosity further lowering the signal-to-noise ratio (SNR). Another related proven diagnostic technique using a second laser is Coherent Anti-Stokes Raman Scattering (CARS), offering higher signal intensity due to a coherent signal beam and single-shot capability when using a broadband dye laser to generate a full CARS spectrum of Raman resonances. As with incoherent Raman scattering, CARS necessitates for wavelength-resolved spectroscopic detection of a full signal spectrum and, due to its non-linear nature, requires high pump laser energy. As gas temperature is determined indirectly from spectral shape - by fitting the sampled spectrum to a theoretical prediction - , the major disadvantage of CARS is posed by the expensive data reduction, mandating for extensive spectral calculations by convolution of Stokes/pump laser profile and spectrometer-detector instrument function [83]. This spectroscopic modelling is further sensitive to background noise, Raman transition linewidth (line profile) and precise spectral location, thus affected by pressure line-broadening which is to be accounted for [82]. Still, CARS has been applied to shock-tunnel experiments to great advantage in the past, particularly within the low-pressure, low-density freestream at the nozzle exit. Absent of multiple single-shot signal averaging - not applicable to short-duration facilities -, Boyce et al. [83] measured vibrational and rotational temperatures in the freestream and spherical testbody shock layer at pressures below 3 bar and attributed single-pulse CARS thermometry accuracy and precision of up to 10% to be limited by pulse-to-pulse amplitude and phase fluctuations of the dye laser profile's mode structure. Pulford et al. [84] measured shock tunnel freestream temperatures of up to

3000 K - assuming rotational /vibrational thermal equilibrium - at a scramjet model inlet at pressures around 1 bar with a single-shot precision up to 11.4%. According to authors' best knowledge, the overall highest pressure of 6.5 MPa at which broadband CARS has been successfully applied so far was met by Grisch el al. [85] who measured temperatures up to 2000 K in a rocket combustor, reporting pressure line broadening to become increasingly difficult to capture/model at simultaneously high pressure and temperature. Thus, despite being suited in principle, CARS application to quantitative single-shot temperature determination in the high-pressure nozzle reservoir of a shock tunnel is deemed difficult by the authors. Another potential technique is laser induced fluorescence (LIF) which - due to its inherent linear nature of a given species' resonant excitation and despite isotropic (incoherent) emission - features signal intensity of magnitudes stronger than Raman scattering [82]. As for spontaneous Raman scattering, a principle strength of LIF is its potential to acquire 2-D spatial distributions of temperature and species concentration which is yet not deemed to provide much additional information in shock tube flows of uniform centerline development. Quantitative analysis of spectrally resolved LIF signals is significantly affected by radiative decay rates of excited states due to predissociation, photoionization and collisional quenching which are difficult to account for - the latter being particularly relevant to shock tube flow due to high pressure and density [84, 86]. Furthermore, rotational and vibrational energy transfer processes are to be modelled by adequate rate models [82]. A variant avoiding this problem of collisional quenching, known as laser-induced pre-dissociation fluorescence (LIPF), was used by Sutton et al. [87] to measure vibrational temperatures within a shock tunnel testbody shock layer, however the severely low fluorescence yield (i.e. signal intensity) of LIPF - in comparison to regular single-pulse LIF - resulted in experimental uncertainty as high as 10-18.6%. As the fluorescence yield of LIF noticeably decreases with increasing pressure and as the signal suffers from diffuse background radiation and flow luminosity, the technique is similarly not deemed applicable to a high-pressure shock tunnel reservoir [81]. As the fluorescence yield of LIF noticeably decreases with increasing pressure and as the signal suffers from diffuse background radiation and flow luminosity, the technique is similarly not deemed applicable to a high-pressure shock tunnel reservoir [81]. Moreover, the general strength of 2-D imaging techniques such as PLIF is best used to advantage within flowfields of inherent spatial variation, as occurs within the free stream downstream of the nozzle exit [88], whereas the flowfield within the shock tube and nozzle reservoir of test facilities is generally considered spatially uniform and thus does not demand for spatial imaging.

In contrast, a technique to be potentially used to advantage within the nozzle reservoir, avoiding many of the problems discussed afore, is emission spectroscopy. Here, a relatively simple optical setup (not requiring any laser excitation at all) allows for the convenient sampling of the species' self-emitted radiation spectrum, however, quantitative analysis of the sampled spectrum necessitates for proper calibration and detailed knowledge of the related species (mainly in ground state or weakly excited electronic levels) to study the gas chemistry involved. In general, description of upper state population in relation to ground state via Boltzmann dis-

tribution hold for thermodynamic equilibrium [81], such that application to the shock tunnel reservoir at high pressure and density is in principle viable. Even without knowledge of total species density, temperatures are derived from qualitative spectral shape, using line intensity ratios or line shape, as opposed to absolute intensity of detected emission [81]. At very high pressures, collisional line broadening will be dominant. Finally, as absorption along the line of sight cannot be separated from the emitted spectrum, the quantitative indirect analysis requires detailed computation of predicted radiation spectra, thus making analysis very complicated. To the authors' best knowledge, emission spectroscopy has so far been applied to thermometry only at atmospheric pressures or below 0.1 MPa [89]. An inherent characteristic of emission spectroscopy is spatially integrated line of sight integration of the signal, preventing spatial information on the measurement volume. A similar line-of-sight method is absorption spectroscopy, relying on the principle of intensity decrease due to stimulated absorption of irradiated light as it transects the measurement volume. Rate of absorption depends on the light source and transition line-shape, respectively, where the latter is determined by spectral scan with a narrow-band or tunable diode laser (TDLAS) and fitted to a computed Voigt profile. Translational temperature can thus be determined from the line strength ratio of two transitions of the same species or by determining the Doppler line width of a single absorption line, further considering collisional and natural line-broadening [81]. Collisional shift in the spectrum can further be used to determine pressure simultaneously. Parker et al. [38] measured translational temperatures up to 563 K at very low pressure of 2.9 kPa in the freestream of the LENS I shock tunnel by TDLAS. Nomura and Komurasaki [90] used crossbeam saturated absorption spectroscopy to measure the translational temperature profile up to 5400 K along the stagnation streamline in front of a sphere, in a rarefied arc-heated argon flow at a pressure of 120 Pa.

3.1.3 Potential of LIGS

Against this background of limited applicability of some established techniques, the advantage of coherent techniques in high-interference, high-pressure environments with restricted optical access was highlighted by Eckbreth [82] who proposed the non-linear technique of degenerate four wave mixing (DFWM). The latter uses a single tunable laser source - thus simpler optical setup than CARS - and is better suited for high-pressure environments, being more robust to quenching effects. In DFWM three phase-matched input beams of identical frequency (resonant to an electronic transition, e.g. in NO or NO_2 [91]) are mixed to generate a fourth signal beam at the same frequency. When described by wave vectors, two parallel polarized (pump) waves intersect to give rise to an optical interference (fringe) pattern of spatially varying intensity, i.e. difference between excited and lower states, known as population grating [91]. At resonance, this refractive index grating induces the third (probe) beam to be coherently scattered away to form the signal beam, analogous to Bragg diffraction off a crystal. Quantitative translational thermometry by DFWM is based on determination of the Doppler broadening of a spectral line-shape fit and requires spectrally resolved signal detection via tuning a sin-

gle narrow-band laser over an entire spectrum. Thus, the technique has poor time resolution (on the order of minutes [92]) and does not grant single-shot acquisition, mandatory for short-duration shock-heated flows. Moreover, signal intensity from population gratings is observed to decrease with higher pressure [82]. In contrast, congruent thermal gratings arising from collisional quenching, an in DFWM originally undesirable byproduct, rise favorably with pressure [91]. Yet, DFWM typically uses non-resonant excitation for temperature measurements only and is gradually impaired by an excitation of resonant gratings [93].

Against this background, a coherent measurement techniques, closely related to DFWM, which can favourable use resonant and non-resonant gratings, is laser-induced grating spectroscopy (LIGS) - also known as laser-induced thermo-acoustics (LITA) in literature. It recently emerged as a promising method to complement the range of established measurement techniques for shock-tube flows and proved particularly promising for application in harsh high-pressure test environments. Based on polarization and/or absorption, both non-resonant (electrostrictive) and resonant (thermal) signals are detected by scattering of a cw probe beam from a local interference grating of two crossed pulsed pump beams, yet at different wavelength. Induced opto/thermo-acoustic gratings are described by two counter-propagating plane sound waves, the temporal propagation of which is described by the linearized hydrodynamic equations of motion - enabling direct sound speed measurements [94]. In contrast to other non-linear techniques - relying on spectrally-resolved signal intensity and line shape profile -, LIGS quantitative signal analysis is straightforward, with information being frequency-encoded by temporal amplitude oscillation of the single, coherent, monochromatic signal beam, sampled by a single-point detector (PMT), thus absent of pump laser scanning, spectrally resolved detection and spectral analysis. Measurements can be made in single-shot, with sub-microsecond temporal resolution on the order of $\sim$100 ns. Deterministic calculation of the scattering (Brillouin) frequency, by frequency analysis or fitting of the signal's temporal evolution, allows local gas temperature to be determined when gas composition is known, i.e. by use of thermo-physical property databases, relating sound speed, translational temperature and pressure via real gas equation of state (EOS) or equilibrium assumptions. This proofs to be particularly advantageous when LIGS is applied to the shock tunnel nozzle reservoir where thermo-chemical equilibrium can be readily assumed due to high pressure and density effects. As both resonant and non-resonant gratings and thus signal oscillation amplitude rise with pressure, the technique is particularly suited to be used in shock heated flows and stagnation regions. Due to its coherence, the signal beam (at dye laser wavelength) can be spatially filtered to reject flow luminosity and background radiation, increasing robustness in harsh environments, and does not suffer from losses when travelling over large distance, provided the beam path is sufficiently geometrically stable [81]. This is most beneficial to yield high detection efficiency even in the harsh high-enthalpy environment of shock tubes, further aggravated by spurious extrinsic light interference from background radiation and metallic impurities encountered [84]. Here, the fact that information is conveyed by modulation frequency rather than spectral line shape, rejects most quantitative error sources of intensity-based spectral techniques and facilitates increased

robustness in self-luminescent environments. Single-shot measurements by LIGS, in contrast, do not demand for a multiplex approach of broadband excitation, e.g., wavelength scanning, and spectrally resolved detection by frequency-resolved detectors but utilize a single-mode laser and time-resolved detector instead and can likewise use resonant and non-resonant excitation to advantage [95, 96].

Regarding the capability of deterministic, time-accurate, pointwise measurement of post-shock sound speed and translational temperature, fluid velocity and Mach number, by a single laser pulse, in conjunction with straightforward signal analysis and data reduction, LIGS proves to be a versatile and robust laser diagnostic technique. As such it is considered well-suited to complement more established methodologies of shock tube research. In light of excessive pressure levels prevalent in high-enthalpy ground testing, the positive correlation of resonant and non-resonant LIGS signal intensity with fluid pressure is considered particularly advantageous. Whereas quantitative measurements by a range of competitive techniques are increasingly impeded at elevated pressures - resultant from a decaying signal strength due to higher collisional quenching rates [97, 98] -, the signal intensity I of LIGS scales with temperature T, benefits from greater pressures p and rises according to Eq. 3.1 [99].

$$I \propto p^2 \cdot T^{-3.4} \tag{3.1}$$

Coherent signal beam nature is most beneficial to yield high detection efficiency even in the harsh high-enthalpy environment of shock tunnels, further aggravated by spurious extrinsic light interference from background radiation and metallic impurities encountered [84]. Sources of uncertainty (particularly single-shot fluctuation) for coherent laser beam techniques in general, such as beam steering and defocusing (induced by gradual beam deflection due to density gradients within the traversed highly compressible flowfield) are known from CARS measurements [85] and likewise apply to LIGS [100]. A strong feature of LIGS, which distinguishes it from a range of established intensity-based diagnostics is the pure frequency-based signal character of LIGS thermometry that reflects its superior robustness to various error sources of quantitative signal intensity deterioration, such as collisional quenching or background luminosity. LIGS is also insensitive to fluctuations in laser intensity. Similarly, once the coherent signal beam is detected and successfully isolated from spurious background radiation, specular reflections and undesired probe and pump beams, via optical bandpass filters and pinhole apertures, respectively, quantitative data reduction is straightforward and unambiguous. This is particularly true in comparison to intensity-based, spatially resolved techniques such as PLIF. Using a photomultiplier tube (PMT), i.e., single-point time-resolved detector, is advantageous in comparison to multichannel detectors - as employed in broadband CARS - by avoiding nonlinear instrument response and without the general need for spectrally-resolved detection by high-resolution spectrometers as employed in multiplex approaches. PMTs offer variable gain to amplify very low intensity signals (as applies to LIGS) and provide for fast (sub-ns) time response. In contrast to techniques utilizing broadband excitation, spectral intensity distributions of the dye laser, i.e., fluctuating power density and mode structure, - as applies to CARS -

can be entirely neglected [85]. Whereas the LIGS signal intensity increases favourably at higher pressures, quantitative thermometry by spectral methods becomes increasingly difficult: e.g., CARS temperature accuracy depends on collisional linewidth due to pressure-broadening that is to be accounted for and - especially at simultaneously high temperatures where Doppler broadening becomes further strong - can only be obtained from linewidth model extrapolation [85].

3.2 LIGS Measurement technique

3.2.1 Application

First successful application of LIGS to the transient test time regime of a small-size double-diaphragm shock tube was demonstrated by Sander et al. [97]], measuring translational temperatures behind the incident and reflected shock by resonant and non-resonant homodyne LIGS, up to 840 K and at 2 MPa. Comparison of measurements to 1-D shock jump relations (ideal gas) based on incident shock Mach number showed maximum single-shot relative deviation of 7-8% from theory. High precision of gas temperature measurement by LIGS at Mach numbers 1.37 - 2.20 was indicated by a standard deviation of maximum 3%, for a shock Mach number of 1.91. The shock tube was spatially fixed in a foundation such that no recoil occurred to induce deflection and laser beam misalignment throughout the experiment. In a similar small-sized conventional, spatially fixed shock tube, Foerster et al. [101] presented simultaneous single-shot temperature and velocity measurements by non-resonant heterodyne LIGS. Experiments in nitrogen and argon at shock Mach numbers 1.67 - 1.96 were conducted behind the incident and reflected shock at post-shock temperature and pressure up to 1000 K and 4.3 MPa, respectively. With measurement precision of gas temperature on the order of 3% and the potential for simultaneous accurate determination of flow Mach number, with a relative deviation as low as 1.4%, the authors reasoned LIGS to be well suited for measurements of shock-heated flows. Recently, Selcan et al. [62] and Altenhöfer et al. [42] successfully demonstrated measurement technique feasibility of LIGS towards in situ determination of total temperature conditions of a full-scale, hypersonic ground test facility for the first time. Using resonant excitation (NO_2-seeded) homodyne LIGS at 593 nm for a representative low-enthalpy test condition at 1.2 MJ/kg, post-reflected shock stagnation temperatures of 900-1100 K at pressures from 5-6 MPa were quantified by single-shot measurements in the nozzle reservoir of the piston-driven reflected shock tunnel HELM. Measurements were conducted in air, at incident shock Mach numbers up to 2.6. Comparing two alternative signal processing procedures, the authors found a time-domain least-squares fit of the temporal LIGS signal to provide a higher precision of 3.04%, in comparison to 3.88% for a frequency-domain analysis by fast Fourier transform (DFT). As for accuracy, mean temperature relative deviation for a single test condition is found to be as low as -1.82% and -0.61% for the DFT and time fit, respectively, indicating single-shot temperature measurements by LIGS to be well correlated and to yield good agreement with 1-D inviscid theory in the low-enthalpy test regime. Thereby, measurement

technique robustness for single-shot stagnation temperature determination and its general applicability to large-scale short-duration ground test facilities has been proven beyond prior use in conventional shock tube configurations and at the overall highest test gas conditions. Selcan et al. [80] reported on single-shot, in situ, homodyne, resonant LIGS measurements in the HELM shock tunnel, extending the stagnation conditions to nozzle reservoir pressures, temperatures and enthalpies of up to 21 MPa, 1900 K and 2.2 MJ/kg, respectively.

3.2.2 Measurement principle

Laser-induced grating spectroscopy (LIGS) is a coherent diagnostic technique which exploits the non-linear generation of a local density pattern (acoustic waves) in a fluid due to induction of a local electric/intensity field as resulting from light interference of two pump laser beams. Probing of the grating by means of a third incident continuous wave (cw) interrogation beam results in the diffraction off the interference pattern under the Bragg angle: the scattered signal beam is guided to a single point detector where information on the measurement volume is conveyed by frequency modulation of signal intensity oscillation. As two short-pulsed pump laser beams intersect at a shallow angle, an interference pattern or electric/intensity field grating is seen to span the intersection region in the test fluid, i.e., sample volume. Fig. 3.1 depicts grating formation as results from intersection of two coherent pulsed pump beams (wave vectors k1 and k2, wavelength λ_{pump}) with crossing full-angle Θ. The grating vector q is perpendicular to the fringe pattern, whereas the grating constant Λ is determined by the pump laser wavelength λ_{pump} and crossing angle Θ according to Eq. 3.2.

$$\Lambda = \frac{\lambda_{pump}}{2 \cdot sin(\Theta/2)} \tag{3.2}$$

In the following, two optoacoustic effects, termed electrostriction and thermalization, lead to the development of a congruent density interference pattern. Electrostriction describes the tendency of polarizable molecules to move toward regions of high electric field intensity and is proportional to the real part of the gas susceptibility [94]. Thermalization in contrast is a multiple-step collisional quenching process, proportional to the imaginary part of the gas susceptibility [102]. As the gas is excited by driver laser light at resonant wavelength, molecules absorb incident radiation and are excited to higher electronic states. Pressure-dependent inelastic collisions in turn convert part of the excited state energy into molecular kinetic, rotational or vibrational energy, which is finally dissipated to heat by elastic molecular collisions equilibrating molecular velocities, thus inducing a rise in temperature and change in particle density. The generated density-perturbation field is composed of two plane acoustic (sound) waves moving in opposite direction, in parallel to the grating vector. Sound wave propagation gives rise to alternating constructive and destructive interference, resulting in a temporal oscillation of local fluid density. Accordingly, the refraction index of test gas in the measurement volume varies in time with a characteristic oscillation (scattering) frequency f_M. It is defined according to the spatial dimension of the density grating (i.e., fringe spacing) and sound wave propagation

within the fluid, according to Eq. 3.3:

$$f_M = c \cdot \frac{a}{\Lambda},$$ (3.3)

where a denotes the speed of sound of the test gas. Constant c yields: $c = 2$ for electrostrictive (non-resonant) and $c = 1$ for thermal (resonant) grating excitation such that signal frequency equals either the one- or twofold of the so called Brillouin frequency. Accordingly, signal oscillation frequency varies by a factor of 2 which serves for unambiguous distinction of contributions by scattering off a thermal (resonant) or electrostrictive (non-resonant) grating [103]. As a cw probe beam (wavelength λ_{probe}) intersects the measurement volume under the Bragg angle ϕ, the probe beam is diffracted off the temporally oscillating grating. This scattered signal beam is coherent in nature and conveys information on the density grating due to frequency modulation of the signal intensity, according to the oscillation frequency as resulting from sound wave propagation. The Bragg angle condition for Bragg angle ϕ is given by Eq. 3.4.

$$2 \cdot sin(\phi) = \frac{\lambda_{probe}}{\Lambda}$$ (3.4)

When acquired by a detector (e.g., photomultiplier), frequency domain analysis of the scattered signal beam via a discrete fast Fourier transform (DFT) yields the oscillation frequency f_M of the induced density grating. Thus, provided the grating constant Λ and nature of the grating (electrostrictive or thermal) are known a priori, the speed of sound within the measurement volume can be calculated from Eq. 3.4. For a known gas composition, local temperature of the single point sample volume spanned by the interference pattern can be calculated from the associated speed of sound.

In the earlier work of Sander et al. [97] and Altenhoefer et al. [42], the local (static) translational fluid temperature was calculated from the measured speed of sound and measured static pressure by linear interpolation of tabulated thermophysical realgas data by Lemmon et al. [104], which lists sound speed for dry air, dependent on temperature and pressure up to temperatures of 2000 K, i.e. in the presence of vibrational excitation and varying chemical composition, however below the onset of dissociation: $T = T_{Realgas}(a,p)$. In the current work [80], the identical approach of calculating translational temperature in dependence of measured sound speed and pressure by backward interpolation is employed, however the realgas EOS thermophysical database is a priori computed by CEA: $T = T_{CEA}(a,p)$. Evidently, as calculated temperature values, particularly in the second LIGS test campaign, often fall between the limits of high temperature ideal gas Rankine-Hugoniot predictions (i.e. frozen thermal DOF and chemical composition) and of low temperature CEA predictions (i.e. full thermo-chemical equilibrium), calculated temperatures will reflect limited systematic deviation from the factually prevalent temperature: biased towards lower temperatures when full equilibrium and biased towards higher temperatures if frozen thermo-chemistry is being assumed, respectively. However, considering a dedicated non-equilibrium calculation of time-varying thermo-chemistry behind the reflected shock for every single experiments to be unfeasible, the current approach is deemed
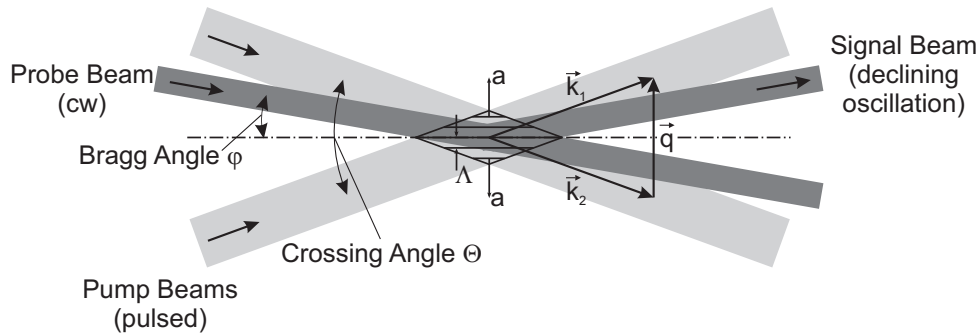
Figure 3.1: Schematic of the LIGS interference grating and laser beam geometry.

justified and accurate enough to substantiate the observations made herein.

Due to heat conduction (thermal diffusion) and acoustic damping (sound wave attenuation), density grating intensity and thus probe beam diffraction decrease with time. Accordingly, the scattered signal beam intensity is characterized by a temporally damped oscillation. A more detailed account on the physical background of laser-induced dynamic light scattering, density grating formation as well as analytical postulation of signal temporal evolution by means of the linearized equations of hydrodynamics and light scattering is given by Cummings et al. [94] and Schlamp et al. [105].

3.2.3 (Non-)resonant grating excitation

While single-shot temperature measurements by LIGS can be likewise conducted exploiting resonant and non-resonant wavelength excitation, thermal, i.e., resonant, gratings are considered particularly well suited for measurement in the adverse environment of a compression-heated, reflected shock tunnel. Precisely, wavelength-independent electrostrictive, i.e., non-resonant, gratings require very large pump beam pulse energies (>100 mJ) [95] which are however prohibitive in the present case of the laser focal point being situated near the optical access windows and shallow beam intersection angles. Resonant excitation of thermal gratings by contrast, does not require high pump beam pulse energies [95] but benefits primarily from higher pressures and associated collisional quenching rates due to rapid thermalization [93]. Thereby, loss in signal intensity due to low pulse energies is compensated by use of selective seeding. Accordingly, electrostrictive (non-resonant) excitation is not deemed applicable by the authors such that LIGS measurements via thermal (resonant) gratings are regarded much more robust and particularly attractive - even at low pump energies dictated by the optical window breaking point - for application in shock tunnels of significantly limited optical access and high stagnation pressure and density. The intrinsic formation of nitric dioxide (NO_2) as active, i.e., resonantly-excited, species at adequate concentrations in the post-shock regime - particularly at higher test gas conditions - will yield increased signal intensities, sufficient for measurements at elevated pressures and temperatures when air is used as test gas, see Eq. 3.1. However, in the case of test facilities where the imperative of low pump beam pulse energies

(as imposed by the optical windows' damage threshold) were significantly alleviated, measurements by electrostrictive (non-resonant) LIGS will - in principle - be likewise possible. For both thermal (resonant) and electrostrictive (non-resonant) gratings alike, decrease in signal amplitude due to elevated temperatures of short-duration facilities is more than compensated by the pressure rise in the shock-processed test gas, eventually yielding a rise in signal intensity at increasingly ground-test-relevant conditions, see Eq. 3.1. In fact, based on signal intensity, as the pressure ratio across the normal shock will always be significantly greater than the corresponding temperature ratio, LIGS is projected to yield sufficient signal intensity even for probing of high-enthalpy conditions in reflected shock tunnels.

3.2.4 Signal detection scheme

LIGS measurements can be readily conducted in two ways: depending on whether only a single signal beam (emanating from the measurement volume) is detected by the PMT or whether this primary signal beam is mixed with a reference beam (not passing the measurement volume) prior to sampling, the detection scheme is termed homodyne or heterodyne detection, respectively.

The homodyne approach, detecting a single signal beam (scattered off the optical grating), allows to acquire local sound speed and temperature within the measurement volume, which are the primary quantities of interest in this work as they enable to deduce reservoir (stagnation) enthalpy. The heterodyne approach, in contrast, uses a second interrogation beam as local oscillator (i.e. reference beam) not passing the measurement volume but being mixed with the signal beam from the measurement volume prior to detection. Interference of both, signal and reference beam enable additional quantification of the local bulk fluid velocity (single component) from the oscillation beat frequency and Doppler shift - thus enabling direct, simultaneous measurement of local flow Mach number via fluid sound speed and velocity: compare Foerster et al. [101] and Richter et al. [106].

In the course of the present study, exclusively the homodyne detection scheme is being used: as quantification of fluid residual velocity in the high vorticity, post-reflected shock stagnation state 5 of a shock tunnel is not of primary interest - based on order of magnitude comparison to enthalpy.

3.3 Advancement of the HELM facility

3.3.1 Prior limitations

In the process of the current work, robustness of the LIGS measurement technique employed for nozzle-reservoir thermometry in the HELM facility was found to be severely affected by limitations of the laser-optical setup and test facility itself. Precisely, for the first optical setup detailed in Altenhöfer [42], the success rate of single-shot measurements conducted in the HELM facility was found to be as low as ~10%, which was notably lower than the success

rate of prior single-shot measurements, which were conducted with a near identical optical setup, yet in a small-scale shock tube facility, see Sander et al. [97]. Three primary sources of error are identified in the current work: Firstly, the observation of a notably higher single-shot success rate in the small-scale shock tube is attributed to the fact that the latter is fixed in a foundation and operated with a conventional shock tube driver, at limited diaphragm burst and stagnation pressures at the ST endwall of 20 MPa and 2 MPa, respectively. Accordingly, experiments in this test bench are characterized by absence of or an entirely negligible mechanical recoil and displacement. The HELM facility, in contrast, is a medium-scale shock tunnel, deliberately mounted on rails in order to compensate the inevitable and strong mechanical recoil of facilities operated with a high-pressure, dynamic FPD. Here, despite an inertia weight of 40 t to limit reaction forces, the net axial displacement amounted up to ~30mm throughout the piston acceleration and deceleration phase, posing significant problems to ensure stable and robust laser beam paths for pump and probe beams, further facilitating successfull grating formation at the ST centerline. To compensate the facility's inevitable axial displacement, this problem was successfully solved by Altenhöfer [42] by guiding laser beams in parallel to the ST as long as possible, mounting 90° turning mirrors - from axial to radial direction, guiding laser beams into and out of the ST - fixed to the outer ST diameter, so as to follow the facility's net displacement and ensure laser beams to pass through the radial optical access bores. However, due to absence of a shock absorber, the facility's axial movement was merely confined by undamped impact on a fixed (rigid) stop until 2017, effectively inducing a buckling behavior of the tubes and hence tremor and (slight) vertical displacement of the ST and optical acces bores. Whether the latter or a transient misplacement of fixed-mounted turning mirrors was more dominant for laser beam displacement was not distinguishable.

Secondly, the primary shortcoming of the former LIGS optical setup - identically used for the first measurement campaign of the current work [62] - is due to optical access windows (Sapphire) to the nozzle reservoir, which have been mounted to the outer ST diameter, described in detail by Altenhöfer [42, 107]. Due to a wall thickness of ~250mm, this recessed-mounted configuration resulted in two-opposing, radially opened cavities of very low aspect ratio D/H ~1/10, inducing strong geometrical non-uniformity and flow disturbance within the HELM nozzle reservoir [108]. Specifically, the post-reflected shock regime - per se characterized by strong vorticity and recirculation behind a highly distorted shock front, following endwall-reflection and viscous BL interaction - will be further disturbed by strong secondary flow, exerted by incident and reflected shock passage over both narrow cavities, see Menevidis [109]. Accordingly, the requirement of traversing a set of four coherent laser beams (2 irradiated pump beams required for grating formation, the cw probe and coherent signal beam) into as well as out of the measurement volume at the ST centerline - i.e. across the stagnated test gas as a high-density perturbed medium of pronounced spatial non-uniformity and high temporal fluctuation - will inevitably be a stochastic process and can be regarded as the limiting bottle-neck of the current setup. As the signal beam is further required to pass through spatially confined pin-hole apertures (mandatory to avoid PMT saturation by pump beams)

before reaching the detector, this setup is prone to interference and will fail even due to slight geometrical displacement and beam steering [100], either failing to induce a transient grating by successfully beam interference at all, or by deflection of the signal beam from the detector path. Evidently, the success rate of the first setup was severely limited due to low beampath robustness and sensitive alignment.

Thirdly, prior experiments in the HELM facility suffered from strong driver and test gas pollution by dust particles, to be manually removed with significant effort after every test run, both in the CT and ST [42]. Optical transmissivity measurements through optical access bores in the nozzle reservoir, by a strong (torch) light source and CMOS high-speed camera, showed gradual darkening to total eclipse following instants after shock reflection and particularly when operating the HELM facility in shock tube mode with closed endwall, see Altenhöfer et al. [107]. Whereas the source of this particle loading was long unclear and only later attributed to pollution of the buffer gas (due to a flaking coating in the secondary reservoir [110]), this was considered an intolerable technical limitation of facility operation, optical diagnostics and conventional measurements alike.

3.3.2 Mechanical revision and redesign

Accordingly, three major mechanical revisions and redesigns of the HELM facility were identified as imperative in order to be able to conduct successfull LIGS measurements in the future.

1. Once the flaking coating on the inner surface of the buffer (secondary reservoir) pressure vessel was identified as the source of particle pollution, the latter was to be overhauled and the flaking coating to be removed in order to ensure clean buffer, driver and test gas in the future.

2. As strong mechanical impact of the last ST segment on the fixed stop was to be avoided in the future, a heavy-duty damping system was to be installed in order to compensate mechanical recoil at fature high-pressure conditions, minimize axial displacement and avoid buckling and tremor of the facility due to a soft reaction force.

3. After having identified the recessed-mounted optical access windows as the primary source of low single-shot LIGS measurement success rate, a new flush-mounted design was to be devised.

Cleaning of the secondary reservoir

Due to its shining metallic character and finally from unambiguous material analysis by FTIR spectroscopy [111], the particle pollution was identified as residuals of the high-temperature, anti-corrosion coating originally applied to the inner and outer surface of the buffer (secondary reservoir) pressure vessel, consisting of aluminum particles embedded in a chemical binder. Local flaking of the coating resulted in material to be carried downstream with the expanding buffer gas through the piston launcher upon, reaching the CT and eventually being carried

into the ST in every experiment. In 2017, the pressure vessel was dismantled and the surface coating was entirely removed by high-pressure cleaning. A repetition of high-speed optical transmissivity measurements in the nozzle reservoir showed no further traces of particle loading or light blockage, demonstrating that the source of particle pollution has been successfully removed [110]. Detailed photographs of qualitative transmissivity are provided in Fig. A.16.

Hydraulic damping system

Despite being equipped with an inertia mass of 40 t weight, an axial displacement of the HELM facility of ∼10 mm was measured upon piston acceleration and deceleration, even for low-pressure experiments of the optical diagnostics test campaign. Reaction forces and mechanical recoil were expected to be even higher by multiples for high-pressure, high-enthalpy experiments, requiring for high buffer pressures or the use of heavier pistons. Until 2019, the facility was yet not equipped with shock absorbers such that axial displacement throughout the experiment was minimized by a fixed (rigid) stop, which exerted strong reaction forces upon mechanical impact and induced a finite vertical displacement <5 mm of the ST and optical access ports to the nozzle reservoir, which significantly affected the success rate of LIGS measurements due to interfering with the laser beam alignment. Accordingly, to cater to the need of minimizing the facility's axial displacement while avoiding mechanical impact and tremor, a hydraulic damping system was devised and constructed. For this purpose, two hydraulic, heavy-duty shock absorbers (Weforma GmbH, type LDS 160-110) with a net counterforce of 0.9 MN and 110 mm stroke each have been arranged symmetrically left and right of the ST, exerting the required reaction force on the inertia weight. Required reaction forces and energy to be dissipated have been determined based on L1d calculations of the FPD, assuming transient pressure balance between the piston and facility. In order to avoid torsional moment, both shock absorbers have been placed vertically in the center of mass and were mounted on buffer stops for this purpose. The latter consist of a reinforced frame of welded, heavy-duty cantilever beams, which are designed to guide transient reaction forces into the foundation. Due to the point of origin of the axial force, the concrete anchorage was to withstand a combined load of axial forces and tension, the latter being particularly critical for concrete foundations. For this reason, a total number of 32 heavy-duty (threaded) anchor rods M30x770mm were placed at deliberate relative distance to securely anchor the buffer stops, while effectively avoiding concrete fissure by critical localized load due to transient tension forces. High-performance injectable epoxy mortar (Hilti AG, type HIT-RE 500 V3) is being used in order to withstand unsteady laods and vibration. As shock absorbers are primarily designed for dynamic loads, the static reaction force of ∼40 kN - exerted on the facility as the test section is being evacuated - is compensated by two elasto-fluidic springs (Weforma GmbH, type WS-F70-2-70B) of sufficient stroke distance. Since construction of the damping system in 2019, transient reaction forces in the HELM facility have been effectively compensated locally at the inertia weight, achieving a significantly smoother operation while entirely avoiding mechanical impact of the downstream ST segment. Photographs by a high-speed camera revealed that the nozzle reservoir section is
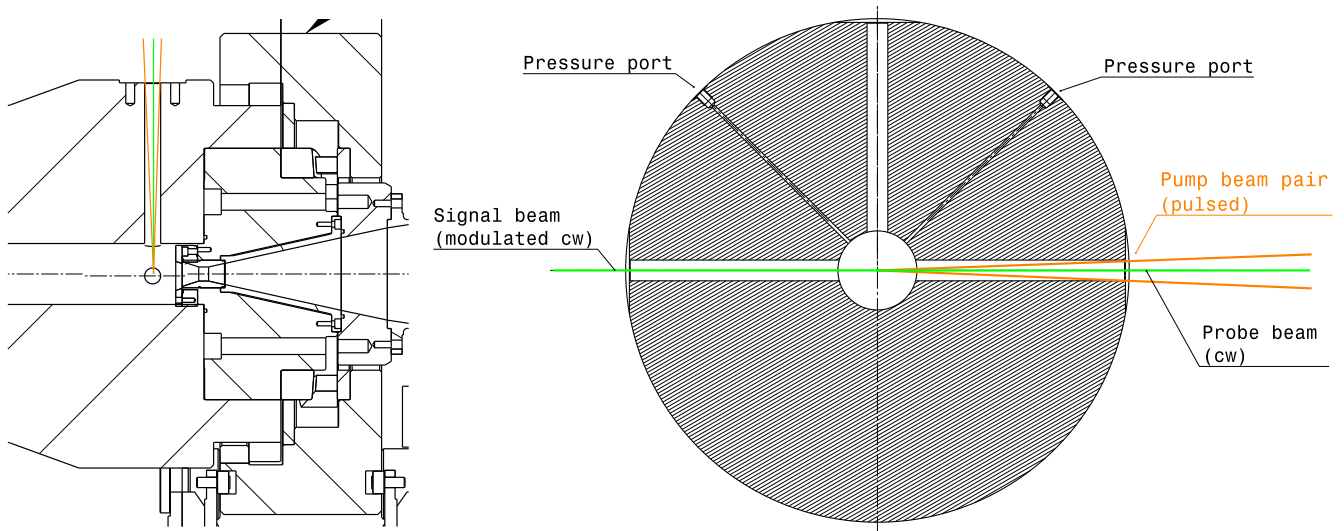
Figure 3.2: Cross-sectional view of the nozzle reservoir section. Left: longitudinal section with measurement volume upstream of Laval and expansion nozzle. Right: transverse section of measurement plane with radial access bores.

not further lifted or displaced, contributing to a significantly enhanced success rate of LIGS measurements in the second test campaign. A photograph of the hydraulic damping system is given in the appendix, see Fig. A.17. Details on the mechanical load calculation are listed in [109]. Shock-absorbing damping systems are also in use at the JAXA HIEST shock tunnel [112] and the RWTH TH2 detonation shock tunnel [113].

Optical access redesign

Towards addressing an active area of research in aerothermodynamics community, the nozzle reservoir section of the HELM facility is equipped with an optical access, a unique characteristic of hypersonic short-duration facilities worldwide [114]. In the course of the present work, this facilitates in situ measurements of the post-reflected shock (stagnation) temperature by LIGS. The measurement volume at the ST centerline is situated 40 mm upstream of the ST endwall (Mylar diaphragm or solid end). The orthogonal measurement plane is radially accessible from different geometrical angles (0° - 45° - 90° - 135° - 180°) via five coplanar, azimuthally staggered bores, three of which (at 0° - 90° - 180°) are equipped with optical (Sapphire or Quartz) glass windows to enable optical diagnostics. The two remaining bores are used for stagnation pressure measurement by wall-flush mounted transducers. A detailed cross-sectional view of the nozzle reservoir measurement volume is provided in Fig. 3.2.

In the course of prior work [42, 107] as well as in the first measurement campaign of this work [62], the success rate of single-shot LIGS measurements for in situ nozzle reservoir thermometry was noticed to be significantly affected by the highly non-uniform and unsteady reflected shock regime. As these works still employed optical windows which were recessed-mounted to the ST outer diameter, the narrow cavities necessitated for coherent laser beams to be traversed

over ∼0.6m through a highly perturbed medium, either totally inhibiting coherent signal beam detection or rendering the latter a stochastic process, with net success rate as low as 10%. Evidently, in light of the significant work effort required for a single test run in the HELM facility, a fundamental adaption of the optical access via flush-mounted windows became mandatory. Hence, upon initiation of this work, a mechanical assembly was designed which allows placement of optical windows directly at the ST inner diameter, while withstanding high stagnation pressures, which was finally mounted in August 2018. The primary problem arises from the fact, that radial access bores are very narrow: with 25 mm in diameter and of 250 mm nominal length across the entire ST wall thickness. For evident reason (precisely, manufacturing and allowance constraints, where machining would require for heavy cutting with an unguided tool over a free-distance of 250 mm), these through-bores are and cannot be equipped with a load-carrying, circumferential thread at the base (i.e. in the depth). Accordingly, whereas a maximum axial load of 49.1 kN (at 1000 bar nominal stagnation pressure p_5) will act on the assembly base surface area, this load can only be carried by the available anchorage of 6 (inward-pointing) M16 bores, drilled into the ST lateral surface. Hence, the new windows assembly was to satisfy the following design constraints:

1. The mechanical assembly is to carry a maximum dynamic axial load of up to 49.1 kN in total.

2. Optical windows are to mechanically withstand high dynamic loads with respect to their maximum free-surface area and diameter (in relation to the maximum pressure of 1000 bar).

3. The mechanical assembly is to be hollow from inside in order to guide laser beams into and out of the ST. For a maximum outer diameter of 25 mm (less the radial gap clearance), the inner bore diameter is to be large enough as to allow for a pump beam crossing angle of Θ ∼3.5° (the former recessed-mounted configuration allowing for a maximum crossing angle of Θ ∼4.8°). The assembly is thus designed as a slender sleeve (tube) of great length and with very thin wall thickness, still being able to withstand the total axial pressure load.

4. Windows are to be wall-flush mounted as close as possible (with respect to the ST inner diameter) and to be mechanically fixed, so as to not shake or be deflected under highly dynamic mechanical shock-loading (to ensure a stable laser beam path), while a flexible support - in contrast to a perfectly rigid support - is to avoid breaking by exceeding local rear contact pressure.

5. Windows are to be kept as thin as possible, so as to limit the laser-beam distance across the (optically dense) window material and hence radial deflection due to twofold light refraction at the medium interfaces, while still withstanding high dynamic loading.

6. Windows are to thermo-mechanically withstand highly focussed laser radiation of 2 pulsed pump beams and a cw interrogation beam (at around half the ST diameter distance, 47.5

mm, from the focal point at the ST centerline). Hence, windows are to be manufactured with superior optical grade (minimum inclusions, microbubbles and crystal twinning) and will not allow for an anti-reflective coating. All of these sources are prone to induce failure by local thermo-mechanical cracking due to intense laser-radiation. Superior surface tolerances (flatness <1μm) by highly polished finishing (lapping), will greatly reduce risks of cracking upon metal contact [115].

7. As an anti-reflective coating on the windows itself is forbidding, the beam path is to be geometrically defined as close as possible, further avoiding specular and diffuse optical reflections by coated, non-reflective surfaces of any other (metallic) parts.

In regards to the base material, after having opted for an inner diameter of 20 mm of the main metal sleeve (to allow sufficiently high laser beam crossing angles), demanding a minimum residual wall thickness of less than 2.5 mm (as dictated by the bore inner diameter of 25 mm), only high-strength steel was deemed sufficient to carry the maximum expected load. The latter was deliberately increased to 0.2 GPa (a safety factor 2 with respect to the highest nominal pressure of 1000 bar), in order to avoid buckling of the narrow, thin-walled sleeve (aspect ratio 10) at all cost. Plastic deformation of the latter within the radial bore with tiny radial gap clearance of <0.1mm (mandated by the high-pressure o-ring seals and to not further decrease the load-carrying area cross section) is evidently intolerable. Here, to further lower the risk of metal galling with the tube wall, use of an enduring separating paste is imperative. Despite stainless steel (e.g. martensitic high-alloyed CrNi-steel 1.4313) would have offered higher corrosion-resistance, tempered steel 42CrMo4 (1.7225) was considered more appropriate due to higher nominal tensile (i.e. compressive) strength of 1.1 GPa.

$$F_1 = \sigma_1 \cdot A_1 = \sigma_2 \cdot A_2 = F_2 \tag{3.5}$$

From a simple static axial force balance, Eq. 3.5, assuming uniform surface pressure on the total front cross section ($\varnothing$25 mm) and the load-carrying annular cross section ($\varnothing$25-20 mm), the expected compression stress amounts to 0.56 GPa, which yields a safety factor of again 2 with respect to the compressive strength of 42CrMo4. Hence, a total safety factor of 4 was deemed more than sufficient to cover any relevant uncertainty from factual dynamic loading and buckling risk, not explicitly considered herein.

By the imperative to withstand strong mechanical loads and very high (peak) temperatures behind the reflected shock wave, while further allowing for relevant transmissivity for optical diagnostics (in the 500-600 nm range), sapphire was determined as the material of choice for the optical windows. In fact, due to higher thermo-mechanical load strength than quartz, sapphire has already been used for the prior recessed-mounted configuration, compare [42]. Monochrystalline sapphire (Al_2O_3) has superior hardness, resistance to mechanical wear and surface scratches, is near chemically inert against acids, corrosive gases and metal vapors, has a very high melting point of 2300 K and superior compressive strength of 2.1 GPa, at a sufficiently high rupture modulus of 0.9 GPa and bending (flexural) modulus of 0.6 GPa [116].

In order to determine the required dimensions for windows from structural mechanics consideration (for thin plates and shell structures), Eq. 3.7 from [117] was considered, valid for a circular plate of finite span under uniform load, where the maximum load (either at the edge or center) is given by:

$$\sigma_{max} = n \cdot p \frac{R^2}{t^2} \tag{3.6}$$

$$t/D = \sqrt{\frac{n}{4} \cdot \frac{p}{\sigma_{max}}}, \tag{3.7}$$

where p denotes pressure (load), R=D/2 and t denote plate radius and thickness, respectively. For a given plate support, constant factor n is given as n=1.24 (free pivot mount) or n=0.75 (clamped mount). Finally, since a semi-rigid PTFE rear support was chosen to allow for minimum clearance to avoid cracking, the higher (conservative) factor of n=1.24 was chosen for safety. As the minimum sleeve thickness (at 20 mm inner diameter) was only required at the outmost radial access bore entrance, the angled beam path allowed for a reduced inner diameter of the assembly (at the window rear) of 10 mm, which thus defines the unsupported (free) diameter D of the window. For highly loaded parts, literature recommends a safety factor of 3-8, with a factor of 5 deemed sufficient. With the rupture modulus of sapphire (0.9 GPa) and at 0.2 GPa load, Eq. 3.7 yields a ratio of window thickness to diameter of t/D=0.58690 and hence suggests a window thickness of ∼6 mm for a window of 10 mm diameter. A factor of t/D=0.49441 was suggested by the manufacturer. Eventually, due to design constraints and increased cracking safety, and since Eq. 3.7 neglects the effect of free (unsupported) to total plate diameter, a window of outer diameter 14 mm and thickness 15 mm was used herein: the resulting thickness-height ratio of t/D=1.07143 is 83% higher than the recommended value, almost entirely ruling out possible failure of sapphire windows due to cracking, even under shock loading throughout the experiment. With respect to an unsupported diameter of 10 mm, this design further satisfies the requirement of Sherman and Stadtmuller [118], who suggested a ratio of $\sqrt{2}$ between outer and unsupported (free) diameter of optical windows up to 16 GPa, yet regardless of the window thickness.

Whereas the window is sealed with a copper washer at the front, a radial FKM o-ring seal and a PTFE shim at the rear, sealing of the annular gap is achieved via two consecutive o-ring seals with minimal gap clearance <0.1 mm. The mechanical assembly is manufactured from five main piece: the front (head) piece incorporates the optical window and has a curvature identical to the ST to avoid any geometrical discontinuitiy, behind, the window is supported by an adapter piece, which itself is connected to the main thin-walled sleeve. The latter is connected to a rear piece to better guide mechanicaly loads into the outer load-carrying flange (gland). Due to design constraints, metallic part connections exploit all techniques available: screw joint via a metric fine thread, press (shrink) fitting and brazing (hard-solering), in order to best achieve concentric alignment of all parts and to remain allowance (tolerances) within the available radial gap clearance - being further mandatory to limit the risk of buckling un-
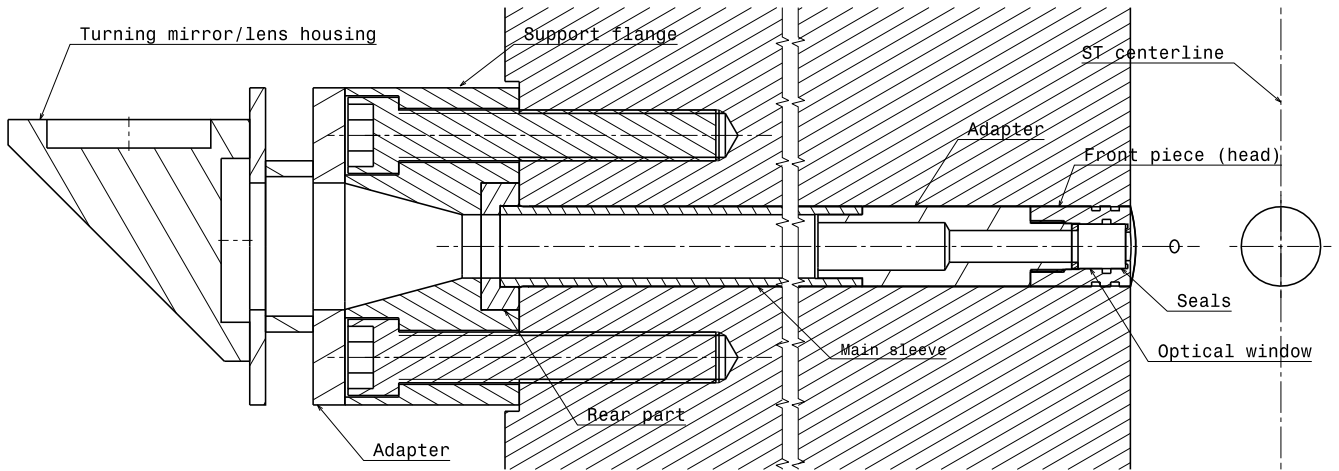
Figure 3.3: Cross-sectional view of the final flush-mounted window assembly for optical access to the HELM nozzle reservoir, indicating optical window and mechanical parts. Dimensions not to scale.

der loading. The assembly allows for free rotation to accurately match front piece curvature to the ST contour. While the massive load-carrying rear flange is made from mild steel, all other highly loaded metallic parts are manufactured from 42CrMo4. A technical drawing of the new window assembly is given in Fig. 3.3.

Photographs of the window assembly are given in Fig. A.21. In order to minimize optical reflections, all metal surfaces facing the laser beam path are sandblasted and parts are integrally subjected to black oxide coating (Fe_3O_4) by bluing. Fig. A.21 further shows the nozzle reservoir with prior recessed-mounted and final flush-mounted window configuration, as used during the first and second LIGS campaign of this work, respectively.

3.4 LIGS Application

3.4.1 Optical setup

The optical set-up for the generation of resonant acoustic gratings consists of a pulsed frequency-doubled Nd:YAG laser (Innolas SpitLight 2000-10; wavelength 532 nm; max. pulse energy 1000 mJ; pulse duration 7 ns) as the pump source and a dye laser (Radiant Dyes NarrowScan; dye Rhodamine B; efficiency ∼30%) to yield an excitation wavelength range of 590–600 nm. The continuous probe beam is provided by an Ar-ion laser (Coherent Innova 90-4) operating at 514 nm. A 500 MHz photomultiplier tube (TSI) is employed for signal detection, and a digital storage oscilloscope (LeCroy) with 1 GHz bandwidth serves for discretization at 10 GS/s. For the measurements presented herein, the power of the irradiated probe beam is 250 mW and the pulse energy of the pump beams measures 40 mJ (20 mJ each). The latter is deliberately kept as low as possible such as to not approach the damage threshold of the optical sapphire windows, yet to yield sufficient amplitudes for thermal (resonant) LIGS measurements. In general, the variation of excitation wavelength allows for separate as well as simultaneous excitation of
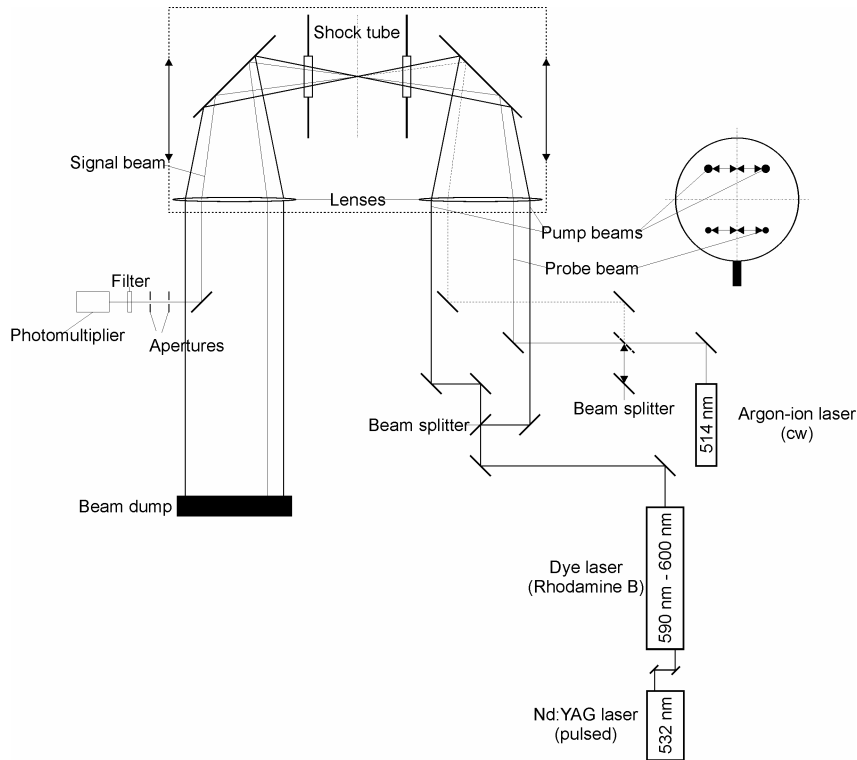
Figure 3.4: Schematic of the LIGS laser-optical setup, from [97].

resonant and non-resonant gratings. In the present investigation, due to the absence of an adequate electronic transition in air, pure resonant gratings are generated by resonant excitation of nitric dioxide (NO_2) at ∼593 nm. The relevant absorption system is a broadband electronic transition of NO_2, ranging from the ultraviolet spectrum (B^2B_2 - X^2A_2) ∼250 nm to the visible (A^2B_1 - X^2A_1) ∼650 nm, exhibiting a global maximum at 435 nm [119, 120]. Due to high overlap of several separate transitions in the wavelength range considered, the absorbance of NO_2 is expected to not decrease noticeably for higher temperatures as in the case of continued depletion of ground states. Particularly at elevated pressures, as present in shock tunnels, this is considered favourable with regard to pressure line broadening which can be an impairment when exploiting single-line absorption features as in the case of many diatomic molecules. Hence, the broadband absorbance of NO_2 will foreseeably not pose an obstacle for LIGS application under high-enthalpy, high-temperature conditions. A schematic of the optical setup is given in Fig. 3.4.

The identical laser-optical setup has been used in both LIGS measurement campaigns to measure post-reflected shock stagnation temperature T_5 in this work. In the first campaign, the facility was not yet equipped with flush-mounted windows, such that the old configuration of recessed mounted windows was used. Moreover, these measurements were conducted prior to overhaul and cleaning of the buffer pressure vessel and installation of the hydraulic damping system. Accordingly, the single-shot success rate in this first campaign was very low ∼10-20%. Due to less geometrical constriction by the window configuration, this allowed for a relatively

large beam crossing angle of $\Theta \sim 3.7°$ to be used [62].

The second test campaign was carried out after the buffer reservoir has been cleaned, the hydraulic damping system was installed and used the flush-mounted window configuration - the latter demanding a notable reduction of the beam crossing angle to $\Theta \sim 1.17°$. As the identical pair of focussing lenses (f =500 mm) was used to interfere laser beams at the ST centerline (with net total distance between focal point and focussing lens/turning mirror maintained fixed), this required a further reduction of the relative distance of all laser beams, running in parallel before reaching the first focussing lens. Geometrical constrictions could only be solved by deliberately reducing the size of optical mirrors by careful grinding of the circular cross-section to a vertical rectangle. Photographs of the flush-mounted optical access, ground reflecting mirrors and the LIGS laser-optical setup are provided in the appendix, Fig. A.21.

A significantly enhanced beam path stability, i.e., robustness of beam alignment, resulted as direct improvement of these measures which now further allows better rejection of spurious reflections and stray light by smaller geometrical pinhole apertures. Accordingly, the ensuing success rate of single-shot LIGS measurements presented herein could be effectively increased to near 90%. As a side effect, inserting flush-mounted windows results in a smaller pump beam intersection angle Θ which entails an increased fringe spacing constant Λ. However, this proves advantageous due to longer signal lifetimes, resulting from an increased number of signal oscillations, i.e., induced sound wave periods, effectively increasing measurement accuracy, particularly when frequency-domain DFT is used for signal processing [121].

3.4.2 Experimental methodology

Technical approach

In the experiments reported herein, time-accurate triggering of a single pump laser pulse is provided by means of the response of the PCB pressure transducer mounted in the measurement plane, when the incident shock transits. A delay generator ensures the laser pulse to pass the measurement volume shortly after reflected shock wave passage. While the pump laser operates at a fixed repetition rate of 10 Hz, a manufacturer-added feature allows firing an additional intermediate laser pulse that is necessary for timeaccurate response to the shock passing event. A manual time delay of 235 μs between single gating of the Nd:YAG laser flash lamp and Q-switch is deliberately set to allow for maximum pump laser beam energy emission, see [97] for details. Jitter on the order of $\sim \mathcal{O}(10\ \mathrm{ps})$ is found to be insignificant for the instant of pulse emission. As direct (geometrical) measurement of the optical setup's pump laser beam intersection angle Θ is unfeasible and prone to error, a unique reference calibration is conducted at ambient temperature and shock tube initial fill pressure (state 1), prior to every single experiment. This is to ensure unambiguous determination of the optical grating constant (interference fringe spacing) Λ from acquired calibration signal oscillation frequency. For means of consistency, reference point calibration employs the identical real gas (EOS) thermophysical reference data according to Lemmon et al. [104], to obtain a unique interpolation value

of air speed of sound at reference pressure and temperature, based on reference thermocouple measurement. Having determined calibration point oscillation frequency and reference speed of sound, the exact grating constant Λ is thus calculated from Eq. 3.3. Throughout the experiment, Λ is henceforth used to derive test gas speed of sound from the oscillation frequency acquired under test conditions (state 5). Analogously, corresponding test gas temperature T_5(exp) is calculated by a backward interpolation of the thermophysical reference data in [104], based on measured pressure and sound speed. Homodyne detection temperature measurements by LIGS are conducted by detection of the diffracted signal beam and subsequent oscillation frequency determination by time- and frequency-domain analysis. Apart from sound speed of sound and temperature -, further fluid thermophysical properties (such as thermal diffusivity and acoustic damping rate) can be determined from the temporal decay rate of the signal envelope [94], which is however not exploited in the current work.

Calibration procedure

As post-shock temperatures and thus intrinsic formation of nitric dioxide due to shock heating are still considered low, NO is seeded as tracer gas (235–500 ppm) in the shock tube section in order to ensure formation of NO_2 (via chemical equilibrium at room temperature) as active species for resonant (thermal) grating excitation at 593 nm. Based on NO_2 seeding concentration and low pump beam pulse energies of 20 mJ, contributions of an electrostrictive (non-resonant) grating component—physically present at very low intensity—are entirely negligible (at no time present, i.e., noticeable, neither in signal time nor in frequency domain) in comparison with the intensity of the deliberately enforced, dominant thermal (resonant) grating exploited throughout both calibration and measurements—compare [95]. In order to ensure homogeneous species distribution, a seeding gas mixture (5000 ppm NO diluted in N_2) is inserted into the shock tube just after evacuation and before setting the ST initial fill pressure p1 by inserting dry air.

Influence of seeding concentration (maximum 0.05 vol%) on specific gas constant R_s is taken into account. For every experiment presented herein, a separate baseline reference calibration of the optical grating is carried out a priori and in situ, immediately before facility operation. To ensure calibration to be most representative of the following test case experiment, (state 1) shock tube initial conditions of the quiescent test gas are set as reference, such that grating calibration is carried out at the shock tube initial fill pressure p_1, with 235-500 ppm NO seeding. Every single calibration involves a set of 200 single-shot LIGS signals, acquired at 10 Hz pump laser repetition rate, to yield a single, 200-fold averaged calibration curve for accurate determination of reference condition oscillation frequency (fringe spacing). Local reference gas temperature is measured via an adjacent thermocouple with 0.1 K precision, to yield air speed of sound at reference condition. For means of consistency with data analysis at test conditions, real gas (equation of state) values according to Lemmon et al. [104] are similarly utilized for calibration purposes. Henceforth, the interference fringe spacing (optical grating constant) Λ is uniquely determined according to Eq. 3.3.

In the first LIGS campaign, throughout 20 s of calibration time duration, fringe spacing and oscillation frequency reflect a normal distribution with nominal values of μ_λ =10.71 μm and 32.043 MHz, respectively. An absolute standard deviation σ_λ =0.021 μm results in a relative standard deviation for the grating constant of $\sigma_\lambda / \mu_\lambda$ =0.20%, reflecting high precision and robustness of a priori optical setup calibration.

In the second LIGS campaign, throughout 20 s of calibration time duration, fringe spacing and oscillation frequency reflected a normal distribution with nominal values of μ_λ =14.55 μm and 23.690 MHz, respectively. An absolute standard deviation σ_λ =0.021 μm results in a relative standard deviation for the grating constant of $\sigma_\lambda / \mu_\lambda$ =0.20%, reflecting high precision and robustness of a priori optical set-up calibration. Employing 10 GHz sampling frequency and deriving the reference calibration curve from a 200-fold waveform average, reference frequency, i.e., fringe spacing, calibration precision is deduced to be even lower, as discussed by Balla and Miller [122]. As two competitive data reduction methodologies are being used for time- and frequency-domain analysis of single-shot LIGS signals to be acquired at experimental test condition, reference condition calibration is likewise conducted by separate application of signal time evolution fitting and DFT; this is to ensure signal analysis for both methodologies to be distinct. A background subtraction routine is used for both techniques to minimize stray light noise influence. With a relevant laser pulse length of $\sim$10 ns, turbulence and convection effects on the opto-acoustic grating (of sub-microsecond duration $\sim$100 ns) are not considered relevant and hence are not treated separately in the data analysis [100, 121]. Individual LIGS calibration curves of four representative test runs for cases C1–C3 of the second LIGS campaign are presented in Fig. 3.5, conducted at room temperature and immediately before the experiment. Each curve presents a 200-fold average of successive single shots. While calibration signal oscillation at reference conditions is seen to last over a time duration of approximately 1 μs and at later time instants gradually decreases due to thermal conduction and acoustic damping [123], only the initial closely correlated signal of the oscillation is used for calibration purposes. As the concentration of NO_2 as resonantly excited species in dry air is too low to obtain a proper calibration signal at room temperature, test cases C1–C3 have a seeding concentration of NO between 235 and 500 ppm, depending on the initial ST pressure. Seeding induces greater (resonant) signal intensity and thus favourably affects the length of the useful calibration curve, varying between 500 and 800 ns. This has, however, no influence on measurement accuracy, as different seeding concentrations are taken into account. In Fig. 3.5, besides the experimentally determined calibration curve, a numerical least-squares fit to the signal's temporal evolution is plotted, illustrating excellent qualitative and quantitative agreement of the oscillation crests and troughs as well as its damped oscillation envelope. Depending on room temperature and beam path, the calibration signal scattering frequency for individual experiments is determined to vary between 22.546 and 23.673 MHz, corresponding to a spatial grating constant Λ of 15.253–14.556 μm. Accordingly, the pump beam crossing angle Θ varied between 1.1° and 1.16°.
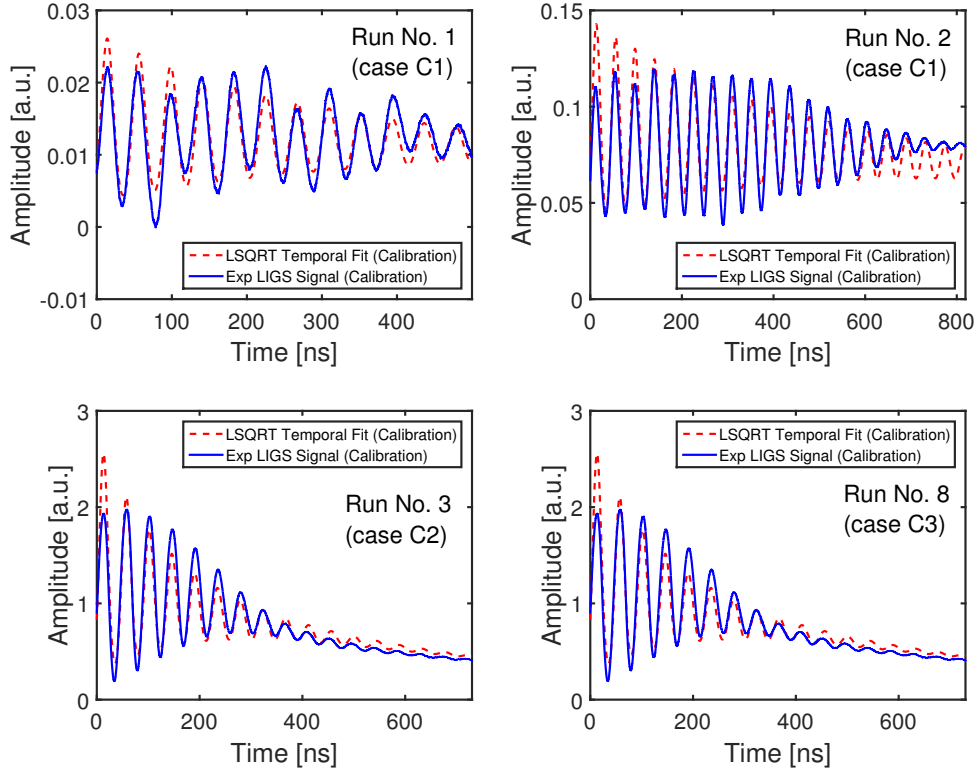
Figure 3.5: Time domain LIGS signals for test cases C1-C3 from test campaign 2 (flush-mounted windows) including curve fit, [80].

Data processing

Local fluid temperatur within the LIGS measurement volume (ellipsoidal) is determined from dominant signal oscillation (modulation) frequency - in the current case of purely thermal (resonant) excitation, the detected signal frequency will equal the Brillouin scattering frequency. Signals with relevant frequency on the order of $\mathcal{O}$(20-30 MHz) are sampled at 10 GHz. Frequency analysis for determination of the signal scattering frequency f_M is performed in two alternative ways, firstly in the frequency domain by a fast-fourier transform - being the common approach in literature - and secondly by time-domain fitting of the waveform. The former case is implemented via a discrete fourier transform (DFT) for a waveform of time-discrete data, using a Hanning window function to most accurately capture the narrowband sine wave signal. The second case is numerically implemented via a non-linear least-squares fitting procedure (via Levenberg-Marquardt fit) of theoretically temporal signal waveform - according to the linearized equations of hydrodynamics and dynamic light scattering, following the postulation of Cummings [99] - to capture the detected signal most accurately. Both, signal amplitude and frequency are dependent on the primary variables as described in [99]; implementation of the numerical fitting procedure is described in the work of Koroll [124]. For both approaches of data processing, the effect of noise (random fluctuations superimposed on the raw signal) was found to be negligible, where a single frequency of the dominant oscillation is clearly distinguished from spurious background distortions for useful signal lifetimes of $\mathcal{O}$(100-1000 ns),

throughout measurement and calibration, respectively. As for uncertainty, the greatest source of error was determined as the finite sampling rate and limited useful signal lifetime (length), which dominates accuracy of the DFT [125]. In case of the time fit, subtraction of the low-frequency offset was found to be beneficial, accuracy being neither affected to (dis-)advantage by high-frequency (background) noise or low-pass filtering, respectively, but being similarly limited by the number of relevant signal periods, i.e. signal lifetime. Accuracy of both methods, DFT and temporal fit, in terms of measured temperature T, are thus estimated to ± 55 K and ± 50 K, respectively. Results of both data processing methods are compared in [62] for a single exemplary test case and 10 experiments, indicating absolute differences on the order of $\Delta T \sim \mathcal{O}$(1-70 K) and reflecting a slightly higher relative deviation (as compared to theoretical mean temperature from 1-D ideal gas theory) of -1.82% for the DFT as opposed to -0.61% of the curve fit.

Uncertainty analysis

Measurement uncertainty is estimated according to the single sample method proposed by Kline and McClintock [126] and Moffat [127], exemplary for the second test campaign [80], being equally valid for the first test campaign [62]. Ambient air reference temperature is read with a thermocouple precision of 0.1 K, such that the absolute uncertainty of baseline calibration test gas temperature is estimated to be at most 0.33% (± 1 K at 300 K room temperature). Henceforth, linear interpolation of high-temperature and high-pressure thermophysical reference data for dry air, provided in Lemmon et al. [104], is employed to obtain air speed of sound from measured thermocouple temperature. Based on 0.2% tabulated uncertainty for air speed of sound, as reported in [104], calibration uncertainties of the LIGS grating constant Λ, intersection angle Θ, and Bragg angle φ are estimated to be 1.07%. Herein, the major contributor to grating calibration uncertainty is the DFT-inherent frequency discretization, which yields deviations below 1.0%. Employing the calibrated grating constant to determine air speed of sound from measured oscillation frequency and henceforth calculating gas temperature, absolute measurement uncertainty of the latter is inferred to amount to ± 55 K and ± 50 K for the DFT and curve fit, respectively. On a relative scale, uncertainty of post-reflected shock wave test gas temperature T_5(exp) amounts to maximum 5.0% and 4.6% when compared to the lowest nominal temperature (1100 K) of test case C1. For higher temperature test conditions C2 and C3, the relative measurement error will hence be notably lower than 4.0%. Similarly, as theoretical reference temperatures are calculated by CEA, based on the experimentally acquired incident shock velocity, measurement uncertainties in shock speed, i.e., Mach number, directly translate to reference temperature variation. Here, Mach number uncertainty is dictated by the data acquisition system's temporal resolution and deviations from the nominal relative distance of PCB wall pressure gauges, which amounts to a maximum error of 0.91% in Mach number. Accordingly, measurement uncertainty in associated post-reflected shock (state 5) reference temperature T_5(th) and pressure p_5(th) is estimated to be 1.5% and 2.7%, respectively. Measurement uncertainty in experimental pressure p5(exp) is negligible, considering a

discretization error of merely 0.02%, as given by the 14-bit amplitude resolution of the transient recorder.

3.5 Measurement results

3.5.1 Test matrix

Two test campaigns with LIGS were conducted for in situ nozzle reservoir thermometry in the HELM facility, with nominal test conditions - as predicted by L1d and CEA - listed in Table 3.1. Whereas nominal test conditions in Table 3.1 are predicted by L1d simulation, reference state 5

Table 3.1: Test matrix for LIGS measurements in the HELM nozzle reservoir: numbering of test cases for both test campaigns identical to primary source [62, 80]. Nominal post-reflected shock (state 5) stagnation quantities are determined by L1d and CEA, respectively. Driver and test gas is dry air. Stated enthalpy is referenced to 0 K.

Campaign	[-]	1	2	2	2
Case	[-]	C1	C1	C2	C3
p_{A0}	[bar]	18.5	25.5	25.5	25.5
p_4	[bar]	115	220	220	220
p_{40}	[bar]	1	1	1	1
p_1	[bar]	2.5	5	2.5	1.5
Ma_s	[-]	2.75	2.85	3.10	3.50
p_5	[bar]	90	225	145	120
T_5	[K]	1100	1200	1360	1650
h_5	[MJ/kg]	1.3	1.4	1.5	1.9

quantities in the nozzle reservoir, in terms of post-reflected shock pressure p_5(exp) and reference temperatures T_5(th), are calculated by NASA's CEA code [9] and ideal gas 1-D (Rankine-Hugoniot) shock jump relations, based on incident shock wave speed for each individual experiment (test run). The latter is determined from time-of-arrival PCB pressure gauges $\sim$350 mm upstream of the ST endwall. All test conditions herein use air as driver and test gas.

3.5.2 Test campaign I

Single-shot measurement results of the first test campaign, in terms of sampled stagnation pressure and temperature at Q-switch time instance, in comparison to theoretical reference from 1-D ideal gas theory are presented in Table 3.2. In the first test campaign, coherent LIGS oscillation signals have been determined at frequencies around 30 MHz throughout initial calibration at room temperature and 55-65 MHz (corresponding to temperatures 900-1200 K) throughout the experiment after the reflected shock.

Attributed to not perfectly reproducible diaphragm rupture, resulting in inevitable shot-to-shot variation, a 1.87% relative standard deviation of incident shock Mach numbers around a mean value of Ma_s 2.58 was observed in the experiment: the variation of experimental parameters

Table 3.2: Measurement data of test runs 1-10 for the single case C1 of the first LIGS campaign [62], detailing incident shock Mach number, post-reflected shock stagnation pressure and single-shot temperature (measured by time- and frequency domain signal processing), in comparison to theorical reference from 1-D ideal gas (shock jump) relations.

Run	Ma_s [-] Exp	p_5 [bar] Th	p_5 [bar] Exp	T_5 [K] Th	T_5 [K] Exp (FIT)	T_5 [K] Exp (DFT)
1	2.47	73.7	55.1	1032	1121	1138
2	2.50	76.4	56.1	1051	1142	1070
3	2.60	85.1	58.9	1111	1087	1014
4	2.60	85.3	61.0	1111	1065	1089
5	2.60	85.4	59.2	1111	1062	1015
6	2.59	84.9	48.4	1099	963	948
7	2.62	87.0	62.9	1145	895	898
8	2.59	84.1	62.5	1087	1063	1074
9	2.61	86.4	60.0	1109	1079	1060
10	2.60	85.3	59.5	1105	1045	1098
Mean	2.58	83.4	58.4	1096	1052	1040

in the current investigation was hence regarded as well behaved. Differences in predicted and sampled shock speed are attributed to a deviation of experimental conditions, as encountered in a real test facility, from those predicted by quasi 1-D facility simulation by L1d. At the time of these experiments, the L1d-model was not yet sufficiently refined, compare section 2.6.

Differences between theoretical and measured pressure levels throughout experiments ensue from divergence of real test rig conditions from idealized 1-D inviscid theory. Here, shock wave attenuation and losses from surface irregularity due to optical bores in the nozzle reservoir (recessed-mounted windows) contribute to lower than predicted pressure levels and fluctuations [108]. Additional limited influence on sampled mean stagnation pressure and temperature due to nonideal temporal variation of stagnation conditions in the post-reflected-shock regime from ideal theory is conceivable, as discussed by Peterson and Hanson [128].

Results of single-shot temperature measurements of all 10 test runs for single case C1 of the first LIGS campaign are plotted in Fig. 3.6, indicating averaged experimental temperature and theoretical reference temperatures from ideal gas.

Q-switch gating and pump laser pulse release throughout the experiment are synchronized to the incident shock passage event, triggered by the rising flank of the pressure gauge coincident with the measurement location. For low-enthalpy case C1 test runs 1–10 presented herein, manual delay is set to 255 μs to gear gating of the Q-switch to a suitable time instant shortly after reflected shock wave passage. Herein, dominant signal beam oscillation with lifetimes of about 200 ns are clearly observed, as well as small-amplitude signal distortion due to spurious background noise. As expected for a laser-induced grating, signal beam oscillation amplitude (envelope) decreases with time, as density grating lifetime is limited by thermal diffusion and acoustic damping. Toward the end of the signal, the SNR is seen to decrease
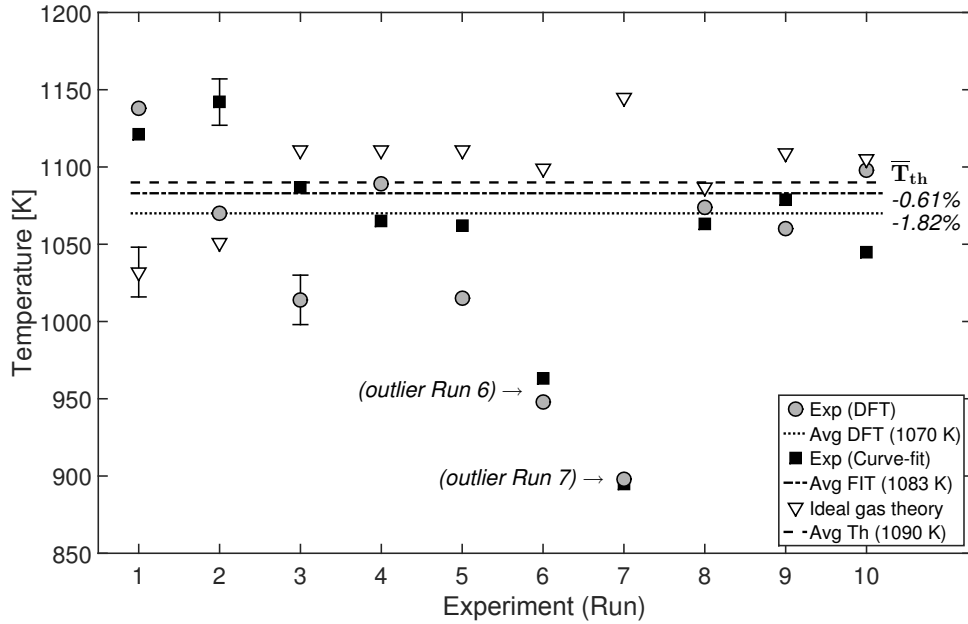
Figure 3.6: Comparison of measured single-shot stagnation temperatures with single points and averages for frequency- and time-domain analysis and ideal gas reference of test campaign 1 (recessed-mounted windows), [62].

continuously, such that, for time instances t > 520 ns, the signal oscillation diminishes and cannot further be separated from background noise [62]. As test runs 6 and 7 were identified as evident statistical outliers of the measurement ensemble for the single low-enthalpy test case C1, they are henceforth not included in the statistical analysis. To provide for a suitable base of comparison for evaluation of measurement technique accuracy, mean temperature values $\overline{T_5}$(exp DFT) and $\overline{T_5}$(exp FIT), as obtained by averaging single-shot temperatures of test runs 1-5 and 8-10, are considered more significant. Here, with a relative standard deviation (i.e., precision) of single-shot temperatures of 3.88% for the DFT and 3.04% for the signal-fitting approach, mean temperature values $\overline{T_5}$(exp DFT) and $\overline{T_5}$(exp FIT) are calculated to 1070 and 1083 K, respectively. This value is considered reasonable, regarding the single-shot standard deviation of the mean of 3% reported by Sander et al. [97] for resonant LIGS post-reflected-shock temperature measurements at Mach number 2.20 and 3.4% by Förster et al. [101] for nonresonant LIGS at Mach number 1.97, both measuring in smaller conventional shock tubes of more well-behaved conditions and employing DFT signal analysis. Considering a theory-predicted statistical mean temperature $\overline{T_5}$(th) of 1090 K, the experimental mean temperature relative deviation from 1-D inviscid theory is found to be as low a -1.82% and -0.61% for the DFT and temporal fit, respectively (see Fig. 3.6). As such, both time- and frequency-domain-based post-processing approaches are found to be in good agreement and to perform comparably well, whereas the time fit reflects slightly higher precision (i.e., lower scatter) in addition to higher accuracy: 1-D ideal theory by mean trend being underestimated by less than 2% for DFT and 1% for time fit, respectively. A possible reason is the useful signal oscillation lifetime, which is limited under adverse test conditions and reasonable to affect uncertainty of frequency-domain

DFT analysis more than time-domain-based waveform fitting. Thus, literature view of signal time fitting to yield potentially more (concurrent) and slightly more accurate information on LIGS measurement volume than plain oscillation frequency analysis is by trend similarly observed herein [122]. The relative variation between theory T_5(th) and single-shot experiment for test runs 1-10 amounts to 10.27% in terms of T_5(exp DFT), in the case of run 1 and 8.68% in terms of T_5(exp FIT) in the case of run 2, the overall best agreement is observed for test run 8. Here, the minimum single-shot relative deviation from theory for both signal analysis approaches is found to be as low as -1.20% and -2.21% for DFT and curve fit, respectively, whereas T_5(exp FIT) and T_5(exp DFT) among each other closely agree to within 1.02% (11 K). In comparison, prior coherent anti-Stokes Raman scattering (CARS) measurements of rotational and vibrational temperature in hypersonic freestream and behind bow shock layers by Boyce et al. [83] and Pulford et al. [84] reported single-shot uncertainties (i.e., relative deviation) of same order of magnitude: as large as 10%.

Upon direct comparison of single-shot temperatures T_5(exp DFT) and T_5(exp FIT) as obtained from frequency- and time-domain signal analysis for every single test run 1-5 and 8-10, relative deviation among each other amounts to maximum 6.72% (73 K) for run 3 and minimum 1.02% (11 K) for run 1, respectively. Thus, whereas singleshot precision of LIGS signal analysis by the temporal fit and DFT indicates room for improvement by further refinement of data reduction procedures in the future, a systematic deviation (i.e., bias) in terms of consistent under-/overestimation of experimental singleshot temperatures as obtained from both methods is not observed herein. On the contrary, both time- and frequency-domain-based methodologies are found to be well correlated in that, despite reasonable to small deviation among one another, single-shot reference temperature T_5(th) for individual test runs 1–10 is either over- or underestimated, yet consistently for both methods (see Fig. 3.6). Therefore, mean temperature measurements in the course of the present investigation are deduced to yield good agreement, whereas single-shot measurement technique uncertainty is inferred to be dominated by reasonable repeatability (i.e., precision) rather than being limited by systematic offset (i.e., lack in accuracy). This is primarily attributed to a 2.86% intrinsic relative standard deviation of reference temperatures T_5(th), as derived from measured incident shock Mach number (σ_M 1.87%) and associated experimental uncertainties, thus facility-inherent shot-to-shot variation of test conditions rather than constituting a feature of the measurement technique itself. Under idealized conditions in a quiescent test chamber, LIGS single-shot precision of the current setup was determined to be as low as 3% by Sander et al. [95]. Besides influence from inherent shot-to-shot variation, experimental scatter observed, and thus deviations from 1-D ideal theory, can further be induced by nonideal temporal variation of post-reflected-shock state conditions, estimated less than 2% for temperature T_5 at test time instant according to Peterson and Hanson [128]. Yet, regarding relative time interval and distance between reflected shock front passage of the measurement plane and Q-switch trigger of less than 50 μs and 30 mm, respectively, overall measurement success rate is deduced to be primarily compromised due to vorticity and density gradient induced beam steering effects in the wake of the reflected shock front,
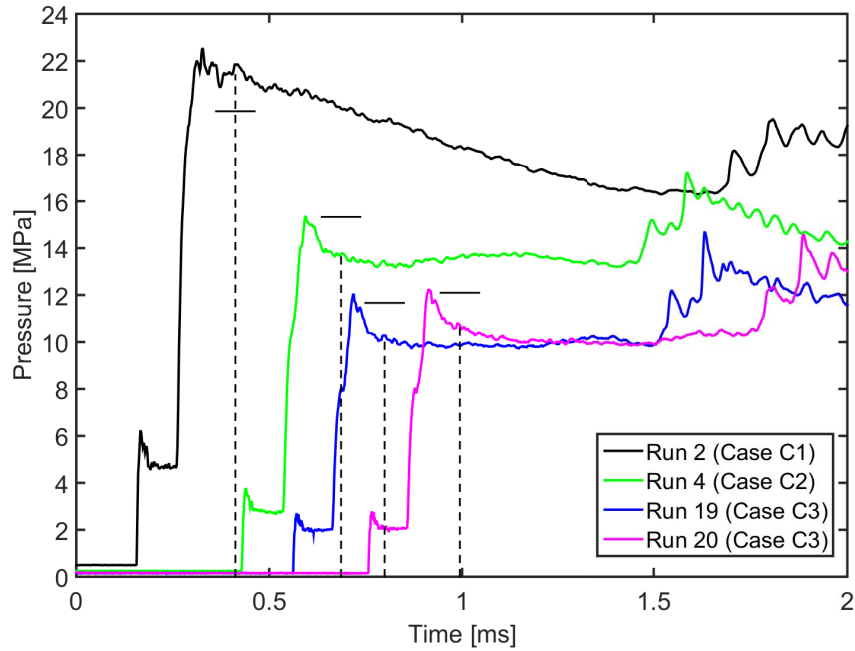
Figure 3.7: Experimental pressure traces in the nozzle reservoir for test cases C1-C3 of test campaign 2 (flush-mounted windows), [80]. Time instant of Q-switch trigger behind the reflected shock wave marked by vertical dashed line.

as already observed by Mizukaki and Matsuzawa [100]. Here, strong density gradients in the shock front vicinity yield considerable laser beam deflection, inducing probe beam shift and detector saturation due to excessive stray light incidence, as well as signal beam deflection from the detector [121].

3.5.3 Test campaign II

In the second test campaign, manual time delay is set to 235 μs to gear gating of the Q-switch to a suitable time instant shortly after reflected shock wave passage. For all three test cases C1-C3, exemplary stagnation pressure traces are illustrated in Fig. 3.7. Timedomain resonant LIGS signals obtained from single-pulse measurements are presented in Fig. 3.8 for four representative test runs of cases C1–C3. Here, for means of illustration of robustness of the temporal least-squares fit post-processing procedure, signal curves are selectively subjected to moving-average (Savitzky–Golay) filters of varying step width. While the temporal signal of run 3 remains unfiltered, noise level is gradually reduced for runs 1, 2, and 8, respectively. Whereas a priori filtering of the raw signal before signal analysis can be advantageous for DFT frequency analysis, the time-domain nonlinear least-squares curve fitting procedure is found to be very robust against background noise and to be entirely unaffected by signal filtering. However, for initial visual identification of relevant signal length, minor filtering can be beneficial. Here, temporal duration of the wellcorrelated single-shot signal is seen to vary between 100 and 300 ns for cases C1–C3, respectively. Within this time period, a dominant and harmonic signal oscillation of a single (discrete) frequency is clearly observed, superimposed by a low level of
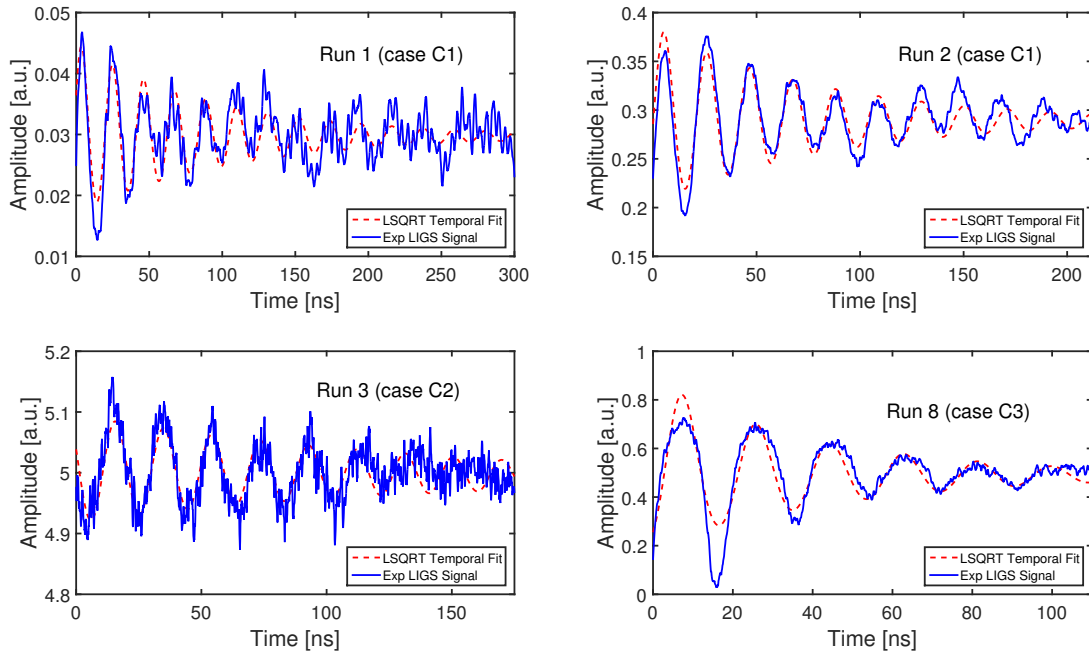
Figure 3.8: Time domain LIGS signals for test cases C1-C3 of second test campaign (flush-mounted windows) including curve fit, [80]. Sorted in ascending order of moving-average filter step width: Run 3, Run 1, Run 2, Run 8.

small-amplitude distortions and spurious background noise. As expected for laser-induced gratings, signal beam oscillation amplitude (envelope) decreases with time, as density grating lifetime is limited by thermal diffusion and acoustic damping. For later time instances, signal oscillation gradually diminishes and cannot be further separated from background noise. For all four runs, the nonlinear curve fit is seen to closely coincide with the experimental signal curve where the dominant oscillation frequency is accurately captured. Moreover, besides signal scattering frequency, signal amplitudes are seen to be well matched by the fit and the gradual amplitude decay to be captured in the beginning as well as towards the end of the signal time period. Furthermore, signal amplitudes of oscillation crests and troughs are observed to be similarly well captured, even at later time instances where the signal gradually decreases to background noise. Overall, the signal with the longest well-correlated lifetime of 300 ns is found to be captured for run 1 (C1), i.e., at near overall highest pressure and lowest temperature, whereas the shortest signal lifetime is observed for run 8 (C3), reflecting lower pressure and higher temperature. Prevalent background noise was determined in the ~1 GHz range, whereas signal oscillations are detected around ~50-60 MHz. Together with a superior SNR > 20, this facilitated unambiguous determination of the dominant scattering frequency for every experiment.

In direct comparison to the first measurement campaign, lower signal scattering frequencies (even though sampled at higher stagnation temperatures) result from a decrease of the pump beam intersection angle. Precisely, the mounting the flush-mounted optical access window assembly mandated a notably smaller pump beam crossing angle Θ of 1.16° in comparison with

the former 3.70°. As a positive side effect, the elliptical LIGS measurement volume extendes over a longer geometrical distance, where (at identical pump laser wavelength) smaller pump beam crossing angles Θ induce larger grating constants Λ, i.e. maximizing the fringe spacing. Precisely, the passage of more wave packets can be observed by an increased number of oscillation periods [121], as reflected by signal lifetimes increased by up to 100 ns. Accordingly, rearranging the beam path geometry to smaller intersection angles is favourable with regard to grating lifetime, which in general decreases with temperature and thus is the limiting factor for measurement accuracy. For cases C1–C3, measurements are conducted in a temperature range from 1100 to 1900 K, with associated signal scattering frequency and local sound speed ranging from 47.6 to 59.9 MHz and 692 to 863 m/s, respectively. Compared to theoretical CEA predictions, experimental data evaluated by curve fits yield almost consistently higher oscillation frequency, sound speed, and thus post-shock temperature. Absolute and relative deviations of experimentally determined temperatures from theoretical reference values by 1-D ideal gas theory and CEA (thermo-chemical equilibrium) are detailed in Table 3.2. For experimental data processing, preference was given to the time-domain fitting, such that stated temperature values are obtained from measured oscillatory signals by the temporal curve-fit only.

Results of single-shot temperature measurements of all 20 test runs of case C1-C3 are plotted in Fig. 3.9, further indicating averaged experimental temperature and theoretical reference temperatures from CEA and ideal gas. For the complete set of 20 measurements presented, varying agreement between experimental temperatures $T_5(\text{exp})$ and CEA theoretical reference temperatures $T_5(\text{th})$ is seen. Precisely, in the case of measurements 1–2 for test condition C1, remarkably good agreement with a relative deviation below 1%, i.e., below 10 K absolute deviation, is observed. Moreover, both individual experiments coincide closely, determining post-shock temperature to around 1100 K. This observation is notable, as condition C1 represents the test case with the overall highest reservoir pressure of 220 bar and lowest shock Mach number $\sim$2.8, reflecting a stagnation pressure profile that is clearly undertailored, see Fig. 3.7. In the case of condition C2, the net incident shock Mach number is increased to around 3.1 and the postreflected shock pressure reduced to around 15 MPa. For the five test runs (no. 3–7) conducted for case C2, notably different agreement between experiment and theory is observed. Test runs 3 and 4 yield temperatures $T_5(\text{exp})$ around 1550–1750 K that are higher than theoretical temperatures $T_5(\text{th})$ 1360–1400 K, with relative deviation ranging from 13.8 to 24.3%. For experiments 3–4, the incident shock Mach number of 3.1 was slightly higher than expected, caused by a greater diaphragm burst pressure. As such, with a relative deviation of 24.3%, test run 4 is identified as an outlier. For experiments 5–7, an incident shock Mach number of consistently 3.0 was measured and yielded post-reflected shock temperatures $T_5(\text{exp})$ of 1300–1320 K measured by LIGS that are in close agreement to theoretical temperatures T5(th) of 1265–1300 K: reflecting a consistent relative deviation as low as 2.2–2.8%. As runs 5–7 are thus very consistent, they indicate high accuracy of LIGS when test conditions are well behaved and shot-to-shot variation of diaphragm burst pressure and incident shock Mach number is kept as low as possible to ensure reproducible facility operation. In contrast, variation of diaphragm

Table 3.3: Measurement data of test runs 1-20 for the three cases C1-C3 of the second LIGS campaign [80], detailing incident shock Mach number, post-reflected shock stagnation pressure and single-shot temperature (signal processing by time-domain fit only). Theoretical reference temperatures according to 1-D ideal gas (IG) relations and CEA (thermo-chemical equilibrium) are stated including absolute and relative deviation to sampled temperatures.

		Ma_s [-]	p_5 [bar]	p_5 [bar]	T_5 [K]	T_5 [K]	ΔT [K]	ΔT [%]	T_5 [K]	ΔT [K]	ΔT [%]
Run	Case	Exp	Exp	Th (CEA)	Exp (Fit)	Th (CEA)	Th (CEA)	Th (CEA)	Th (IG)	Th (IG)	Th (IG)
1	C1	2.68	214.0	165.2	1098	1089	9	0.8	1151	-53	-4.6
2	C1	2.86	218.7	198.6	1115	1120	-5	-0.5	1278	-163	-12.8
3	C2	3.11	151.7	145.2	1548	1360	188	13.8	1478	70	4.7
4	C2	3.17	137.8	153.3	1737	1398	339	24.3	1528	209	13.7
5	C2	2.96	161.5	125.3	1303	1267	36	2.8	1367	-64	-4.7
6	C2	2.98	174.0	128.5	1313	1282	31	2.4	1386	-73	-5.3
7	C2	2.99	147.2	129.6	1320	1292	28	2.2	1398	-78	-5.6
8	C3	3.57	112.3	127.5	1775	1676	99	5.9	1877	-102	-5.4
9	C3	3.19	136.2	93.0	1350	1412	-62	-4.4	1544	-194	-12.6
10	C3	3.27	94.8	100.3	1361	1471	-110	-7.5	1618	-257	-15.9
11	C3	3.49	107.1	119.8	1694	1624	70	4.3	1812	-118	-6.5
12	C3	3.60	116.9	130.3	1887	1703	184	10.8	1913	-26	-1.4
13	C3	3.57	114.3	127.8	2231	1691	540	31.9	1900	331	17.4
14	C3	3.59	113.0	129.6	1914	1705	209	12.3	1917	-3	-0.2
15	C3	3.50	106.3	120.5	1916	1638	278	17.0	1831	85	4.6
16	C3	3.55	111.3	125.1	1834	1676	158	9.4	1880	-46	-2.5
17	C3	3.48	106.4	119.3	1857	1631	226	13.9	1822	35	1.9
18	C3	3.33	99.7	105.4	1692	1525	167	11.0	1686	6	0.4
19	C3	3.54	102.8	116.7	1660	1614	46	2.9	1799	-139	-7.7
20	C3	3.50	107.5	121.0	1771	1650	121	7.3	1845	-74	-4.0

burst pressure and shock speed can result in evident deviations. However, considering the overall agreement between experiment and theory of below 10% for the majority of test runs, a relative deviation of beyond 20%, as in the case of test run 4, is regarded as an evident outlier. This is consistent with the first test campaign, where intermittent outliers were similarly observed and easily identified as such. For the third test condition C3 at the overall highest shock Mach number of 3.5 and the lowest post-reflected shock pressure of 110 bar, 13 measurements (no. 8–20) were conducted. Here, experimental temperatures T_5(exp) measured by single-shot LIGS range from 1350 to 1915 K, where stagnation condition variation is attributed to variation in burst pressure and shock Mach number, the latter ranging from 3.19 to 3.60. Absolute and relative temperature variations between T_5(exp) and T_5(th) of minimum 46 K (2.9%) for run 19 and maximum 278 K (17.0%) for test run 15 are observed. In contrast, run 13, with a deviation of 540 K (31.9%), reflecting an unrealistically high temperature of 2231 K, is easily identified as an outlier and thus omitted from further analysis. Interestingly, the LIGS time oscillation signal for run 13 was by no means of lesser quality, i.e., lower SNR, or of shorter duration than
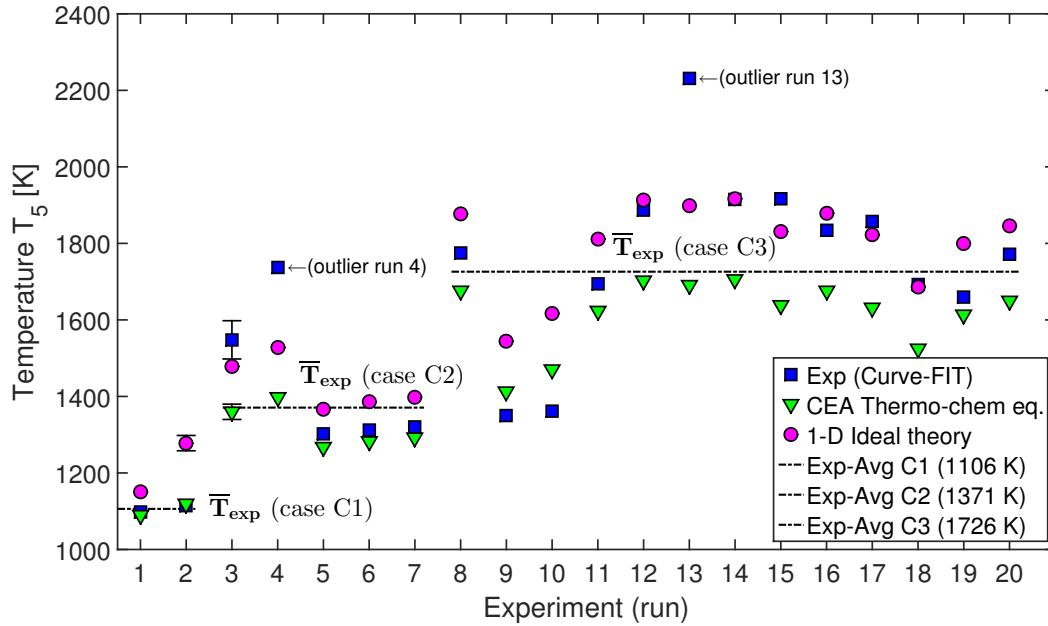
Figure 3.9: Comparison of measured single-shot stagnation temperatures with single points and averages for curve-fit, CEA, and ideal gas reference of test campaign 2 (flush-mounted windows), [80].

for other test runs (Fig. 3.8) and was independently confirmed by frequency-domain signal analysis by DFT. Overall, 7 out of 13 LIGS measurements for condition C3 reflect a relative deviation between T_5(exp) and T5(th) of below 10%, whereas five experiments indicated relative deviation between 10 and 20% from CEA reference predictions.

It is interesting to note that whereas LIGS almost consistently overpredicts temperatures as predicted by CEA, i.e., assuming thermo-chemical equilibrium, temperatures predicted by Rankine–Hugoniot (shock jump) equations, i.e., 1-D inviscid ideal gas theory, are almost consistently higher than experimental values, see Table 3.3. Here, relative deviation of T_5(exp) from T_5(th) according to ideal gas theory is negative in the majority of cases. Particularly for case C3, at the overall highest post-shock temperature 1600–1800 K and lowest stagnation pressure ~110 bar, closer agreement of experiments with theory is obtained when employing ideal gas relations as temperature reference. Specifically, for 8 out of 13 measurements for condition C3, the relative deviation reduces notably when comparing T_5(exp) against 1-D inviscid theory instead of CEA. For a limited number of four experiments (12, 14, 17, and 18), this reduction is as large as an order of magnitude, where relative deviation reduces from initially above 10% to now below 5% (Table 3.3). Most interestingly, the opposite trend is observed for the undertailored condition C1, i.e., at the overall lowest post-shock temperature ~1100 K and highest stagnation pressure of 220 bar of all test conditions. Here, for both test runs 1 and 2, initially excellent agreement between experiment and theory according to CEA is reflected by a remarkably low relative deviation of well below 1%. This relative deviation rises up to around -5% and -13% for experiments 1 and 2, respectively, as T5(exp) is compared with T_5(th) predicted according to 1-D ideal

gas theory, now reflecting an obvious underprediction of reference temperature. In the case of the intermediate condition C2, i.e., with post-shock temperature 1300–1500 K and stagnation pressure 15–16 MPa, the identical trend is observed. This observation is, however, less evident which is in part attributed to a larger spread of stagnation quantities for a nominally identical test condition. Both test runs 3 and 4 of lower pressure 13–15 MPa and higher temperature 1600–1700 K reflect relative deviation to CEA temperatures as large as 14% and 24% which is reduced to 5% and 14%, respectively, when compared with ideal gas theory. Hence, even though reference temperature is still consistently overpredicted, absolute and relative deviations reduce notably. By contrast, for three additional test runs 4, 5, and 6 at higher pressure 15–17 MPa and higher temperature ∼1300 K, the CEA temperature was initially closely matched, yet slightly overpredicted, as is reflected by a very consistent relative deviation of 2–3%. As the experimental temperature T_5(exp) is now compared against 1-D ideal theory, relative deviation is observed to consistently rise in magnitude and to turn negative, thus indicating an underprediction of reference temperature by around -5%. Average experimental temperatures of T_5(exp) for conditions C1–C3 have been calculated to 1106 K, 1371 K, and 1726 K, respectively. Standard variation from arithmetic average for conditions C1–C3 (omitting outliers for run 4 and 13) is calculated to be 1.1%, 8.6%, and 11.2%, respectively. However, due to mere limited (statistically insignificant) number of measurements for condition C1 and C2, this quantity is only deemed a statistically significant measure of sample variance for condition C3. Therefore, errorbars in Fig.3.9 indicate calculate uncertainty of experimental measurements and numerical predictions which hold for all test conditions C1-C3. Yet, as a more indicative measure of expected test case repeatability and inherent dataset variation, the relative standard deviation of incident shock Mach number for conditions C1–C3 is calculated to be 4.5%, 3.1%, and 3.7%, respectively. Evidently, variation and scatter of measured temperatures is not predominantly attributed to LIGS measurement uncertainty, but ensues to a large extent from the variation of incident shock Mach number (i.e. attributed to varying diaphragm opening and burst pressure), being the most influential quantity to affect post-reflected shock quantities at otherwise identical initial conditions in the ST (set pressures p_1 were identical while the variation of initial temperature T_1 was negligible). This trend becomes very evident for test runs 9 and 10 for condition C3, where a considerably lower Mach number is evident to entail a largely reduced post-shock temperature T_5 in the experiment and lower theoretically predicted temperatures. Precisely, if those two values are similarly omitted from statistics, the arithmetic mean temperature for C3 rises to 1800 K, coupled with a halved standard variation of mere 96 K absolute and 5.3% relative - i.e. much more consistent with the scatter already observed for incident shock Mach number.

3.6 Discussion

For means of clarity of numbering, abbreviations C1-C3 for conditions of test campaign 2 are retained, while the single condition of campaign 1 is abbreviated by C0 in the following. Towards

the end of the first test campaign, single-shot temperature measurements by resonant LIGS in the low-enthalpy regime of a full-scale transient test facility were deduced to be well correlated and to yield good mean temperature accuracy, even for a limited range of experiments. Considering 2.86% intrinsic relative standard deviation of reference temperatures derived from incident shock Mach number, measurement precision (singleshot relative standard deviation) is determined to be 3.88% for the DFT and 3.04% for the time-fit signal processing approach. As for accuracy, mean temperature relative deviation is found to be as low as -1.82 and -0.61% for the DFT and time fit, respectively, indicating single-shot temperature measurements by LIGS to be well correlated and to yield good agreement with theory. Statistical outliers indicate acquired single-shot temperatures to correlate with instantaneous pressure fluctuations deviating from average stagnation pressures, further highlighting LIGS to be capable of sub-microsecond time-accurate post-shock temperature measurements. Due to recessed-mounted configuration of the optical windows, the success rate of single-shot measurements for the single case C0 throughout the first test campaign amounted to mere 10-20%, attributed to dominant flow perturbations, significantly impairing coherent signal beam detection.

In contrast, the success rate of single-shot measurements throughout the second test campaign could effectively be raised to 90-100% for all three cases C1-C3, attributed to the aforementioned technical facility advancements. Here, experimental temperatures T_5(exp) were found to consistently range higher than reference temperatures computed by CEA, assuming full thermo-chemical equilibrium, and to be lower than temperatures calculated according to Rankine–Hugoniot (shock jump) relations of an ideal gas. Against this background, it is interesting to note that, for all 20 single-shot measurements presented herein, a consistent trend in terms of variation of agreement of T_5(exp) with reference temperature T_5(th) has been observed, as the post-shock conditions were systematically varied for cases C1–C3. Initially, measurements for condition C1, at the highest overall pressure and lowest temperature, reflected excellent agreement with CEA, assuming full thermo-chemical equilibrium, whereas agreement with ideal gas theory was much poorer. A systematic decrease in pressure (from initially 220 bar for C1 to 110 bar for C3) and a corresponding increase in stagnation temperature (from initially 1100 K for C1 up to 1900 K for C3) resulted in experimental temperatures T_5(exp) to reflect continually better agreement with ideal gas predictions of T5(th) for cases C2 and C3. Particularly, experimental measurements 8–20 for condition C3 showed much closer agreement with ideal gas theory, as opposed to a notable overprediction of temperatures predicted by CEA. Considering stagnation temperature below 2000 K and thus excluding chemical dissociation of O_2 or N_2, as well as high densities within the nozzle reservoir to induce rapid thermal equilibrium of translational and rotational energies [129], the spread between reference temperatures T_5(th) calculated according to CEA and ideal gas relations is attributed to an excitation of vibrational degrees of freedom. Hence, the general trend of data to be continuously well represented by reference values by 1-D ideal gas theory and less well captured by CEA predictions, as pressure was decreased and temperature was increased, is indicative of a limited influence of vibrational excitation. For the relevant species and bath gases involved, vibrational relaxation times τ_{relax}
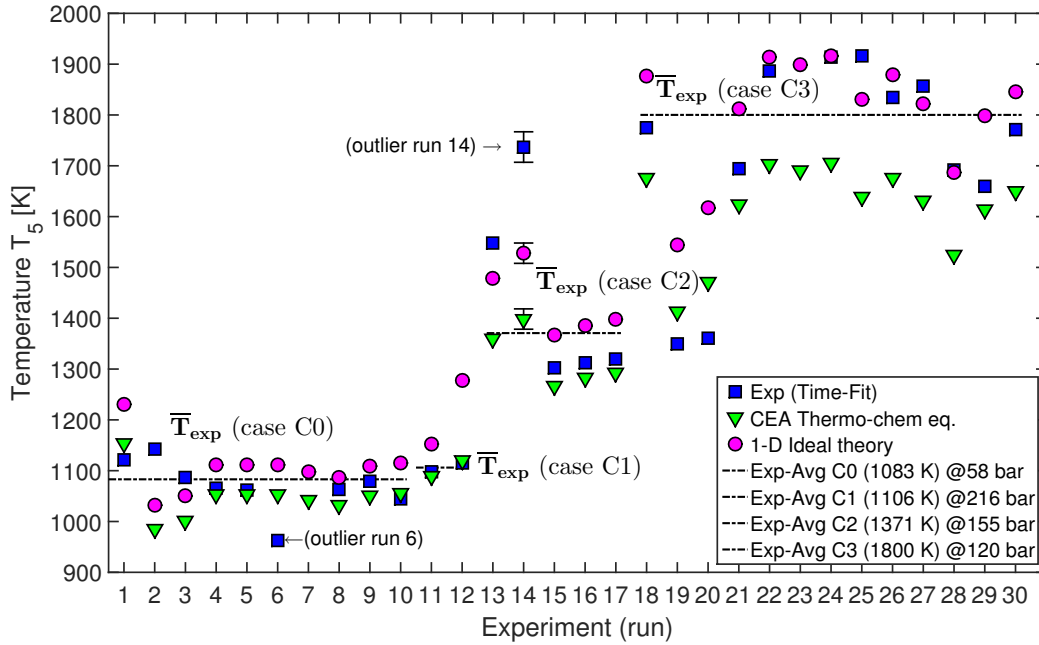
Figure 3.10: Global comparison of measured LIGS single-shot stagnation temperatures for all four test conditions (C0-C3) from both LIGS test campaigns in comparison to theoretical reference temperature by ideal gas reference (frozen composition) and CEA (full thermo-chemical equilibrium). For means of clarity of numbering, abbreviations C1-C3 for conditions of test campaign 2 are retained, while the single condition of campaign 1 is abbreviated by C0 herein. Experimental temperatures are determined from time-domain analysis of the LIGS signal.

of collisional partners O_2–O_2 and N_2–N_2 and NO–N textsubscript2 were calculated for stagnation pressures and temperatures of conditions C1–C3 according to the Landau–Teller model [130] and were found in the range of τ_{relax}<10 μs. In experiments presented in this article, the relative time difference between release of the pump laser pulse and reflected shock passage amounts to 120–150 μs, depending on incident shock Mach number Ma_s. While this timescale is generally not considered to be of the same order as relevant vibrational relaxation timescales in the high-pressure, high-density post-shock regime, moderate influence due to finite-rate vibrational relaxation is conceivable, yet. This becomes evident when considering the relaxation time τ_{relax} to merely represent the time interval, where initial vibrational energy rises by a factor e and does not yet reach its full thermal equilibrium value. The general qualitative trend of vibrational relaxation time τ_{relax} to rise with temperature and drop with pressure has been tentatively observed in the experimental data for conditions C1–C3 that is continuously better represented by ideal gas theory than CEA.

The overall trend of stagnation temperature variation is plotted in Fig. 3.10. Here, starting from condition C0 (campaign 1) with the lowest stagnation temperature around 1100 K and at the lowest stagnation pressure ∼60 bar, the measurent condition is observed to be well behaved and to show relatively low scatter. Experimental values are found to fall in between the limits of ideal gas and CEA prediction. When increasing stagnation pressure by a factor

of ~3, at otherwise identical stagnation temperature 1100 K (condition C1), experimental mea-surements are found to closely coincide with CEA predictions (lower limit), whereas being far below the high temperature limit. For condition C2, i.e. at increased stagnation temperature 1370 K and lower pressure of 155 bar, measurements again observed to fall within the theo-retical range: showing greater temperatures than CEA and lesser temperatures than ideal gas. In contrast, when the temperature is further increased to ~1800 K (condition C3) - despite the overall largest scatter of all test conditions -, experimentally measured temperatures reflect a remarkably close agreement with the frozen composition prediction, obviously much higher than the CEA low temperature limit. From a global perspective, this observation substantiates the theoretical prediction of higher pressure at lower temperature to favour rapid equilibrium by high collisional quenching rates, and lower pressure at higher temperature to favour the high-temperature frozen composition limit. A similar trend of LIGS single-shot temperature data at lower stagnation pressure to yield better agreement with ideal gas theory than CEA was observed in the work of Altenhoefer et al. [107].

Two out of 20 measurements with individual relative deviation beyond 20% are clearly iden-tified as outliers. Absolute temperatures derived from the time-domain fit have been inde-pendently confirmed by cross-checking with a frequency-domain data analysis by DFT. The most likely cause for such obvious outliers, far from anticipated temperature levels, are tran-sient distortions of the induced density grating. This becomes evident when considering tem-peratures to be extracted from single-shot measurements, i.e., by induction of a local density grating into a highly perturbed flow, as present in the stagnated endwall region. However, in addition to grating perturbations by laser beam steering and deflection in the wake of the re-flected shock front, as reported by Mizukaki and Matsuzawa [100], some of these fluctuations pertain to variation of the stagnated gas properties, as induced by secondary compression and expansion waves within the shock tube. Such undesirable waves are typically caused by a free-piston driver which is not exactly tuned, as in the present study, and propagate downstream to the nozzle reservoir. Further influence can result from under- and overtailoring where ex-pansion and compression waves between the contact surface and ST-endwall can entail distor-tions of the transient LIGS grating. Therefore, operating short-duration facility with a tuned piston driver and in tailored mode is considered to be generally beneficial in order to avoid LIGS single-shot measurements to be affected by transient fluctuations. However, as has been demonstrated by the majority of successful measurements presented herein, LIGS single-shot measurements of stagnation temperature within the nozzle reservoir are also possible with-out tuned piston and tailored interface operation. Accordingly, the relatively large scatter ob-served, particularly for conditions C2 and C3, is not primarily due to random variation of LIGS single-shot measurements, but attributed to variation of main diaphragm burst pressure and hence incident shock Mach number Ma_s. This is exemplified by an inherent relative standard deviation of Ms between 3.1 and 4.5% for cases C1–C3 and associated experimental uncer-tainties. Besides influence from inherent shot-to-shot variation, experimental scatter observed

can further be affected by non-ideal temporal variation of postreflected shock conditions, estimated less than 2% for temperature T_5 at test time instant according to Peterson and Hanson [128]. Similar findings were reported by Richter et al. [106] who observed a negative frequency chirp, i.e., temporally decreasing signal frequency, that is indicative of gradually decreasing sound speed and temperature in the post-reflected shock regime, even for tailored interface conditions.

Hence, single-shot uncertainty of measurements presented herein is inferred to be dominated by reasonable repeatability, i.e., precision, due to facility-inherent shot-to-shot variation rather than being limited by systematic offset, i.e., lack in accuracy. As such, when excluding those evident outliers from statistical analysis of an otherwise reproducible test condition, single-shot measurements have been demonstrated to be well correlated with the mean value [62]. Under idealized conditions in a quiescent test chamber, LIGS single-shot precision of the current set-up was determined to be as low as 3% by Sander et al. [95]. In comparison, prior broadband coherent anti-Stokes Raman scattering (CARS) measurements of rotational and vibrational temperatures in hypersonic freestream and behind bow shock layers by Boyce et al. [83] and Pulford et al. [84] reported single-shot uncertainties, i.e., relative deviation, as large as 10%, thus of same order of magnitude as LIGS single-shot measurements presented herein. However, as stated in the Introduction, application of CARS measurements to in situ nozzle reservoir thermometry is deemed impractical due to high density and pressure in the post-shock regime. Hence, the positive correlation of LIGS signal intensity with pressure is considered particularly useful, as it complements the range of established optical diagnostics by a technique, viable for remote temperature measurements under high-pressure conditions. It is thus particularly useful for application to short-duration ground test facilities.

3.7 Requirements for elevated enthalpy application

Evidently, a single-shot LIGS success rate of 10-20% in the first test campaign is in clear contrast to a significantly increased success rate of >90% in the second test campaign, which was achieved by a combination of the three facility advancements: buffer pressure vessel cleaning, installation of a hydraulic damping system and installation of flush-mounted optical access windows to the nozzle reservoir, compare [109, 110, 131]. Since all of these technical measures have been carried out in between the first and second test campaign, no single advancement can be identified as the sole or most beneficial factor. Yet, as a success rate of 100% is still not achieved and signal beam detection can further be regarded as a stochastic process (though the likelihood of detection has been increased by almost a magnitude), the installation of optical access windows, effectively avoiding open cavities (and hence strong secondary flow) and significantly decreasing the free laser beam path length through the stagnated and perturbed medium within the nozzle reservoir by a factor of ~6, is regarded to have been the most important technical measure. Nevertheless, the effectiveness of the buffer pressure vessel cleaning [110] and hydraulic damping system installation [109] was clearly demonstrated.

Despite all of these advancements, as yet, the test range of LIGS at the HELM shock tunnel appears to be systematically impaired - although not entirely inhibited. Two main reasons have been identified, based on current experience. On the first hand, the notably increased success rate of >90% in the second test campaign was only achieved at enthalpy levels <2.5 MJ/kg and, more importantly, only for the specific conditions C1-C3 listed herein. Other test conditions - in a similar stagnation pressure and enthalpy range, and despite considerable effort - have not been measured successfully, detecting no useful signal in most cases. It is therefore reasoned by the author that the qualitative stagnation pressure trace at the time of measurement (as the primary indicator of test gas perturbation) is of primary importance for single-shot success. Precisely, the second test campaign is deduced to have been as successful due to a post-reflected shock regime which is very well behaved, indicating a relatively long duration of remarkably steady pressure and very low fluctuations behind the reflected shock. Precisely, most test conditions were identified as either undertailored or overtailored - the latter facilitating a near non-perturbed test environment prior to secondary shock incidence (as resulting from CS reflection), see Fig. 3.7. This is in clear contrast to a highly perturbed test regime in the first test campaign and prior work, compare [62, 107]. On the second hand, the notably increased success rate of >90% in the second test campaign was only achieved at enthalpy levels <2.5 MJ/kg; the latter in fact representing the highest specific enthalpy and temperatures at which LIGS has been successfully used at the HELM facility and - according to the authors best knowledge - elsewhere. Test conditions at higher enthalpy and regardless of the pressure trace (as resulting from under-/over-/tailored CS) could not be measured due to a pollution of the optical access windows, starting at enthalpies >4-5 MJ/kg and becoming further intense for higher enthalpies, see Fig. A.22. FTIR spectroscopy analysis [132] of the coating residuals indicated the latter to contain mainly ferrous oxide due to corrosion. Pollution layers could be mostly removed manually in assembled state by organic chemical solvents such as acetone and petroleum. If coatings are not removed over a series of higher-enthalpy experiments, disassembly and cleaning in an ultrasonic bath become necessary.

3.7.1 Technical recommendations

The main requirements to pave the way for LIGS nozzle reservoir thermometry at higher enthalpies are listed in the following, some being conjectural (deduced from physical reasoning) and not yet entirely confirmed, some being factual due to prior experience:

1. The seeding concentration of NO diluted in N_2 - required for deliberate formation of NO_2 as the primary active species for resonant LIGS excitation -, currently 200-500 up to 1000 ppm, is to be deliberately reduced in order to decrease corrosion of metal surfaces within the ST. Although not being the sole and primary driver for optical window pollution, higher concentrations of NO were evidence to promote surface corrosion, particularly of non-stainless steel components. Whereas the ST is, as yet, entirely seeded with the

required amount of NO/N_2-mixture prior to setting initial pressure p_1 by test gas injection (so as to facilitate uniform seeding concentration), a local injection of tracer gas at the nozzle reservoir section, with the ST already being pressurized with test gas, is regarded beneficial. This step is self-evident, considering LIGS measurements to be only carried out shortly upstream of the ST endwall. For this purpose, two of the five radial access bores are available. Eventually, this will reduce the absolute amount of substance of corrosion-promoting nitric oxides (NO/NO_2) by orders of magnitude, potentially reducing the intensity of optical window pollution.

2. Regardless of the specific enthalpy level, prior results indicated the positive influence of a quasi-steady pressure trend with effectively suppressed fluctuations in the post-reflected shock regime. Hence, the careful fine-tuning of test conditions to a well-behaved pressure development in the nozzle reservoir is considered of utmost importance. Precisely, regardless of the chosen test-/driver gas, the specific test conditions and procedure for FPD driver tuning and CS tailored in the HELM facility developed herein are regarded a key-aspect to gear test conditions to a reflected shock regime, beneficial and conducive to LIGS single-shot measurements.

3. In general, higher stagnation pressure is particularly advantageous - and indeed required - for successfull LIGS measurements, as it compensates the decrease in signal intensity at rising temperatures. In fact, by relating signal intensity at calibration condition (initial ST pressure p_1 and ambient temperature T_1) to stagnation quantities (p_5 and T_5) in the test regime, via Eq. 3.1, a first approximation of expected signal intensity throughout the experiment is feasible. Although the latter is not considered the primary limiting factor herein, careful tuning of the test condition is required, as the resulting signal intensity ratio (throughout experiment and calibration) can vary between $I_{exp}/I_{cal} \sim \mathcal{O}(0.1\text{-}50)$ - depending on calibration pressure p_{cal}, which can be set lower than initial pressure p_1, and NO-seeding concentration. Current experiments were conducted at a minimum ratio $I_{exp}/I_{cal} \sim 1.6$, with calibration at $p_1 = 1.5\text{-}5$ bar.

4. As a matter of fact, all LIGS measurements which have been carried out as yet have only been successful when operating the HELM facility in shock tube model, i.e. with closed endwall. In contrast, effort to conduct measurements - for the otherwise identical test case and parameters - with open endwall, i.e. Mylar diaphragm and subsequent nozzle expansion, have failed. While the exact reason remains unknown so far, it is reasoned that a net bulk velocity of the fluid in the nozzle reservoir - induced by test gas expansion into the downstream nozzle - will result in a net axial displacement of the locally induced density grating, the latter being advected downstream towards the nozzle throat. This assumption is in line with the observation of Schlamp et al. [121] who measured local (static) fluid temperature in a supersonic jet at lower than ambient pressure, where detection of the coherent signal beam - being reflected off the density grating - was only possible by a deliberate (relative) axial displacement of the pump beam focal

point from the interrogation (probe) beam location, the latter being placed further downstream. While this adjustment is evidently possible for a continuously running test rig, adaption in a short-duration, intermittently operated facility - with a single LIGS shot per test run - is considered significantly less feasible. Nevertheless, (reflected) shock processing abides the laws of energy conservation in both cases, regardless of open oder closed endwall. Hence, even though a simultaneous performance of LIGS in situ nozzle reservoir thermometry and free-stream stagnation heat flux measurements (being the established means for experimental-numerical rebuilding of test conditions of short-duration facilities and hence for stagnation enthalpy determination so far) is not easily foreseen by the author, a consecutive performance of two experiments (in shock tube/- tunnel mode) with in situ and ex situ measurements is nevertheless reasoned to eventually yield results of the same physical significance, as if both measurements were carried out simultaneously for a single experiment.

5. At elevated incident shock Mach numbers, shock processing will not only result in higher stagnation pressure and temperature, but test gas density will further increase - all the more when assuming thermo-chemical equilibrium. Accordingly, all coherent laser beams are to be traversed across a gaseous medium of increasing density, which will inevitably result in rising beam deflection (by refraction) at every interface from an optically thin-dense medium and vice versa. Accordingly, finite (static) beam deflection in between the laser beam geometrical pathway at calibration (being carefully adjusted at low pressure and density) to the beam path throughout the experiment (at high fluid density) can be a relevant factor, firstly impairing successful pump and probe beam intersection and secondly inhibiting coherent signal beam detection. In comparison to other sources of error, this point is however regarded of secondary influence.

6. In fact, beam path geometrical tolerance of the optical setup, primarily on the side of the PMT detector, was determined a dominant factor for successfull signal beam detection in the past. Precisely, (geometrically) closely confined pin-hole aperatures are mandatory to effectively separate the dominant, high-intensity pump beams (which similarly exit the measurement volume as probe and signal beam) from a very low-intensity probe beam (too faint for visual perception by the eye). The latter can only be detected by a PMT with high gain, which is however itself easily saturated by stray light from the high-intensity pump beams. As beams prior to grating excitation run in parallel to another before entering the measurement volume, with small relative distance, all beams similarly run close and in parallel to another on the detector side, after having exited the ST. Here, the effective separation of coherent pump beams by geometrical pin-holes and beam dumps and the rejection of spurious stray light by optical band-pass filters (with steep edges and very high/low transmission, Chroma Inc.) allowed for the deliberate increase in pin-hole aperture in the past, see [109]. Accordingly, although having been conducted at higher incident shock Mach numbers and pressures - thus deducing higher conceivable

beam deflection - the significantly increased success rate from the first to the second LIGS campaing is indeed reasoned to - among other reasons - have been enabled by higher geometrical tolerance (allowance of beam deflection) in the detection pathway. Eventually, this point is considered a primary factor to enable successful LIGS measurements at higher shock Mach numbers.

7. Change of the test gas from dry air to nitrogen N_2 or helium/argon mono-atomic noble gas is considered beneficial in the current and elevated test regime in the future, for two reasons. Firstly, deliberate absence of (molecular) oxygen will results in a significantly lowered metal surface oxidation and hence is deduced to mitigate coating of the optical windows by residuals (particulate and gaseous phase) of high-temperature corrosion. The latter will, by trend, increase at higher incident shock speeds, which tend to stir up particles from the tube wall, accumulating in the nozzle reservoir. Here, purely reasoned from ideal gas relations, see Fig. 1.4, the use of mono-atomic test gas will facilitate to yield higher stagnation temperatures T_5 after reflected shock processing for relatively lower Mach numbers, than would be required for a di-atomic gas. At moderate-high enthalpies ≥ 2 MJ/kg, use of mono-atomic gas will effectively avoid dissociation, which will otherwise be inevitable and potentially present another source of error.

8. Finally, purely in the course of measurement technique development, the use of mono-/di-atomic driver gas is regarded as a tradeoff-consideration: on the first hand, mono-atomic driver gas (helium/argon) is required for FPD tuning and hence will enable to effectively mitigate (strong) pressure fluctuations to propagate from upstream to the down-stream nozzle reservoir. For di-atomic driver gas (nitrogen or air), dominant incident secondary pressure waves arising in the driver are inevitable. On the other hand, higher fractions of helium in the driver gas tend to induce high-frequency fluctuations to the test gas, the effect of which on the LIGS success in yet unknown, but not reasoned to be beneficial for evident reason. However, strong pressure flucuations in the nozzle reservoir can thereby be avoided. Accordingly, molecular nitrogen or atomic argon are suggested for the next steps of LIGS development. Further, increase in Mach number via burst pressure and compression ratio - rather than higher helium driver gas fractions - is suggested.

4 Nozzle Free-Stream Characterization

4.1 Hypersonic free-stream calibration

In addition to an a priori prediction of suitable shock tunnel operation conditions, the free-stream test regime at the axisymmetric nozzle exit of any short-duration, high-enthalpy facility is most accurately determined by a dedicated free-stream calibration, which is a standard method in hypersonic facilities worldwide [133, 134]. Of primary interest are the spatial and temporal uniformity, so as to determine size of the core-flow region available for model testing and the quasi-steady test time interval, as well as non-dimensional similarity parameters: Reynolds number, Mach number and stagnation enthalpy, so as to scale viscous effects, compressibility and flow field shape as well as thermo-chemical effects, respectively. This ensemble is required to establish the available test and operation envelope for hypervelocity and hypersonic ground testing. Whereas spatial and temporal flow field uniformity are readily determined from pitot pressure radial distribution, other state properties, such as static pressure and static temperature, density and total enthalpy are not easily measureable. Particularly in case of reflected shock tunnels - employing shock-heating to achieve high total flow enthalpy - thermo-chemical state of the stagnated test gas prior to nozzle expansion is vital for the analysis of (non-)equilibrium effects of the nozzle flow. Here, inaccurate numerical definition of both, nozzle inlet and free-stream quantities can a priori entail large error in the comparison of experimental data and CFD [21, 135]. Therefore, a more accurate determination of caloric quantities within the nozzle reservoir of short duration facilities is highly desirable in order to accurately determine nozzle inlet-conditions and eventually increase the accuracy of calculated free-stream quantities [83].

4.1.1 Shock tube modeling

Typically, total (i.e. stagnation) flow enthalpy of many short duration impulse facilities is determined by 1-D inviscid numerical codes of low computational cost such as CEA [9], ESTC [25], STN [136], CREST [21], based on measured incident shock Mach number (i.e. shock velocity) and assuming 1-D normal shock jump relations. These established tools are commonly employed for analysis of individual experiments and assume quasi-steady conditions after incident shock reflection (i.e. properly tailored-interface conditions), whereas accuracy is however compromised by neglecting viscous effects [21]. In practice, physical 3-D phenomena are more complex due to presence of the shock tube wall boundary layer and endwall-reflected shock bifurcation such that post-reflected conditions in a reflected shock tunnel are prone to

vary over time [137]. Spatial and temporal inhomogeneities of the stagnated test gas in the nozzle reservoir after incident shock reflection off the (often non-planar) ST endwall have been demonstrated by detailed CFD investigations by Tokarcik-Polsky and Cambier [138] and Jacobs [22], who reported on considerable distortion of the otherwise planar shock front due to strong and long-lasting vorticity. In effect, the time interval of constant post-shock temperature (and species concentration) can be smaller than quasi-steady pressure duration (i.e. test time), even in tailored interface mode due to premature driver gas contamination [9, 10]. Along these lines, Hornung [50] suggested operation in overtailored mode to be sometimes necessary. To this end, more complex codes such as L1d [22], Kasimir [23] and Jaguar [139] employ a Riemann solver of quasi-1-D wave dynamics and hence provide for a true time-resolved computation of stagnation quantities, apt to closely capture over- and untertailored conditions, distinct wave phenomena and where viscous boundary layer losses are taken into account. Whereas transient codes typically serve for the in-depth design of test conditions, steady codes are commonly used for the analysis of individual test runs where incident shock speed and Mach number can vary from the design point due to facility inherent shot-to-shot variation [27]. With the exception of [139], both, steady and transient codes predominantly assume global equilibrium thermo-chemistry [9] within the nozzle reservoir after shock reflection, due to high pressures, densities and hence rates of particle collision and recombination [81]. Some codes further account for high-density effects by excluded-volume correction [26, 30]. Still, pressures $p_5(exp)$ measured in the post-reflected shock regime of impulse facilities are typically notably smaller than pressures $p_5(th)$ theoretically predicted by inviscid 1-D normal shock relations [140]. To implicitly account for various loss mechanisms, ESTCj and STN utilize the widespread assumption of an isentropic expansion within the post-shock regime in order to match measured and computed total pressure [128, 140]. Yet, this analogously imposes a decrease in total temperature and enthalpy which may however not be generally justified and entails a level of uncertainty of the stagnated test gas' caloric state as long as the latter cannot be accurately quantified and validated, either by in situ measurement or exact numerical rebuilding.

4.1.2 Nozzle flow simulation

In order to compute free-stream quantities at the nozzle exit, CFD is a powerful tool to determine the holistic ensemble of state and flow quantities, most of which are not available to direct measurement, such as temperature, density and Mach number. Moreover, particularly at high-enthalpy conditions in reflected shock tunnels and in case of high Mach numbers, rapid nozzle expansion ratios give rise to variable degrees of thermo-chemical non-equilibrium (e.g. freezing) which can prevail until the nozzle exit. The effect of even a finite degree of chemical dissociation and thermal vibration within the free-stream of a reflected shock tunnel on blunt body flow and ensuing divergence of flow fields predicted by CFD was demonstrated by MacLean et al. [21] for CO_2 at moderate enthalpy. Results highlighted the importance to account for non-equilibrium thermo-chemistry particularly in case of reflected shock tunnels,

as opposed to expansion tubes which avoid flow stagnation. Besides laminar flow, numerical computations of hypersonic nozzle flow employ a range of turbulence models in order to capture streamwise development of the wall boundary layer which is vital in order to correctly quantify velocity and displacement thickness and hence size of the core flow region and free-stream Mach number, respectively. Chemical and thermal equilibrium and non-equilibrium can be modeled by several finite-rate mechanisms of variable complexity and for a range of species [141]. Established approaches of free-stream computation employ a stepwise approach of concatenated (quasi 1-D) reduced codes to holistically model the relevant gasdynamics of facility operation, such as piston compression, diaphragm rupture, shock propagation, endwall reflection and nozzle expansion [27]. Beyond, mostly hybrid approaches are being used, employing reduced codes exclusively for shock tube modeling and to determine nozzle reservoir stagnation quantities, whereas detailed (2-D axisymmetric/ 3-D) CFD uses these inlet boundary conditions for fully-resolved computation of the nozzle flow [21, 27]. For higher fidelity, incident shock propagation and endwall-reflection within the shock tube itself can be modeled by CFD [76], yet at the expense of higher computational cost and thus being largely limited to analysis of nominal design points rather than individual experiments. Accuracy of such concatenated methods is affected by correct determination of interface boundary conditions whereas exclusive modeling of complex multiphysical phenomena such as shock-boundary-layer-interaction, shock reflection and bifurcation, radiation losses and non-equilibrium nozzle flow may induce uncertainty in the estimated free-stream conditions [2]. Precisely, the accuracy of numerical computations of the nozzle expansion and hence quantification of free-stream quantities by CFD is dictated by the accuracy of physical, thermal and chemical boundary and interface conditions imposed at the upstream domain inlet, particularly the nozzle reservoir.

4.1.3 Free-stream measurements

Direct, high accuracy and time-resolved measurement of the free-stream quantities of interest within the test section (i.e. nozzle exit) of a short duration facility is highly desirable in order to accurately define the duplicated test regime. Whereas stagnation (i.e. pitot) pressure is easily measureable with high accuracy and time resolution, direct measurement of related state quantities such as density, static temperature and Mach number is not as trivial. Free-stream static pressure is considered a key quantity by time-resolved numerical rebuilding methods of test conditions as it is directly measureable by conventional means, characterizes the physical nozzle expansion process [19] and is an indicator of the test gas' thermo-chemical state [13]. Yet, direct measurement by conventional slender lance probes can be technically challenging and requires numerical correction due to viscous effects [142, 143]. Wall temperature, surface and stagnation point heat flux on test bodies are commonly determined by fast coaxial thermocouples, thin film gauges, and advanced gauges such as ALTP [144], respectively. In contrast, detailed information on the thermo-chemical state of the test gas is experimentally only available by means of advanced laser diagnostics. A range of different measurement techniques are useful in the determination of chemical species' individual concentration as well as distinct

quantification of translational, rotational and vibrational temperature. Accuracy of laser diagnostics is limited by noise, specific measurement uncertainty and limited time-resolution of pulsed laser systems [81].

4.1.4 Experimental-numerical rebuilding

A relevant test time interval in short duration facilities is usually defined by the time over which state and flow quantities in the free-stream are quasi-steady and only reflect small variation around a representative mean value. The easiest way to determine the test time interval is based on the temporal development of stagnation (i.e. total) pressure locally in the nozzle reservoir which is directly measureable and reflects the characteristics of under- and overtailored reservoir conditions which thereafter propagate into the downstream test section. However, driver gas contamination finite starting time and flow passing through the nozzle renders test time determination based on free-stream measurements of pitot and/or static pressure more accurate. In order to calculate and monitor all relevant free-stream quantities over the entire time interval of short duration facilities and determine relevant test time from there, numerical rebuilding procedures have been developed which employ measurement of a limited number of experimentally tractable quantities to facilitate time-resolved calculation of all missing parameters. Whereas several of these rebuilding methods exist, they all agree in the correlation of selective flow quantities in the nozzle reservoir (stagnation state prior to nozzle expansion) and the free-stream state (i.e. after nozzle expansion). All methods alike depend on the measurement of free-stream pitot pressure and convective heat flux at the stagnation point of a sphere which are related to stagnation (total) flow enthalpy via alternative theoretical and/or semi-empirical, analytical formulations according to the theory of e.g. Fay and Riddell [32], Verant [20], Zoby [145] and Tauber [146]. Similarly, the nozzle expansion process is either described by assuming a prefect isentropic expansion and utilizing reservoir total pressure [147] or by measurement of free-stream static and pitot pressure alone, without use of any reservoir quantity [19]. Therefore, on the one hand, an advantage of numerical rebuilding methods in general and those which exclusively rely on free-stream measurements in particular is the minimum input required from numerical modelling of upstream, complex flow processes within the shock tube and overall limited use of CFD. On the other hand, rebuilding procedures utilizing fundamental analytical expressions may themselves be limited in terms of enthalpy range and accuracy due to physical and chemical modelling assumptions of underlying theory [2, 32]. Irrespective of any specific approach, rebuilding methodologies in general – and in addition to common measurement of freestream static -, pitot pressure and stagnation point heat transfer – consist of a combination of up to 3 successive stages, namely: (I) numerical and/or experimental determination of stagnation conditions within the nozzle reservoir, (II) numerical simulation or theoretical description of the nozzle expansion as well as (III) numerical simulation of free-stream flow around a reference body (e.g. sphere), see Fig. 4.1.
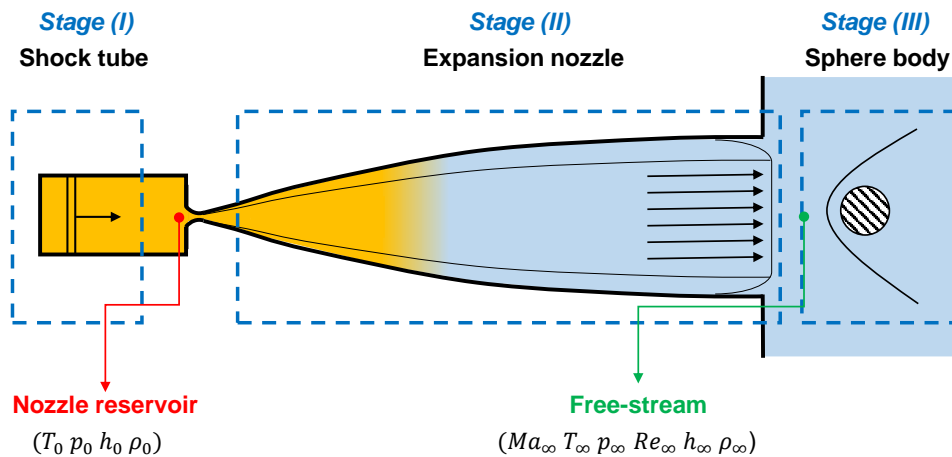
Figure 4.1: Schematic of consecutive stages for numerical-experimental rebuilding procedures for short-duration hypersonic facilities.

Nozzle reservoir based methods

An early holistic method to compute time-resolved free-stream quantities was presented by Simeonides [147] who developed an iterative procedure which utilizes measured values in both, the nozzle reservoir as well as the test section of the VKI longshot tunnel. This method is a two-stage approach, based on stages (I) and (II). The formulation of Fay and Riddell is utilized to relate sphere stagnation point heat flux measured in the free-stream to total flow enthalpy in addition to pitot pressure which is temporally related to reservoir total pressure. This method is distinct from others as the assumption of an isentropic nozzle expansion renders direct measurement of static pressure within the free-stream unnecessary. As total and static free-stream quantities are related by isentropic assumption, accuracy of predicted free-stream variables (such as static temperature, static pressure and velocity) is strongly dependent on accuracy of nozzle exit Mach number determination. Specifically, Grossir [142] demonstrated the isentropic flow assumption to be unsuitable to describe the physical processes of nozzle expansion as – despite negligible (non-)equilibrium thermo-chemical effects and heat losses in the core flow region of a cold gas gun tunnel – strong deviations from measured free-stream quantities ensued: as large as 50% in Reynolds number, 30% in Mach number and 100% in static pressure. In order to circumvent the isentropic assumption, still without measuring static pressure, Vetter [113] suggested to mathematically close the iteratively solved system of conservation equations (mass, momentum, energy) by describing the remaining unknown by free-stream static enthalpy, to be determined by CFD of the nozzle expansion. This approach is, however, evidently recursive as the required nozzle upstream inlet conditions (primarily total enthalpy) are not known a priori but, on the contrary, were to be determined by the rebuiling procedure itself. Vetter [113] resorted to this approach as measurements of static pressure in the TH-2 shock tunnel were unfeasible due to flow divergence at the conical nozzle exit, used at that time. It was hence confirmed that in situ measurement of free-stream static pressure is most suitable to describe the nozzle expansion process [19, 148]. Divergence from isentropic expan-

sion is partially imparted by vibrational non-equilibrium and thermo-chemical freezing of the rapidly expanded nozzle flow due to an altered ratio of specific heats, further affecting static flow quantities (density, pressure, temperature) at the nozzle exit [130, 149]. It is worth to note that any approach temporally relating measurement variables in the reservoir and free-stream (e.g. reservoir and free-stream stagnation pressure) suffers from uncertainty from the temporal correlation of data traces sampled at two distinct locations, which inherently encompass time delay due to nozzle starting flow and transit time.

Free-stream based methods

The first notable and holistic rebuilding method exclusively relying on free-stream measurements was presented by Olivier [19], who makes extensive use of the Fay Riddel theory to relate sphere stagnation point heat flux and flow total enthalpy in order to iteratively solve the mass, energy and momentum conservation equations to calculate the time-resolved free-stream properties within the TH-2 detonation shock tunnel. This is a one-stage approach, based on rebuilding-stage (II) only. To this end, free-stream static pressure is introduced as the single relevant quantity rendering any closure assumption in the relation of reservoir and free-stream quantities unnecessary. Slender lance probes have been proposed to accurately measure free-stream static pressure [143] which have been extensively used in other facilities thereafter such as the VKI longshot tunnel [142] and HEG free-piston shock tunnel [13]. Olivier's numerical rebuilding approach based on Fay Riddel theory was similarly adopted by Grossir [142] who demonstrated superior accuracy of static pressure measurements over isentropic flow assumption. Rebuilding methods using free-stream stagnation point heat flux, pitot (stagnation) pressure and static pressure measurements have since then become the technical standard in some short duration facilities worldwide [136].

Limitations

The theory of Fay and Riddell [32] is of central importance since its advent and in use in a range of rebuilding methods today. The analytical expression is based on the underlying assumptions of binary molecular diffusion, constant thermophysical properties (Prandtl and Lewis number), thermo-chemical equilibrium in the virtual stagnation point at the boundary layer edge, assumption of (non-)catalytic wall and was derived from multiple numerical similarity solutions of the flow around a sphere. The stagnation point tangential velocity gradient is considered the most influential parameter after sensitivity analysis and can be determined from static and pitot pressure as well as shock standoff distance by alternative analytical expressions [19, 150]. According to an extensive review by Gu [2], the use of numerical rebuilding methods employing Fay Riddel theory is limited to low-/ and medium-enthalpy due to non-equilibrium effects and inaccurate stagnation heat flux measurements at elevated to high-enthalpy conditions. Not only to this end has Fay Riddell theory been the model for a range of alternative expressions with the same purpose of relating stagnation point heat flux to total flow enthalpy.

Such formulations of reduced complexity were proposed by e.g. Verant [20, 151], Zoby [145] and Tauber [146], being in use at many hypersonic test facilities worldwide [152]. Whereas the original theory of Fay and Riddell [32] only considered air (diatomic species), theories of Zoby [145], Tauber [146] and Sutton and Graves [33] were developed to cover different gases and mixtures of those. The most general form:

$$\dot{q}_s = k \sqrt{\frac{p_{t2}}{R_N}} \cdot \left(\frac{h_s - h_w}{RT_{ref}}\right)^n \tag{4.1}$$

relates the (sought) driving enthalpy gradient $h_s - h_w$ to measured stagnation point heat flux $\dot{q}_s$ and pitot pressure p_{t2} on a sphere of radius R_N, where either reference experimental or numerical data is fitted via factor k and exponent n: a detailed overview of existing correlations is given by Lettl [153] and Eitelberg et al. [154]. R and $T_{ref} = 273.15$ K denote the specific gas constant and reference temperature.

4.2 HELM Rebuilding procedure

In order to achieve a holistic calibration of the free-stream flow regime at the nozzle exit, two rebuilding procedures proposed in prior literature have been adopted and put to use in the HELM facility. The first method is similar to the approach of Simeonides, which can be used without static pressure measurements and assumes an isentropic and adiabatic nozzle expansion of the test gas. The second methods is similar to the approach of Olivier, making deliberate use of free-stream static pressure measurements by a dedicated slender lance probe in order to avoid any physical/chemical assumption of the nozzle expansion. Both methods developed and implemented in the current work are described in the work of Lettl [153, 155] for the same data set. In agreement with the majority of relevant literature and in order to ensure the best comparability, the Fay-Riddell equation is used to relate (convective) heat flux in the stagnation point of a sphere to total (stagnation) enthalpy:

$$\dot{q}_s = 0.94 (\rho_s \mu_s)^{0.4} (\rho_w \mu_w)^{0.1} \sqrt{\left(\frac{du_t}{dy}\right)_s} (h_s - h_w)\xi \tag{4.2}$$

valid for Pr=0.71. Eq. 4.2 relates the stagnation point heat flux (density) $\dot{q}_s$ to stagnation point enthalpy h_s, where ρ and μ denote static density and dynamic viscosity, respectively. According to the theoretical flow topology illustrated in Fig. 4.2, index w denotes (measureable) wall quantities and index e/s - according to the definition of Fay and Riddell - signifies the (virtual) stagnation point locally at the boundary layer edge, on the stagnation streamline. It is to be pointed out that point e/s is merely theoretically defined in order to allow for an inviscid (isentropic) relation to point 2, directly behind the shock, and can thus be interpreted as a virtual stagnation point on the sphere and if the flow were purely inviscid, as thus sufficiently described by the Euler-equations. In accordance, the term $(du_t/dy)_s$ describes the tangential velocity gradient, locally at the intersection of boundary layer edge and stagnation streamline.
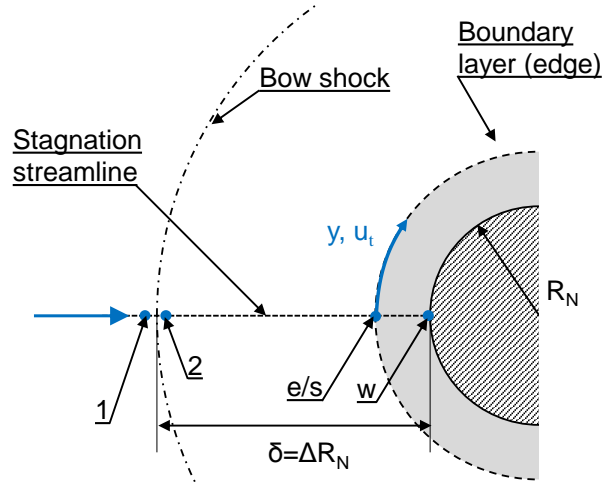
Figure 4.2: Nomenclature and schematic of stagnation point flow topology.

Further, term ξ in Eq. 4.2 scales thermo-chemical state of the boundary layer, where:

$$\xi = 1 + (Le^{0.52} - 1)\frac{h_D}{h_s} \tag{4.3}$$

$$\xi = 1 + (Le^{0.63} - 1)\frac{h_D}{h_s} \tag{4.4}$$

$$\xi = 1 - \frac{h_D}{h_s} \tag{4.5}$$

signify a BL in thermo-chemical equilibrium, frozen BL with catalytic wall and frozen BL with non-catalytic wall (Le=0), respectively. h_D represents the dissociation enthalpy as the sum of specific heats of formation $\Delta_B h_i^0$ (at T=0 K) of species atomic oxygen and nitrogen, weighed by the mass fraction:

$$h_D = \sum_i y_{i,,s} \Delta_B h_i^0. \tag{4.6}$$

In Eq. 4.2 and for a sphere of radius R_N, see 4.2, mathematical formulations of the tangential velocity gradient is one of the largest factors of influence [150], where different (alternative) formulations of varying complexity have been developed and are listed by Oliver [156]:

$$\left(\frac{du_t}{dy}\right)_s = \frac{u_\infty}{R_N} \tag{4.7}$$

$$\left(\frac{du_t}{dy}\right)_s = \frac{1}{R_N}\sqrt{\frac{2(p_s - p_\infty)}{\rho_s}} \tag{4.8}$$

$$\left(\frac{du_t}{dy}\right)_s = \frac{u_2}{R_N}\left[1 + \frac{1 + 0.5(1 + \Delta)^3}{(1 + \Delta)^3 - 1}\right] \tag{4.9}$$

$$\left(\frac{du_t}{dy}\right)_s = \frac{u_\infty}{R_N}\frac{(1 + \Delta)}{\Delta}\frac{(p_s - p_2)}{\rho_\infty u_\infty^2}\frac{\rho_2}{\rho_s}, \tag{4.10}$$

where $\Delta = \delta/R_N$ denotes the (stagnation line) shock standoff-distance and u_2 denotes flow velocity directly behind the bow shock. Whereas the simple Newton model 4.7 is evidently

simplistic, the modified Newton model 4.8 is derived from 1-D momentum conservation, yet does not capture 3-D flow or thermochemical effects. The model of Stokes 4.9 is derived from potential theory, explicitly scales with the shock standoff-distance, yet assumes incompressible flow in between the bow shock and body contour, does not account for non-equilibrium and vorticity. According to Olivier, formulation 4.10 is valid for compressible flow in the presence of vorticity and real gas effects (at high total enthalpy), explicitly scaling the shock standoff-distance and density ratio. Evidently, the most accurate results are obtained when directly measuring the shock standoff-distance in the experiment. In the scope of the current work, however, Schlieren measurements indicated the latter to fluctuate too strong, see Fig. B.1, such that the shock standoff-distance is analytically described according to Oliver [156]:

$$\Delta = \frac{\delta}{R_N} = 0.82\frac{\rho_\infty}{\rho_2}. \tag{4.11}$$

As is highlighted by Gu and Olivier [2] and summarized by Lettl [155], accuracy of the Fay-Riddell-equation is limited by the following assumptions:

- Flow at the (virtual) stagnation point s/e at the BL edge is to be in thermo-chemical equilibrium, requiring (nose) sphere radii sufficiently larger than the relaxation length.

- Free-stream range limited to $450\,\text{Pa} < p_\infty < 37600\,\text{Pa}$, $1770\,\text{m/s} < u_\infty < 7000\,\text{m/s}$, $300\,\text{K} < T_w < 3000\,\text{K}$.

- Only a binary mixture of di-atomic species oxygen and nitrogen is considered - invalidated by onset of ionization.

- Thermophysical properties (Pr, Le) are assumed constant within the BL, inducing error particularly at elevated enthalpy.

- The transport mechanism of thermal diffusion is neglected, causing uncertainty for assumed frozen BL.

- According to Fay and Riddell [32], 40% of total uncertainty in the SP heat flux result from uncertainty on the dynamic viscosity μ_s in the virtual SP. The latter is described by Sutherland's law and significantly affects viscous BL thickness and hence convective heat transfer.

Numerical rebuilding routines developed herein use measured data traces of pitot (stagnation) pressure $p_{t2}(t)$, stagnation point heat flux rate $\dot{q}_s$ as well as either reservoir (total) pressure $p_0(t)$, or free-stream static pressure $p_\infty(t)$ as input. The Fay-Riddell-equation, Eq. 4.2, is used to correlate SP heat flux to total temperature, where wall-quantities ρ_w and μ_w are determined from measured (absolute) temperature $T_w(t)$ by assuming isentropic relations for an ideal gas, in analogy to Vetter and Olivier [19, 113]. Similarly, whereas the latter employ the thermo-chemical equilibrium gas relations of Esser [23], and Grossir et al. [142] describe equilibrium by the VKI Mutation library, the current work employs equilibrium state surfaces according to

CEA [9]. Dynamic viscosity μ for determination of the free-stream Reynolds number, Eq. 1.19, is calculated from Sutherland's law:

$$\frac{\mu(T)}{\mu_{suth}} = (\frac{T}{T_{suth}})^{1.5} \cdot \frac{T_{suth} + C_{suth}}{T + C_{suth}}, \tag{4.12}$$

where reference constants μ_{suth}, T_{suth}, C_{suth} are taken from White [4]. The simple (reservoir-based) method employs reservoir pressure $p_0(t)$ instead of free-stream static pressure $p_\infty(t)$ as input and determines free-stream Mach number $Ma_\infty(t)$ from the Rayleigh-Pitot equation, Eq. 4.13, and total pressure ratio across a normal shock wave, Eq. 4.14:

$$\frac{p_{t2}}{p_\infty} = (\frac{\kappa+1}{2} \cdot Ma^2)^{\frac{\kappa}{\kappa-1}}[1 + \frac{2\kappa}{\kappa+1}(Ma^2-1)]^{-\frac{1}{\kappa-1}} \tag{4.13}$$

$$\frac{p_{02}}{p_{01}} = [\frac{(\kappa+1)Ma_\infty^2}{2+(\kappa-1)Ma_\infty^2}]^{\frac{\kappa}{\kappa-1}} \cdot [\frac{2\kappa Ma_\infty^2 - (\kappa-1)}{\kappa+1}]^{-\frac{1}{\kappa-1}}, \tag{4.14}$$

where total pressure in front of an behind the shock, $p_{01}(t) = p_0(t)$ and $p_{02}(t) = p_{t2}(t)$, equal measured reservoir and pitot pressure, respectively, due to isentropic assumption. All other relevant quantities, such as static temperature, enthalpy, density, absolute velocity - and hence mass- and momentum-flow - are henceforth derived based on the isentropic assumption. Evidently, this idealization will induce large error in the presence of viscous losses and residual thermo-chemical effects in the free-stream, as was shown by Grossir [142].

The second method thus uses measured free-stream static pressure instead of reservoir pressure and hence deliberately avoids the relation via isentropic assumption. Instead, the conservation equations of mass, momentum and energy are arranged as suggested by Olivier [19] and solved iteratively:

$$u_2 = \rho_\infty u_\infty \frac{RT_s}{p_{t2}} \tag{4.15}$$

$$\rho_\infty u_\infty = \frac{p_{t2}}{RT_s}\sqrt{2(h_0 - h_\infty)}(1 - \sqrt{1 - \frac{RT_s}{p_{t2}}\frac{p_{t2} - p_\infty}{h_0 - h_\infty}}) \tag{4.16}$$

$$\rho_\infty u_\infty^2 = 2\frac{p_{t2}}{RT_s}(h_\infty - h_0)(1 - \sqrt{1 - \frac{RT_s}{p_{t2}}\frac{p_{t2} - p_\infty}{h_0 - h_\infty}}). \tag{4.17}$$

The system of equations is efficiently solved numerically by the secant method (root-finding algorithm) proposed by Simeonides [147]. For every time step in the total data trace to be processed, initial (start) values are set for total temperature T_0 in case of the reservoir-method (w/o static pressure) and for free-stream Mach number Ma_∞ and total temperature T_0 in case of the free-stream method (w/ static pressure). Furthermore, depending on the specified tangential velocity gradient, Eq. 4.7-4.10, an additional starting values for u_2 is required. Total quantities in the reservoir (prior to nozzle expansion) are determined by CEA according to:

$$(h_0, \rho_0) = f_{CEA}(T_0, p_0) \tag{4.18}$$

and for the stagnation point according to:

$$(h_s, \rho_s, y_{O_s}, y_{N_s}) = f_{CEA}(T_s, p_{t2}),$$ \hfill (4.19)

where $h_s = h_0$ reflects total enthalpy to be conserved, whereas $T_s < T_0$ indicates total tempera-
ture in the stagnation point (s) to be generally lower than in the reservoir (0). Precisely, as pitot
(stagnation) pressure $p_{t2} \sim \mathcal{O}(1\,\text{bar})$ will be around 2 magnitudes lesser than reservoir pressure
$p_0 \sim \mathcal{O}(100\,\text{bar})$, the dissociation degree in the stagnation point will be of magnitudes greater
than in the reservoir $\alpha_s \gg \alpha_0$, such that the dissociation enthalpy will be greater $h_{D_s} > h_{D0}$, en-
tailing lower remaining thermal (translational) fraction h_{tr} and hence translational temperature
$T_s(h_s, p_{t2}, \alpha_s) > T_0(h_0, p_0, \alpha_0)$. In every step of the iteration loop, the dissociation enthalpy h_{D_s} in
the Fay-Riddell-eq., Eq. 4.2, is determined from dissociated species mass fraction according to
4.6, where:

$$y_{i_s} = f_{CEA}(T_s, p_{t2})$$ \hfill (4.20)

in the (boundary layer edge) stagnation point s/e. Convergence is reached based on iterative
variables T_0, Ma_∞, u_2, $(du_t/dy)_s$ and h_∞, respectively. Detailed flow charts for both variants of
the iteration algorithm are given by Lettl [153, 155].

4.3 Measurement techniques

4.3.1 Calibration rake

Total (stagnation) pressure in the nozzle reservoir and prior to nozzle expansion is measured by
piezoelectric pressure gauges (PCB Inc., type 109C11) suitable for high-enthalpy, high-pressure
applications. Measurements of free-stream flow quantities throughout the experiments are con-
ducted by means of a conventional test rake. The latter is instrumented with a set of radially
staggered piezoelectric pressure sensors (PCB Inc., type 113B28) for temporally- and spatially-
resolved acquisition of pitot pressure across the nozzle cross section as well as two slender
lance probes for measurement of static pressure at the nozzle exit, used within the free-stream
rebuilding procedure. Spherical probes of different diameter facilitate measurement of stagna-
tion point heat flux at three different radial locations. A photograph of the instrumented test
rake is given in Fig. 4.3. The calibration rake is designed such that sampling locations of all
probes (pressure and temperature/ heat transfer) are located within the same radial plane and
at identical axial distance from the nozzle exit plane.

4.3.2 Static pressure probe

Static pressure at the nozzle exit is a flow quantity of primary importance in the characteriza-
tion of the hypersonic nozzle expansion process as well as to quantify and distinguish thermo-
chemical (non-)equilibrium states within the free-stream. Here, due to very small static pres-
sure magnitude after nozzle expansion, the difference in static pressure between equilibrium
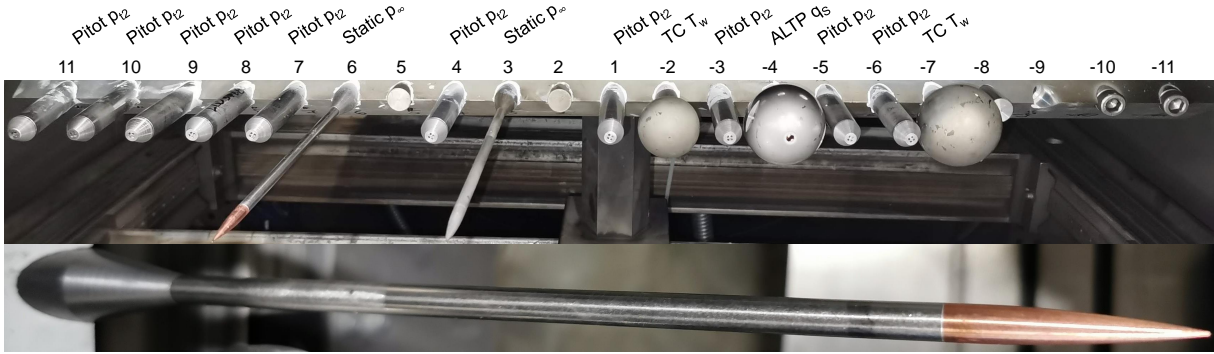
Figure 4.3: Top: Photograph of the instrumented test rake employed for free-stream measurements in the HELM facility. Bottom: Close-up view of the slender lance probe employed for static pressure measurements.

and non-equilibrium test flow can be as low as 100-200 Pa absolute or 10% relative to nominal static pressure [13]. Considering time-resolved measurement of static pressure to be the single measured free-stream quantity to distinguish more accurate free-stream rebuilding methods [19] from less-accurate reservoir methods [147], the latter is to be sampled with highest-possible accuracy and low uncertainty, such as to accurately describe the nozzle expansion and hence to yield accurate prediction of free-stream quantities. For this purpose, an extensive review of static pressure probe geometries and suitable pressure gauges described in prior literature [142, 143, 156–158], (formerly) being in use at short-duration facilities worldwide has been carried out in the work of Groll [159] and Theisen [160]. Based on this work, a slender lance probe was designed herein to best fulfill all requirements for use in the HELM shock tunnel. The probe is made from a stainless steel (DIN EN 10216-5 / 1.4571) hydraulic tube with 6mm diameter of the cylindrical section and measures a total length of 170 mm. The nosepiece is made from a chromium-zirconium-copper alloy (DIN EN CW106C / 2.1293) in order to prevent ablation and withstand mechanical load - so as to retain its geometry and nose radius - due to high thermal conductivity and transient heat flux resistance. Precisely, for assumed constant heat flux $\dot{q}_w$, the time for surface temperature to reach the material's melting point (i.e. temperature difference ΔT) scales with the thermophysical properties of density ρ, heat capacity c_p and thermal conductivity k [161] according to:

$$t \propto \Delta T^2 \rho c_p k. \tag{4.21}$$

The conical nosepiece is machined according to a polynomial shape geometry to provide for a smooth tangential transition from the $\varnothing 0.2$ mm nosetip to the cylindrical body. Wall static pressure is sampled at an axial distance L/D 23 downstream of the nosetip by a single pressure gauge (Kulite Inc., type XCQ-093-abs.) via 4 holes ($\varnothing 1$ mm w/o chamfer), staggered 90° in circumferential direction from one another in order to compensate for possible probe misalignment by hydraulic averaging. Due to low-density (i.e. Reynolds number) and high-velocity (i.e. Mach number) freestream, viscous interaction between hypersonic inviscid flow and viscous wall boundary layer displacement becomes important. Due to an overexpansion at the

geometrical transition from conical to cylindrical probe section, sampled wall pressure at the downstream measurement location is typically lower than static pressure of the unperturbed freestream flow [13, 162]. A common underprediction of below 5% at test locations L/D~20 in the experiment is corrected for each individual test condition by dedicated CFD simulation of viscous flow around the lance probe, for the relevant, expected freestream conditions and Reynolds- and Mach number regime, compare [142]. The newly devised HELM static pressure probe thus satisfies all recommendations from literature:

1. An axial distance of L/D~16-32 is recommended to ensure BL egalization and sufficiently wall-parallel streamlines.

2. Nose radii R/D~0.05-0.08 are recommended as a trade-off between minimized flow disturbance and resistance to thermo-mechanical loads of an attached shock wave.

3. Chamfer of radial pressure-communicating bores is of secondary importance.

4. Recessed mounted pressure sensors suffer from viscous attenuation, time delay and thus low bandwidth, such that sensor mount directly at the pressure bores is imperative.

5. Mechanical stiffness is mandatory in order to avoid noise from mechanical vibration, thus favouring a mechanically integral design over (screwed) assemblies.

6. Due to very large aspect ratios L/D~30, slender lance probes are to be accurately aligned with the flow field, not tolerating for angles of attack >2°.

A technical drawing of the slender lance probe geometry is given in Fig. B.2.

Static probe calibration

As is pointed out, very low static pressure magnitudes ~1000-5000 Pa are expected at the nozzle exit for a typical ST test run, where relative amplitudes of ~100-200 Pa are required to be accurately resolved in order to distinguish test gas thermo-chemical (non)-equilibrium. Accordingly, suitable low-amplitude pressure instrumentation is required which further necessitates for dedicated calibration in the low-pressure regime. Thus, in order to facilitate high-accuracy measurements of freestream static pressure, a similar test and calibration procedure as proposed by Grossir et al. [142] is utilized. Precisely, a fast response, absolute pressure gauge (Kulite Inc., type XCQ-093-abs.) of amplitude range ±1.7 bar was deemed appropriate. Though the latter is far higher than the relevant static pressure range to be measured, intermittent over-pressure due to (reflected) pressure waves within the test section and dump-tank (throughout and after the experiment) is to be sufficiently lower than twice the nominal range, so as to not induce changes to the calibration curve (plastic deformation of the MEMS diaphragm). Evidently, the manufacturer-provided (linear regression and static offset) calibration is thus not suitable for the amplitude range required herein. A dedicated and individual probe calibration has thus been carried out, a schematic is provided in Fig. B.3, see Lettl [153,

155] for details. Precisely, the test section is hermetically closed with a sealed lit, in order to minimize leakage from ambient, and evacuated to a minimum achieved absolute pressure of 5.7 Pa as (referenced) starting point. The latter is accurately measured with an absolute pressure gauge (WIKA GmbH, type CPT6400) of nominal range 250 mbar, which was deliberately calibrated (NIST-/DIN EN - traceable) for low absolute pressure (range 0.1-500 Pa) and ± 2 Pa conservative accuracy by the manufacturer. A low-volume reference pressure vessel is attached to the test section and initially evacuated to the identical reference pressure of 5.7 Pa, and henceforth detached from the test section by a vacuum valve, so as to retain the reference pressure. Throughout the calibration procedure, primary pressure sensors (Kulite XCQ-093, already mounted in slender lance probes) are exposed to an absolute (static) pressure increase in the test section by deliberately venting the latter, at a controlled pressure increase rate, to facilitate a pressure increase of 7000 Pa over a time interval of 5 minutes. Over this relevant pressure range, a dedicated reference (differential) pressure gauge (Kulite XCQ-062) captures the pressure difference between the test section and the initially evacuated reference pressure volume. The latter is itself accurately calibrated by a dedicated pressure calibrator (GE Inc., DPI 612 pFlex) with two low-amplitude differential pressure modules PM 620 of range 2500 Pa (± 2.5 Pa, $\pm 0.1\%$ FS) and 7000 Pa (± 3.3 Pa, $\pm 0.047\%$ FS), absolute and relative accuracy, respectively. By correlation of (differential) reference sensor reading and (absolute) static sensor signal at known initial pressure, accurate calibration curves for both slender lance probes were formulated. The latter were obtained from non-linear regression fitting via a polynomial of degree 10-15 in the non-linear region up to < 2500 Pa, while data points in the range 2500-7000 Pa are sufficiently described by a linear regression. Calibration curves for both probes employed herein are illustrated in the appendix, see Fig. B.4. Leakage rates in between both pressure vessels and from ambient over the calibration duration are separately measured and accounted for, see Lettl [155] for details. Notably, if a dedicated non-linear calibration at low absolute pressures had not been carried out, sensor signal evaluated by the manufacturer-provided sensitivity and offset would measure a pressure of $\sim$-240 Pa, at a factual pressure of 5.7 Pa: this observation highlights the importance and validity of the current approach, further justifying the significant effort.

4.3.3 Heat transfer measurements

Both rebuilding procedures developed herein use time-resolved heat flux in the stagnation point of a sphere for correlation to total flow enthalpy via the Fay-Riddell-equation, Eq. 4.2. For this purpose, spherical probes of different diameter (D_N=38.1 mm and 50.0 mm) are placed at three different radial distances from the nozzle symmetry axis, so as to measure heat flux in the core flow region and further towards the free shear flow, momentum-deficit region in the wake of the nozzle wall boundary layer. Due to dependence of the stagnation point tangential velocity gradient and bow shock standoff-distance on the sphere radius, measured heat flux magnitude in the experiment varies for individual probes. Both are accounted for by complementary CFD simulations of free-stream flow around the spherical probes. In the current work,

stagnation point heat flux is acquired by two separate means: indirectly and directly. In the first case, fast-response coaxial thermocouples (SWL RWTH-Aachen, type-E) are being used to acquire the transient wall (i.e. surface) temperature rise, which is employed as boundary condition for calculation of time-resolved surface heat flux by assuming transient conduction into a semi-infinite body and only considering 1-D heat flux normal to the surface. For brevity, the numerical routine (based on 1-D transient heat transfer theory) used for thermocouple temperature data processing is described in the appendix B.1.3. In general, coaxial thermocouples are less prone to influence from high-temperature, high-speed particle impact than other kinds of sensors such as thin film gauges [163]. Calculation of instantaneous surface temperature from voltage signal employs non-linear correlation of NIST (NIST ITS 90) and DIN (DIN EN 60584-1) discretized reference data via a least-squares fitted rational function [164]. A similar approach is chosen for cold temperature compensation, which is required as the ambient temperature (measured via a thermomometer of ± 0.1 K accuracy) is used as reference temperature, rather than a 0°C ice bath. Thermophysical properties of each thermocouple, such as density, thermal conductivity and specific heat capacity $\sqrt{\rho c k}$ are individually calibrated by the manufacturer in order to ensure high fidelity of surface temperature and heat flux measurements by thermocouples. In the second case, time-resolved heat flux is directly measured by the use of ALTP (atomic layer thermopile) sensors, which exploit the transverse Seebeck effect. Thin film thicknesses of 500-700 nm grant high analog bandwidths (300 kHz w/ protective coating, 1 MHz w/o coating) while providing a linear voltage output over ranges $0.1 \, \text{W/m}^2$-$200 \, \text{MW/m}^2$ [165], having facilitated stagnation point heat transfer measurements in the past [144]. ALTP sensors used herein are individually calibrated by the manufacturer, with 5-10% stated uncertainty. In order to yield a high level of consistency within the measurement and calculation of stagnation point heat flux, thermocouples located at the sphere stagnation point are equipped with a central bore such as to enable coincident pitot pressure measurements on the identical probe (via a piezoresistive Kulite XCQ-093).

4.3.4 Data acquisition

Throughout facility operation, static and dynamic pressure traces are acquired at a sampling rate of 1 MHz via the TransCom-X-XL2 transient recorder, with 14-bit and 16-bit ADC amplitude resolution. Piezoresistive (Kulite) pressure gauges use a 10 VDC supply voltage and are amplified at gain 200 (AC-coupling) by an analog signal amplifier (Dewetron GmbH, HSI-STG-D) with deliberate Bessel-type analog low-pass filtering at 300 kHz cutoff (-3 dB). Absolute (static) and pitot (stagnation) pressure sensors are off-set corrected by the reference (static) pressure $\sim$30 Pa (measured via WIKA CPT6400) in the test section at the onset of the experiment. Thermocouple signals are analog amplified by gain 200 (DC-coupling) with a 100 kHz LP-filter cutoff. ALTP-sensors deliberately use a constant (lead acid) battery supply voltage (12.4 VDC) in order to avoid any source of power supply fluctuation. ALTP-signals are subjected to analog amplification (1 MHz analog bandwidth) by a manufacturer supplied, dedicated amplifier: high DC signal magnitudes of stagnation point heat flux necessitate for the lowest-possible,

pre-defined gain of 1000 - in fact, even this setting resulted in saturation (amplifier clipping), such that - even though the ALTP-sensor (w/ coating) itself maintained operational - no useful signal was obtained for enthalpies >4 MJ/kg. It is to note that - though not of interest in this work - the AC-signal of ALTP-sensors uses a fixed gain of 5000, dictated by the amplifier. Finally, in order to reduce the effect of noise on the numerical-experimental rebuilding routines, pitot-, static-pressure and thermocouple data traces are digitally filtered (5-10 kHz cutoff) as required.

4.4 Reference rebuilding conditions

In order to validate the current numerical-experimental rebuilding approach prior to application to a test run in the HELM facility, a sanity check was carried out by comparison to relevant literature reference values. Precisely, three test conditions in total, one of the detonation driver shock tunnel TH2 at RWTH-Aachen University, two of the piston driver shock tunnel HEG at DLR Göttingen, state quantities in the free-stream and reservoir of which are comprehensively documented in open literature, are defined as reference cases. Reference values of the HEG are taken from Eitelberg et al. [24, 154], who listed state quantities at the nozzle exit for (former) HEG test conditions I and III while comparing stagnation point heat flux rates (measured on a sphere R_N=0.01 m) against different heat flux correlation, among them the Fay-Riddell-equation. As for the TH2 facility, the state properties listed by Vetter [113] and Olivier and Grönig [166] for low-enthalpy condition DI is taken as a reference, where stagnation point heat flux is similarly measured on a sphere R_N=0.01 m. Since time-resolved data was not available, all reference quantities are time-averaged values as listed in primary literature, with input quantities being listed in Tables 4.2-4.3.

Table 4.1: Input quantities for current rebuilding routines, applied to reference conditions I and III of the HEG and DI of the TH2 shock tunnel.

Reference condition	p_0 [bar]	$\dot{q}_s$ [MW/m^2]	p_{t2} [bar]	p_∞ [Pa]	R_N [m]
TH2 DI	273	3.4	1.84	2270	0.01
HEG I	390.6	16.24	0.5	520	0.01
HEG III	467.9	11.15	0.6	640	0.01

Evidently, for condition TH2-DI, Table 4.2, overall excellent to fair agreement with stated reference quantities is reached by both rebuilding procedures implemented herein. Depending on the definition the tangential velocity gradient, total caloric quantities h_0 and T_0 are captured within minimum -0.25% to maximum 8.54% - this observation applies to both methods, reservoir (R) and free-stream (FS) alike. In general, the latter approximates stated static free-stream quantities much more accurately than the former: this applies to u_∞, ρ_∞, T_∞, where deviation of R to TH2-DI reference is up to magnitudes greater than relative deviation of FS, for all tangential velocity gradients alike. Particularly free-stream Mach number Ma_∞ is captured within

Table 4.2: Output quantities (absolute) for different rebuilding methods and relative deviation of current rebuilding routines, each from listed reference quantities of TH2-condition DI. FS and R denote free-stream (w/ static pressure) and reservoir (w/o static pressure) rebuilding method, respectively. Three definitions of the tangential velocity gradient are compared: Oliver, modified Newton and Stokes. Calculations assume an initial wall temperature $T_w = 300$ K.

Reference / rebuilding	h_0 [MJ/kg]	T_0 [K]	T_∞ [K]	ρ_∞ [kg/m^3]	u_∞ [m/s]	Ma_∞ [-]	Re_∞ [1/m]	T_s [K]
TH2 DI	2.4	2107	180	0.0436	2120	7.9	7.60E6	-
FS (Olivier)	2.47	2142	184	0.0429	2136	7.91	7.40E6	2139
Δ [%]	2.75	1.67	2.39	-1.61	0.74	0.13	-2.63	-
FS (New.mod.)	2.61	2245	195	0.0406	2195	7.91	6.86E6	2239
Δ [%]	8.54	6.55	8.24	-6.88	3.54	0.13	-9.74	-
FS (Stokes)	2.39	2082	178	0.0444	2101	7.91	7.75E6	2080
Δ [%]	-0.58	-1.17	-0.97	1.83	-0.9	0.13	1.97	-
R (Olivier)	2.39	2088	138	0.0508	1980	8.42	1.06E7	2086
Δ [%]	-0.25	-0.88	-23.53	16.51	-6.62	6.58	39.45	-
R (New.mod.)	2.60	2240	148	0.0474	2050	8.42	9.58E6	2234
Δ [%]	8.25	6.32	-17.98	8.72	-3.29	6.58	26.05	-
R (Stokes)	2.30	2021	133	0.0525	1948	8.42	1.11E7	2020
Δ [%]	-4.0	-4.08	-26.00	20.41	-8.14	6.58	46.32	-

0.13% when considering free-stream static pressure, as opposed to 6.58% deviation when neglecting the latter. Accordingly, considering a much more accurate approximation of T_∞ and ρ_∞, due to impact on calculated viscosity by Eq. 4.12, the FS-method approximates the unit Reynolds number Re_∞ within a deviation of +2/-10%, in contrast to 26-46% over-prediction by the R-method. Thence, it is deduced that both methods present plausible approximations of stated reference quantities for condition TH2-DI, which are physically sane. As was initially expected, relative deviation clearly indicates the FS-method, with explicit use of static pressure, to be a much more accurate approximation of factual free-stream quantities than the R-method, which neglects static pressure. Finally, based on a deviation within 0.13-2% from the complete set of reference quantities, of magnitudes smaller than for other combinations of rebuilding methods and velocity gradient definition, the TH2-DI condition is best approximated by the FS-method with use of Stokes' velocity gradient, Eq. 4.9, where the shock standoff-distance $\Delta = \delta/R_N$ is calculated according to Eq. 4.11. As this is the identical combination employed for analytical modeling in the original work of Vetter [113], the current rebuilding methods are hence proven to be physically exact and the numerically implementation to be correct. For the sake of completeness, even though not provided as TH2-DI reference, total temperature in the stagnation point T_s is listed for the current methods. The latter is generally smaller than total temperature in the reservoir T_0, with relative deviation -0.1/-0.3% reflecting negligible or only incipient degree of dissociation for air, which agrees with the stated total enthalpy and temperature level.

Reference quantities and comparison to current rebuiling results for the medium-enthalpy con-

dition III and high-enthalpy condition I of the HEG are given in Tables 4.3 and 4.4, respectively.

Table 4.3: Output quantities (absolute) for different rebuilding methods and relative deviation of current rebuilding routines, each from listed reference quantities of HEG-condition III. FS and R denote free-stream (w/ static pressure) and reservoir (w/o static pressure) rebuilding method, respectively. Three definitions of the tangential velocity gradient are compared: Oliver, modified Newton and Stokes. Calculations assume an initial wall temperature $T_w = 300$ K.

Reference / rebuilding	h_0 [MJ/kg]	T_0 [K]	T_∞ [K]	ρ_∞ [kg/m³]	u_∞ [m/s]	Ma_∞ [-]	Re_∞ [1/m]	T_s [K]
HEG III	12.9	7185	612	0.0035	4757	9.44	5.43E5	-
FS (Olivier)	12.82	7148	867	0.0026	4888	8.51	3.30E5	5555
Δ [%]	-0.65	-0.51	41.63	-26.78	2.75	-9.85	-39.23	-
FS (New.mod.)	12.23	6954	830	0.0027	4784	8.51	3.47E5	5455
Δ [%]	-4.83	-3.22	35.56	-23.36	0.57	-9.85	-36.01	-
FS (Stokes)	14.48	7685	982	0.0023	5194	8.51	2.87E5	5809
Δ [%]	12.22	6.96	60.38	-35.33	9.19	-9.85	-47.15	-
R (Olivier)	11.14	6517	218	0.0051	3557	12.01	1.28E6	5196
Δ [%]	-13.64	-9.29	-64.31	46.44	-25.22	27.22	135.36	-
R (New.mod.)	12.25	6943	233	0.0048	3672	12.01	1.18E6	5449
Δ [%]	-5.07	-3.37	-61.98	37.61	-22.82	27.22	116.39	-
R (Stokes)	11.84	6791	228	0.0049	3631	12.01	1.21E6	5364
Δ [%]	-8.20	-5.48	-62.81	40.74	-23.66	27.22	122.84	-

Overall, stated HEG reference quantities are less well aproximated by both current rebuilding methods, than the TH2-DI low-enthalpy condition. However, as was previously noted for TH2-DI, the FS-method (w/ static pressure) similarly yields notably better agreement than the R-method (w/o static pressure) in terms of free-stream similarity parameters Ma_∞ and Re_∞. Precisely, for condition HEG-III and all three tangential velocity gradients alike, FS-method yields a consistent deviation of -9.85% for Ma_∞, opposed to consistent deviation 12.01% of the R-method. Overall poor agreement is achieved in terms of Re_∞, with varying underprediction of -36/-47% by the FS-method and varying overprediction of 116/135% by the R-method. The same trend is observed for high-enthalpy HEG-I condition, FS-method consistently underpredicting Ma_∞ by -10.5% (as opposed to 12.0% overprediction by R-method), while Re_∞ is underpredicted by -43/-61% by the FS-method (as opposed to 131/149% overprediction by the R-method). It is worth to note that for both conditions HEG-I and HEG-III, consistent underprediction of both, Mach- and Reynolds-number, by the FS-method and consistent overprediction of both variables by the R-method is evident to directly result from its dependence on free-stream (static) density and (static) temperature: $Ma_\infty \propto T_\infty^{-1/2}$ and $Re_\infty \propto \rho_\infty$. Specifically, this trend is caused by a consistent underprediction of static density ρ_∞ and overprediciton of static temperature T_∞ by the FS-method and - exactly opposed - consistent overprediction of ρ_∞ and underprediction of T_∞ by the R-method. Even though a (minor) consistent overprediction of free-stream velocity u_∞ by the FS-method and major consistent underprediction of u_∞ by

Table 4.4: Output quantities (absolute) for different rebuilding methods and relative deviation of current rebuilding routines, each from listed reference quantities of HEG-condition I. FS and R denote free-stream (w/ static pressure) and reservoir (w/o static pressure) rebuilding method, respectively. Three definitions of the tangential velocity gradient are compared: Oliver, modified Newton and Stokes. Calculations assume an initial wall temperature $T_w = 300$ K.

Reference / rebuilding	h_0 [MJ/kg]	T_0 [K]	T_∞ [K]	ρ_∞ [kg/m^3]	u_∞ [m/s]	Ma_∞ [-]	Re_∞ [1/m]	T_s [K]
HEG I	21.21	9085	807	0.0019	5939	9.63	3.11E5	-
FS (Olivier)	21.07	9059	1406	0.0013	6270	8.62	1.59E5	6401
Δ [%]	-0.66	-0.28	74.18	-32.81	5.58	-10.49	-48.87	-
FS (New.mod.)	19.18	8721	1277	0.0014	5982	8.62	1.77E5	6249
Δ [%]	-9.59	-4.01	58.24	-26.04	0.73	-10.49	-43.09	-
FS (Stokes)	27.22	9970	1823	0.0001	7126	8.62	1.20E5	6835
Δ [%]	28.33	9.74	126.0	-48.23	19.98	-10.49	-61.41	-
R (Olivier)	17.24	8324	279	0.0034	4020	12.01	7.73E5	6075
Δ [%]	-18.73	-8.37	-65.46	75.00	-32.31	24.71	148.55	-
R (New.mod.)	19.13	8711	292	0.0032	4113	12.01	7.30E5	6245
Δ [%]	-9.82	-4.11	-63.85	67.19	-30.75	24.71	134.73	-
R (Stokes)	19.60	8801	295	0.0032	4134	12.01	7.20E5	6285
Δ [%]	-7.58	-3.13	-63.48	65.10	-30.40	24.71	131.51	-

the R-method acts opposed to the former mechanism, the latter is observed to be of secondary influence only.

As for total caloric quantities h_0 and T_0 of both conditions HEG-I and HEG-III, the latter are consistently underpredicted (by trend) for all combinations of rebuilding method and velocity gradient. Nevertheless, all reference values are, evidently, best matched by the combination of FS-method and velocity gradient according to Olivier: with a relative deviation of consistently well below 1%. This observation is all the more notable, since - according to Eitelberg et al. [133] - listed HEG reference quantities make use of the modified Newton velocity gradient instead.

Eventually, for all three reference test conditions available, TH2-DI and HEG-I/III, the current results reflect a physically plausible relation between (stagnation point) total temperature T_s and (reservoir) total temperature T_0. Precisely, T_s is determined to be up to 30% lower than T_0 for high-enthalpy test condition HEG-I ($h_0 = h_s \sim 20$ MJ/kg), around 20% lower for medium enthalpy condition HEG-III (~ 13 MJ/kg) and finally found to coincide with $T_s = T_0$ for low-enthalpy condition TH2-DI (~ 2 MJ/kg). This observation reflects the physical trend of total (translational) temperature to gradually decrease at rising degrees of dissociation α (and dissociation enthalpy h_D) - as in the case of the free-stream flow brought to rest in the stagnation point of an intrusive probe, where a notably lower stagnation- than total (nozzle reservoir) pressure $p_s \ll p_0$ induces a much higher degree of dissociation $\alpha_s \ll \alpha_0$, imparting a lower stagnation temperature $T_s < T_0$. Consistency of current results with this physical mechanism corroborates the validity of thermo-physical modeling and correct numerical implementation

in the scope of both current rebuilding routines. Eventually, the by far largest relative deviation of up to 150% in Tables 4.2-4.4 is observed for FS Reynolds number Re_∞, which is attributed to different approaches for calculating dynamic viscosity. In the current work and - due to remarkably low relative deviation - potentially also in the case of condition TH2-DI, the Sutherland's law, Eq. 4.12, is used for simplicity. Evidently, considering the relative deviation of other predicted state quantities to be of magnitudes lower than that of Reynolds number (and hence viscosity), conditions HEG-I and HEG-III have made use of a different and more in-depth viscosity model. This fact does however not invalidate any of the aforementioned conclusions, considering Reynolds number to be only a dependent variable in the current rebuilding procedures.

4.5 CFD Simulation

Despite the fact that (non-)equilibrium states can be distinguished in principle by free-stream static pressure measurements, all rebuilding procedures considered herein fall short to explicitly quantify residuals of thermo-chemical excitation after nozzle expansion: such as dissociation degree, species mole fraction and thermal non-equilibrium (rotational, vibrational) temperatures. Accordingly, an accurate and satisfactory determination of free-stream quantities of a short-duration hypersonic ground test facility can only be achieved by the deliberate combination of in situ measurements at the nozzle exit with detailed CFD simulation of the nozzle flow. In analogy to the consecutive steps of free-stream rebuilding, Fig. 4.1, a three-tier approach has been devised in order to systematically simulate test gas expansion through the current HELM Mach 8 conical expansion nozzle, downstream establishment of the free-stream flow field in the test section and external flow past intrusive probes used within calibration experiments. In order to capture thermo-chemical real gas effects of the stagnated test gas, numerical RANS (Reynolds-averaged Navier-Stokes) simulations are conducted by the non-commercial finite-volume flow solver NSMB (Navier-Stokes Multi Block) [167]. Based on the geometry, numerical meshes for the conical expansion nozzle, expansion nozzle and downstream test section, and slender lance/ spherical stagnation probes were devised in the consecutive work of Hesse [168], Zoll [169], Kröger [170, 171] and Theisen [160, 172, 173]. Selected test cases are simulated by NSMB and henceforth compared to experimental measurements and results from experimental-numerical rebuilding methods in order to lay the foundation for a detailed calibration of the HELM facility's test conditions.

4.5.1 NSMB Code

NSMB is a parallelized, compressible, 3-D, full Navier-Stokes solver, capable of steady and transient simulations, using higher-order discretization schemes and multi-grid approach - details of the code are listed by Hoarau et al. [167]. For hypersonic applications, real gas (finite rate) thermo-chemistry is incorporated by several numerical models and for different number of species, among them the established non-equilibrium 5-species model for air by Park

[174] used herein. Thermal non-equilibrium is described by the Landau-Teller model for the translational-vibrational energy exchange, with relaxation time from the semi-empirical formula of Millikan and White [175]. While other models are available, thermo-physical quantities in NSMB simulations conducted herein are calculated according to the model of Blottner [176]. While a range of simple to more complex turbulence models with different number of transport-equations is available, preference - in the scope of the current work - is given to the one-equation model of Spalart-Allmaras [177], which was successfully used for simulation of the wall-bounded hypersonic nozzle flow of the HEG shock tunnel [13]. The two-equation k-ω and k-ω-SST models [178] are deemed more suitable for wall-bounded flow around the intrusive free-stream probes [172], whereas the k-ε-model proved more accurate for unbounded free-shear flow, where the wall BL locally detaches at the nozzle exit to form the free-stream flow field [171]. The RANS governing equations solved by NSMB and details of thermo-chemical models are listed in the appendix B.2.

4.5.2 Numerical parameters and boundary conditions

In the present work, a 2nd order central scheme for space discretization is employed, as well as isothermal wall boundary conditions (T_w =300 K) for expanding nozzle flow and external flow over slender lance and spherical probes. A no-slip wall boundary condition is imposed for all geometries considered. For expanding hypersonic nozzle flow, the Spalart Allmaras one-equation turbulence model is used, whereas simulations of flow over probes uses the k-omega SST two-equation turbulence model. For thermo-chemical (non-)equilibrium computations, the 5-species air model of Park is used, see appendix B.2.

4.5.3 Computational geometries

For space-discretization, different schemes are being used in this work, including an upwind scheme (1st-order accuracy) with AUSMW (Advection Upstream Splitting Method - Wada) flux-splitting for expanding hypersonic flow at negative pressure gradients, and central-scheme discretization (2nd-order accuracy) for flow over the slender lance and spherical probe, in the presence of detached bow-shock waves. Moreover, the 1-eq. Spalart-Allmaras turbulence model is used to study wall-bounded shear flow within the expansion nozzle and the 2-Eq. k-ϵ model is used in simulations of the detached shear flow of the free-stream within the downstream test section. Finally, the k-ω-SST model is used for simulations of wall-bounded shear flow over the slender lance and spherical probe. Whereas an increased number of blocks was favourable to adapt cell size and distribution over long geometries, such as the expansion nozzle, test section and lance probe, a small number of blocks was sufficient for low aspect-ratio geometries such as the spherical stagnation probe. In the former case, a set of wall-near blocks facilitates to sufficiently resolve the hypersonic boundary layer - with dimensionless wall distance y+<1 and particularly in the region of the nozzle throat - while cell-size is continuously increased towards the centerline and nozzle exit. In the latter case, the boundary layer region is

similarly resolved with $y^+<1$ while the mesh was manually refined to match the test condition-specific shock standoff-distance. Exact block number is defined according to the number of cores/CPU for parallelized computing. All simulations are carried out in steady state, where numerical parameters of current simulations are summarized in the appendix, table B.2. Based on the technical drawings and physical dimensions from CAD, numerical meshes (structured grids with 2-D axisymmetric topology around the centerline axis) were generated in ICEM. A detailed view of the computational geometries is given in the appendix, Fig. B.5.

4.6 Results

4.6.1 Reference test condition

In order to assess feasibility of the current rebuilding approach, a single medium-enthalpy, moderate λ TUP-TI test condition is defined as exemplary HELM reference condition RC-1, the free-stream quantities of which are measured at the conical nozzle exit by a fully instrumented test rake, see Fig. 4.3. Operation condition RC-1 is predicted according to the TUP-TI theory of Itoh and for the lightweight compression piston. Due to an underestimation of diaphragm burst pressure by $\sim10\%$, the resulting (measured) incident shock Mach number is similarly 10% higher than the a priori theoretical prediction, see Fig. 2.11 and 2.12. Nevertheless, due to slight adaptation of intial ST-pressure p_1 in the experiment, measured stagnation pressure agrees with the theoretical prediction to within $\sim5\%$. Experimental operation parameters and measurement values are summarized in Table 4.5.

Table 4.5: Operation point parameters (CT and ST) and measurement values of HELM reference condition RC-1. Stated stagnation enthalpy is determined from a priori design point prediction.

x_4 He/Ar [%]	p_4 [bar]	β [-]	A^*/A_1 [-]	A^*/A_4 [-]	m_p [kg]	p_{A0} [bar]	p_{40} [bar]
90/10	780	1.4	0.67	0.0755	62.835	65.0	0.84
λ .[-]	x_1 Air [%]	p_1 [bar]	p_2 [bar]	p_5 [bar]	v_s [m/s]	Ma_s [-]	h_5 [MJ/kg]
60.3	100	0.395	40	280	3381	9.86	13.0

In order to determine real gas caloric stagnation quantities in the nozzle reservoir, serving as upstream inlet condition for CFD simulation of the downstream nozzle flow8, stagnation quantities are predicted by CEA and ESTCj, based on measured incident shock speed, Table 4.6.

Results indicate significant overestimation of stagnation pressure p_5 of $\sim73\%$ by CEA, such that preference is given to stagnation quantities predicted by ESTCj, where equilibrium pressure behind the reflected shock wave is adapted to measured pressure $p_e=p_5$ by an isentropic expansion. The latter predicts stagnation temperature and enthalpy to be $\sim10\%$ lower than values of CEA. Here, the computational prediction of nozzle reservoir stagnation conditions

Table 4.6: Stagnation quantities of HELM reference condition RC-1, predicted by CEA and ESTCj. Stated enthalpy is referenced to 0 K.

Code	v_s [m/s]	p_5 [bar]	T_5 [K]	ρ_5 [kg/m^3]	h_5 [MJ/kg]	κ_5 [-]
CEA	3381	484	7033	20.636	12.47	1.222
ESTCj	3381	280	6429	13.215	11.26	1.315

corresponds to stage I of the consecutive stages for numerical-experimental rebuilding procedures, see Fig. 4.1, serving as upstream inlet conditions for computational analysis of the nozzle expansion (stage II).

ESTCj is further employed to estimate a time-average value of free-stream quantities at the nozzle exit, which is expected to yield a representative time-mean value, within 5-10% bounds to factual values in the experiment, see [27]. ESTCj is used to predict two reference conditions, once with the nominal (inviscid) area aspect ratio of 507 for the current Mach 8 conical nozzle (throat diameter $d^* =30$ mm) and once with a corrected effective area aspect ratio of 436, which is to account for area contraction due to viscous wall BL displacement. Therein, the nominal nozzle exit diameter of 675.5 mm is reduced by a circumferential displacement thickness of $\delta^* =24.5$ mm computed by 2-D CFD (NSMB) of the nozzle flow, which is further found to be in good agreement with the prediction of hypersonic nozzle flow BL displacement thickness $\delta^* =28.2$ mm according to the semi-empirical, analytical formula of Edelfield, Eq. 4.27, see Table 4.9. ESTCj results for both area ratios are summarized in Table 4.7, indicating a strong influence of viscous BL displacement, inducing notable relative deviation of up to 22% in FS static pressure, 17% in static density and 16% in Reynolds number. While other dynamic quantities are much less affected, the dominant change in static pressure exemplifies the latter to be a sensitive measurable indicator of viscous effects of the nozzle flow, itself being strongly affected by flow over-/underexpansion. ESTCj results in Table 4.7 serve as an order of magnitude reference in the following CFD-analysis..

Table 4.7: Free-stream quantities for HELM reference condition RC-1 as predicted by ESTCj, based on incident shock velocity and measured nozzle reservoir pressure, for nominal and viscous corrected nozzle area ratio A_E/A^*=507 and 436, respectively. Relative deviation is given with respect to nominal area ratio. Stated enthalpy is referenced to 0 K.

Code	A_E/A^* [-]	p_∞ [bar]	p_{t2} [bar]	ρ_∞ [kg/m^3]	T_∞ [K]	h_∞ [MJ/kg]	v_∞ [m/s]	a_∞ [m/s]	Ma_∞ [-]	Re_∞ [1/m]
ESTCj	507	2110	1.068	5.6006E-3	1312	1.41	4437	704	6.30	5.12E5
ESTCj	436	2586	1.238	6.5388E-3	1378	1.49	4419	720	6.14	5.95E5
Δ [%]	-14.0	22.6	15.9	16.8	5.0	6.4	-0.4	2.3	-2.5	16.2

4.6.2 CFD results

Conical expansion nozzle

For reference condition RC-1, steady state, viscous, turbulent flow through the conical expansion nozzle is computed in thermo-chemical equilibrium state by NSMB (2-D axisymmetric CFD) as stage II of the consecutive rebuilding stages I-III, see Fig. 4.1. Two highlight the relevance of a priori predicted stagnation pressure and enthalpy, two cases are defined and computed by NSMB which employ the two upstream inlet boundary conditions (nozzle reservoir) according to CEA and ESTCj, see Table 4.6. Distributions of static temperature T, axial velocity v_x, atomic oxygen mass fraction y_O and Mach number Ma are plotted in Fig. 4.4 for the CEA and Fig. 4.5 for the ESTCj inlet condition. For both total inlet conditions, free-stream quantities of the expanding nozzle flow computed by NSMB (equilibrium, fully turbulent) are summarized in Table 4.8. Evidently, deviation is FS Mach number is negligible, where increase in velocity for the CEA case is outweighed by an elevated sound speed, due to higher FS static temperature as induced by a $\sim$10% higher predicted stagnation enthalpy and temperature, in comparison to ESTCj, see 4.6. In contrast, the $\sim$73% higher prediction of stagnation pressure by CEA directly translates downstream and manifests in notably higher values for FS static pressure, density and Reynolds number of 70%, 50% and 47.5%, respectively.

Table 4.8: Free-stream quantities of HELM reference condition RC-1 as computed by NSMB (2-D CFD, equilibrium, 1-eq. Spalart-Almaras turbulence model), based on total inlet conditions by CEA and ESTCj. Relative deviation is given in reference to the ESTCj values.

Inlet case	p_∞ [Pa]	ρ_∞ [kg/m^3]	T_∞ [K]	h_∞ [MJ/kg]	v_∞ [m/s]	a_∞ [m/s]	Re_∞ [1/m]	Ma_∞ [-]
CEA	5336	9.0943E-3	2052	2.33	4883	874	6.86E5	5.59
ESTCj	3132	6.0350E-3	1817	2.02	4655	823	4.65E5	5.66
Δ [%]	70.4	50.7	12.9	15.4	4.9	6.2	47.5	-1.2

For both test cases, viscous BL growth along the conical nozzle wall is quantified and summarized in Table 4.9. Here, velocity, displacement and momentum (loss) BL thicknesses are defined as follows [4]:

$$u(\delta) = 99\% \cdot u_e \tag{4.22}$$

$$\delta^* = \int_0^\infty (1 - \frac{\rho u}{\rho_e u_e})dy \tag{4.23}$$

$$\theta = \int_0^\infty \frac{\rho u}{\rho_e u_e}(1 - \frac{u}{u_e})dy. \tag{4.24}$$

CFD results of the BL velocity and displacement thickness, δ and δ^*, within the conical expansion nozzle are compared against the semi-empirical correlation of Edenfield [179], Eq. 4.27, as

Table 4.9: Velocity (99%), displacement and momentum BL thickness along the conical nozzle wall quantified at 6 axial locations of surface coordinate chord length, normalized by the distance between nozzle throat and exit plane. Relative deviation for velocity and displacement thickness of predictions by Edenfield's correlation to current CFD results is indicated.

Inlet case		12%	22%	45%	68%	92%	100%
CEA	δ [mm]	3.1	6.4	16.8	30.1	46.4	52.4
	δ^* [mm]	0.2	0.9	3.7	8.6	16.0	18.9
	θ [mm]	0.18	0.47	1.48	2.72	4.09	4.56
Edenfield	δ [mm]	8.8	15.6	33.3	52.8	74.5	82.0
	Δ [%]	184	144	98.2	75.4	60.6	56.5
	δ^* [mm]	2.1	4.0	9.1	15.4	22.4	25.2
	Δ [%]	950	345	146	79.1	40	33.3
ESTCj	δ [mm]	3.7	7.8	20.5	36.5	55.8	62.6
	δ^* [mm]	0.4	1.3	5.1	11.4	20.9	24.5
	θ [mm]	0.27	0.68	2.00	3.47	4.98	5.48
Edenfield	δ [mm]	9.4	16.8	35.8	56.6	79.9	87.9
	Δ [%]	154	115	74.6	55.1	43.2	40.4
	δ^* [mm]	2.4	4.5	10.3	17.3	25.2	28.2
	Δ [%]	500	246	102	51.8	20.6	15.1

suggested by Habermann [134] and Hannemann [180]:

$$\frac{\delta}{x_D} = 0.195 \cdot Ma_\infty^{0.375} \cdot Re_{x_\infty}^{-0.166} \tag{4.25}$$

$$\frac{\delta^*}{x_D} = 0.42 \cdot \left(Re^*\right)^{-0.2775} \tag{4.26}$$

$$(Re_x)_D^* = \frac{\rho_\infty u_\infty}{\mu_\infty} \cdot x_D = Re_\infty \cdot x_D, \tag{4.27}$$

where Reynolds number Re^* is computed from inviscid quantities at the BL edge (i.e. Re_∞) according to Eckert's reference enthalpy method, see Hirschel [6], and the length x_D represents the local distance from the nozzle cone apex, see Edenfield [179]. Correlations of nozzle wall BL growth in Eq. 4.27 have been used to estimate the useful (uniform) nozzle core diameter and optimum nozzle length, see [161], and are used as an order of magnitude comparison to current results, compare [181, 182]. Evidently, velocity and displacement BL thickness of current CFD results differ by up to an order of magnitude from predictions according to Edenfield's correlation. While the exact reason is unknown, the most plausible explanation is attributed to differences in the dynamic viscosity, where the Blottner viscosity model and Sutherland's law will yield significant deviation at elevated temperatures. This conjecture is in agreement with the clear trend, according to which the overall largest differences are observed towards the farthest upstream position near the nozzle throat, monotonically reducing in downstream direction. Here, for both test cases of different inlet conditions, velocity BL thickness reflects notably larger differences, of 57% and 40% for case CEA and ESTCj, respectively, in contrast to 33.3% and 15.1% in terms of the displacement thickness.
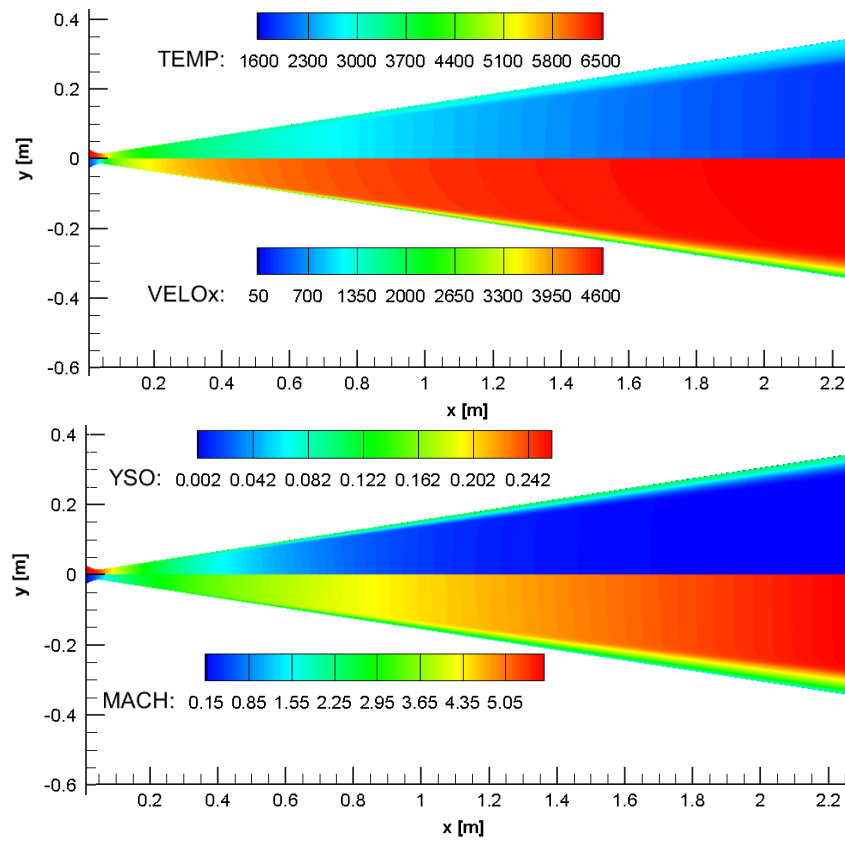
Figure 4.4: Distribution of static temperature T [K], axial velocity v_x [m/s], atomic oxygen mass fraction y_O [-] and Mach number Ma [-] within the HELM conical expansion nozzle for reference condition RC-1. Total inlet conditions imposed according to CEA prediction.
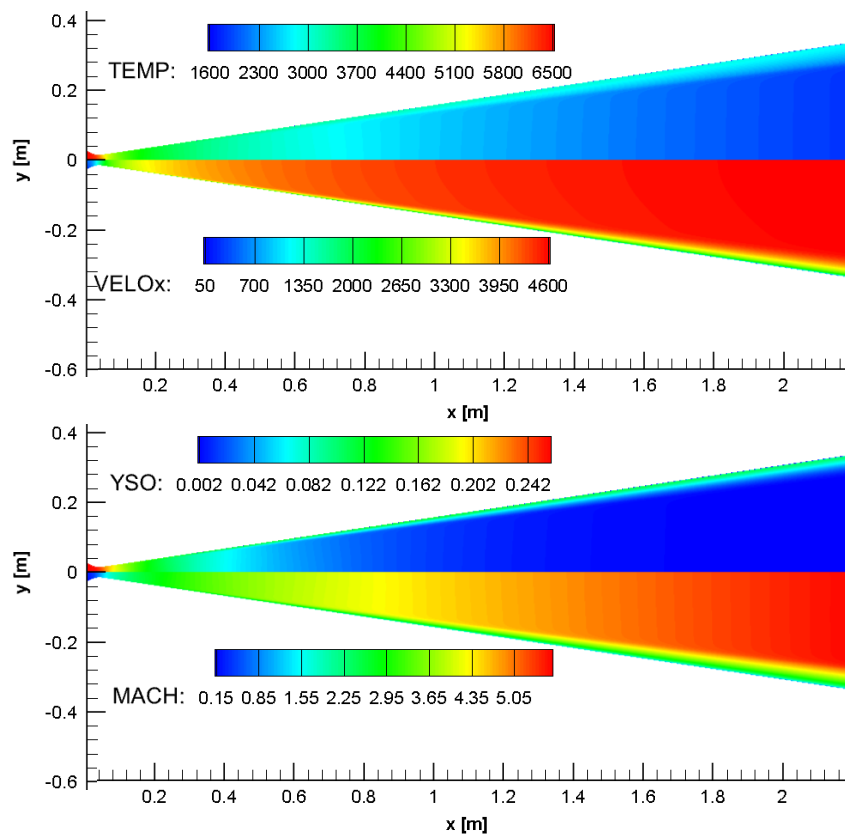
Figure 4.5: Distribution of static temperature T [K], axial velocity v_x [m/s], atomic oxygen mass fraction y_O [-] and Mach number Ma [-] within the HELM conical expansion nozzle for reference condition RC-1. Total inlet conditions imposed according to ESTCj prediction.

State quantities along the nozzle centerline and across the exit plane for condition RC-1 computed by NSMB for total inlet conditions according to CEA and ESTCj are compared in Fig. 4.6 and Fig. 4.7. Based on the centerline results from 2-D CFD and using Sutherland's law, Eq. 4.12, to calculate the dynamic viscosity - considering air in the freestream to have fully equilibrated for both inlet conditions -, the free-stream Reynolds number is calculated to Re_∞=6.86E5 [1/m] for the CEA and Re_∞=4.65E5 [1/m] for the ESTCj inlet condition, respectively.

Slender lance probe

As stage III of the rebuilding procedure steps for reference condition RC-1, the flow over intrusive test rake probes is computed by NSMB, with FS inlet conditions imposed according to FS quantities from preceding stage II results (nozzle flow computation). In case of the slender lance probe, the distribution of wall static pressure to free-stream pressure ratio over axial distance x is plotted in Fig. 4.8. At the location of geometry transition from contoured to cylindrical shape (x/D~5), a steep decline marks pressure decrease due to an expansion from increased pressure behind the oblique shock wave, emanating from the probe tip. An overexpansion beyond the static FS pressure is characteristic for such probe geometries and attributed to growth of viscous BL displacement, gradually recovering in axial direction due to flow egalization and reduced streamline curvature. At the pressure transducer location, the local wall static pressure (measured) is observed to have adapted to the FS static pressure to within 3%. Minor fluctuations in the decreasing pressure curve reflect limited (numerical) shock oscillations. Further, small discontinuities along the curve are non-physical but artifacts of block edges in the computational geometry. In contrast, the notable rise of wall pressure far downstream is attributed to the base probe geometry, see Fig. B.2. The qualitative trend is in close agreement with observations in literature [13, 162], as is the quantitative correction within the expected range of 5%.

Spherical probe

Based on the nozzle exit (FS) quantities, determined by stage II nozzle flow computation and summarized in Table 4.8, the steady, equilibrium, turbulent (2-eq. k-ω), viscous flow field (NS-eq.) over a sphere of R_N=25 mm with isothermal wall boundary condition (T_w=300 K) is computed for both cases of total inlet conditions. In order to study the flow field over the spherical stagnation probe, spatial distribution of Mach number, static pressure and temperature ahead of the probe are plotted in Fig. 4.9. As expected from temperature and enthalpy magnitude, the net reduction of molecular nitrogen mass fraction y_{N_2} amounts to less than 0.1%. However, molecular oxygen is observed to have near fully dissociated behind the detached bow-shock wave, gradually recovering due to recombination along the sphere perimeter (tangential surface coordinate). Relevant results in the stagnation point are compared in Table 4.10. Here, nozzle reservoir and subsequent free-stream conditions based on CEA resulted in a shock standoff distance along the stagnation streamline of δ =2.0398 mm, entailing a stagnation point heat
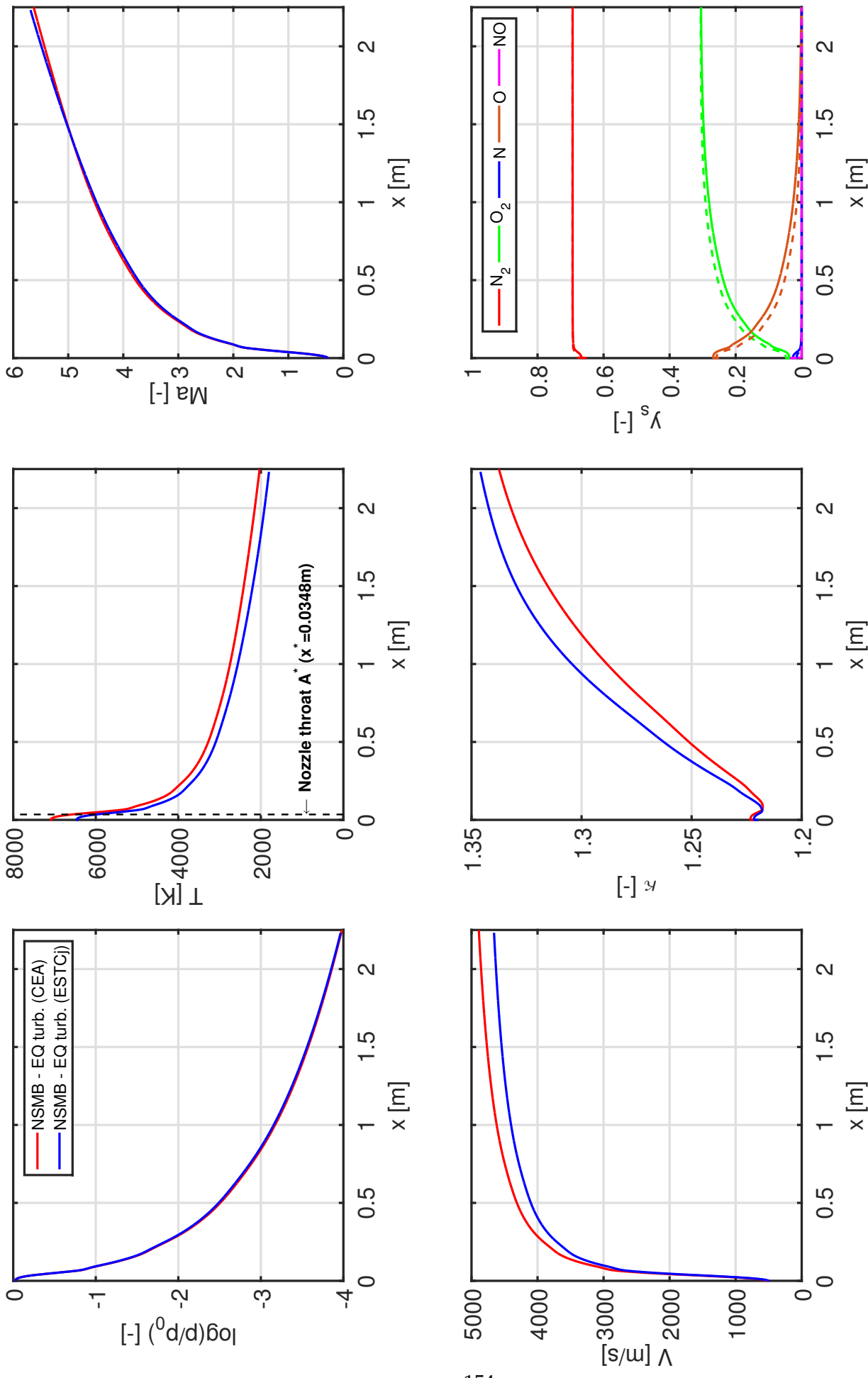
Figure 4.6: Distribution of state quantities along the centerline of the conical expansion nozzle for HELM reference condition RC-1, with total inlet conditions imposed according to CEA and ESTCj, respectively. Plotted are normalized static pressure, static temperature, Mach number, velocity, ratio of specific heats and species mass fraction – in the latter case, solid and dashed lines represent identical species for CEA and ESTCj results, respectively.
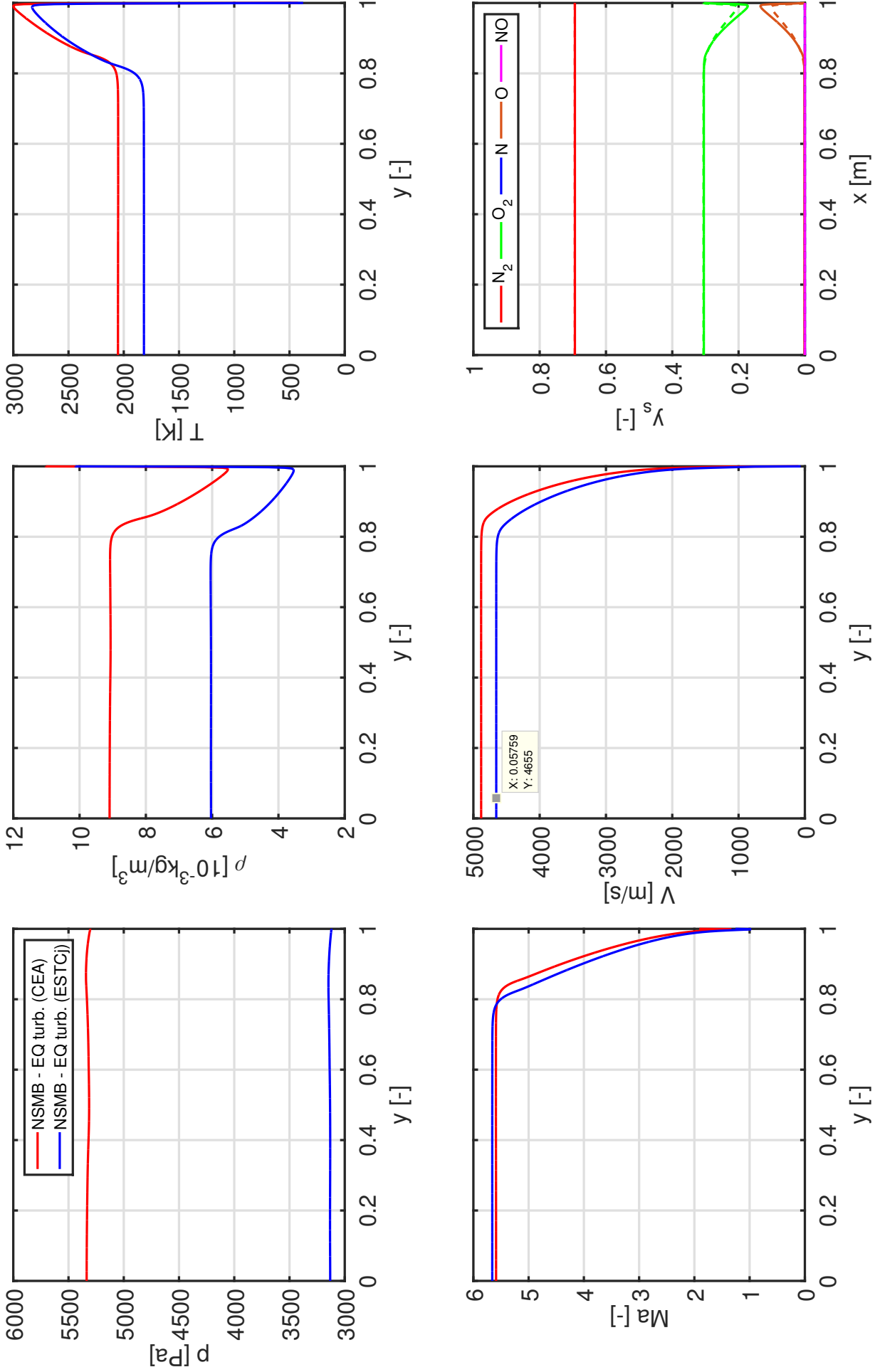
Figure 4.7: Distribution of state quantities across the exit plane of the conical expansion nozzle for HELM reference condition RC-1, with total inlet conditions imposed according to CEA and ESTCj, respectively. Plotted are normalized static pressure, static temperature, Mach number, velocity, ratio of specific heats and species mass fraction - in the latter case, solid and dashed lines represent identical species for CEA and ESTCj results, respectively.
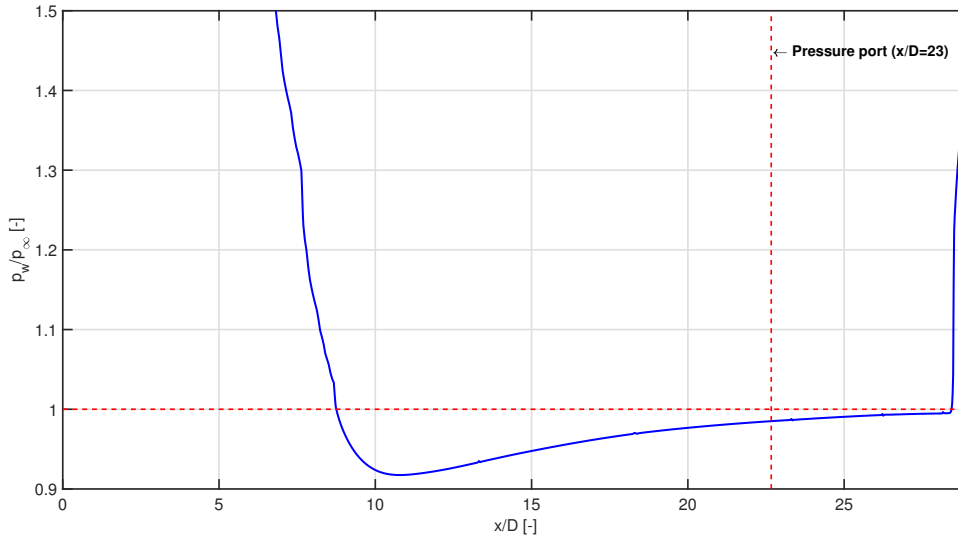
Figure 4.8: Ratio of local wall static pressure magnitude p_w to free-stream (inlet) pressure p_∞ along the slender lance probe. Horizontal line marks ratio of 1 (no viscous correction) and vertical line marks pressure port location at x/D~23.

flux rate of $\dot{q}_s$ ~11.10 MW/m^2. In contrast, a shock standoff distance of δ =2.0368 mm and heat flux rate of $\dot{q}_s$ ~7.21 MW/m^2 were determined for ESTCj based inlet conditions. These values are found to be notably lower than the stagnation point heat flux of $\dot{q}_s$ ~20 MW/m^2 measured in the subsequent experiment. Viscous BL growth along the sphere surface coordi-

Table 4.10: Stagnation point (Pitot) pressure, shock standoff distance and heat flux rate on a sphere (R_N=25.0 mm) with isothermal wall T_w=300, as computed by NSMB (viscous NS, equilibrium, k-ω turbulent) for cases CEA and ESTCj. Imposed free-stream (inlet) static pressure from nozzle flow computations listed for completeness.

Code	p_∞ [Pa]	p_{t2} [bar]	Δx [mm]	$\dot{q}_s$ [MW/m^2]
CEA	5336	2.289	2.0398	11.10
ESTCj	3132	1.343	2.0368	7.21

nate is quantified in Table 4.11. Here, the wall BL velocity thickness δ is determined with the 99%-criterion based on total enthalpy $h_0 = h + v^2/2$, see [182, 183].

As a sanity check, inviscid flow field computations (Euler-eq., equilibrium, k-ω-SST) with adiabatic wall boundary condition ($\dot{q}_s = 0$) have been carried out for both free-stream test cases (here a no-penetration BC u_n =0 is imposed on the solid wall instead of the no-slip condition u =0 for viscous flow), similar to Rödiger et al. [144]. Results in terms of discrete values of the tangential velocity along the sphere surface coordinate $u_t(y)$ are polynomially-fitted by a twice-differentiable cubic spline, based on minimized least-squares residuals, in order to compute the local tangential velocity gradient in the sphere stagnation point, see Theisen [172] for further details. Due to inherent rotational symmetry of the flow field (at absent angle of attack), a boundary condition imposed on the second derivative $d^2u_t/dy^2(y = 0) = 0$ is enforced locally in the SP, see Fig. 4.10.
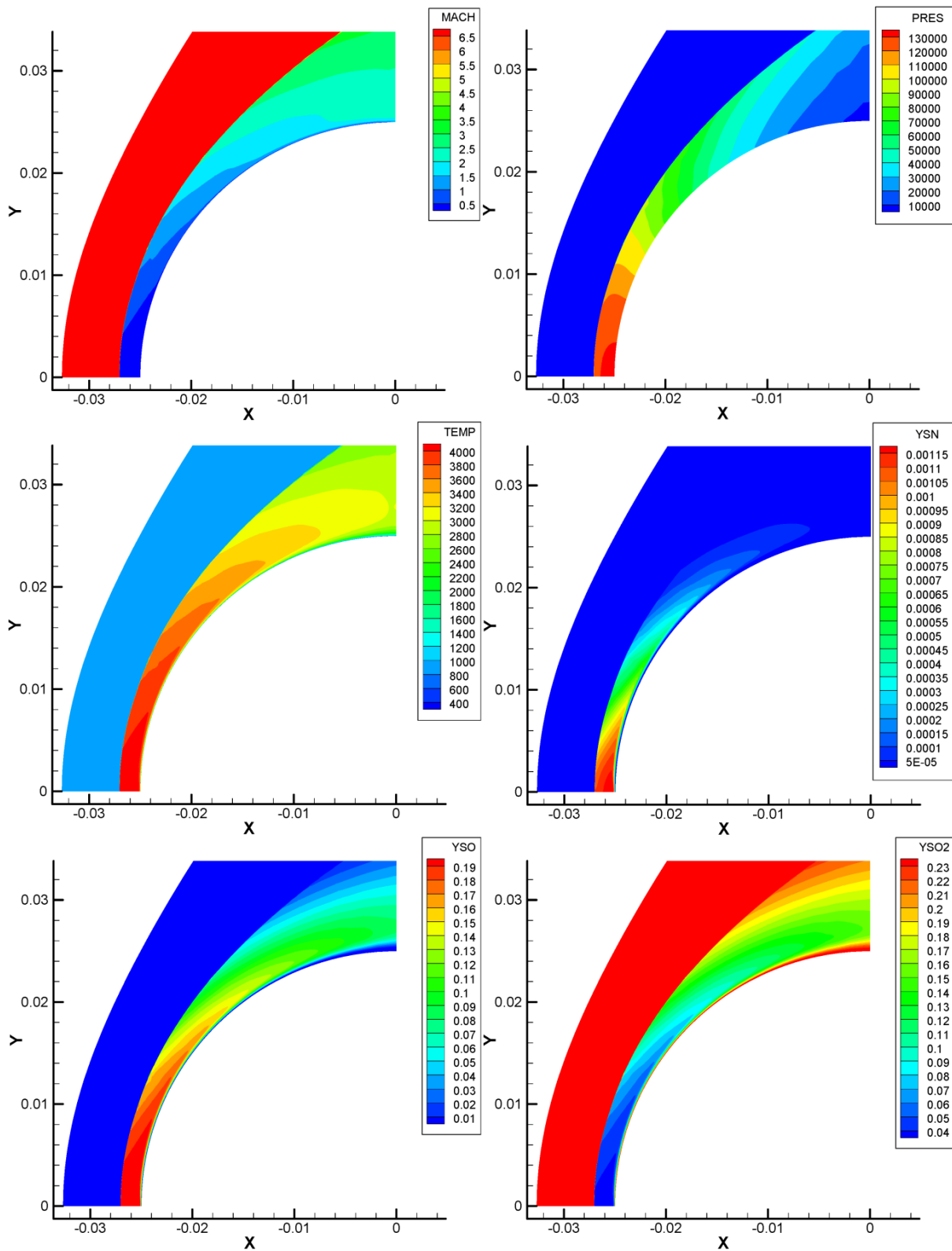
Figure 4.9: Representative results of NSMB computations of the external flow field and bow shock ahead of the spherical stagnation probe (R=25 mm) for HELM reference condition RC-1 (CEA inlet conditions, equilibrium, k-ω, isothermal wall T_w=300 K). Plotted are (total) Mach number, static pressure [Pa], static temperature [K] and mass fractions [-] of N, O and O_2.
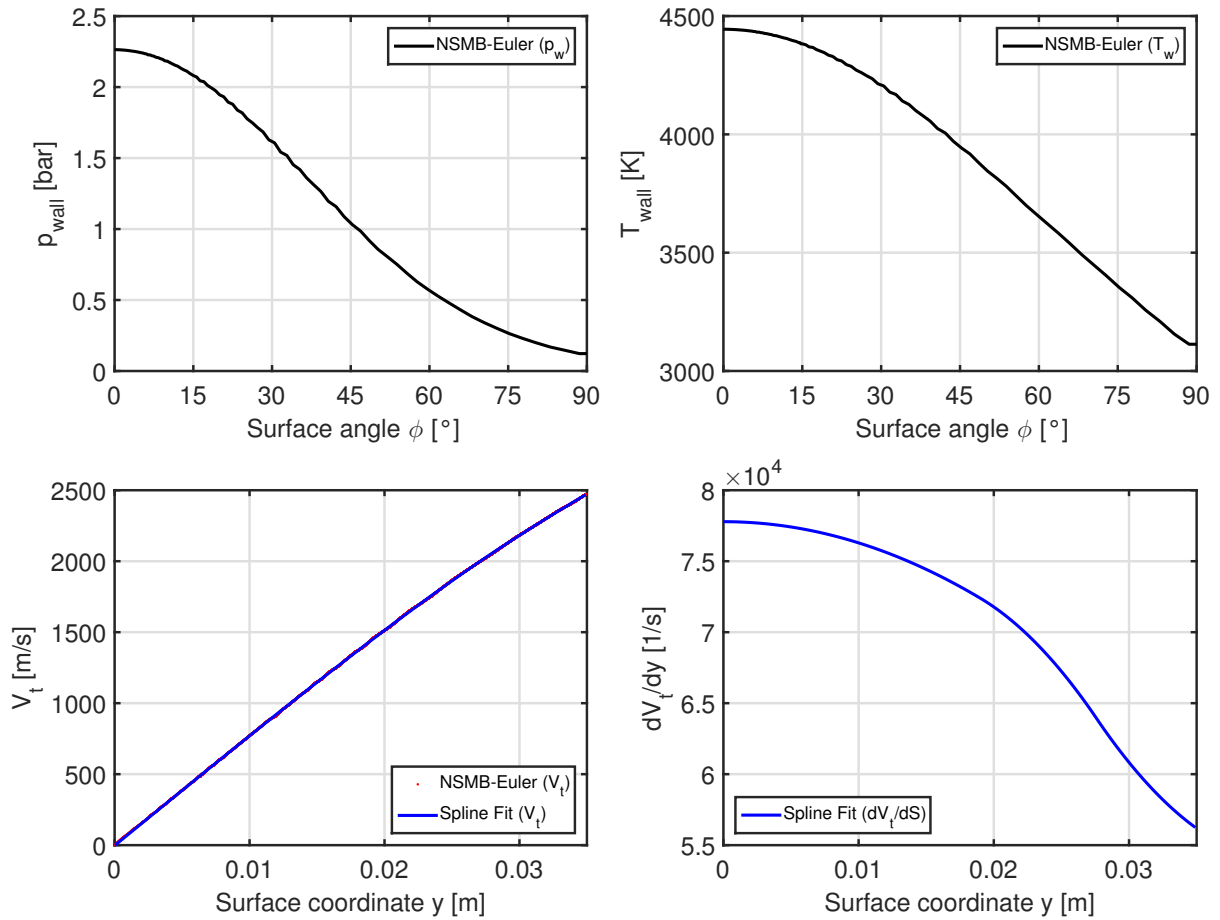
Figure 4.10: Representative results of the inviscid Euler-flow computations over the spherical probe (R=25 mm) for HELM reference condition RC-1 (CEA inlet conditions, equilibrium, fully turbulent k-ω-SST, adiabatic wall, non-penetrating condition). Plotted are wall pressure and temperature over surface angle φ =0-90°. Wall tangential velocity and first spatial derivative are plotted over surface coordinate y=0-0.035 m, corresponding to surface angle interval φ =0-80° used for the polynomial fit.

Table 4.11: Velocity, temperature, displacement and momentum BL thickness over the sphere surface coordinate a 6 positions, quantified by the inclination angle from 0-90°, for conditions RC-1 and cases CEA and ESTCj. Computations by NSMB with equilibrium, k-ω turbulence model, isothermal wall T_w=300 K.

Code		1°	18°	36°	54°	72°	86°
CEA	δ [mm]	0.04	0.25	0.29	0.42	0.69	1.10
	δ_T [mm]	0.25	0.38	0.40	0.56	1.02	2.42
	δ^* [mm]	0.00	0.01	0.01	0.03	0.07	0.18
	θ [mm]	0.00	0.04	0.05	0.07	0.11	0.16
ESTCj	δ [mm]	0.05	0.31	0.36	0.51	0.83	1.27
	δ_T [mm]	0.32	0.46	0.48	0.69	1.28	2.36
	δ^* [mm]	0.00	0.02	0.02	0.04	0.10	0.23
	θ [mm]	0.00	0.05	0.06	0.08	0.13	0.18

Results listed in Table 4.12 reflect inviscid NSMB-simulations to yield a suitable prediction of the SP tangential velocity gradient, which lies exactly in between the theoretical predictions according to the modified Newton and Olivier definition, with a relative deviation of -10.8% and 9.4%, respectively. Interestingly, when inserting the NSMB-computed SP velocity gradient of 77,784 1/s into the Fay-Riddell eq., the latter yields an associated SP heat transfer of $\sim$22 MW/^{2}, which - even though appearing suprisingly high for a medium-enthalpy test condition - is found to be in good agreement with the measured heat flux rate for condition RC-1. Results with the more realistic freestream conditions - based on ESTCj-predicted stagnation enthalpy - however, reflect a notably lower predicted tangential velocity gradient, which is again within the bounds of theoretical values predicted by the Newton and Olivier formulation. Evidently, the associated lower SP HT is more representative of the order of magnitude of time-resolved stagnation quantities measured in the experiment, see Fig. 4.11.

Table 4.12: Tangential velocity gradient in the sphere stagnation point (R_N=25.0 mm) as computed by NSMB (adiabatic Euler, polynomial-fitted), in comparison to theoretical values according to the Newton and Olivier definition, based on computed static and Pitot (stagnation) pressure and shock standoff distance.

Code	NSMB	NSMB	Newton	Olivier
	$\dot{q}_s$ [MW/m^2]	$\frac{du_t}{dy}$ [1/s]	$\frac{du_t}{dy}$ [1/s]	$\frac{du_t}{dy}$ [1/s]
CEA	22.2	77,784	69,407	85,082
ESTCj	14.4	51,868	44,584	55,948

4.6.3 Free-stream measurements

Simultaneously to numerical CFD predictions, free-stream measurements at the nozzle exit have been conducted with an instrumented test rake for reference condition RC-1 in the HELM facility. The temporal development of state quantities relevant for FS rebuilding procedures,

nozzle reservoir stagnation pressure as well as Pitot pressure (measured by a piezoresistive Kulite XCQ-093 transducer mounted in a spherical probe SP), static pressure in the FS measured by two slender lance probes, and absolute wall temperature in the stagnation point of two spheres of different radii, relative wall temperature rise from ambient (measured by coaxial thermocouples in the SP of two spherical probes) and calculated transient SP heat flux rate for both spherical probes is plotted in Fig. 4.11. For measurement of FS quantities, the calibration rake is placed such that its measurement plane closely coincides with the nozzle exit plane. Accordingly, due to BL egalization length upstream of the static pressure port of slender lance probes, this necessitates the latter to protrude into the conical expansion nozzle by $\sim$144 mm in axial direction.

Temporal development of stagnation pressure p_5=280 bar in the nozzle reservoir indicates a quasi-steady time-interval of $\sim$1 ms. Similar to the stagnation pressure trace, pitot pressure reflects an intermittent plateau around 0.95-0.85 bar, for a duration of $\sim$1 ms, indicating the useful test time period of condition RC-1. However, in this time interval from 165.2-166.2 ms, static pressure measured by the two probes at rake position 3 and 6 (located 10.5 and 21mm off the centerline axis, respectively) reflect a notably inconsistent development: whereas probe 2 measures a continuous decrease from initially $\sim$3700-2700 Pa, probe 1 samples a continuous increase from $\sim$600-1600 Pa, indicating a quantitatively and qualitatively dissimilar trend. In contrast, absolute and relative wall temperature (rise) measured in the SP of both spherical probes are consistent and only differ in magnitude due to varying probe radius. This is consistently observed in the instantaneous SP heat flux development which scales reciprocally to probe radius and is hence of generally larger amplitude for the smaller radius probe. Evidently, despite a relatively steady mean of stagnation and pitot pressure, SP heat flux is not constant but shows a monotonic decrease from initially 21.5 and 25.5 MW/m^2 to a mean level of $\sim$12.4 and 13.7 MW/m^2. The two preceding peaks sampled by probe 1 (closest to the centerline) are not as pronounced for probe 2. Due to obvious spatial non-uniformity in the FS flow field, only one signal trace each, with the steadier development (lance probe 2 for static pressure and sphere probe 2 for SP heat flux and wall temperature), is chosen as the reference value for numerical rebuilding procedures. Due to excessive SP heat flux rates and amplifier clipping even at the lowest gain level, the ALTP reference sensor - being primarily designed to measure high-frequency low-amplitude fluctuations off the SP [165] - was found to be unsuitable to yield a direct comparison of measured SP heat flux rates.

4.6.4 Free-stream rebuilding

Free-stream quantities according to both rebuilding methods (FS-method w/ static pressure and R-method w/o static pressure) for the chosen time interval of 1 ms are plotted in Fig. 4.12 and 4.13. Current results are computed by considering the Fay-Riddell-equation, Eq. 4.2, and using the modified Newton tangential velocity gradient, Eq. 4.8. For the sake of completeness and to serve as a sensitivity analysis of current results, FS quantities of test condition RC-1 have been computed by the Fay-Riddell-equation while varying formulations of the tangential
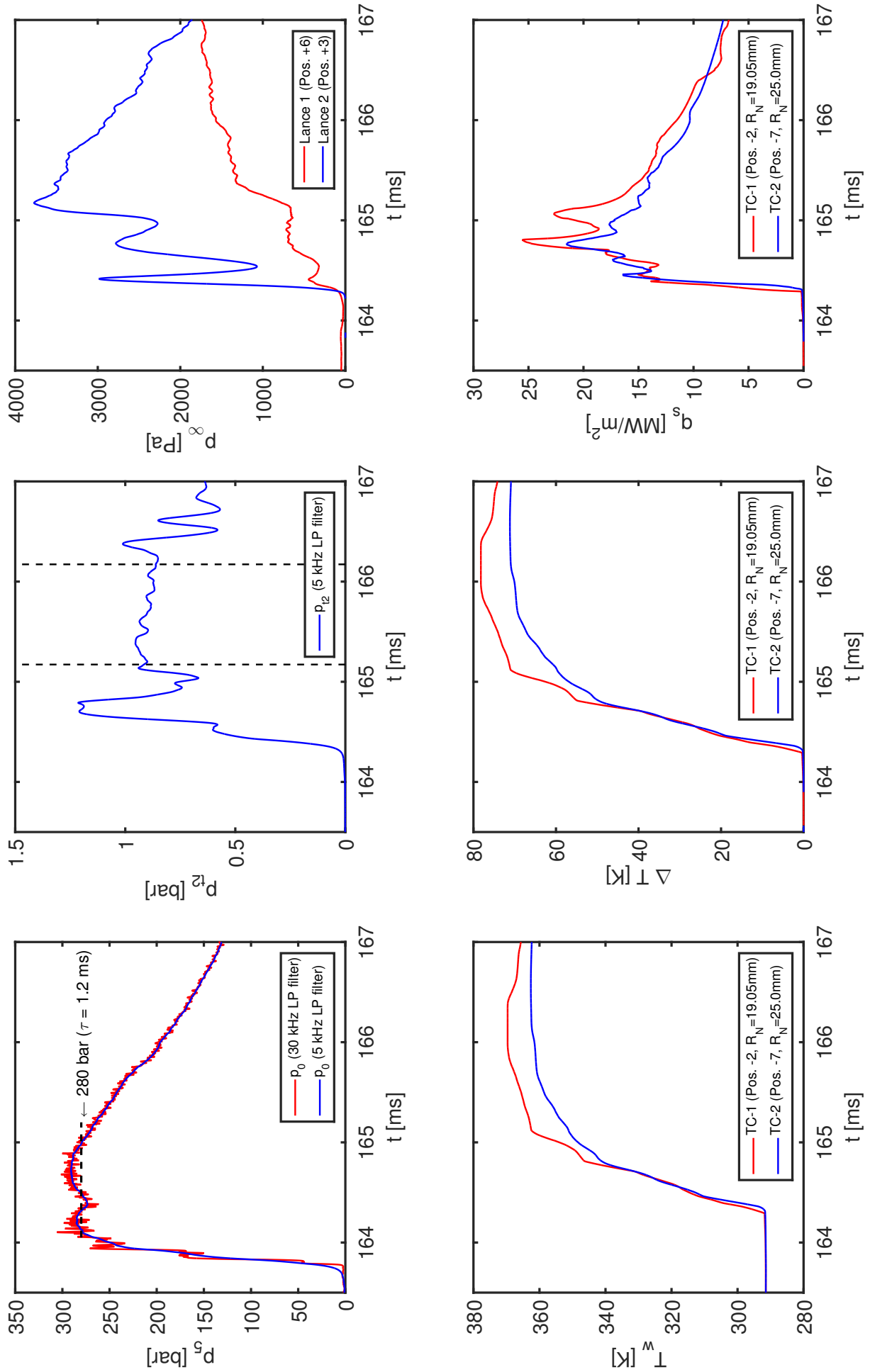
Figure 4.11: Reservoir (total) pressure, Pitot (stagnation) pressure, free-stream static pressure, sphere stagnation point temperature, temperature increase, stagnation point heat flux.

velocity gradient as well as by assuming the modified Newton velocity gradient and varying the SP heat-flux-enthalpy-relation from Fay-Riddell to Verant, Sutton-Graves and Zoby. For brevity, influence on computed FS quantities is discussed in the appendix B.

Stagnation point heat flux rate is calculated from transient temperature rise of coaxial thermocouple probe 2. Time-resolved results of both FS- and R- rebuilding methods are contrasted to steady state predictions of NSMB, based on ESTCj- and CEA-provided nozzle reservoir inlet conditions. Relative differences between the FS- and R-method are plotted underneath each graph for every single computed quantity and in reference to the FS-method provided values. Here, a relative deviation of less than 1% between both methods in terms of calculated stagnation enthalpy and temperature evidently indicates static pressure measurement to not affect the stagnation quantities. Values based on measured quantities are notably higher than the CFD-provided references, where higher stagnation enthalpy and temperature provided by CEA reflect the assumed isentropic expansion used within ESTCj. The relative discrepancy in amplitude of 80-90% in terms of static pressure and temperature by the R-method in reference to the FS-method highlights the dominant influence of (neglected) in situ static pressure measurement. Moreover, the monotonic decrease of measured static pressure is transferred to calculated static temperature by the FS-method, whereas the R-method (using static pressure as a dependent variable) predicts an effectively steady value for both quantities (as imposed by a measured quasi steady pitot pressure), which - despite evident inconsistency in the static pressure measurement - shows a dissimilar quantitative and qualitative behavior. From literature, see Lettl [155] and Grossir et al. [142], the R-method - by assuming an isentropic, adiabatic expansion - is known to underpredict FS static pressure by up to 100%, resulting in a significant overprediction of Mach number. This trend is similarly observed in current results, where the measurement of FS static pressure is found to yield a discrepancy of $\sim$100% and -25% in predicted FS density and absolute velocity, see Fig. 4.13. Moreover, the overall largest differences of up to 130% and 500% are observed in terms of derived Mach- and Reynolds number. Here, considering a nozzle area ratio of 500 in the presence of viscous BL displacement and medium enthalpy flow near thermo-chemical equilibrium, the CFD-predicted Mach numbers of 6.2 and 6.5 - in reference of a inviscid prediction for an ideal gas of 8.9 - appear much more plausible than the rebuilding-predicted values of $\sim$9.9 and 4.3 for the R- and FS-method, respectively.

4.7 Discussion

The obviously erroneous magnitude of rebuilding predicted Mach numbers for the current measurement is illuminating in two regards. Firstly, FS nozzle calibration conducted in the absence of in situ static pressure measurement (and assuming isentropic flow expansion) is inherently biased due to a strong underprediction of static pressure which entails a largely overpredicted Mach number by definition. Secondly, considering an overly unplausible Mach number of 4.3 calculated by the FS-rebuilding method, static pressure measured by lance probes in the current experiment is considered the largest and most influential source of uncertainty. In
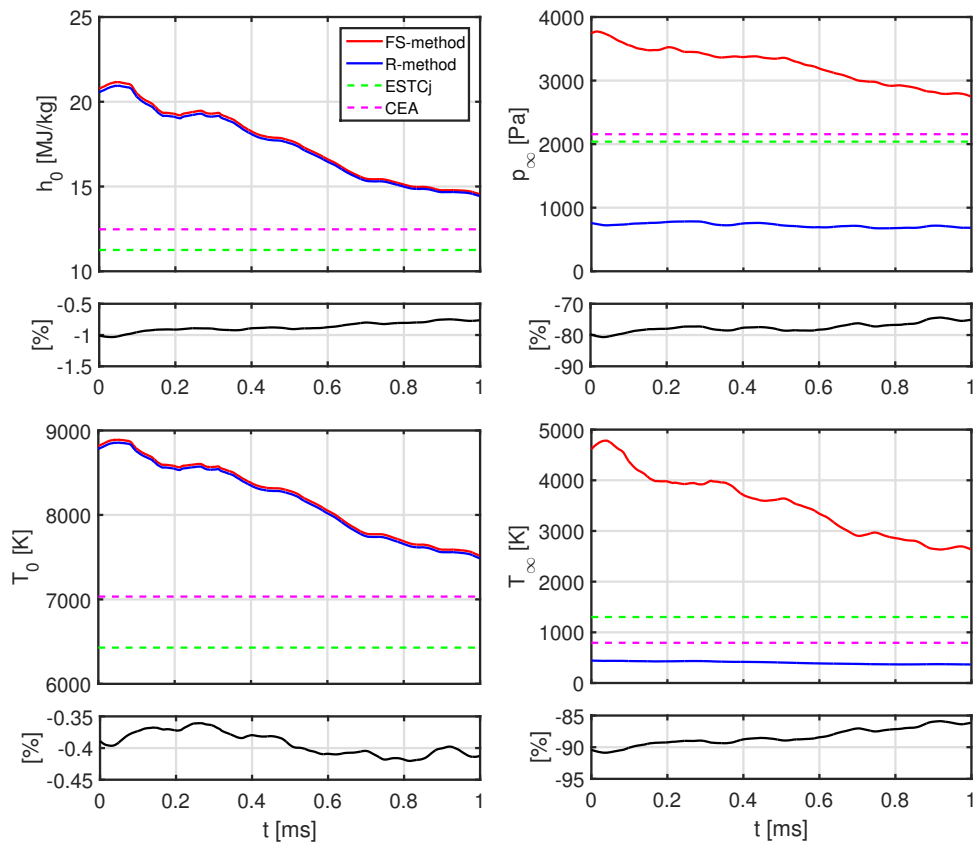
Figure 4.12: Comparison of free-stream quantities predicted by both rebuilding methods (w/ and w/o static pressure measurement). Total enthalpy and temperature, free-stream static pressure and static temperature are plotted over time for HELM reference condition RC-1.
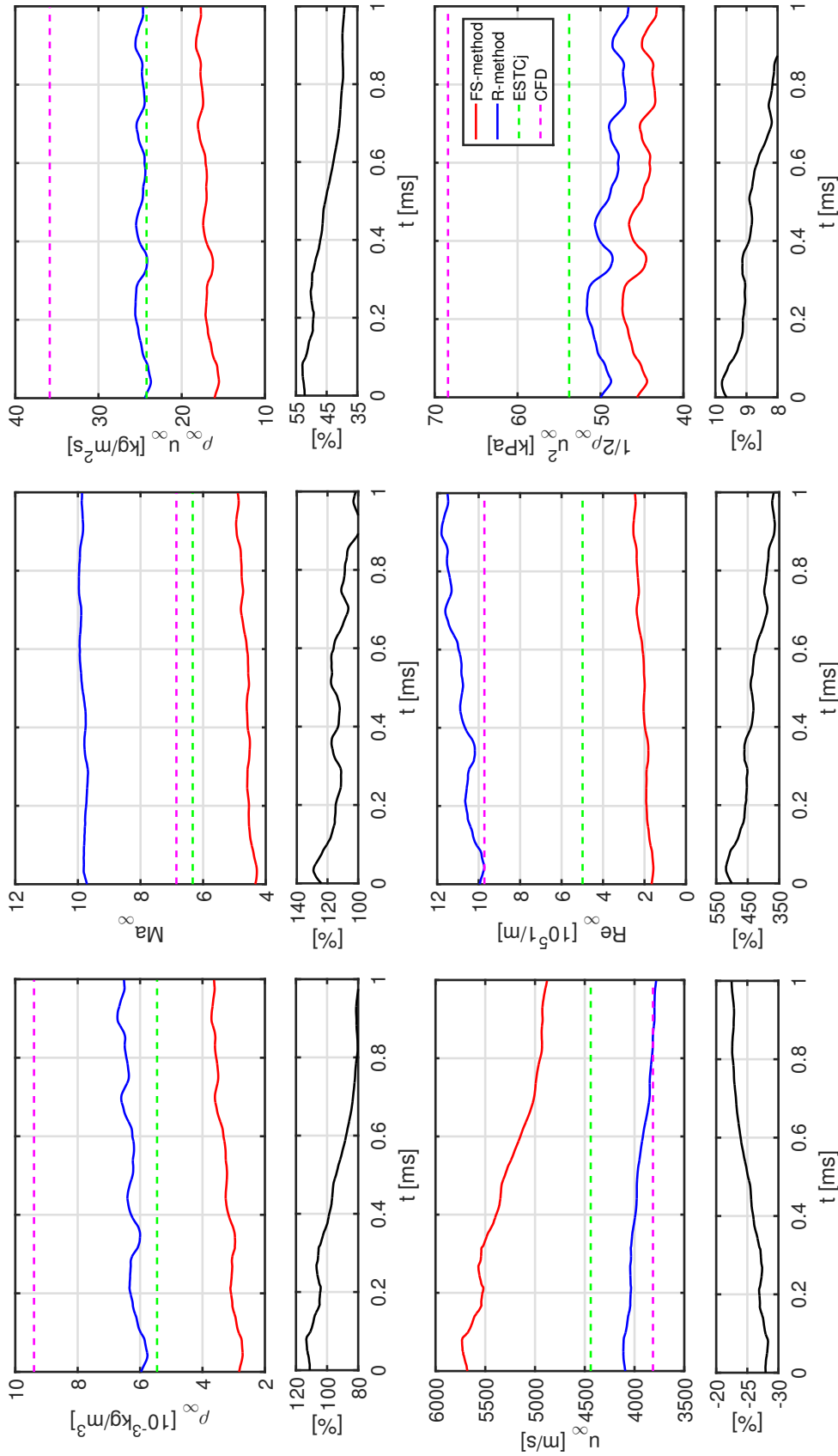
Figure 4.13: Comparison of free-stream quantities predicted by both rebuilding methods (w/ and w/o static pressure measurement). Static density, absolute velocity, Mach and Reynolds number as well as specific mass and momentum flow are plotted over time for HELM reference condition RC-1.

order to rule out random error, the measurement presented herein was repeated twice for the identical RC-1 operation condition, showing high reproducibility due to near identical sampled amplitudes and dynamic trends for all sensors. Eventually, after the correctness of static pressure probe calibration was scrutinized and confirmed, it can be concluded that the inherently spatially inhomogeneous, diverging flow field at the exit of a conical nozzle is not suitable to be characterized by slender lance probes, but indeed impaired the current approach. Notable over-expansion of the nozzle flow after exiting the conical expansion nozzle (8.5° half opening angle) for reference condition RC-1 is observed from Fig. 4.14, where relevant free-stream quantities are plotted along the test section centerline over an axial distance of 1 m. As is clearly observed, only the absolute velocity remains almost constant whereas other quantities reflect a strong monotonic gradient in axial direction. Precisely, over a distance of 0.5 m, the smallest divergence is seen for Mach number, which increases by up to 9%, whereas static density and Pitot pressure drop to less than 70% of the nozzle exit value and static temperature decreases to 85%. Yet, the overall strongest decrease is observed for static pressure which plummets to 58% at 0.5 m distance and to 38% of it's initial value at 1 m distance. Such overexpansion was found to be near independent of the specific test condition, irrespective of high-/low stagnation pressure-/enthalpy, but to be dictated by the nozzle geometry instead. Similar considerations on an expansion nozzle of formerly conical shape at the TH2 shock tunnel lead Vetter [113] to the conclusion that, in the strive to establish experimental-numerical rebuilding routines, free-stream static pressure measurements at the conical nozzle exit will be in vain by definition. This conclusion is substantiated by inconsistent magnitudes and dynamic trends of static pressure measurements which do not reflect relative flow-steadiness, as demonstrated by the stagnation and Pitot pressure probe, but rather highlight a conical expansion nozzle to be generally unsuitable for attaining a spatially homogeneous flow field. Due to inherent streamline divergence, slender lance probes located off-centerline cannot be properly aligned with the FS but will experience angles of attack as large as the nozzle opening angle, where a 3-D flow field imparts flow separation and unsteadiness by definition. In fact, even if a single probe was accurately aligned with the centerline, the dominating axial gradient of a low magnitude quantity such as FS static pressure would still invalidate measurements. For this reason, the requirement of a contoured expansion nozzle with parallel exit flow field becomes even more obvious for the HELM facility.
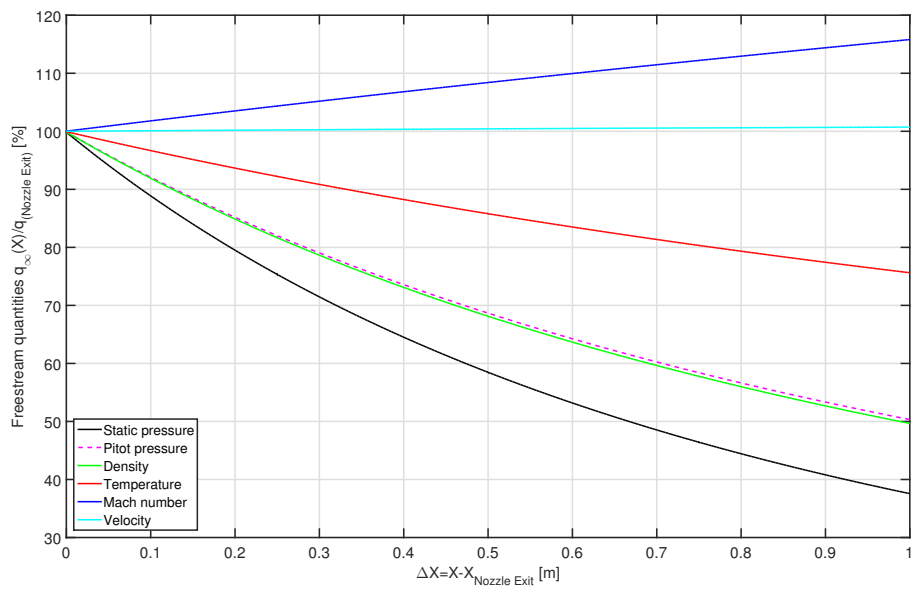
Figure 4.14: Distribution of free-stream quantities along the nozzle centerline over an axial distance of 1 m from the nozzle exit into the test section; quantities are normalized by their local value at the nozzle exit plane. Computation by NSMB with turbulent flow in thermo-chemical equilibrium based on ESTCj upstream inlet (nozzle reservoir) conditions for condition RC-1.

5 Conclusion

In the course of the present work, the fundamental concept of a contribution to a more accurate determination of nozzle upstream inlet conditions and hence free-stream conditions of hypersonic, high-enthalpy, short-duration ground test facilities by the use of targeted optical diagnostics was devised. For this purpose, in situ measurements of stagnation temperature and enthalpy within the nozzle reservoir were to be achieved by non-intrusive laser spectroscopy via LIGS, results of which were to be contrasted to established methods of nozzle inlet condition determination via numerical codes of varying complexity, and finally to be contrasted and validated against predictions by established numerical-experimental rebuilding methodologies, themselves utilizing free-stream static pressure and stagnation point heat flux measurements. The accuracy of measurements by slender lance and spherical probes throughout nozzle rake calibration was to be complemented and enhanced by detailed viscous, thermochemical CFD simulation of the nozzle flow, free-stream establishment and external flow over intrusive probes in the test section. Evidently, due to the inherent sensitivity of nozzle reservoir and free-stream measurements, sufficient quasi-steadiness of the flow upstream as well as downstream of the expansion nozzle was required, which necessitated for the development of safe and refined facility operation conditions, where predicted free-piston driver dynamics were to be validated by detailed accelerometer measurements. The work process of this concept naturally divided into three main threads, which were carried out largely in parallel and form the framework of this thesis.

To address the first thread of full-range operation condition development, the HELM facility's compression piston has been significantly revised by mechanical redesign and choice of materials, allowing for safe and efficient full-range operation up to 1000 bar burst pressure and 100% helium driver gas for the first time. Three alternative, established theories from literature have been adopted and utilized to derive a complete set of free-piston driver operation conditions for two piston masses, satisfying the tuned-piston and safe landing condition in the driver tube. Coupling with the thermo-chemical equilibrium calculations of tailored-interface conditions in the shock tube results in a complete map of free-piston reflected shock tunnel operation conditions across the entire test envelope of the HELM facility, i.e. up to 1000 bar burst pressure and 20 MJ/kg stagnation enthalpy. Predicted trajectories of the compression piston have been validated against an on-board, high-resolution accelerometer for a full stroke for the first time. Even though aspired quasi-steadiness of the driver and test flow is not yet fully satisfactory - as is evident from to the reduced character of 1-D analysis -, it sufficed for the purpose of this work, besides proving the underlying concept. Naturally, increased quasi-steadiness will be

achieved by empirical refinement - as is the case for every ground test facility with decades of experience worldwide -, which is however beyond the scope of this work for evident reason.

In the second thread of this work, non-intrusive in situ determination of stagnation temperature and enthalpy within the nozzle reservoir has been achieved by the extension of homodyne, resonant laser-induced grating spectroscopy up to the limit of 220 bar, 1900 K and 2.1 MJ/kg behind reflected shock waves up to Mach 3.6 in air. This was accomplished by the deliberate design of wall-flush mounted optical windows, allowing safe optical access to the nozzle reservoir up to stagnation pressures of 1000 bar while minimizing secondary flow and spatially-transient perturbations, thus satisfying a key requirement of optical diagnostics by LIGS. Therein, a newly devised hydraulic damping system by heavy duty shock absorbers limits axial recoil and facility displacement to allow for a safe operation of the HELM facility up to design limit burst pressures for the first time. Even though low repetition rate of the Nd:YAG-laser grants only single-shot measurements and despite the fact that measurements have only been successfull in shock-tube mode with closed endwall so far, this approach yields singularly valuable data for the validation and correction of established methods of stagnation enthalpy prediction and will hence contribute to a more accurate determination of nozzle inlet and free-stream conditions of short-duration test facilities in the future. Current limitations of the technique and its robustness are addressed in detail and suggestions are made for a successful application of LIGS at higher stagnation pressures and temperatures in the future.

The last thread of this work detailed the implementation of two numerical-experimental rebuilding routines by calibration rake measurements at the nozzle exit, utilizing stagnation point heat transfer measurements on a sphere, which have been utilized in the HELM facility for the first time. For a single reference test condition at 10 MJ/kg medium enthalpy, the implemented methodologies were validated against time-averaged quantities from three distinct low-, medium- and high-enthalpy reference conditions of two established reflected-shock ground test facilities. Along the use of alternative modeling formulations of the tangential velocity gadient and stagnation enthalpy-heat transfer relation, the impact of (neglected) in situ free-stream static pressure measurements is demonstrated. In comparison to reference values from detailed CFD - which highlighted the importance of accurate determination of nozzle reservoir stagnation conditions by quantifying resulting relative difference in free-stream quantities -, the current static pressure measurements were demonstrated to be largely affected and in fact impeded by the spatially inhomogeneous, diverging flow field in the wake of a conical expansion nozzle.

Eventually, the initial goal of deliberately combining and contrasting the results of different approaches of measuring and predicting nozzle reservoir and inlet conditions could not be achieved conclusively due to technical limitations. Yet, exactly for this reason, the current work concludes with the insight that an accurate determination of nozzle inlet conditions is mandatory to increase the accuracy of free-stream quantities in short-duration ground test facilities and is technically achievable by dedicated non-intrusive in situ diagnostics. In regards to the present facility, the near-term use of contoured expansion nozzles is recommended.

6 Literature

[1] Anderson, J. *Hypersonic and High-Temperature Gasdynamics*. McGraw-Hill Series in Aeronautical and Aerospace Engineering. McGraw-Hill, 1989. ISBN: 1563477807.

[2] Gu, S. and Olivier, H. "Capabilities and Limitations of Existing Hypersonic Facilities." In: *Progress in Aerospace Sciences* 113 (2020). DOI: `https://doi.org/10.1016/j.paerosci.2020.100607`.

[3] Hornung, H. "28th Lanchester Memorial Lecture - Experimental Real-Gas Hypersonics." In: *The Aeronautical Journal* 92.920 (1988), pp. 379–389. DOI: `https://doi.org/10.1017/S0001924000016511`.

[4] White, F. *Viscous Fluid Flow*. McGraw-Hill Series in Mechanical Engineering. McGraw-Hill, 1991. ISBN: 0001259002128.

[5] Olivier, H. and Gu, S. "Operation, Capabilities and Limitations of Existing Hypersonic Facilities." In: *Flow Characterization and Modeling of Hypersonic Wind Tunnels*. Vol. STO-AVT-VKI Lecture Series 2018/19 - AVT 325. von Karman Institute for Fluid Dynamics, Rhode Saint Genèse, Belgium, Mar. 2018.

[6] Hirschel, E. *Basics of Aerothermodynamics*. AIAA, 2005. ISBN: 3-540-22132-8.

[7] Oertel, H. *Stossrohre*. Springer, 1966. ISBN: 3211807748.

[8] Anderson, J. *Modern Compressible Flow with Historical Perspective*. McGraw-Hill Series in Aeronautical and Aerospace Engineering. McGraw-Hill, 1990. ISBN: 0-07-001673-9.

[9] Gordon, S. and McBride, B. *Computer Program for Calculation of Complex Chemical Equilibrium Compositions and Applications, I: Analysis, II: Users Manual and Program Description*. Tech. rep. NASA Reference Publication 1311. NASA Lewis Research Center, Cleveland, OH, USA, 1994.

[10] Holden, M., Wadhams, T., MacLean, M., Mundy, E., and Parker, R. "Experimental Studies in LENS I and X to evaluate Ral Gas Effects on Hypervelocity Vehicle Performance." In: *45th AIAA Aerospace Sciences Meeting and Exhibit*. Vol. AIAA 2007-204. Reno, NV, USA, Aug. 2007. DOI: `https://doi.org/10.2514/6.2007-204`.

[11] Gildfind, D. "Development of High Total Pressure Scramjet Flow Conditions using the X2 Expansion Tube." PhD Thesis. The University of Queensland, Australia, 2012.

[12] Crombrugghe, G. de, Gildfind, D., Zander, F., McIntyre, T., and Morgan, R. "Design of Test Flows to Investigate Binary Scaling in High Enthalpy CO2-N2 Mixtures." In: *19th Australasian Fluid Mechanics Conference*. Melbourne, VIC, Australia, Aug. 2014. ISBN: 9780646596952.

[13] Gildfind, D., Jacobs, P., Gollan, R., Toniato, P., McIntyre, T., Adrianatos, A., James, C., and Morgan, R. "Flow Characterization and Numerical Modeling of the DLR High-Enthalpy Shock Tunnel Göttingen (HEG)." In: *Flow Characterization and Modeling of Hypersonic Wind Tunnels*. Vol. STO-AVT-VKI Lecture Series 2018/19 - AVT 325. von Karman Institute for Fluid Dynamics, Rhode Saint Genèse, Belgium, Mar. 2018.

[14]   Schneider, S. "Effects of High-Speed Tunnel Noise on Laminar-Turbulent Transition." In: *Journal of Spacecrafts and Rockets* 38.3 (2001), pp. 323–333. DOI: `https://doi.org/10.2514/2.3705`.

[15]   Muylaert, J., Walpot, L., and Vennemann, D. "A Review of European Code-Validation Studies in High-Enthalpy Flow." In: *Philosophical Transactions: Mathematical, Physical and Engineering Sciences* 357.1759 (1999), pp. 2249–2278. DOI: `https://doi.org/10.1098/rsta.1999.0430`.

[16]   Holden, M., Wadhams, T., Smolinski, G., MacLean, M., Harvey, J., and Walker, B. "Experimental and Numerical Studies on Hypersonic Vehicle Performance in the LENS Shock and Expansion Tunnels." In: *44th AIAA Aerospace Sciences Meeting and Exhibit*. Vol. AIAA 2006-0125. Reno, NV, USA, Sept. 2006. DOI: `https://doi.org/10.2514/6.2006-125`.

[17]   MacLean, M., Candler, G., and Holden, M. "Numerical Evaluation of Flow Conditions in the LENS Reflected Shock-Tunnel Facilities." In: *43rd AIAA Aerospace Sciences Meeting and Exhibit*. Vol. AIAA 2005-903. Reno, NV, USA, Oct. 2005. DOI: `https://doi.org/10.2514/6.2005-903`.

[18]   Simeonides, G. "Generalized Reference Enthalpy Formulations and Simulation of Viscous Effects in Hypersonic Flow." In: *Shock Waves* 8.3 (1998), pp. 161–172. DOI: `https://doi.org/10.1007/s001930050109`.

[19]   Olivier, H. "An improved Method to determine Free Stream Conditions in Hypersonic Facilities." In: *Shock Waves* 3 (1993), pp. 129–139. DOI: `https://doi.org/10.1007/BF02115892`.

[20]   Verant, J. and Sagnier, P. "Assessment of Total Conditions and Flow Thermochemical Nature in the Onera F4 High Enthalpy Wind Tunnel." In: *19th AIAA Advanced Measurement and Ground Testing Technology Conference*. Vol. AIAA 96-2239. New Orleans, LA, USA, 17-20 June 1996. DOI: `https://doi.org/10.2514/6.1996-2239`.

[21]   MacLean, M. and Holden, M. "Numerical Assessment of Data in Catalytic and Transitional Flows for Martian Entry." In: *9th AIAA/ASME Joint Thermophysics and Heat Transfer Conference*. Vol. AIAA 2006-2946. San Francisco, CA, USA, May 2006. DOI: `https://doi.org/10.2514/6.2006-2946`.

[22]   Jacobs, P. "Quasi-One-Dimensional Modeling of a Free-Piston Shock Tunnel." In: *AIAA Journal* 32.1 (1994), pp. 137–145. DOI: `https://doi.org/10.2514/3.11961`.

[23]   Esser, B. "Die Zustandsgrößen im Stosswellenkanal als Ergebnis eines exakten Riemannlösers." PhD Thesis (German). RWTH-Aachen University, Germany, 1991.

[24]   Eitelberg, G., Beck, W., Schneider, M., Chue, R., and Widdecke, N. "Performance Comparison of the Conical and Contoured Nozzle in the HEG." In: *20th AIAA Advanced Measurement and Ground Testing Technology Conference*. Vol. AIAA 98-2773. Albuquerque,NM, USA, 15-18 June 1998. DOI: `https://doi.org/10.2514/6.1998-2773`.

[25] McIntosh, M. *Computer Program for the Numerical Calculation of Frozen and Equilibrium Conditions in Shock Tunnels*. Tech. rep. Technical Note CPD 169. Department of Supply, Australien Defence Scientific Service, Weapons Research Establishment, Australia, 1970.

[26] Lordi, J., Mates, R., and Moselle, J. *Computer Program for the Numerical Solution of Nonequiblibrium Expansions of Reacting Gas Mixtures*. Tech. rep. CAL-Report AD-1689-A-6. Cornell Aeronautical Laboratory, Buffalo, NY, USA, 1965.

[27] McGilvray, M., Dann, A., and Jacobs, P. "Modelling the Complete Operation of a Free-Piston Shock Tunnel for a Low Enthalpy Condition." In: *Shock Waves* 23 (2013), pp. 399–407. DOI: `https://doi.org/10.1007/s00193-013-0437-8`.

[28] Candler, G. "Hypersonic Nozzle Analysis Using an Excluded Volume Equation of State." In: *38th AIAA Thermophysics Conference*. Vol. AIAA 2005-5202. Toronto, Ontario, USA, June 1998. DOI: `https://doi.org/10.2514/6.2005-5202`.

[29] Park, C. "Assessment of Two-Temperature Kinetic Model for Ionizing Air." In: *AIAA Journal of Thermophysics and Heat Transfer* 3.3 (1989), pp. 233–244. DOI: `https://doi.org/10.2514/3.28771`.

[30] Walpot, L., Simeonides, G., and Muylaert, J. "High Enthalpy Nozzle Flow Sensitivity Study and Effects on Heat Transfer." In: *Shock Waves* 6 (1996), pp. 197–204. DOI: `https://doi.org/10.1007/BF02511376`.

[31] Lordi, J. and Mates, R. *Non-Equilibruim Expansions of High-Enthalpy Airflows*. Tech. rep. ARL 64-206. Cornell Aeronautical Laboratory, Buffalo, NY, USA, 1964.

[32] Fay, J. and Riddell, F. "Theory of Stagnation Point Heat Transfer in Dissociated Air." In: *Journal of the Aeronautical Sciences* 25.2 (1958), pp. 73–85. DOI: `https://doi.org/10.2514/8.7517`.

[33] Sutton, K. and Graves, R. *A General Stagnation-Point Convective-Heating Equation for Artibrary Gas Mixtures*. Tech. rep. NASA-TR-R-376, L-7885. NASA Langley Research Center, Hampton, VA, USA, 1971.

[34] Verant, J. *Numerical Enthalpies Rebuilding for Perfect Gas and Non-Equilibrium Flows. Application to High Enthalpy Wind Tunnels*. Tech. rep. ONERA RT 69/6121 SY. ONERA, Chatillon, France, 1994.

[35] Edney, B. "Temperature Measurements in a Hypersonic Gun Tunnel using Heat-Transfer Methods." In: *Journal of Fluid Mechanics* 27.3 (1967), pp. 503–512. DOI: `https://doi.org/10.1017/S0022112067000503`.

[36] Buttsworth, D. and Jones, T. "High Bandwidth Stagnation Temperature Measurements in a Mach 6 Gun Tunnel Flow." In: *Experimental Thermal and Fluid Science* 27.2 (2003), pp. 177–186. DOI: `https://doi.org/10.1016/S0894-1777(02)00281-9`.

[37] Bonham, C., Thorpe, S., Erlund, M., and Stevenson, R. "Stagnation Temperature Measurement using Thin-Film Platinum Resistance Sensors." In: *Measurement Science and Technology* 25 (2014), pp. 1–16. DOI: `http://doi.org/10.1088/0957-0233/25/1/015101`.

[38] Parker, R., Wakeman, T., MacLean, M., and Holden, M. "Measuring Nitric Oxide Freestream Concentration Using Quantum Cascade Lasers at CUBRC." In: *44th AIAA Aerospace Sciences Meeting and Exhibit*. Vol. AIAA 2006-926. Reno, NV, USA, Sept. 2006. DOI: `https://doi.org/10.2514/6.2006-926`.

[39] Simmons, J. "Measurement Techniques in High-Enthalpy Hypersonic Facilities." In: *Experimental Thermal and Fluid Science* 10.4 (1995), pp. 454–469. DOI: `https://doi.org/10.1016/0894-1777(94)00066-H`.

[40] Parker, R., Wakeman, T., MacLean, M., and Holden, M. "Measuring Nitric Oxide Freestream Velocity Using Quantum Cascade Lasers at CUBRC." In: *45th AIAA Aerospace Sciences Meeting and Exhibit*. Vol. AIAA 2007-1329. Reno, NV, USA, Aug. 2007. DOI: `https://doi.org/10.2514/6.2007-1329`.

[41] Schemperg, K. "Gasdynamische Auslegung und Entwicklung des kolbengetriebenen Stosswellenkanals HELM." PhD Thesis (German). University of the federal armed Forces Munich, Germany, 2009.

[42] Altenhoefer, P. "Aufbau und Anwendung eines LIGS-Messsystemss am Stosswellenkanal HELM." PhD Thesis (German). University of the federal armed Forces Munich, Germany, 2017. ISBN: 978-3-8439-3103-8.

[43] Nishida, M. *Shock Tubes, in Handbook of Shock Waves - Volume 1, Theoretical, Epxerimental, and Numerical Techniques*. Ed. by Ben-Dor, G., Igra, O., and Elperin, T. Academic Press, 2001. ISBN: 0-12-086431-2.

[44] Hornung, H. "Performance Data of the New Free-Piston Shock Tunnel at GALCIT." In: *28th Joint Propulsion Conference and Exhibit*. Nashville, TN, USA, June 1992. DOI: `https://doi.org/10.2514/6.1992-3943`.

[45] Mirels, H. *Attenuation in a Shock Tube Due to Unsteady-Boundary-Layer Action*. Tech. rep. NACA Technical Report TN 1333. NACA, USA, 1957.

[46] Itoh, K., Ueda, S., Komura, T., Sato, K., Takahashi, M., Miyajima, H., Tanno, H., and Muramoto, H. "Improvement of a Free Piston Driver for a High-Enthalpy Shock Tunnel." In: *Shock Waves* 8 (1998), pp. 215–233. DOI: `https://doi.org/10.1007/s001930050115`.

[47] Tanno, H., Itoh, K., Komuro, T., and Sato, K. "Experimental Study on the Tuned Operation of a Free Piston Driver." In: *Shock Waves* 10 (2000), pp. 1–7. DOI: `https://doi.org/10.1007/s001930050174`.

[48] Gildfind, D., Morgan, R., McGilvray, M., Jacobs, P., Stalker, R., and Eichmann, T. "Free-Piston Driver Optimisation for Simulation of High Mach Number Scramjet Flow Conditions." In: *Shock Waves* 21 (2011), pp. 559–572. DOI: `https://doi.org/10.1007/s00193-011-0336-9`.

[49] Hannemann, K., Itoh, K., Mee, D., and Hornung, H. *Free Piston Shock Tunnels HEG, HIEST, T4 and T5 in: Experimental Methods of Shock Wave Research*. Ed. by Igra, O. and Seiler, F. Springer, 2015, pp. 181–264. DOI: `https://doi.org/10.1007/978-3-319-23745-9`.

[50] Hornung, H. and Bélanger, J. "Role and Techniques of Ground Testing for Simulation of Flows up to Orbital Speed." In: *16th Aerodynamic Ground Testing Conference*. Seattle, WA, USA, 18-20 June 1990. DOI: https://doi.org/10.2514/6.1990-1377.

[51] Itoh, K. "Private Communication." In: 20 October 2020.

[52] Stalker, R. "A Study of the Free-Piston Shock Tunnel." In: *AIAA Journal* 5.12 (1967), pp. 2160–2165. DOI: https://doi.org/10.2514/3.4402.

[53] Hornung, H. *The Piston Motion in a Free-Piston Driver for Shock Tubes and Tunnels*. Tech. rep. FM 88-1. Graduate Aeronautical Laboratories, California Institute of Technology, Pasadena, CA, USA, 1970.

[54] Mundt, Ch. and Altenhoefer, P. "Study of Numerical Simulations for Optimized Operation of the Free Piston Shock Tunnel HELM." In: *15th AIAA International Space Planes and Hypersonic Systems and Technologies Conference*. Vol. IWSST. Dayton, OH, USA, 28 April - 1 May 2008. DOI: https://doi.org/10.2514/6.2008-2653.

[55] Gardner, A. *HyShot Scramjet Testing in the HEG*. Tech. rep. Technical Report DLR-FB 2007-14. DLR Göttingen, Germany, 2007. URL: https://elib.dlr.de/51689.

[56] DKI (Deutsches Kupferinstitut Berufsverband e.V.) *Kupfer-Aluminium-Legierungen*. Tech. rep. Informationsdruck i.6. DKI , Düsseldorf, Germany, 2010. URL: www.kupferinstitut.de/kupferwerkstoffe/kupfer-legierungen/kupfer-aluminium-legierungen.

[57] Jacobs, P. and Gardner, A. *Gas-Dynamic Modelling of the HEG Shock Tunnel*. Tech. rep. Technical Report DLR-IB 224 - 2003 A 02. DLR Göttingen, Germany, 2003. URL: https://www.researchgate.net/publication/244483647_Gas-dynamic_modelling_of_the_HEG_shock_tunnel.

[58] Krek, R. and Eitelberg, G. *Calibration of the HEG Facility at High Compression Ratios*. Tech. rep. Technical Report IB 223-96 A 19. DLR Göttingen, Germany, 1996. URL: https://elib.dlr.de/37443.

[59] Byrne, T. "A Piston Braking Model for the L1d CFD Code." Bachelor Thesis. The University of Queensland, Australia, 2016. URL: https://core.ac.uk/download/pdf/83976938.pdf.

[60] Doherty, L. "An Experimental Investigation of an Airframe Integrated Three-Dimensional Scramjet Engine at a Mach 10 Flight Condition." PhD Thesis. The University of Queensland, Australia, 2014.

[61] Itoh, K., Komura, T., Sato, K., Ueda, S., Tanno, H., and Takahashi, M. "Characteristics of the Free-Piston Shock Tunnel HIEST (1st Report, Tuned Operation of Free-Piston Driver)." In: *Transactions of the Japan Society of Mechanical Engineers, Part B* 68 (675 2002), pp. 2968–2975. DOI: https://doi.org/10.1299/kikaib.68.2968.

[62] Selcan, C., Sander, T., Altenhoefer, P., Koroll, F., and Mundt, Ch. "Stagnation Temperature Measurements in a Shock-Tunnel Facility using Laser-Induced Grating Spectroscopy." In: *AIAA Journal of Thermophysics and Heat Transfer* 32.1 (2016), pp. 1–11. DOI: `https://doi.org/10.2514/1.T5199`.

[63] Rothkopf, E. and Low, W. "Diaphragm Opening Process in Shock Tubes." In: *Physics of Fluids* 17 (6 1974), p. 1169. DOI: `https://doi.org/10.1063/1.1694860`.

[64] Mundt, Ch., Boyce, R., Jacobs, P., and Hannemann, K. "Validation Study of Numerical Simulations by Comparison to Measurements in Piston-Driven Shock-Tunnels." In: *Aerospace Science and Technology* 11 (2-3 2007), pp. 100–109. DOI: `https://doi.org/10.1016/j.ast.2006.12.002`.

[65] Smith, L. "Numerical Simulation of the HELM Shock Tunnel for Martian Entry Conditions." ENGG7280 Thesis Project. The University of Queensland, Australia, 2015.

[66] Ilich, Z. and Grossir, G. "Private Communication." In: Mar. 2018.

[67] Häußlein, L. "Optimierung des L1d-Modells für die Auslegung von Betriebskonditionen des Stoßwellenkanals HELM." Bachelor Thesis B-18/53-CS (German). Institute for Thermodynamics, University of the federal armed Forces Munich, Germany, 2019.

[68] Häußlein, L. "Auslegung von Betriebszuständen eines Helium/Argon-Treibers des Stoßwellenkanals HELM mittels L1d." Project Thesis P-19/38-CS (German). Institute for Thermodynamics, University of the federal armed Forces Munich, Germany, 2020.

[69] Kruijssen, L. van der. "Weiterentwicklung des L1d-Modells für Betriebskonditionen des Stoßwellenkanals HELM." Bachelor Thesis B-19/60-CS (German). Institute for Thermodynamics, University of the federal armed Forces Munich, Germany, 2020.

[70] Kruijssen, L. van der. "Berechnung und Bewertung von Betriebspunkten für den freien Kolbentreiber des Stoßwellenkanals HELM." Project Thesis P-20/46-CS (German). Institute for Thermodynamics, University of the federal armed Forces Munich, Germany, 2021.

[71] Atcitty, C. and McIntyre, T. *Pistons and Compression Tubes - Piston Motion in the High Enthalpy Shock Tunnel (HEG)*. Tech. rep. Technical Report DLR-IB 222 - 90 C 20. DLR Göttingen, Germany, 1991. URL: `https://elib.dlr.de/36807`.

[72] Bélanger, J. and Hornung, H. "Numerical Predictions and Actual Behavior of the Free Piston Shock Tunnel T5." In: *25th Plasmadynamics and Lasers Conference*. Colorado Springs, CO, USA, 20-23 June 1994. DOI: `https://doi.org/10.2514/6.1994-2527`.

[73] Byrne, T. "Modeling Piston Motion in T-ADFA Free Piston Shock Tunnel." Report. UNSW Canberra at the Australian Defence Force Academy, Canberra, Australia, 2008. URL: `https://ojs.unsw.adfa.edu.au/index.php/juer/article/download/137/96`.

[74] Zhixian, B., Bingbing, Z., Hao, Z., Xing, C., Junmuo, S., Chen, L., and Riming, S. "Experiments and Computations on the Compression Process in the Free Piston Shock Tunnel FD21." In: *5th International Conference on Experimental Fluid Mechanics –ICEFM*. Munich, Germany, Feb. 2018. URL: `https://athene-forschung.unibw.de/doc/124228/124228.pdf`.

[75] Mizoguchi, M. and Aso, S. "The Effect of Diaphragm Opening Time on the Feasibility of Tuned Operation in Free Piston Shock Tunnels." In: *Shock Waves* 19 (2009), pp. 337–347. DOI: `https://doi.org/10.1007/s00193-009-0214-x`.

[76] Gildfind, D., Jacobs, P., Gollan, R., Toniato, P., McIntyre, T., Adrianatos, A., James, C., and Morgan, R. "Flow Characterization and Modeling of the X2 and X3 Expansion Tubes." In: *Flow Characterization and Modeling of Hypersonic Wind Tunnels*. Vol. STO-AVT-VKI Lecture Series 2018/19 - AVT 325. von Karman Institute for Fluid Dynamics, Rhode Saint Genèse, Belgium, Mar. 2018.

[77] Outa, E., Tajima, K., and Hayakawa, K. *Shock Tube Flow Influenced by Diaphragm Opening (Two-Dimensional Flow near the Diaphragm), in Proceedings of the 10th International Symposium on Shock Waves and Shock Tubes*. International Shock Wave Institute, 1975, pp. 312–319.

[78] Gildfind, D., Hines, T., Jacobs, P., Stennett, S., and Dimitrijevic, I. "Use of Acceleration and Optical Waypoint Measurements to Estimate Piston Trajectory in an Impulse Facility." In: *Shock Waves* 29 (2019), pp. 873–899. DOI: `https://doi.org/10.1007/s00193-018-0877-2`.

[79] Edwards, T. "An Improved Wavelet Correction for Zero Shifted Accelerometer Data." In: *Shock and Vibration* 10 (2003), pp. 159–167. DOI: `https://doi.org/10.1155/2003/972829`.

[80] Selcan, C., Sander, T., and Mundt, Ch. "In situ Nozzle Reservoir Thermometry by Laser-Induced Grating Spectroscopy in the HELM Free-Piston Reflected Shock Tunnel." In: *Shock Waves* xx (2020), pp. 1–11. DOI: `https://doi.org/10.1007/s00193-020-00982-9`.

[81] Danehy, P., Bathel, B., Johansen, C., Winter, M., O'Byrne, S., and Cutler, A. *Molecular-Based Optical Diagnostics for Hypersonic Nonequilibrium Flows, in: Hypersonic Nonequilibrium Flows: Fundamentals and Recent Advances*. Ed. by Josyula, E. AIAA, Reston, VA, USA, 2015, pp. 343–470. DOI: `https://doi.org/10.2514/5.9781624103292.0343.0470`.

[82] Eckbreth, A. *Laser Diagnostics for Combustion Temperature and Species*. Taylor and Francis, 1996. ISBN: 9056995324.

[83] Boyce, R., Pulford, D., Houwing, A., and Mundt, Ch. "Rotational and Vibrational Temperature Measurements using CARS in a Hypervelocity Shock Layer Flow and Comparisons with CFD Calculations." In: *Shock Waves* 6.1 (2009), pp. 41–51. DOI: `https://doi.org/10.1007/BF02511403`.

[84] Pulford, D., Newman, D., and Houwing A. Sandeman, R. "The Application of Coherent Anti-Stokes Raman Scattering to Temperature Measurements in a Pulsed High Enthalpy Supersonic Flow." In: *Shock Waves* 4.3 (1994), pp. 119–125. DOI: `https://doi.org/10.1007/BF01417427`.

[85] Grisch, F., Bouchardy, P., and Clauss, W. "CARS Thermometry in High Pressure Rocket Combustors." In: *Aerospace Science and Technology* 7.4 (2003), pp. 317–330. DOI: `https://doi.org/10.1016/S1270-9638(03)00017-8`.

[86] Danehy, P., Palma, P., Houwing, A., and McIntyre, T. "Comparison of Theoretical Laser-Induced Fluorescence Images with Measurements performed in a Hypersonic Shock Tunnel." In: *AIAA Advanced Measurement and Ground Testing Technology Conference*. Vol. AIAA 96-2236. New Orleans, LA, USA, 17-20 June 1996. DOI: `https://doi.org/10.2514/6.1996-2236`.

[87] Sutton, D., Houwing, A., Palma, P., and Sandeman, R. "Vibrational Temperature Measurements in a Shock Layer using Laser Induced Predissociation Fluorescence." In: *Shock Waves* 3 (1993), pp. 141–148. DOI: `https://doi.org/10.1007/BF02115893`.

[88] Palmer, J., McMillin, B., and Hanson, R. "Planar Laser-Induced Fluorescence Imaging of Velocity and Temperature in Shock Tunnel Free Jet Flow." In: *30th Aerospace Sciences Meeting and Exhibit*. Reno, NV, USA, June 1992. DOI: `https://doi.org/10.2514/6.1992-762`.

[89] Laux, C., Spence, T., Kruger, C., and Zare, R. "Optical Diagnostics of Atmospheric Air Plasmas." In: *Plasma Sources Science and Technology* 12.2 (2003), pp. 125–138. DOI: `https://doi.org/10.1088/0963-0252/12/2/301`.

[90] Nomura, S. and Komurasaki, K. "Translational Temperature Measurements in a Shock Layer by Point-Measurement Laser Absorption Spectroscopy." In: *AIAA Journal of Thermophysics and Heat Transfer* 29.4 (2015), pp. 649–652. DOI: `https://doi.org/10.2514/1.T4498`.

[91] Fantoni, R., De Dominics, L., Giorgi, M., and Williams, R. "Pressure Dependence of Degenerate Four-Wave Mixing in NO and NO2: Effects of Population and Thermal Gratings." In: *Chemical Physics Letters* 259.3-4 (1996), pp. 342–346. DOI: `https://doi.org/10.1016/0009-2614(96)00796-8`.

[92] Danehy, P., Farrow, R., Lucht, R., and Reichardt, T. "Degenerate Four-Wave Mixing Velocimetry and Translational Temperature Measurements." In: 3 (1999), pp. 756–757. DOI: `https://doi.org/10.1109/CLEOPR.1999.817817`.

[93] Danehy, P., Farrow, R., Lucht, R., and Reichardt, T. "Thermal-Grating Contributions to Degenerate Four-Wave Mixing in Nitric Oxide." In: 12.9 (1995), pp. 1564–1576. DOI: `https://doi.org/10.1364/JOSAB.12.001564`.

[94] Cummings, E. "Laser-Induced Thermal Acoustics: Simple Accurate Gas Measurements." In: *Optics Letters* 19.17 (1994), pp. 1361–1363. DOI: `https://doi.org/10.1364/OL.19.001361`.

[95] Sander, T., Altenhoefer, P., and Mundt, Ch. "Development of Laser-Induced Grating Spectroscopy for Application in Shock Tunnels." In: *AIAA Journal of Thermophysics and Heat Transfer* 28.1 (2014), pp. 27–31. DOI: `https://doi.org/10.2514/1.T4131`.

[96] Latzel, H., Dreizler, A., Dreier T. Heinze, J., Dillmann, M., Stricker, W., Lloyd, G., and Ewart, P. "Thermal Grating and Broadband Degenerate Four-Wave Mixing Spectroscopy of OH in High-Pressure Flames." In: *Applied Physics B* 67 (1998), pp. 667–673. DOI: `https://doi.org/10.1007/s003400050563`.

[97] Sander, T., Altenhoefer, P., and Mundt, Ch. "Temperature Measurements in a Shock Tube Using Laser-Induced Grating Spectroscopy." In: *AIAA Journal of Thermophysics and Heat Transfer* 30.1 (2016), pp. 62–66. DOI: `https://doi.org/10.2514/1.T4556`.

[98] McIntyre, T., Kleine, H., and Houwing, A. "Optical Imaging Techniques for Hypersonic Impulse Facilities." In: *The Aeronautical Journal* 111.1115 (2007), pp. 1–16. DOI: `https://doi.org/10.1017/S0001924000001718`.

[99] Cummings, E., Leyva, I., and Hornung, H. "Laser-Induced Thermal Acoustics (LITA) Signals from Finite Beams." In: *Applied Optics* 34.18 (1995), pp. 3290–3302. DOI: `https://doi.org/10.1364/AO.34.003290`.

[100] Mizukaki, T. and Matsuzawa, T. "Application of Laser-Induced Thermal Acoustics in Air to Measurement of Shock-Induced Temperature Changes." In: *Shock Waves* 19.5 (2009), pp. 361–369. DOI: `https://doi.org/10.1007/s00193-009-0218-6`.

[101] Foerster, F., Baab, S., Lamanna, G., and Weigand, B. "Temperature and Velocity Determination of Shock-Heated Flows with Non-Resonant Heterodyne Laser-Induced Thermal Acoustics." In: *Applied Physics B* 121.3 (2015), pp. 235–248. DOI: `https://doi.org/10.1007/s00340-015-6217-7`.

[102] Eichler, H., Günter, P., and Pohl, D. *Laser-Induced Dynamic Gratings*. Springer, 1986. ISBN: 978-3-540-39662-8. DOI: `https://doi.org/10.1007/978-3-540-39662-8`.

[103] Sander, T. "Optische Messmethoden in der Aerothermodynamik/Thermofluiddynamik." Habilitation (German). University of the federal armed Forces Munich, Germany, 2016. ISBN: 978-3-943207-18-7.

[104] Lemmon, E., Jacobsen, R., Penoncello, S., and Friend, D. "Thermodynamic Properties of Air and Mixtures of Nitrogen, Argon, and Oxygen from 60 to 2000 K at Pressures to 2000 MPa." In: *Journal of Physical and Chemical Reference Data* 29.3 (2000), pp. 331–385. DOI: `https://doi.org/10.1063/1.1285884`.

[105] Schlamp, S., Cummings, E., and Hornung, H. "Beam Misalignments and Fluid Velocities in Laser-Induced Thermal Acoustics." In: *Applied Optics* 38.27 (1999), pp. 5724–5733. DOI: `https://doi.org/10.1364/AO.38.005724`.

[106] Richter, J., Mayer, J., and Weigand, B. "Accuracy of Non-Resonant Laser-Induced Thermal Acoustics (LITA) in a Convergent–Divergent Nozzle Flow." In: *Applied Physics B* 124.19 (2018). DOI: https://doi.org/10.1007/s00340-017-6885-6.

[107] Altenhoefer, P., Sander, T., Koroll, F., and Mundt, Ch. "LIGS Measurements in the Nozzle Reservoir of a Free Piston Shock Tunnel." In: *Shock Waves* 29 (2019), pp. 307–320. DOI: https://doi.org/10.1007/s00193-018-0808-2.

[108] Selcan, C., Altenhöfer, P., Sander, T., and Mundt, Ch. "Recent Progress towards High-Temperature Gasdynamics in the Free-Piston Shock Tunnel HELM." In: *11th International Workshop on Shock Tube Technology (IWSTT)*. DLR Göttingen, Germany, June 2016.

[109] Menevidis, K. "Maßnahmen zur Optimierung des Anlagenbetriebs des Hochenthalpie Labors München zur Anwendung der Laser induzierten Gitterspektroskopie." Master Thesis M-18/40-CS (German). Institute for Thermodynamics, University of the federal armed Forces Munich, Germany, 2018.

[110] Selcan, C., Sander, T., Thele, M., and Mundt, Ch. "Research Status and Recent Results in the HELM Shock-Tunnel." In: *12th International Workshop on Shock Tube Technology (IWSTT)*. JAXA Kakuda, Japan, Apr. 2018.

[111] Eibl, S. "WIWeB Technical Communication, Wehrwissenschaftliches Institut für Wehr- und Betriebsstoffe, Erding, Germany." In: 2017.

[112] Tanno, H. "Private Communication." In: 2018.

[113] Vetter, M. "Hyperschallumströmung von Modellen im Stoßwellenkanal." PhD Thesis (German). RWTH-Aachen University, Germany, 1993. ISBN: 3-925714-81-2.

[114] Mundt, Ch. *Development of the New Piston-Driver Shock Tunnel HELM in: Experimental Methods of Shock Wave Research*. Ed. by Igra, O. and Seiler, F. Springer, 2016, pp. 181–264. DOI: https://doi.org/10.1007/978-3-319-23745-9.

[115] Manning, W. and Labrow, S. *High Pressure Engineering*. Leonard Hill, London, 1971. ISBN: 0-249-44035-0.

[116] GWI Sapphire. *Technical Datasheet of Monochrystalline Sapphire*. 2019. URL: https://sappro.de/wp-content/uploads/2019/05/TDB-Saphir.pdf.

[117] Rumpel, G. and Sondershausen, H. *Festigkeitslehre in: Dubbel - Taschenbuch für den Maschinenbau*. Ed. by Beitz, W. and Küttner, K. 15th ed. Springer, 1983. ISBN: 3-540-12418-7.

[118] Sherman, W. and Stadtmuller, A. *Experimental Techniques in High-Pressure Research*. John Wiley and Sons, 1987. ISBN: 0-471-10313-6.

[119] Schneider, W., Moortgat, G., Tyndall, G., and Burrows, J. "Absorption Cross-Sections of NO2 in the UV and Visible Region (200–700 nm) at 298 K." In: *Journal of Photochemistry and Photobiology A: Chemistry* 40.2-3 (1987), pp. 195–217. DOI: https://doi.org/10.1016/1010-6030(87)85001-3.

[120] Hsu, D., Monts, D., and Zare, R. *Spectral Atlas of Nitrogen Dioxide 5330 to 6480 Å*. Academic Press, New York, 1978. ISBN: 0123579503.

[121] Schlamp, S., Rösgen, T., Kozlov, D., Rakut, C., Kasal, P., and Wolfersdorf, J. von. "Transient Grating Spectroscopy in a Hot Turbulent Compressible Free Jet." In: *Journal of Propulsion and Power* 21.6 (2005), pp. 1008–1018. DOI: https://doi.org/10.2514/1.13794.

[122] Balla, R. and Miller, C. *Signal Analysis Algorithms for Optimized Fitting of Nonresonant Laser Induced Thermal Acoustics Damped Sinusoids*. Tech. rep. NASA/TM-2008-215327. NASA Langley Research Center, Hampton, VA, USA, 2008.

[123] Schlamp, S., Hornung, H., Sobota, T., and Cummings, E. "Accuracy and Uncertainty of Single-Shot, Nonresonant Laserinduced Thermal Acoustics." In: *Applied Optics* 39.30 (2000), pp. 5477–5481. DOI: https://doi.org/10.1364/AO.39.005477.

[124] Koroll, F. "Konzeption und Realisierung eines LIGS-Aufbaus am Stoßwellenkanal HELM." Master Thesis M-15/23-PA (German). Institute for Thermodynamics, University of the federal armed Forces Munich, Germany, 2015.

[125] Voigt, F. "Messgenauigkeit und Fehleranalyse der Laser-Induzierten Gitterspektroskopie am Stoßwellenkanal HELM." Master Thesis M-19/48-CS (German). Institute for Thermodynamics, University of the federal armed Forces Munich, Germany, 2019.

[126] Kline, S. and McClintock, F. "Describing Uncertainties in Single Sample Experiments." In: *Journal of Mechanical Engineering* 75 (1953), pp. 3–8.

[127] Moffat, R. "Describing the Uncertainties in Experimental Results." In: *Experimental Thermal and Fluid Science* 1 (1 1988), pp. 3–17. DOI: https://doi.org/10.1016/0894-1777(88)90043-X.

[128] Peterson, E. and Hanson, R. "Nonideal Effects Behind Reflected Shock Waves in a High-Pressure Shock Tube." In: *Shock Waves* 10 (6 2001), pp. 405–420. DOI: https://doi.org/10.1007/PL00004051.

[129] Blackman, V. "Vibrational Relaxation in Oxygen and Nitrogen." In: *Journal of Fluid Mechanics* 1.1 (1956), pp. 61–85. DOI: https://doi.org/10.1017/S0022112056000056.

[130] Vincenti, W. and Kruger, C. *Introduction to Physical Gas Dynamics*. Krieger Publishing Company, New York, 1977. ISBN: 0882753096.

[131] Selcan, C., Sander, T., and Mundt, Ch. "Nozzle Reservoir Thermometry by LIGS in the HELM Free Piston Reflected Shock Tunnel." In: *32nd International Symposium on Shock Waves (ISSW)*. NUS Singapore, Singapore, July 2019.

[132] Greiner, L. "WIWeB Technical Communication, Wehrwissenschaftliches Institut für Wehr- und Betriebsstoffe, Erding, Germany." In: 2020.

[133] Eitelberg, G., Beck, W., Carl, M., and Widdecke, N. *Free Stream Nozzle Flow in the HEG*. Tech. rep. Technical Report DLR-IB 223 - 97 A 13. DLR Göttingen, Germany, 1991.

[134] Habermann, M. "Erzeugung von Hochenthalpieströmungen im Hyperschall mit einem Detonationsgetriebenen Stoßwellenkanal." PhD Thesis (German). RWTH-Aachen University, Germany, 2001. ISBN: 3-925714-81-2.

[135] Slotnick, J., Khodadoust, A., Alonso, J., Darmofal, D., Gropp, W., Lurie, E., and Mavriplis, D. *CFD Vision 2030 Study: A Path to Revolutionary Computational Aerosciences*. Tech. rep. NASA Technical Report CR–2014-218178. NASA Langley Research Center, Hampton, VA, USA, 2014.

[136] Giese, T. "Kalibrierung der Anströmungsbedingungen und Charakterisierung der Störgrößen am Hochenthalpiekanal Göttingen (HEG)." Master Thesis (German). Technical University Berlin, Germany, 2013. URL: https://elib.dlr.de/82879.

[137] Stalker, R. and Crane, K. "Driver Gas Contamination in a High-Enthalpy Reflected Shock Tunnel." In: *AIAA Journal* 16.3 (1978), pp. 277–279. DOI: https://doi.org/10.2514/3.7520.

[138] Tokarcik-Polsky, S. and Cambier, J. "Numerical Study of Transient Flow Phenomena in Shock Tunnels." In: *AIAA Journal* 32 (5 2020). DOI: https://doi.org/10.2514/3.12082.

[139] MacLean, M., Dufrene, A., Wadhams, T., and Holden, M. "Numerical and Experimental Characterization of High Enthalpy Flow in an Expansion Tunnel Facility." In: *48th AIAA Aerospace Sciences Meeting*. Vol. AIAA 2010-1562. Orlando, FL, USA, Apr. 2010. DOI: https://doi.org/10.2514/6.2010-1562.

[140] Jacobs, P., Gollan, R., Potter, D., Zander, F., Gildfind, D., Blyton, P., Chan, W., and Doherty, L. *Estimation of High-Enthalpy Flow Conditions for Simple Shock and Expansion Processes using the ESTCj Program and Library*. Tech. rep. Mechanical Engineering Report 2011/02. Center for Hypersonics, The University of Queensland, Australia, 2014. URL: https://espace.library.uq.edu.au/view/UQ:321755.

[141] Park, C. "Evaluation of Real-Gas Phenomena in High-Enthalpy Impulse Test Facilities: A Review." In: *AIAA Journal of Thermophysics and Heat Transfer* 11.1 (1997), pp. 10–18. DOI: https://doi.org/10.2514/2.6217.

[142] Grossir, G., Hove, B. van, Paris, S., Rambaud, P., and Chazot, O. "Free-Stream Static Pressure Measurements in the Longshot Hypersonic Wind Tunnel and Sensitivity Analysis." In: *Experiments in Fluids* 57.64 (2016), pp. 1–13. DOI: https://doi.org/10.1007/s00348-016-2137-5.

[143] Kindl, H. "Einfluss des Treibergases auf die Strömung in Stoßwellenkanälen." PhD Thesis (German). RWTH-Aachen University, Germany, 2000. URL: https://d-nb.info/962853852/34.

[144] Rödiger, T., Knauss, H., Wagner, S., Kraemer, E., Bountin, D., Smorodsky, B., Chirkashenko, V., Zvegintsev, V., and Maslov, A. "The Atomic Layer Thermopile - A Fast Heat Flux Sensor for Measureing High Heat Loads in Short Duration Hypersonic Ground Testing

Facilities." In: *13th International Conference on Methods of Aerophysical Research ICMAR*. Akademgorodok, Novosibirsk, Russia, May 2007.

[145] Zoby, E. *Empirical Stagnation-Point Heat-Transfer Relation in Several Gas Mixtures at High Enthalpy Levels*. Tech. rep. NASA Technical Note D-4799. NASA Langley Research Center, Hampton, VA, USA, 1968.

[146] Tauber, M., Bowles, J., and Yang, L. "Use of Atmospheric Braking during Mars Missions." In: *AIAA Journal of Spacecraft and Rockets* 27 (5 1990), pp. 514–521. DOI: `https://doi.org/10.2514/3.26174`.

[147] Simeonides, G. *The VKI Hypersonic Wind Tunnels and Associated Measurement Techniques*. Tech. rep. Technical Memorandum 46. von Karman Institute for Fluid Dynamics, Rhode Saint Genèse, Belgium, 1990.

[148] Grossir, G., Dias, B., Chazot, O., and Magin, T. "High Temperature and Thermal Nonequilibrium Effects on the Determination of Free-Stream Flow Properties in Hypersonic Wind Tunnels." In: *Physics of Fluids* 30.126102 (2018), pp. 1–13. DOI: `https://doi.org/10.1063/1.5058098`.

[149] Cutler, A., Magnotti, G., Cantu, L., Gallo, E., Danehy, P., Baurle, R., Rockwell, R., Goyne, C., and McDaniel, J. "Measurement of Vibrational Nonequilibrium in a Supersonic Freestream Using Dual-Pump CARS." In: *28th Aerodynamic Measurement Technology, Ground Testing, and Flight Testing Conference*. Vol. AIAA 2012-3199. New Orleans, LA, USA, 25-28 June 2012. DOI: `https://doi.org/10.2514/6.2012-3199`.

[150] Ilich, Z., Grossir, G., and Chazot, O. "Evaluation of the Stagnation-Point Velocity Gradient in Low-Enthalpy Hypersonic Flows." In: *33rd AIAA Aerodynamic Measurement Technology and Ground Testing Conference*. Vol. AIAA 2017-3984. Denver, CO, USA, May 2017. DOI: `https://doi.org/10.2514/6.2017-3984`.

[151] Sagnier, P. and Verant, J. "Flow Characterization in the ONERA F4 High-Enthalpy Wind Tunnel." In: *AIAA Journal* 36.4 (1998), pp. 522–531. DOI: `https://doi.org/10.2514/2.425`.

[152] Fujiwara, Y., Tezuka, A., Shimamura, K., Okamoto, T., Yamada, K., Komuro, T., and Tanno, H. "Measurement of Stagnation Heat Flux in HEK-X Expansion Tube." In: *32nd International Symposium on Shock Waves (ISSW)*. NUS Singapore, Singapore, July 2019. DOI: `https://doi.org/10.3850/978-981-11-2730-4_0214-cd`.

[153] Lettl, M. "Methoden zur Nachbildung von Versuchskonditionen des Stoßwellenkanals HELM durch Messungen von Staupunkt-Wärmestrom und statischem Druck." Bachelor Thesis B-19/54-CS (German). Institute for Thermodynamics, University of the federal armed Forces Munich, Germany, 2019.

[154] Eitelberg, G., Krek, R., and Beck, W. "Stagnation Point Heat Transfer Testing in Non-Equilibrium Flow Produced by the HEG." In: *7th International Space Planes and Hypersonic Systems and Technologies Conference*. Vol. AIAA 96-4504. Norfolk, VA, USA, 18-22 September 1996. DOI: `https://doi.org/10.2514/6.1996-4504`.

[155] Lettl, M. "Vermessung der freien Anströmung zur rechnerischen Nachbildung von Versuchskonditionen des Stoßwellenkanals HELM." Project Thesis P-20/41-CS (German). Institute for Thermodynamics, University of the federal armed Forces Munich, Germany, 2020.

[156] Olivier, H., Grönig, H., and Schulze, B. "Instrumentation Techniques of the Aachen Shock Tunnel TH2." In: *19th International Congress on Instrumentation in Aerospace Simulation Facilities (ICIASF 95)*. Wright-Patterson AFB, OH, USA, 18-21 July 1995. DOI: `https://doi.org/10.1109/ICIASF.1995.519106`.

[157] Papinniemi, A. "Design, Development and Application of a Static Pressure Probe for Free-Piston Shock Tunnels." Student Thesis. Australian National University (ANU), Canberra, Australia, 1999.

[158] Grossir, G. "Longshot Hypersonic Wind Tunnel Flow Characterization and Boundary Layer Stability Investigations." PhD Thesis. von Karman Institute for Fluid Dynamics, Rhode Saint Genèse, Belgium, 2015. DOI: `https://doi.org/10.35294/phdt201505`.

[159] Groll, F. "Entwurf und Realisierung einer Totaltemperatur- und statischen Drucksonde zur Bestimmung der freien Anströmung des Stoßwellenkanals HELM." Project Thesis B-18/34-CS (German). Institute for Thermodynamics, University of the federal armed Forces Munich, Germany, 2018.

[160] Theisen, S. "Numerische Simulation der Hyperschall-Umströmung von Sondenkörpern im Stoßwellenkanal HELM mittels NSMB." Student Thesis S-19/220-CS (German). Institute for Thermodynamics, University of the federal armed Forces Munich, Germany, 2019.

[161] Lukasiewicz, J. *Experimental Methods of Hypersonics*. Marcel Dekker, New York, 1973. ISBN: 0-8247-1424-5.

[162] Karl, S. "Numerical Investigation of a Generic Scramjet Configuration." PhD Thesis. Technical University Dresden, Dresden, Germany, 2011. URL: `https://nbn-resolving.org/urn:nbn:de:bsz:14-qucosa-68695`.

[163] Olivier, H. *Thin Film Gauges and Coaxial Thermocouples for Measuring Transient Temperatures*. Tech. rep. SWL Technical Report. Shock Wave Laboratory (SWL), RWTH-Aachen University, Aachen, Germany, 1995.

[164] Mosaic Industries Inc. *Type E Thermocouple Calibration*. 2019. URL: `http://www.mosaic-industries.com/embedded-systems/microcontroller-projects/temperature-measurement/thermocouple/type-e-calibration-table`.

[165] Rödiger, T. "The Atomic Layer Thermopile - A New Heat Transfer Measurement Technique in Fluid Mechanics and Thermodynamics." PhD Thesis (German). Stuttgart University, Germany, 2010. ISBN: 9783868534726.

[166] Olivier, H. and Grönig, H. *The Aachen Shock Tunnel TH2*. Tech. rep. SWL Technical Report. Shock Wave Laboratory (SWL), RWTH-Aachen University, Aachen, Germany, 1995.

[167] Hoarau, Y., Pena, D., Vos, J., Charbonnier, D., Gehri, A., Braza, M., Deloze, T., and Laurendeau, E. "Recent Developments of the Navier Stokes Multi Block (NSMB) CFD Solver." In: *54th AIAA Aerospace Sciences Meeting*. Vol. AIAA 2016-2056. San Diego, CA, USA, Apr. 2016. DOI: https://doi.org/10.2514/6.2016-2056.

[168] Hesse, A. "Strömungssimulation des Stoßwellenkanals HELM mittels NSMB und Vergleich der Lösung mit experimentellen Ergebnissen." Master Thesis M-17/34-CS (German). Institute for Thermodynamics, University of the federal armed Forces Munich, Germany, 2017.

[169] Zoll, F. "Vergleichende numerische Simulation der Randbedingungen der Hyperschall-Düsenströmung im Stoßwellenkanal HELM mittels NSMB." Master Thesis M-18/38-CS (German). Institute for Thermodynamics, University of the federal armed Forces Munich, Germany, 2018.

[170] Kröger, N. "Numerische Simulation der Hyperschall-Düsenströmung des Stoßwellenkanals HELM." Project Thesis P-18/35-CS (German). Institute for Thermodynamics, University of the federal armed Forces Munich, Germany, 2018.

[171] Kröger, N. "Numerische Simulation thermisch-chemischer Effekte der Hyperschall- Düsenströmung des Stoßwellenkanals HELM." Project Thesis M-19/46-CS (German). Institute for Thermodynamics, University of the federal armed Forces Munich, Germany, 2019.

[172] Theisen, S. "Numerische Simulation der Hyperschallumströmung von sphärischen Modellkörpern im Stoßwellenkanal HELM mittels NSMB." Bachelor Thesis B-19/59-CS (German). Institute for Thermodynamics, University of the federal armed Forces Munich, Germany, 2019.

[173] Theisen, S. "Validierung der kombinierten Simulationsumgebung des HELM." Project Thesis P-20/45-CS (German). Institute for Thermodynamics, University of the federal armed Forces Munich, Germany, 2019.

[174] Park, C. "Review of Chemical-Kinetic Problems of Future NASA Missions. I - Earth Entries." In: *AIAA Journal of Thermophysics and Heat Transfer* 7.3 (1993), pp. 385–398. DOI: https://doi.org/10.2514/3.431.

[175] Leyland, P., Vos, J., Kemenade, V. van, and Ytterstrom, A. "NSMB: A Modular Navier Stokes Multiblock Code for CFD." In: *33rd Aerospace Sciences Meeting and Exhibit*. Vol. AIAA 1995-0568. Reno, NV, USA, Sept. 1995. DOI: https://doi.org/10.2514/6.1995-568.

[176] Blottner, F., Johnson, M., and Ellis, M. *Chemically Reacting Viscous Flow Program for Multi Component Gas*. Tech. rep. Technical Report SC-RR-70-754 / NSA-26-027700. Sandia National Laboratories, Albuquerque, NM, USA, 1964.

[177] Spalart, P. and Allmaras, S. "A One-Equation Turbulence Model for Aerodynamic Flows." In: *30th Aerospace Sciences Meeting and Exhibit*. Vol. AIAA 92-0439. Reno, NV, USA, June 1992. DOI: `https://doi.org/10.2514/6.1992-439`.

[178] Menter, F. "Zonal Two Equation k-w Turbulence Models For Aerodynamic Flows." In: *23rd Fluid Dynamics, Plasmadynamics, and Lasers Conference*. Vol. AIAA 93-2906. Orlando, FL, USA, June 1992. DOI: `https://doi.org/10.2514/6.1993-2906`.

[179] Edenfield, E. "Contoured Nozzle Design and Evaluation for Hotshot Wind Tunnels." In: *3rd Aerodynamics Testing Conference*. Vol. AIAA 1968-369. San Francisco, CA, USA, Aug. 1968. DOI: `https://doi.org/10.2514/6.1968-369`.

[180] Hannemann, K. *Design of an Axisymmetric, Contoured Nozzle for the HEG*. Tech. rep. Technical Report DLR-FB 90-04. DLR Göttingen, Germany, 1990. URL: `https://elib.dlr.de/38503/`.

[181] Jacobs, P. and Stalker, R. "Hypervelocity Flow in Axisymmetric Nozzles." In: *10th Australasian Fluid Mechanics Conference*. Melbourne, VIC, Australia, Nov. 1989.

[182] Jacobs, P. "Transient, Hypervelocity Flow in an Axisymmetric Nozzle." In: *29th Aerospace Sciences Meeting*. Vol. AIAA-91-0295. Reno, NV, USA, July 1991. DOI: `https://doi.org/10.2514/6.1991-295`.

[183] Jewell, J. and Kimmel, R. "Boundary-Layer Stability Analysis for Stetson's Mach 6 Blunt-Cone Experiments." In: *Journal of Spacecrafts and Rockets* 54.1 (2017), pp. 258–265. DOI: `https://doi.org/10.2514/1.A33619`.

[184] Schultz, D. and Jones, T. *Heat Transfer Measurements in Short-Duration Hypersonic Facilities*. Tech. rep. 165. Advisory Group for Aerospace Research and Development (AGARD), 1973.

[185] Vos, J., Leyland, P., Kemenade, V. van, Gacherieu, C., Duquesne, N., Lotstedt, P., Weber, C., Ytterstrom, A., Saint Requier, C., and Kimmerl, J. *NSMB Handbook*. Tech. rep. Version 6.14. CFS Engineering (EPFL), Lausanne, Switzerland, 2019.

[186] Bethea, R., Duran, B., and Boullion, T. *Statistical Methods for Engineers and Scientists*. CRC Press, New York, 1995. ISBN: 9780367401825.

A Appendix

A.1 Tailored-interface calculation - continued

TI-Iteration for thermo-chemical equilibrium gas

Quantitative state surfaces in thermo-chemical equilibrium (as predicted by CEA) of pressure ratios across the incident and reflected shock wave as well as post-incident shock absolute velocity and post-reflected shock temperature for air in a representative range of incident shock Mach number and intial ST pressure are illustrated in Fig. A.1.

Loss factors - caloric quantities

Even though Nishida's formulation (Eq. 2.19) does not explicitly require accurate knowledge of the shock-processed test gas' caloric quantities, such as post-incident/-reflected shock temperature (T_2, T_5) and enthalpy (h_2, h_5), to unambiguously calculate TI conditions, the latter are nevertheless of high relevance for characterizing the thermo-chemical state in the nozzle reservoir. Hence, they are considered of great interest, even in an a priori prediction of suitable driver and shock tube operation conditions. The established procedure in relevant literature comprises of an a posteriori determination of stagnation enthalpy, by hypothesizing an isentropic expansion of the test gas behind the reflected shock, which implies irreversible processes not only to impart total pressure losses, but to analagously entail lower total temperature of the stagnated test gas:

$$\frac{T_{5e}}{T_5} = \left(\frac{p_{5e}}{p_5}\right)^{\frac{\kappa-1}{\kappa}} \tag{A.1}$$

where subscript 'e' denotes the experimentally measured 'equilibrium' pressure p_{5e}, as opposed to stagnation pressure p_5, obtained from 1-D inviscid theory [140]. For any constant pressure p_5 or p_{5e}, such a reduction in temperature T_5 inevitably imparts and artificial reduction of stagnation enthalpy h_5, which violates energy conservation in the form of the first law of thermodynamics. In the absence of another suitable approach, this assumption may be regarded as an acceptable makeshift remedy, the physical justification of which is however contested by the author and hence not used herein. Instead, the present work applies empirical correction factors ξ_{exp} exclusively to kinematic quantities, precisely to model stagnation pressure loss Δp_t, whereas temperature and enthalpy are calculated based on the inviscid ideal gas or equilibrium relation and not subjected to further correction.

In the process of RST condition prediction, satisfying the tailored-interface conditions for the incident contact surface is of importance in order to avoid premature test-interval termination
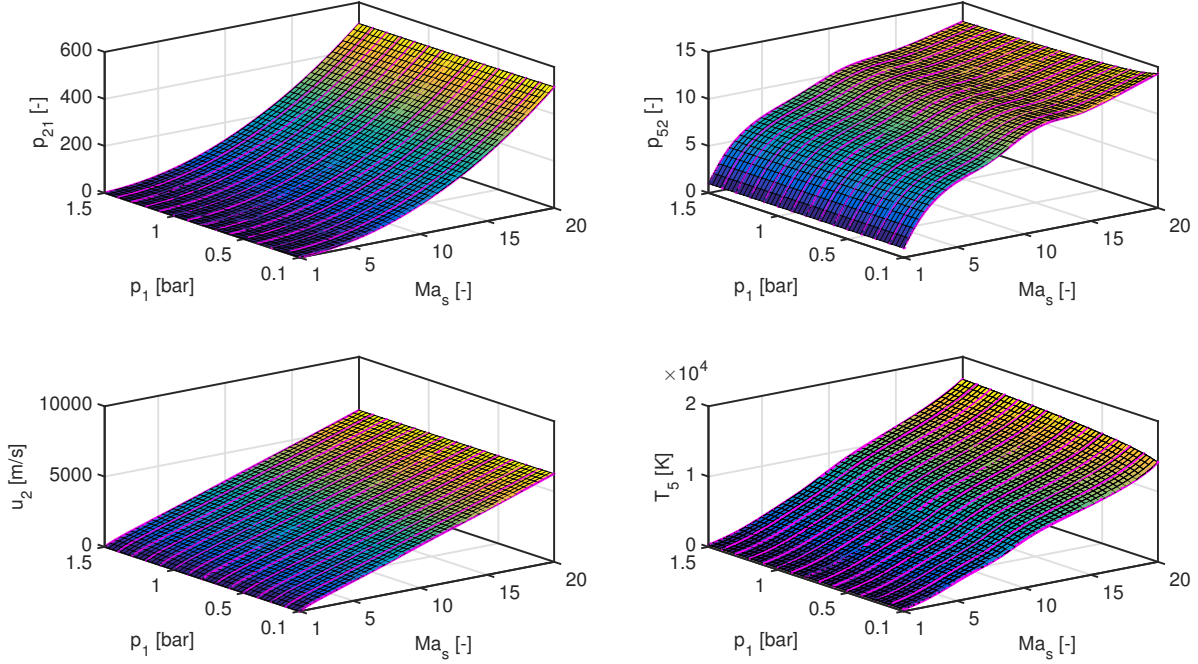
Figure A.1: Representative surface fit of state quantities (ratios) across the normal (incident and reflected) shock wave, assuming thermo-chemical equilibrium according to CEA for test gas air ($T_1 = 290K$).

by secondary expansion fans or shock waves upon reflected shock permeation of the contact surface. Herein, pressure balancing across the CS is required in order to bring the latter to rest, which requires for an accurate prediction of post-incident/-reflected shock state quantities, primarily pressure and temperature. Attributed to dissipative (irreversible) processes of non-ideal shock-endwall reflection and boundary layer interaction, stagnation pressures experimentally measured within the nozzle reservoir of a RST will range notably below values predicted from 1-D inviscid theory, typically around $\xi_5 = p_{5e}/p_5 \sim 0.8$. Temperature and enthalpy, in contrast, are not as easily measurable and hence have to be predicted differently. Due to lack of accurate knowledge, the latter are commonly determined by hypothesizing an isentropic expansion of the shock-processed test gas and behind the reflected shock front from state 5 to state 5e. However, this a posteriori correction of temperature T_5 will inevitably imply a corresponding reduction in enthalpy h_5. Considering the twice shock-processed test gas to be assumed as being perfectly brought to rest (at least in the aspired tailored-interface condition, where $u_5 = 0$ is to be achieved), this vanishing velocity suggests a reduction in total enthalpy across the shock, which is clearly not physical but violates energy conservation due to the first law of thermodynamics:

$$h_t = h + \frac{u^2}{2} = const. \tag{A.2}$$
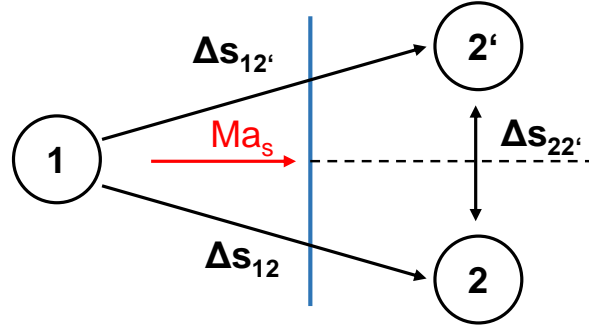
Figure A.2: Schematic of state change across normal shock wave, from initial state 1 to alternative states 2 and 2'.

In the following a perfect gas is considered to write the second law of thermodynamics:

$$Tds = dh - vdp = c_p dT - vdp \tag{A.3}$$

$$ds = c_p ln(\frac{dT}{T}) - Rln(\frac{dp}{p}) \tag{A.4}$$

For the purpose of testing the validity of the isentropic expansion, the change of state quantities across a normal shock wave from initial state 1 to two alternative states 2 and 2' (representing the theoretical and experimental post-reflected shock states 5 and 5e) according to Fig. A.2 is regarded.

Considering the change from an arbitrary (static) state 1 to its total (stagnated) state 1t to be isentropic, the entropy change between (static) states 1 to 2 and total states 1t to 2t, respectively, is identical, such that integration of Eq. A.4 yields:

$$\Delta s_{12} = \Delta s_{1t2t} = c_p ln(\frac{T_2}{T_1}) - Rln\frac{p_2}{p_1} = c_p ln(\frac{T_2 t}{T_1 t}) - Rln\frac{p_2 t}{p_1 t} \tag{A.5}$$

For a perfect gas, where $c_p = const$ and $h = c_p T$, energy conservation is written in terms of constant total temperature $T_{1t} = T_{2t} = T_t = const$, such that the second-last term in Eq. A.5 vanishes. When, further writing $c_p = \frac{\kappa}{\kappa - 1} R$, Eq. A.5 yields:

$$\frac{\kappa}{\kappa - 1} ln(\frac{T_2}{T_1}) = ln(\frac{p_2}{p_1}) - ln(\frac{p_2 t}{p_1 t}) = ln(\frac{p_2}{p_1} \cdot \frac{p_1 t}{p_2 t}). \tag{A.6}$$

By introducing the loss factors for static and total pressure between the post-shock states 2 and 2' (so as to model empirical pressure loss from states 5 to 5e):

$$p_{2't} = \xi_t \cdot p_{2t}, p_{2'} = \xi \cdot p_2 \tag{A.7}$$

with $\xi, \xi_t \leqslant 1$, post-shock temperatures T_2 and $T_{2'}$ are written as:

$$\frac{T_2}{T_1} = \left(\frac{p_2}{p_1} \cdot \frac{p_{1t}}{p_{2t}}\right)^{\frac{\kappa-1}{\kappa}} \tag{A.8}$$

$$\frac{T_{2'}}{T_1} = \left(\frac{p_{2'}}{p_1} \cdot \frac{p_{1t}}{p_{2't}}\right)^{\frac{\kappa-1}{\kappa}}. \tag{A.9}$$

Rewriting pressures of state 2' by Eq. A.7, this yields:

$$\frac{T_{2'}}{T_1} = \left(\frac{\xi}{\xi_t} \cdot \frac{p_2}{p_1} \cdot \frac{p_{1t}}{p_{2t}}\right)^{\frac{\kappa-1}{\kappa}} = \left(\frac{\xi}{\xi_t}\right)^{\frac{\kappa-1}{\kappa}} \cdot \frac{T_2}{T_1} \tag{A.10}$$

and hence:

$$\frac{T_{2'}}{T_2} = \left(\frac{\xi}{\xi_t}\right)^{\frac{\kappa-1}{\kappa}}. \tag{A.11}$$

From Eq. A.11 it is seen that temperature in the post-shock regime for both cases is determined by the ratio the static to total pressure loss factor between experimentally measured and theoretically predicted pressure. As - in the aspired case of a tailored contact surface - the test gas behind the reflected shock is brought to rest (i.e. perfectly stagnated with $u_5 = 0$), the dynamic component vanishes and static pressure in the nozzle reservoir will be identical to total (stagnation) pressure $p_5 = p_{5t}$. Hence, the experimentally obseved pressures loss factor (states 5-5e) will be identical for static and total pressure, such that $\xi = \xi_t < 1$ holds. For this case Eq. A.11 predictes an identical post-shock (static) temperature of $T_2 = T_{2t}$. Accordingly, in the present case of test gas shock-processing and stagnation in a RST nozzle reservoir, the post-reflected shock temperature $T_{5e} = T_5$ attained in the experiment is deduced to be identical to the theoretically predicted post-reflected shock temperature, even in the case of net total (and static) pressures losses.

The argument of an hypothesized isentropic expansion from states 5-5e is best analyzed by writing the entropy for exemplary state change according to Fig. A.2 in terms of:

$$\Delta s_{12} = -R \cdot ln\left(\frac{p_{2t}}{p_{1t}}\right) \tag{A.12}$$

$$\frac{\Delta s_{12}}{R} = ln\left(\frac{p_{1t}}{p_{2t}}\right) \tag{A.13}$$

$$\Delta s_{12'} = -R \cdot ln\left(\frac{p_{2't}}{p_{1t}}\right) \tag{A.14}$$

$$\frac{\Delta s_{12'}}{R} = ln\left(\frac{1}{\xi_t} \cdot \frac{p_{1t}}{p_{2t}}\right) = ln\left(\frac{1}{\xi_t}\right) + ln\left(\frac{p_{1t}}{p_{2t}}\right). \tag{A.15}$$

Due to linearity of entropy, the entropy difference between states 2 and 2' can be written by subtracting the entropy change from inital state 1 to states 2 and 2' according to Eq. A.15, which yields:

$$\frac{\Delta s_{22'}}{R} = \frac{\Delta s_{12'} - \Delta s_{12}}{R} = ln\left(\frac{1}{\xi_t}\right) \tag{A.16}$$

Accordingly, an assumed isentropic change between states 2 and 2' would require a fully re-

versible process in the absence of pressure losses: $\xi_t = 1 \rightarrow \Delta s_{22'} = 0$, which evidently does not reflect empirical observation of pressures losses $\xi_t \sim 0.8 < 1$. Only the latter, however, fully satisfies the physically required increase in entropy of $\Delta s_{22'} \geqslant 0$.

Against this background, the established approach for analyzing high-enthalpy experiments in RST assumes full thermo-chemical equilibrium in the post-reflected state 5 within the nozzle reservoir. Further, as especially caloric quantities are not easily measurable, the stagnated test gas' temperature T_{5e} and enthalpy h_{5e} of any experiment is calculated a posteriori, based on the theoretically attained temperature T_5 - predicted by inviscid theoretical Typical analysis and prediction of

The latter explicitly apply to kinematic quantities (pressure and velocity) only, whereas - as derived from entropy argument due to the second law of thermodynamics for an exemplary ideal gas EOS - caloric quantities, such as temperature T_5 and enthalpy h_5 of the stagnated test gas, will not be affected. and hence for defining expansion nozzle upstream inlet conditions throughout the test time interval, compare chapter 1

A.2 TUP-TI Operation conditions - continued

A.2.1 Over-drive variation

Tuned FPD and TI operation points based on the analysis of Hornung, where the over-drive parameter is reduced from nominal $\beta = 1.4$ to the original $\beta = 1.0$ of Hornung's theory, are presented in Fig. A.3. As is observed from comparison with Fig. 2.7, only suggested piston buffer pressure p_{A0} and piston speed at diaphragm rupture u_{rupt} are affected by a decrease to over-drive $\beta = 1.0$, being up to 42% and 29% lower, respectively, than for $\beta = 1.4$. As all other driver state quantities are unaffected by this change, predicted TI conditions in the ST will be identical for both over-drive parameters (and are thus only given in Fig. 2.8 to avoid redundance). The expected factual change of explicitly time-dependent quantities in an experiment, however, such as driver pressure holding time and thus stagnation pressure recovery, are evidently not captured by this model. Analysis of which over-drive β will eventually be more conducive is therefore only feasible via a time-resolved simulation, e.g. by the L1d code, or by experimental verification.

A.2.2 Heavy piston

In the following, TUP-TI operation conditions for all three theories are listed for the heavier compression piston. It is to be noted here that experimental validation experiments, including those for empirical determination of the incident shock attentuation and stagnation pressure losses, have been only conducted for the lightweight piston. Operation points for the heavy piston listed herein have thus been computed, based on empirical loss factors determined with the lightweight piston (with lower driver pressure holding times in the experiment). Thus, as stagnation pressure recovery p_5/p_4 will rise with driver holding time τ_{hold} [46], and consider-
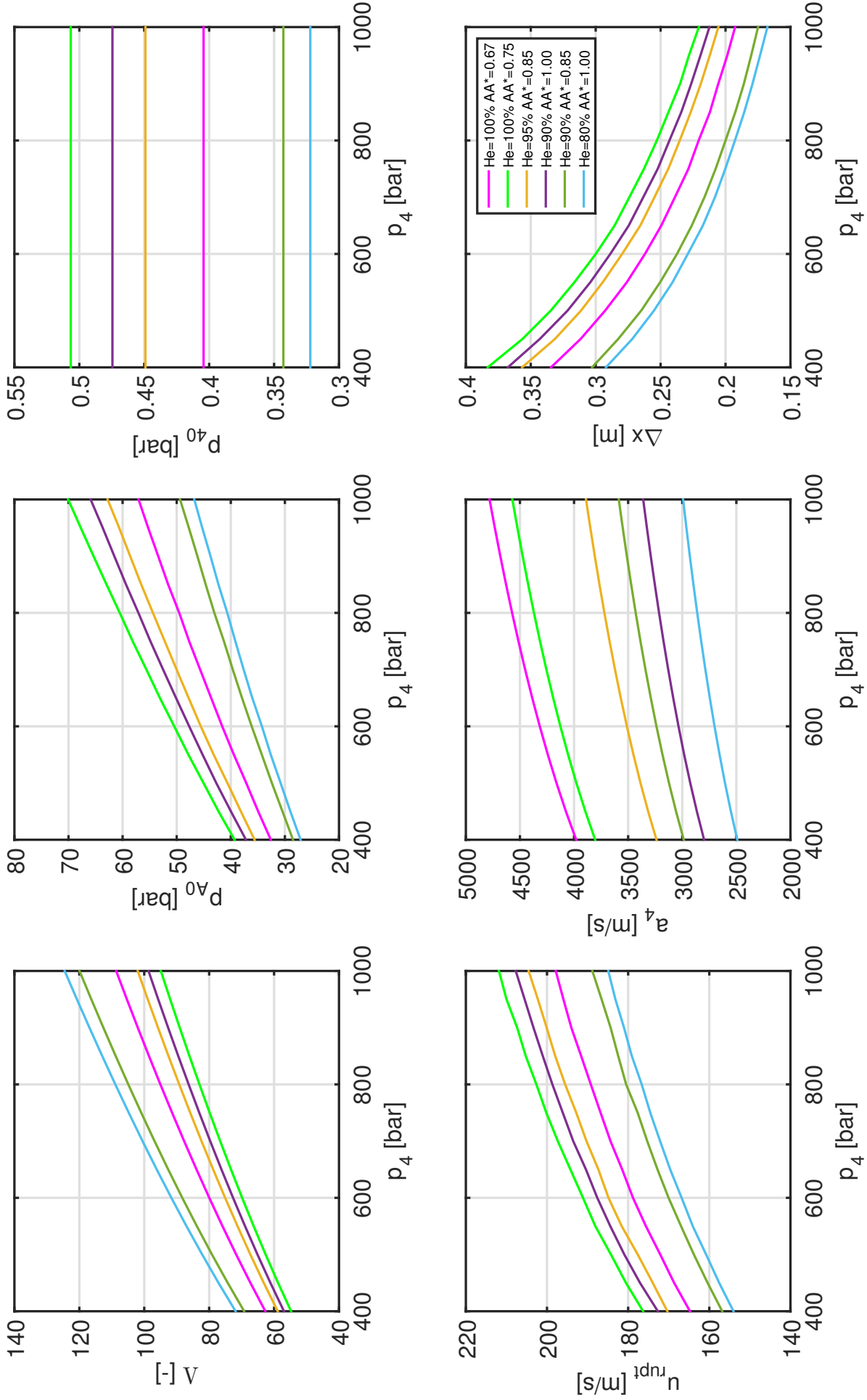
Figure A.3: Parameters for tuned-piston driver according to Hornung and Bélanger theory. Values are calculated for an over-drive parameter of $\beta = 1.0$, leightweight piston $m_p = 62.835 kg$.
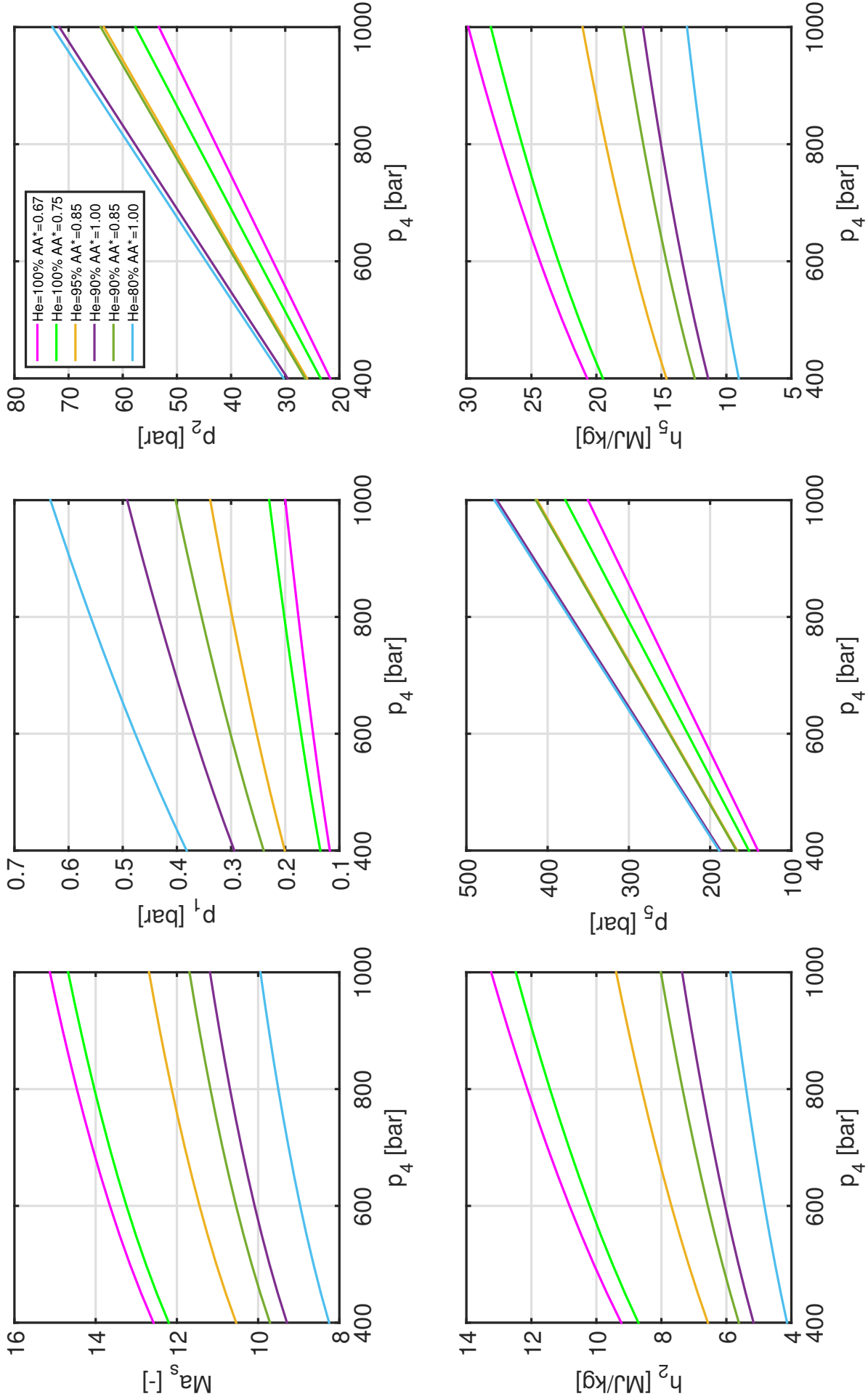
Figure A.4: Parameters for tailored-interface operation according to Nishida's theory - driver values based on Hornung and Bélanger analysis for tuned-piston ($\beta = 1.0$), leightweight piston $m_p = 62.835kg$.

ing the latter to be generally larger for a heavier piston, stagnation pressures p_5 listed herein will be generally underestimated and biased. In fact, based on L1d-predictions, the heavy piston facilitates stagnation pressures of up to $p_5 \sim 800 bar$ with tuned driver and tailored CS. Yet, in order to TI-theory to capture such changes in stagnation state 5, an adaption of the empirical loss factors due to validation experiments will be required in the future.

Facility operation conditions which achieve tuned FPD operation according to Hornungs's theory and TI characteristics according to Nishida's theory for the heavy compression piston are detailed in Fig. A.5-A.6.

Facility operation conditions which achieve tuned FPD operation according to Stalker's theory and TI characteristics according to Nishida's theory for the heavy compression piston are detailed in Fig. A.7-A.8.

Facility operation conditions which achieve tuned FPD operation according to Itoh's theory and TI characteristics according to Nishida's theory for the heavy compression piston are detailed in Fig. A.9-A.10.

A.2.3 Experimental validation - continued

Dynamic pressure traces towards the CT endwall (upstream of the diaphragm station) and ST endwall (nozzle reservoir) for reference experiments 4-9 with operation points according to Itoh's tuned piston theory and reference experiments 13-15 with operation points according to Stalker's tuned piston theory are listed in Fig. A.11-A.12 and Fig. A.13, respectively.

A.3 HELM Facility advancement - continued

A.3.1 Compression piston redesign

Detailed photographs of the old and new HELM compression piston design are given in Fig. A.14 and Fig. A.15.

A.3.2 Secondary reservoir overhaul

Detailed photographs indicating qualitative light transmissivity in the HELM nozzle reservoir prior to and after buffer pressure vessel overhaul and cleaning are provided in Fig. A.16. Experiments are conducted for identical test case p_4 =55bar, Ma_s =2.6 in air, with open and closed enwall.

A.3.3 Hydraulic damping system

A detailed photograph of the new heavy-duty hydraulic damping system is given in Fig. A.17.
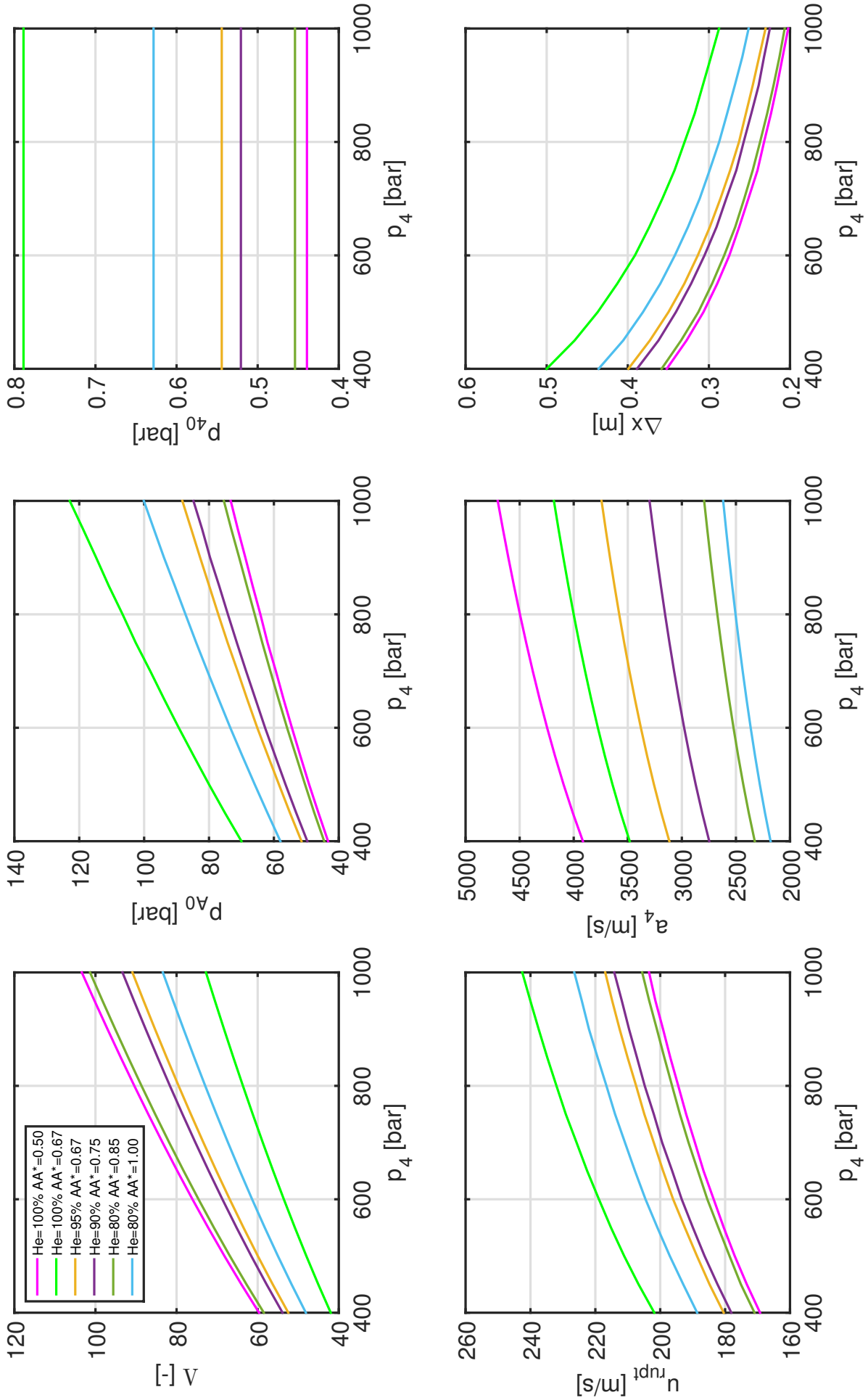
Figure A.5: Parameters for tuned-piston driver according to Hornung and Bélanger theory. Values are calculated for an over-drive parameter of $\beta = 1.4$, heavy piston $m_p = 122.58kg$.
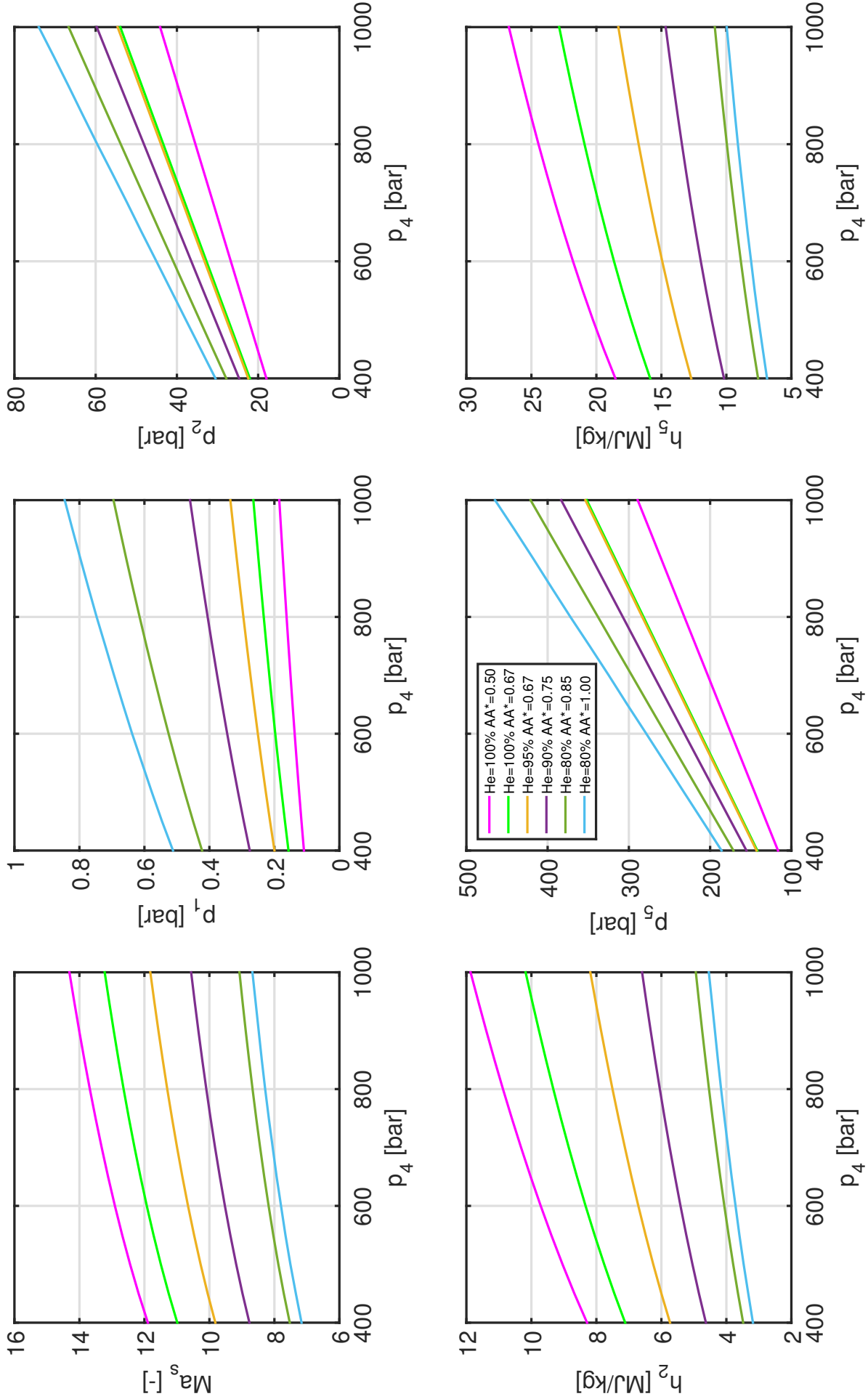
Figure A.6: Parameters for tailored-interface operation according to Nishida's theory - driver values based on Hornung and Bélanger analysis for tuned-piston ($\beta = 1.4$), heavy piston $m_p = 122.58 kg$.
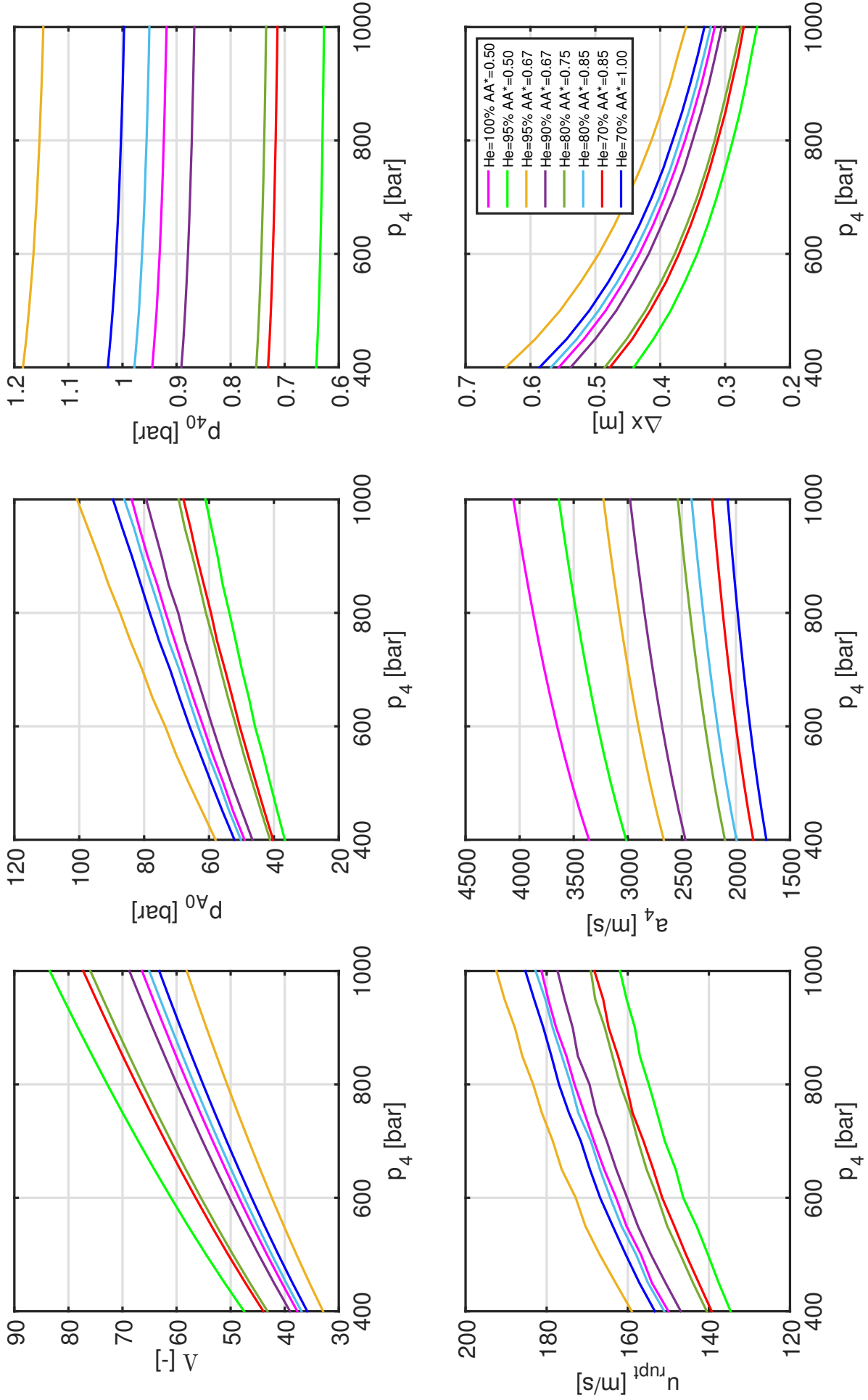
Figure A.7: Parameters for tuned-piston driver according to Stalker's theory. Values are calculated for an over-drive parameter of $\beta = 1.4$, heavy piston $m_p = 122.580 kg$.
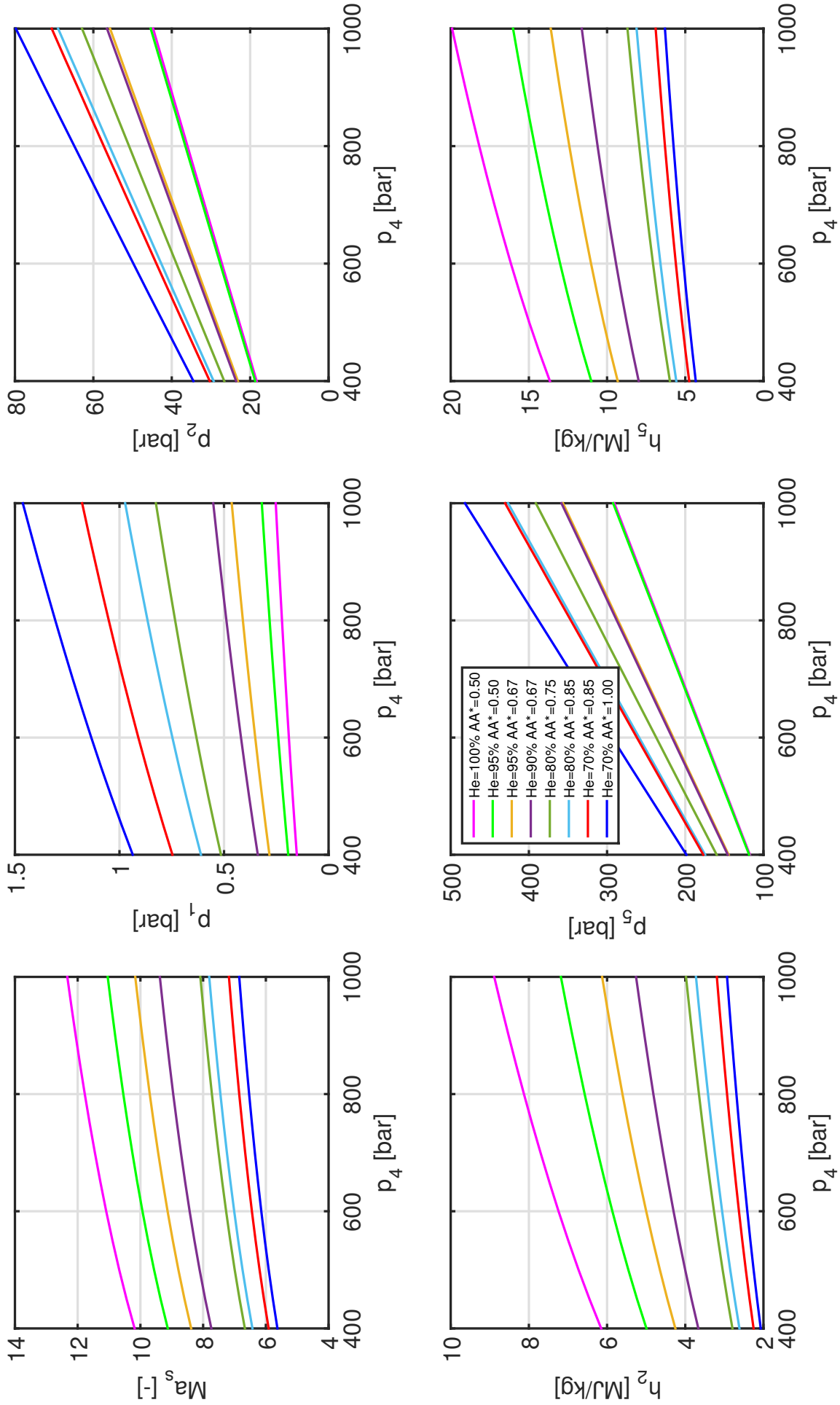
Figure A.8: Parameters for tailored-interface operation according to Nishida's theory - driver values based on Stalker's analysis for tuned-piston ($\beta = 1.4$), heavy piston $m_p = 122.580 kg$.
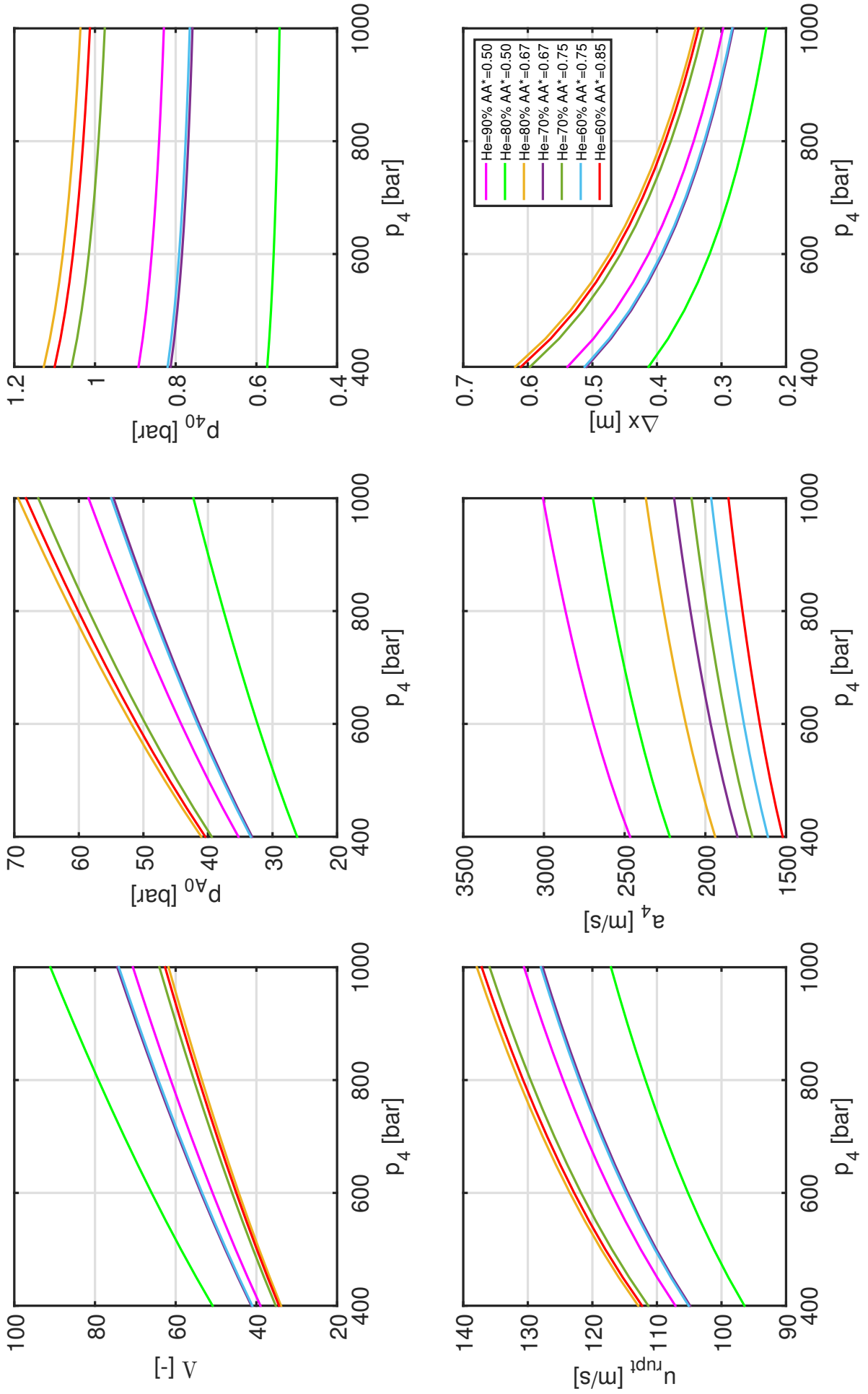
Figure A.9: Parameters for tuned-piston driver according to Itoh's theory. Values are calculated for an over-drive parameter of $\beta = 1.4$, heavy piston $m_p = 122.580 kg$.
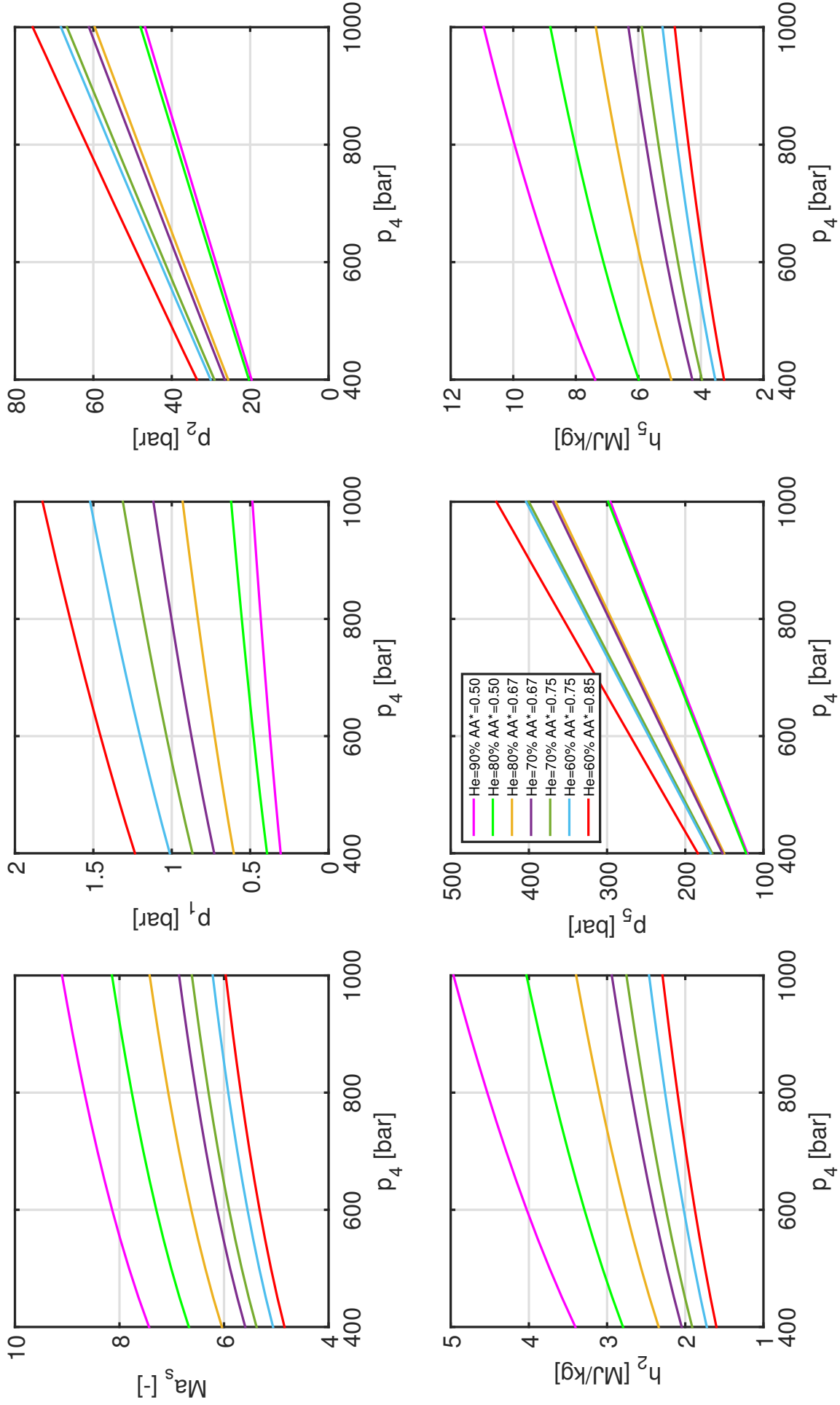
Figure A.10: Parameters for tailored-interface operation according to Nishida's theory - driver values based on Itoh's analysis for tuned-piston ($\beta = 1.4$), heavy piston $m_p = 122.580kg$.
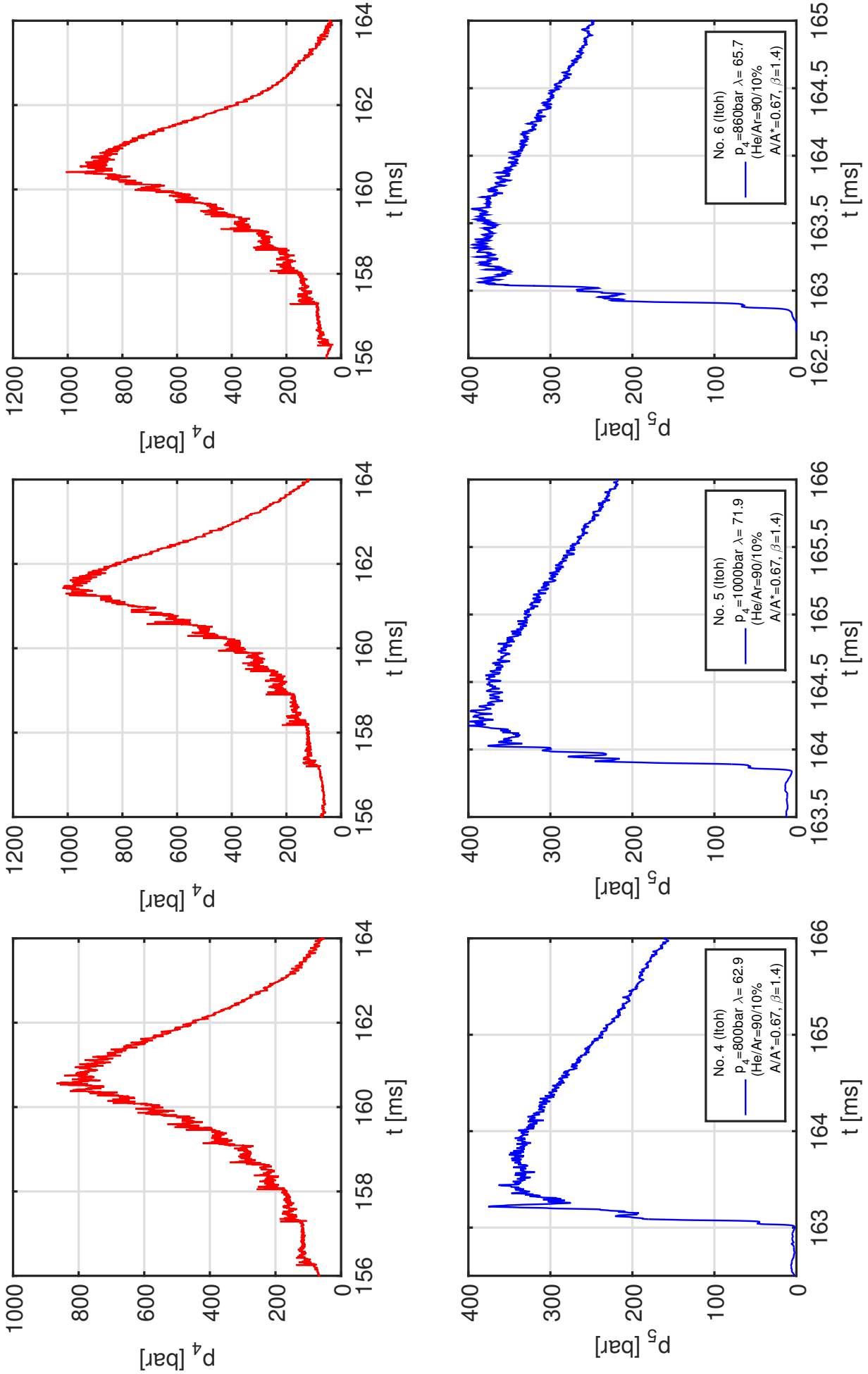
Figure A.11: Driver and shock tube pressure traces for three representative conditions (No. 4-6) according to Itoh's tuned piston theory and for the lightweight piston $m_p = 62.835 kg$. ST pressure p_5 filtered by 30kHz LP-filter for means of illustration.
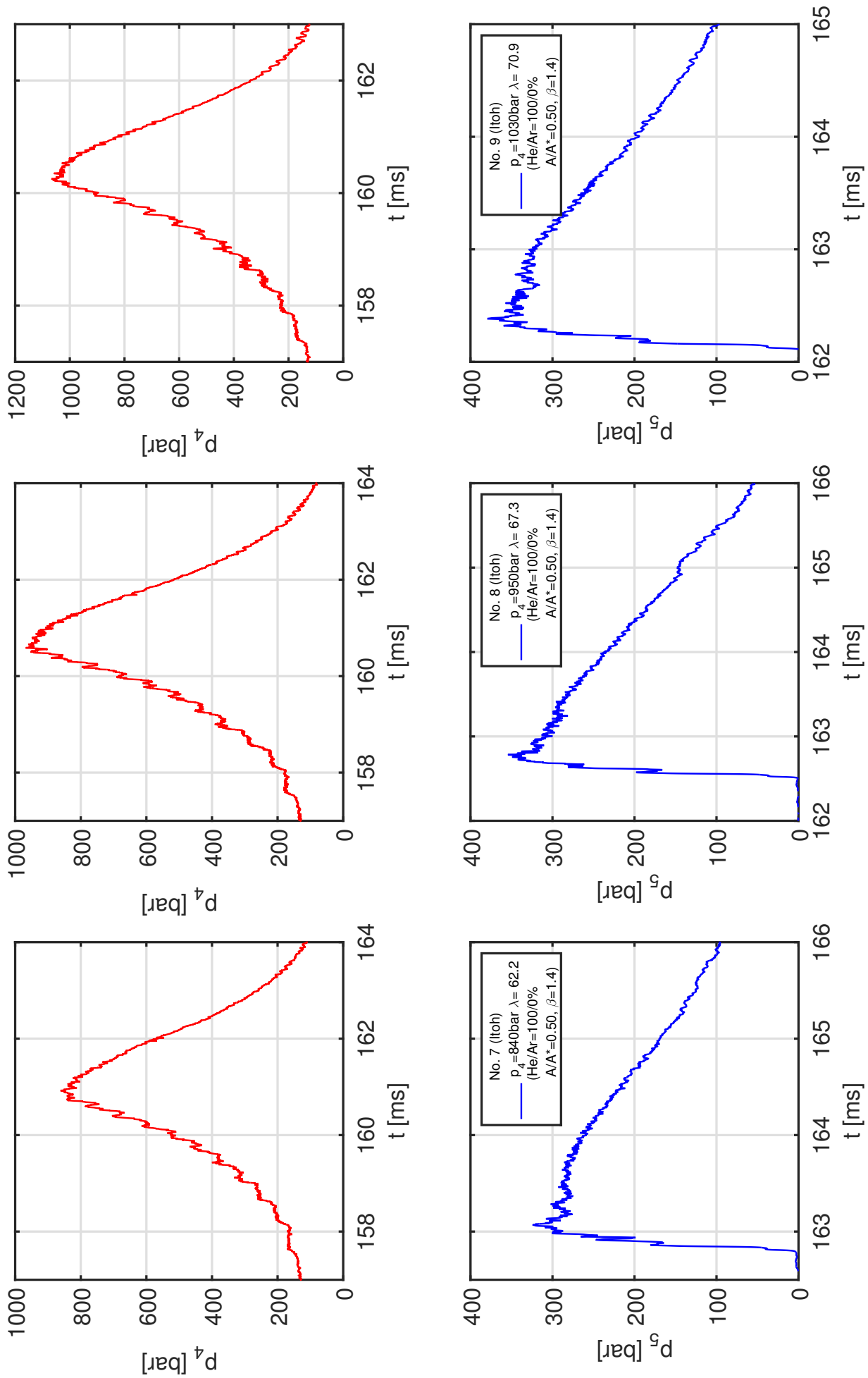
Figure A.12: Driver and shock tube pressure traces for three representative conditions (No. 7-9) according to Itoh's tuned piston theory and for the lightweight piston $m_p = 62.835kg$. ST pressure p_5 filtered by 30kHz LP-filter for means of illustration.
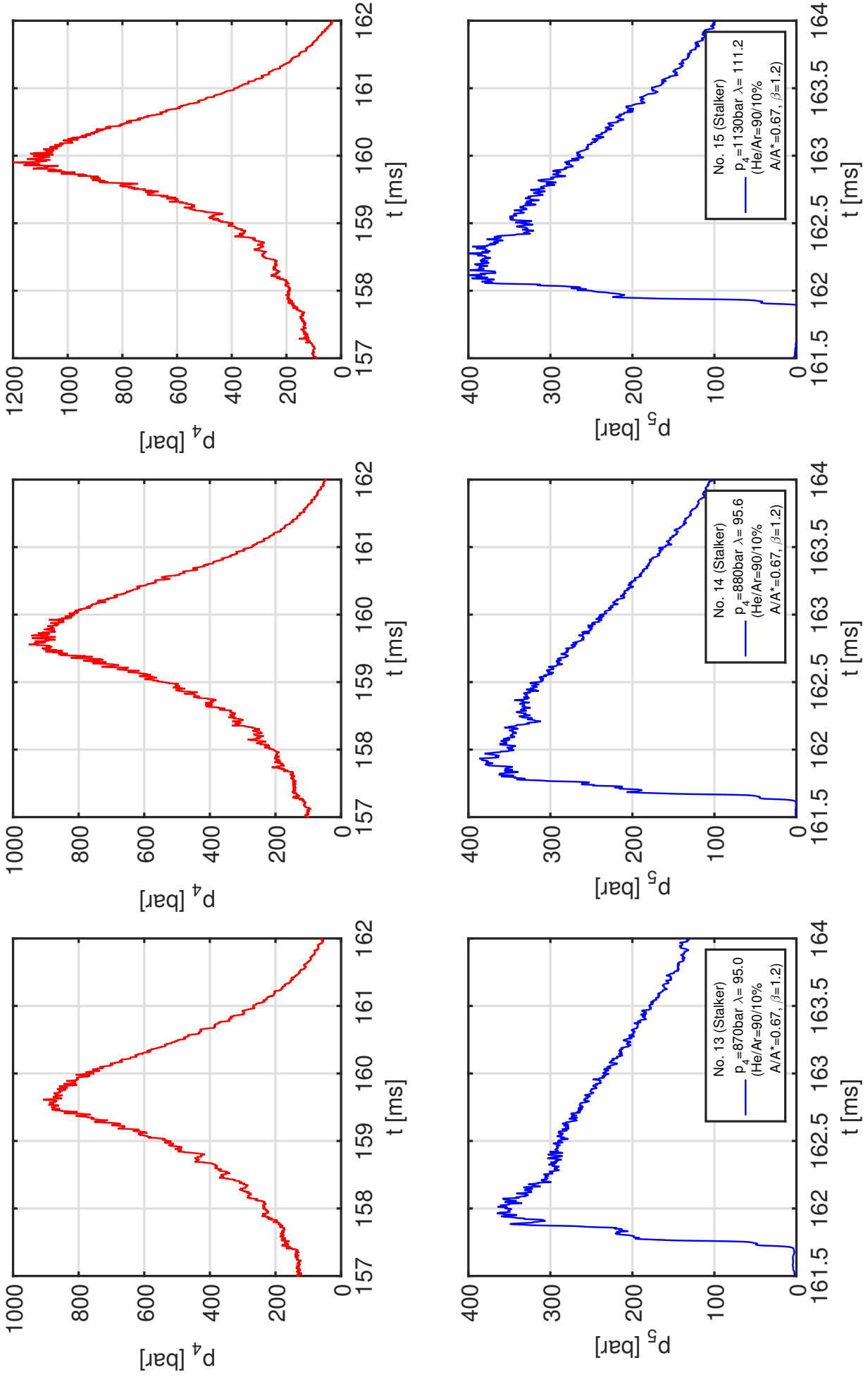
Figure A.13: Driver and shock tube pressure traces for three representative conditions (No. 13-15) according to Stalker's tuned piston theory and for the lightweight piston $m_p = 62.835kg$. ST pressure p_5 filtered by 30kHz LP-filter for means of illustration.

No. 13 (Stalker)
p_4=870bar λ= 95.0
(He/Ar=90/10%
A/A^*=0.67, β=1.2)

No. 14 (Stalker)
p_4=880bar λ= 95.6
(He/Ar=90/10%
A/A^*=0.67, β=1.2)

No. 15 (Stalker)
p_4=1130bar λ= 111.2
(He/Ar=90/10%
A/A^*=0.67, β=1.2)
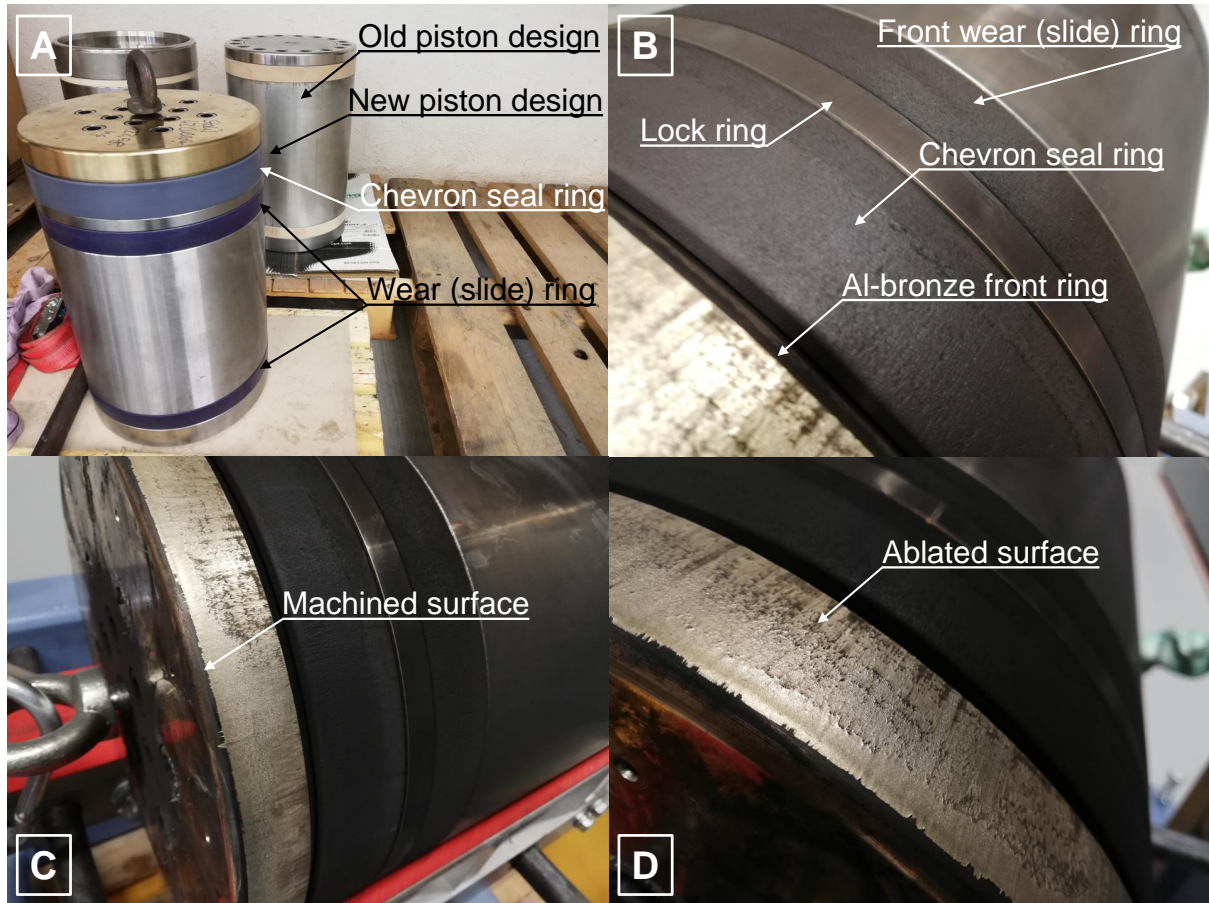
Figure A.14: Detailed view of the HELM compression piston. A: Old and new piston design with components before first use. B: Components of the new compression piston after a series of high-pressure, high-enthalpy experiments - abrasive wear of the Chevron wedge-seal ring and front slide ring is observed. C: Detailed view of the front plate highlights the original machined (lathed with smooth finish) surface of the frontal Al-bronze plate. D: Detailed view of the front plate highlights the ablated circumferential surface due to high temperature, high sound speed driver gas leakage around the piston perimeter.

Figure A.15: Detailed view of the new HELM compression piston, highlighting initial design and first (final) revision. A: Initial new piston design, front view of main body with heat resistant ceramic sealing and separating paste, 12 M16x70 bores for DIN-flathead screws. B: Disassembly of the initial piston design with torn screw bodies after flat screw head failure. C: Revised new piston design, main body with 18 M20x80 bores for regular DIN-head screws. D: Revised new piston design, front plate with bores and conterbores for regular DIN-head screws.
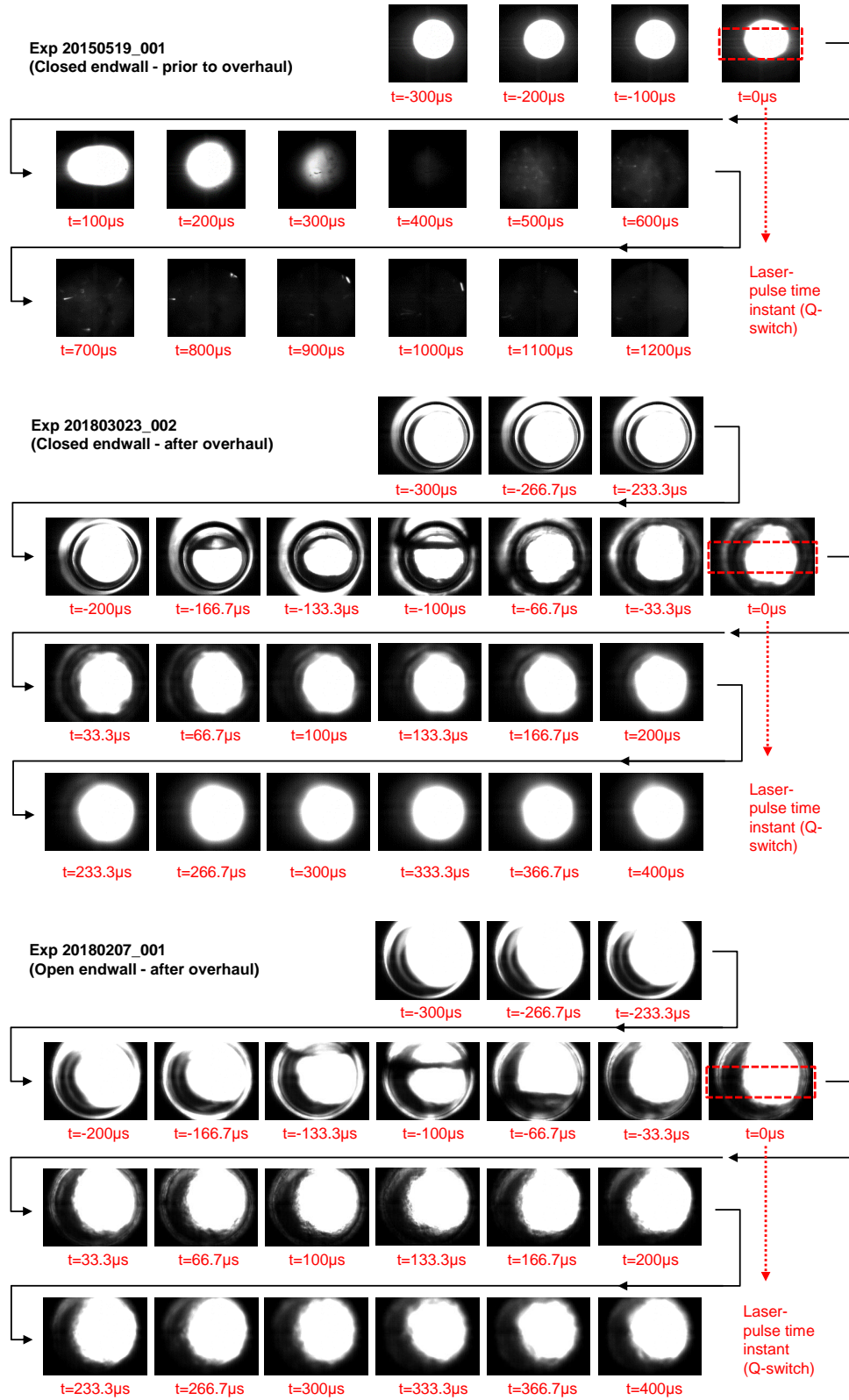
Figure A.16: Qualitative light transmissivity in the HELM nozzle reservoir prior to and after buffer cleaning and overhaul. Photographs are acquired by a high-speed CMOS camera (Redlake) at 10,000 fps ($\Delta t = 100\mu s$) with $5\mu s$ exposure (top [42]) and 30,000 fps ($\Delta t = 33.3\mu s$) with $3\mu s$ exposure (middle, bottom [110]), respectively.
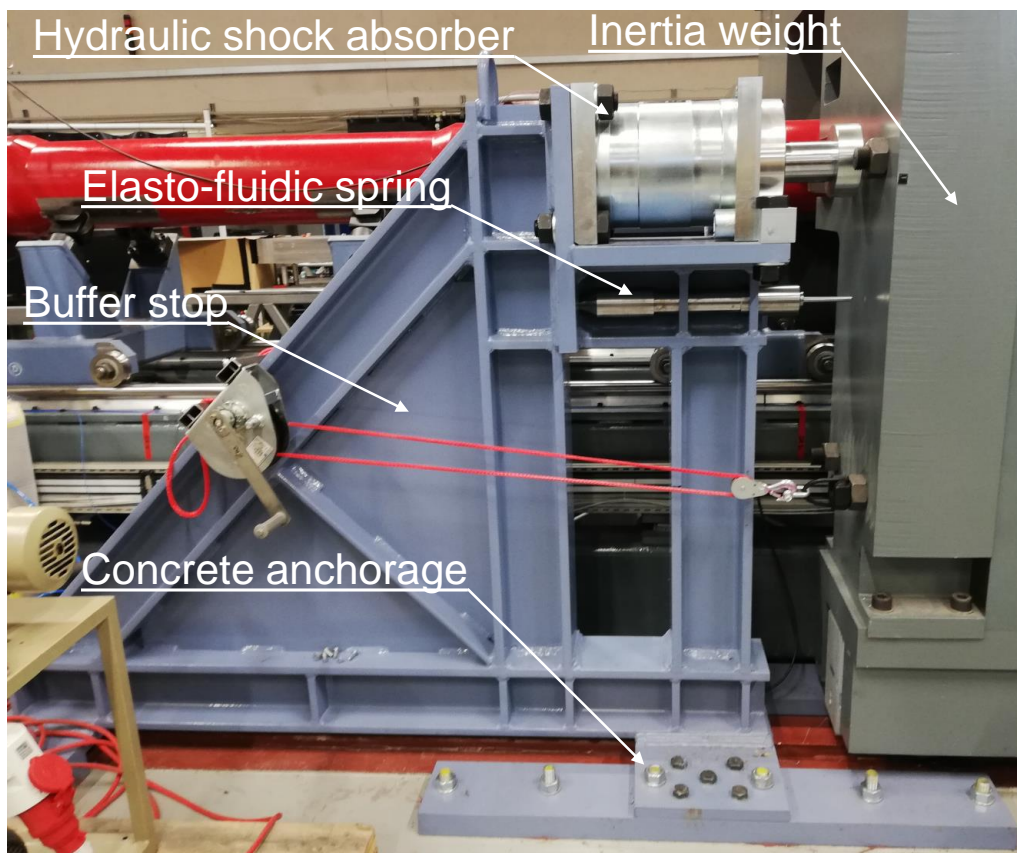
Figure A.17: Detailed photograph of the new hydraulic damping system, highlighting heavy-duty hydraulic shock absorbers, elasto-fluidic springs, mechanical buffer stop, concrete anchorage and inertia weight.

A.3.4 Piston buffers

The piston buffers used for prior work in the HELM facility [42] were made from microcellular PUR elastomer (Cellasto), a material which was deemed inadequate for full-range experiments due to inferior temperature stability, insufficient hardness and low energy absorption. Towards the beginning of the current work, new piston impact buffers from vulcanized high-temperature resistant rubber (FKM) with high hardness (Sh 80) were devised (GMT GmbH). The latter grant high energy absorption (sufficient for moderate impact velocities >50 m/s) due to elastic deformation, offer a long-time temperature stability up to 200 °C and can withstand intermittent peak temperatures that are far higher. In the current case of FPD operation with high-temperature noble gases argon and helium, with peak temperatures up to ∼5000 K after adiabatic compression, the material undergoes pyrolysis, yet only at the surface. Rubber buffers were tempered in the process of manufacturing to limit the release of gaseous substances throughout the experiment. Since 2018, rubber buffers have been successfully used for 260 experiments in the HELM facility, until the maximum FPD operation point of 1000 bar and 5000 K, without any metal-metal contact (piston impact). In the case of (moderate) piston impact (∼50 m/s), a set of 7 rubber buffers withstands up to 5 consecutive test runs, whereas continuously more pieces will break away, see Fig. A.18. Even at high driver pressures of up to 1100 bar, (near) tuned FPD operation decreases mechanical loads on the buffers to a negligible minimum, whereas high temperatures up to 5000 K will continue to embrittle the surface, limiting lifetime to ∼10 consecutive experiments.

Nevertheless, residuals of pyrolyzed polymer from the piston wear and seal ring and rubber buffers were observed to cover and darken surfaces at the diaphragm station. Whereas the latter were deduced to be negligible for conventional free-stream model experiments, any gaseous phase and particle loading of the test gas was to be avoided for laser diagnostics in the nozzle reservoir. Accordingly, the second test campaign of LIGS measurements was conducted with piston buffers made from PTFE (virginal white), effectively avoiding any release of gaseous substances due to superior temperature stability and thus ensuring a clean test gas. Yet, this comes at the price of predominantly plastic deformation, where PTFE buffer tend to break and to be shattered to pieces in case of a single piston impact. The use of similar PA buffers is reported for the X2 facility [48]. In the case of the HEG facility, heavy pistons of up to 700 kg weight are stopped by a set of solid, sacrificial copper buffers [55]. In the course of LIGS experiments, NO-seeding concentrations ∼500-1000 ppm induce corrosion on the non-corrosion-resistant steel surfaces, where loose particles can potentially block coherent laser beams - high-alloyed tube surfaces are not affected.

A.4 Accelerometer measurements - continued

A.4.1 Accelerometer

A detailed photograph of the accelerometer is given in Fig. A.19.
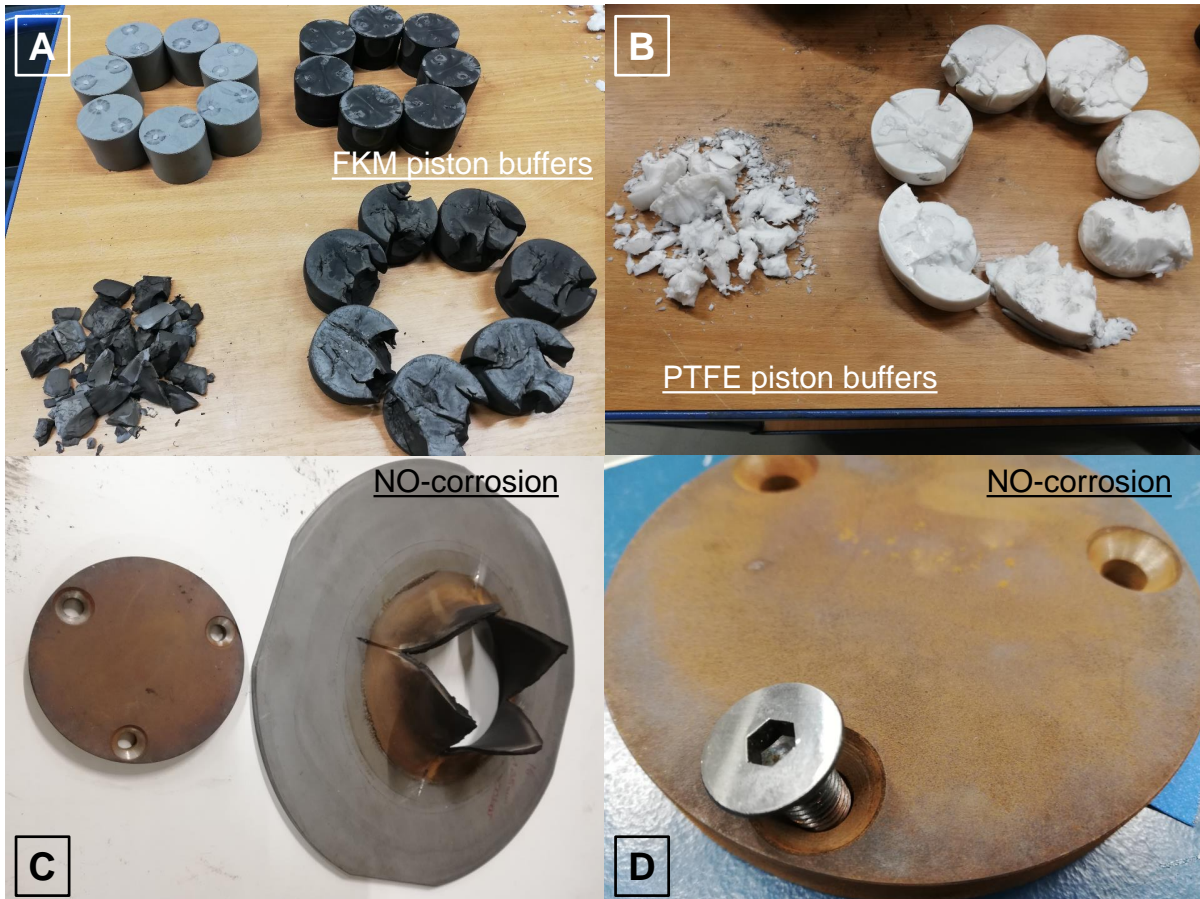
Figure A.18: Detailed view of the FKM rubber buffers and diaphragm and endwall-piece corrosion due to NO-corrosion. A: FKM rubber buffers in original state, after use in high-pressure, high-temperature experiments without piston impact, as well as after ~5 piston impacts, including fragments. B: PTFE piston buffers after single piston impact, including fragments. C: Effect of corroded surfaces of the diaphragm (mild steel) and ST-endwall-piece (high-strength tempered steel, not corrosion-resistant) due to NO-seeding in the test gas. D: Close-up view of the ST-endwall-piece due to NO-corrosion, after a series of LIGS test runs and a downtime of days before cleaning the facility. Notably, the screw from non-corrosive steel is seen to not be affected.
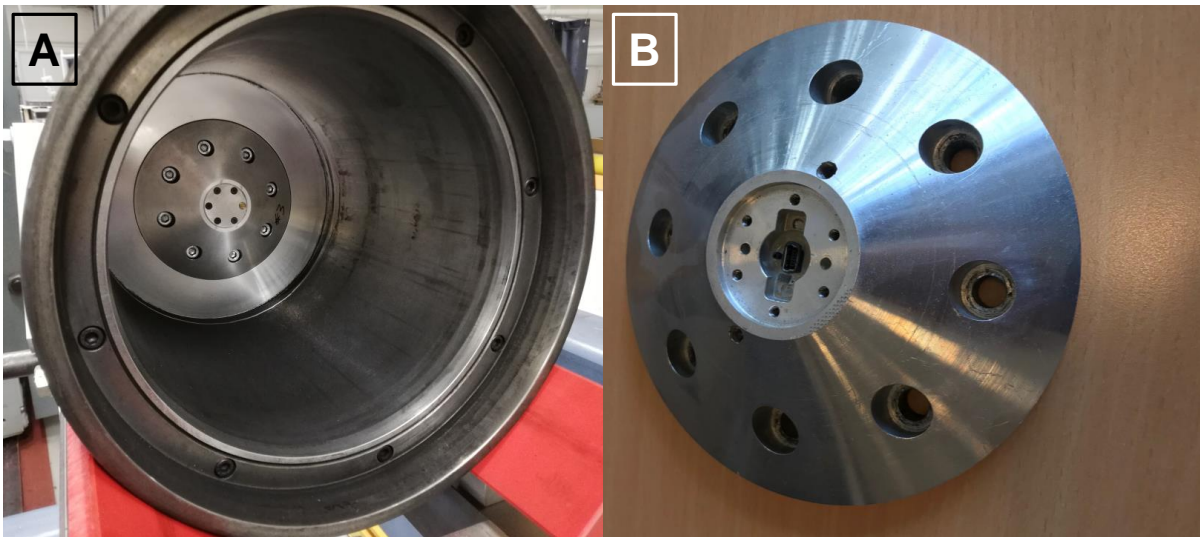
Figure A.19: Detailed view of the accelerometer device. A: Accelerometer mounted to the inner back-face of the piston. B: Accelerometer housing without lit, showing USB-port and LED.

A representative data trace of inductive proximity sensors, mounted along the CT and serving as discrete waypoint-markers for sensitivity correction is provided in Fig. A.20.

A.5 LIGS Application - continued

A.5.1 Optical access redesign

A detailed view of the optical access to the HELM nozzle reservoir, mechanical windows assembly and LIGS laser-optical setup are given in Fig. A.21.
A detailed view of the flush-mounted optical window access to the HELM nozzle reservoir and Sapphire windows is given in Fig. A.22.
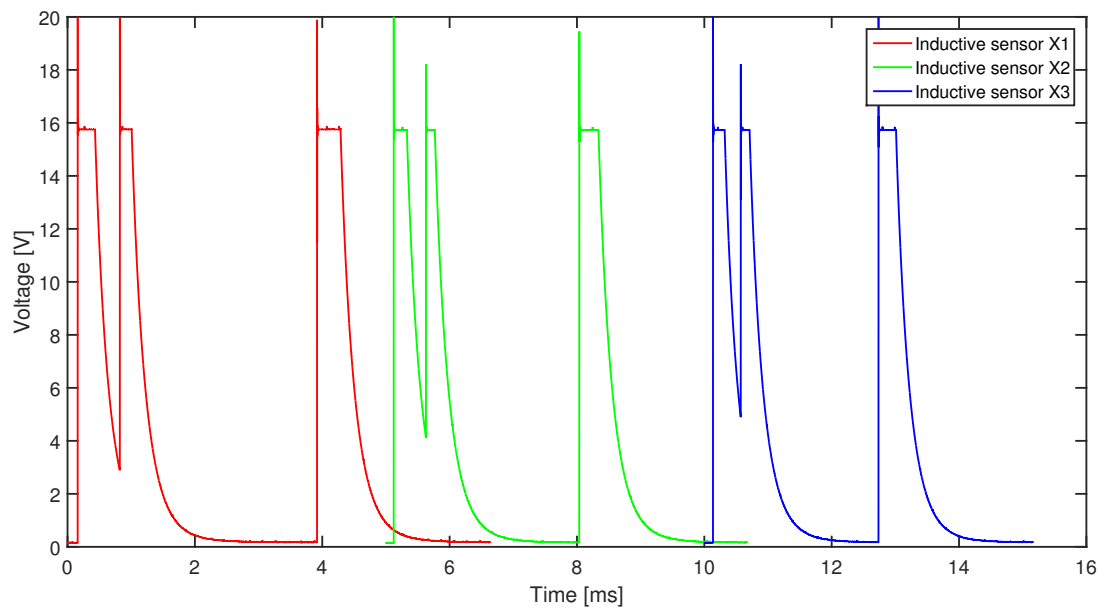
Figure A.20: Representative data trace of wall-flush mounted inductive proximity sensors X1-X3 used for point-discrete detection of piston arrival and passage within the CT via rising and falling (digital) signal flanks.
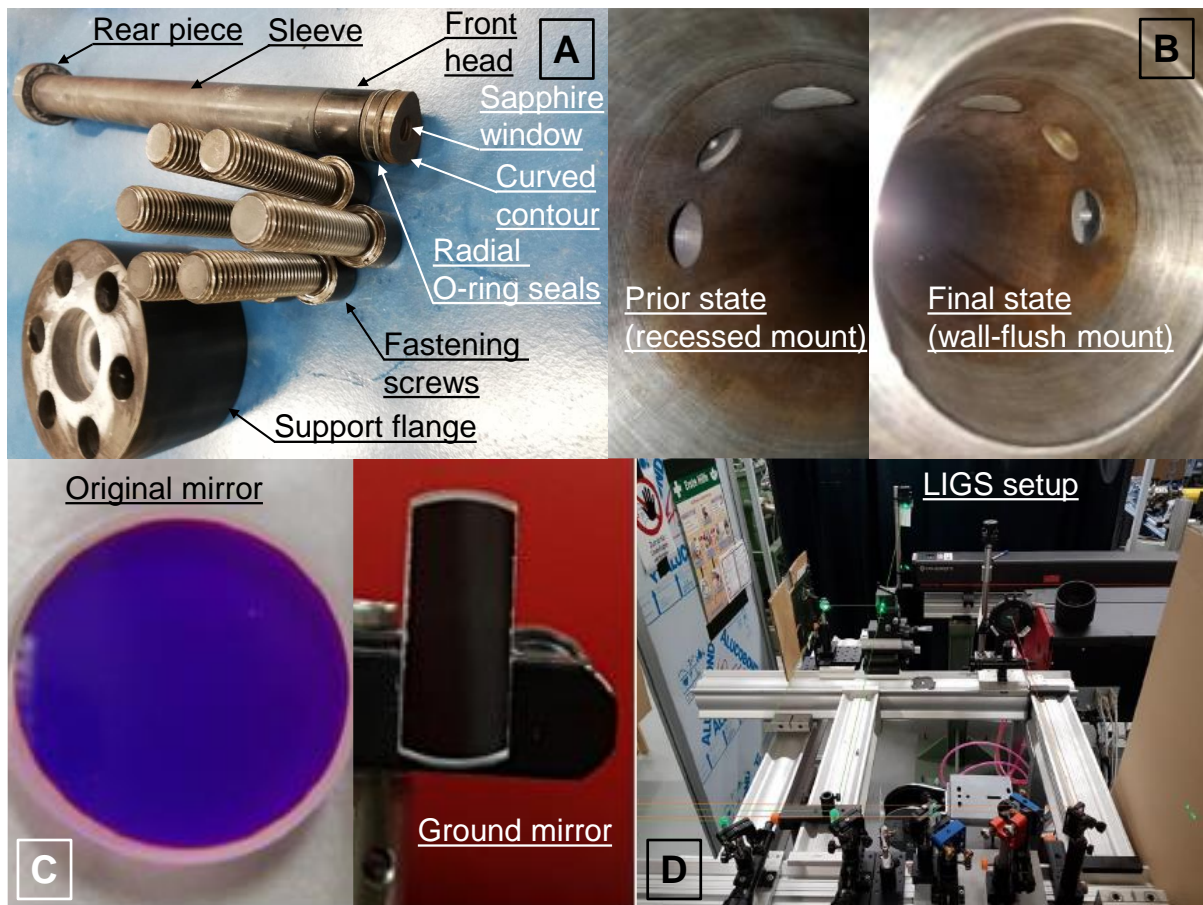
Figure A.21: Detailed view of the nozzle reservoir optical access and window assembly. A: Photograph of the window assembly, highlighting mechanical parts, radial o-ring seals and curved front contour. B: Photographs comparing prior and final state of recessed-mounted and wall-flush mounted transducers and optical windows, respectively. C: Photograph of the optical turning mirrors in original and mechanically ground state. D: Photograph of the LIGS laser-optical setup used in the current work.
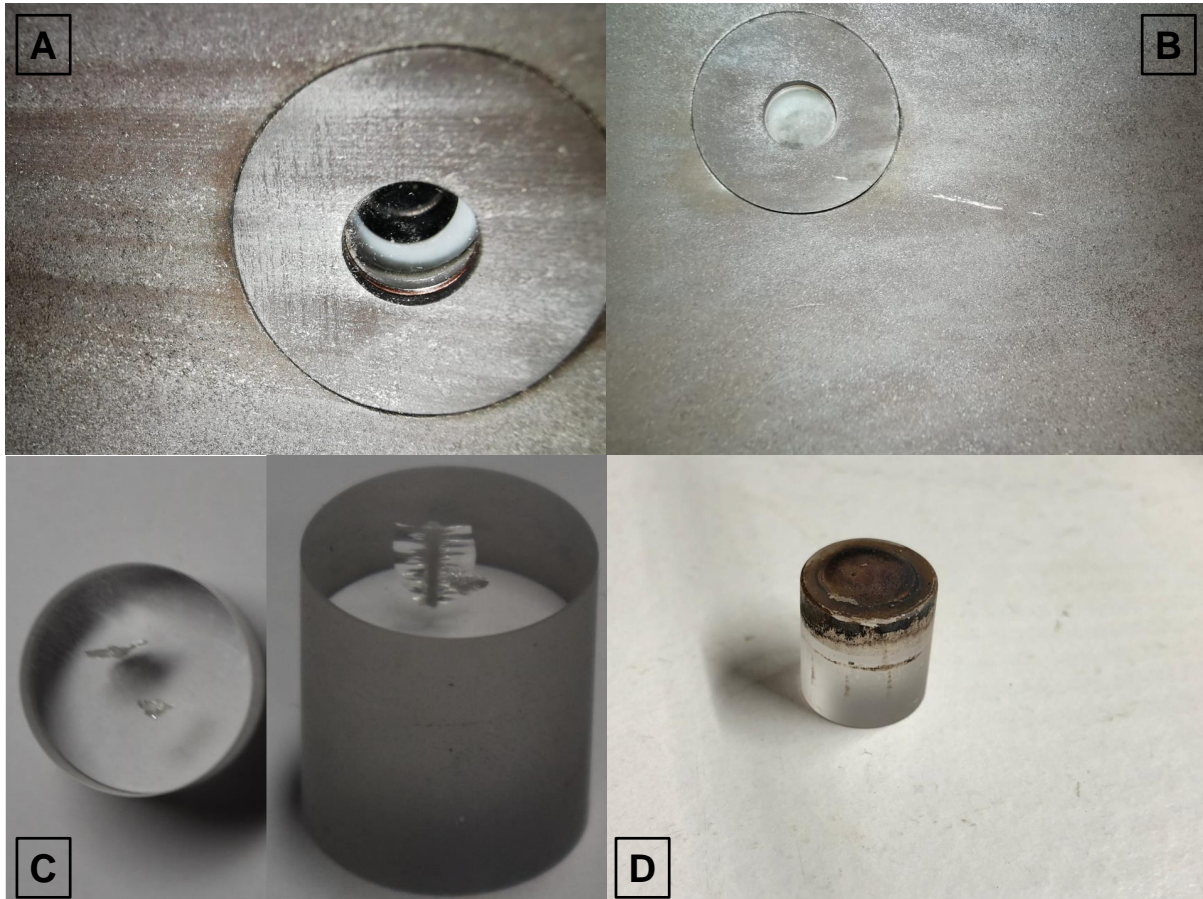
Figure A.22: Detailed view of the flush-mounted optical access windows. A: Photograph of in cleaned state prior to an experiment, remaining lints from a cleaning cloth are visible. B: Photograph of the optical access after an experiment in the $\sim$3 MJ/kg range, indicating an opaque, faint whitish coating on the front surface. C: Photograph of the optical window after local thermo-mechanical cracking due to pump laser beam power beyond the damage threshold. D: Photograph of the optical window after a series of elevated enthalpy $>$10 MJ/kg experiments without intermittent cleaning. A thick brownish, metal-oxidic coating is visible, further indicating gas leakage past the front face washer seal until the recessed radial o-ring seal.

B Appendix

B.1 Free-stream rebuilding

B.1.1 Schlieren visualization

Photographs of the spherical probes used within the current free-stream calibration experiments are given in Fig. B.1. Here, evident unsteadiness of the flow field is observed to induce strong fluctuations of the bow shock standoff-distance, which rendered the determination of a single, measured, time-averaged (quasi-steady) mean distance δ - to be used within the current rebuilding procedures - unfeasible. Instead, the useful test-time was determined to $\sim$1 ms from the Pitot pressure and stagnation pressure profiles, see Fig. 4.11, and the shock standoff-distance was calculated theoretically.

B.1.2 Free-stream static pressure calibration

A technical drawing of the slender lance probe geometry is given in Fig. B.2.
Fig. B.3 provides a schematic illustration of the absolute pressure sensor calibration procedure, utilized for free-stream static pressure measurements at the nozzle exit. Obtained individual calibration curves for (piezoresistive) absolute pressure gauges, mounted on slender lance probes, are plotted in Fig. B.4, indicating the non-linear polynomial and linear regression fit, respectively.

B.1.3 One-dimensional heat transfer theory

Classical theory for heat transfer in short duration measurements typically uses the approach of Schulz and Jones [184], who considered 1-D transient heat conduction into a semi-infinite body (slab). Here, the solid is assumed to have infinite thickness such that heat transfer is determined from measured temperature variation $T_s(t)$ on the surface and assuming an isothermal boundary condition at the back. Here, the governing equation of transient heat conduction into an isotropic solid of constant thermal conductivity:

$$\frac{\partial^2 T}{\partial x^2} + \frac{\partial^2 T}{\partial y^2} + \frac{\partial^2 T}{\partial z^2} = \frac{1}{\alpha}\frac{\partial T}{\partial t} \tag{B.1}$$

is simplified for 1-D heat transfer normal to the surface:

$$\frac{\partial^2 T}{\partial x^2} = \frac{1}{\alpha}\frac{\partial T}{\partial t} \tag{B.2}$$
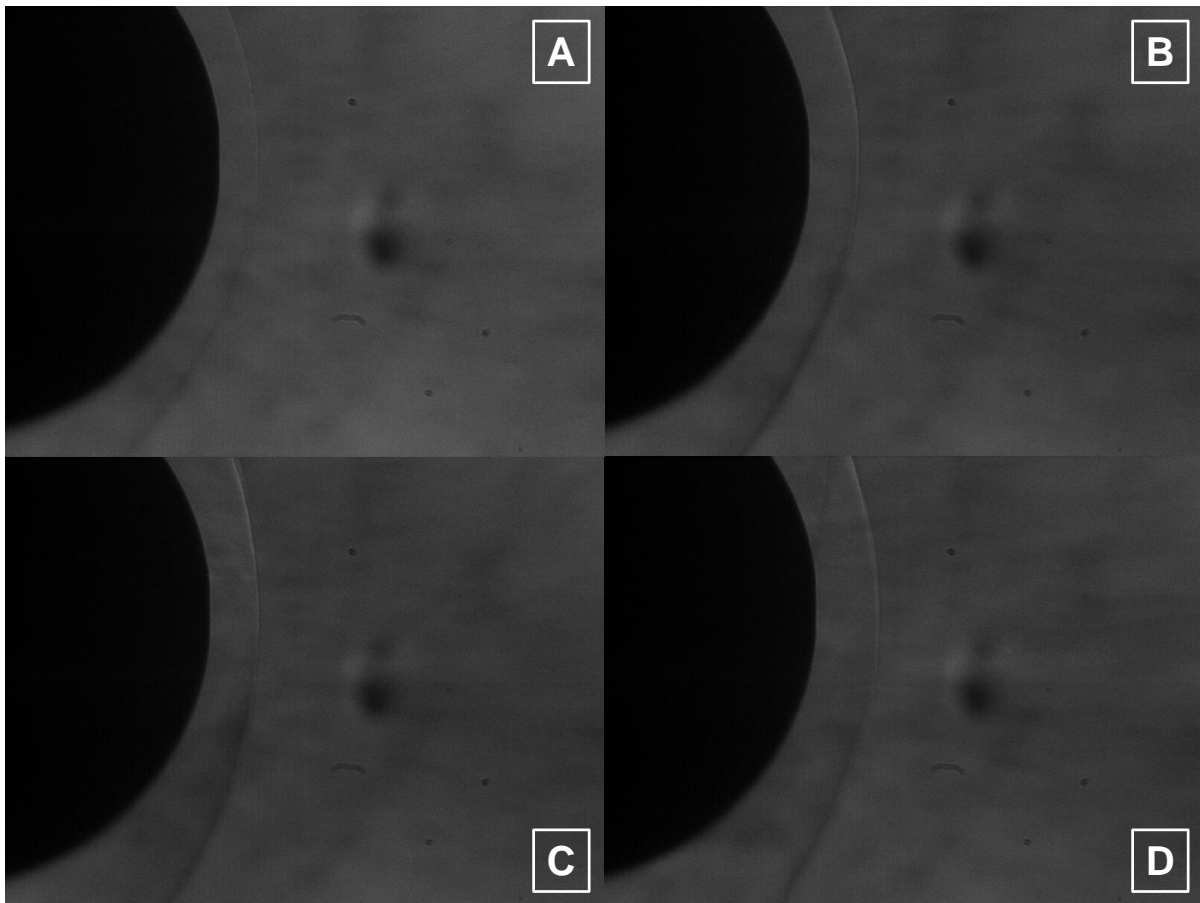
Figure B.1: Photographs of Schlieren visualization for experiment 2019.12.13.001, acquired at a frame rate of 30,000 fps ($\Delta t = 33.3 \mu s$) with a high-speed CMOS camera (Redlake) for a sphere of radius R_N=19.05 mm. Images illustrate unsteadiness of the free-stream flow field, bow shock topology and shock standoff-distance. A: $\delta = 2.62$ mm, time record -74 (-2.467 ms). B: $\delta = 3.32$ mm, time record 22 (0.733 ms). C: $\delta = 3.37$ mm, time record 31 (1.033 ms). D: $\delta = 4.28$ mm, time record 59 (1.967 ms).
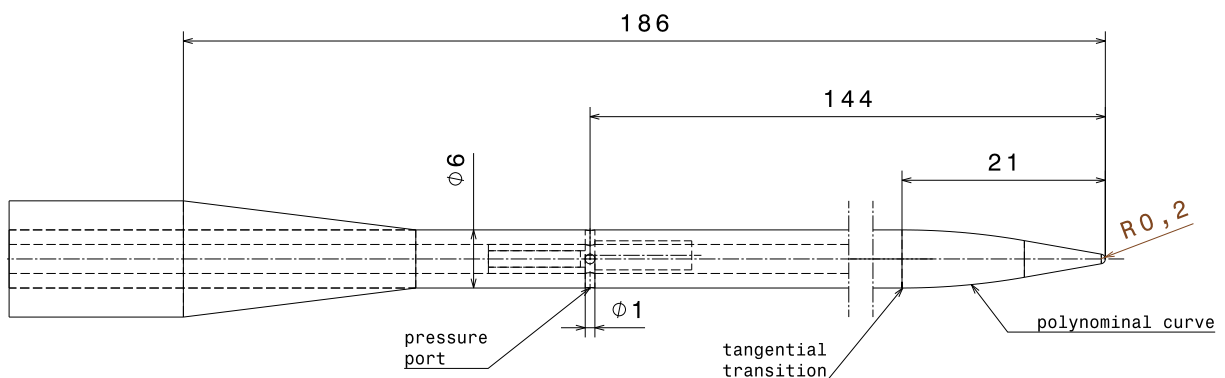
Figure B.2: Schematic of the slender lance probe geometry for measurements of free-stream static (absolute) pressure in the HELM facility. Dimensions not to scale.
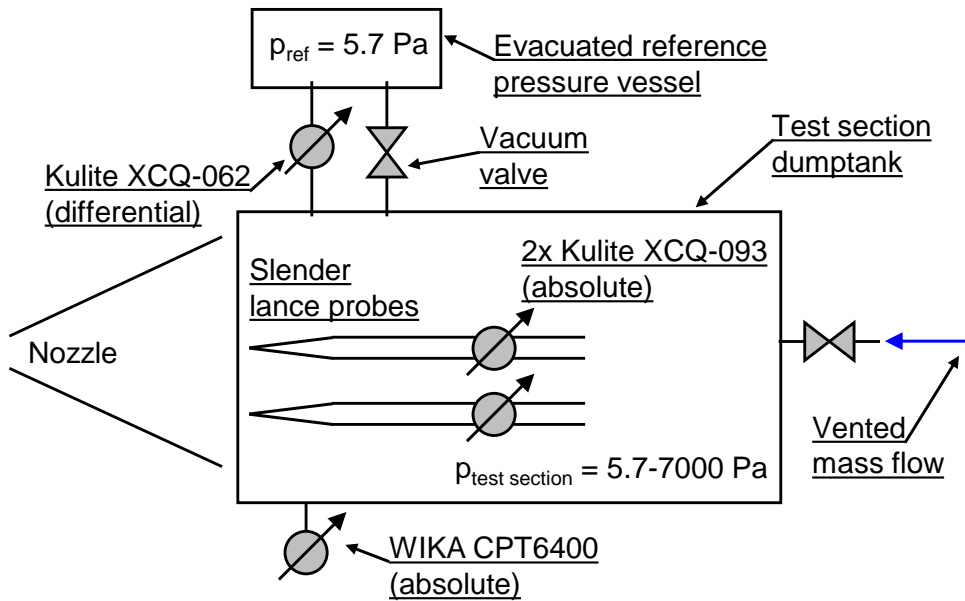
Figure B.3: Schematic of the slender lance probe (Kulite XCQ-093-abs) calibration for measurements of free-stream static (absolute) pressure in the HELM facility.
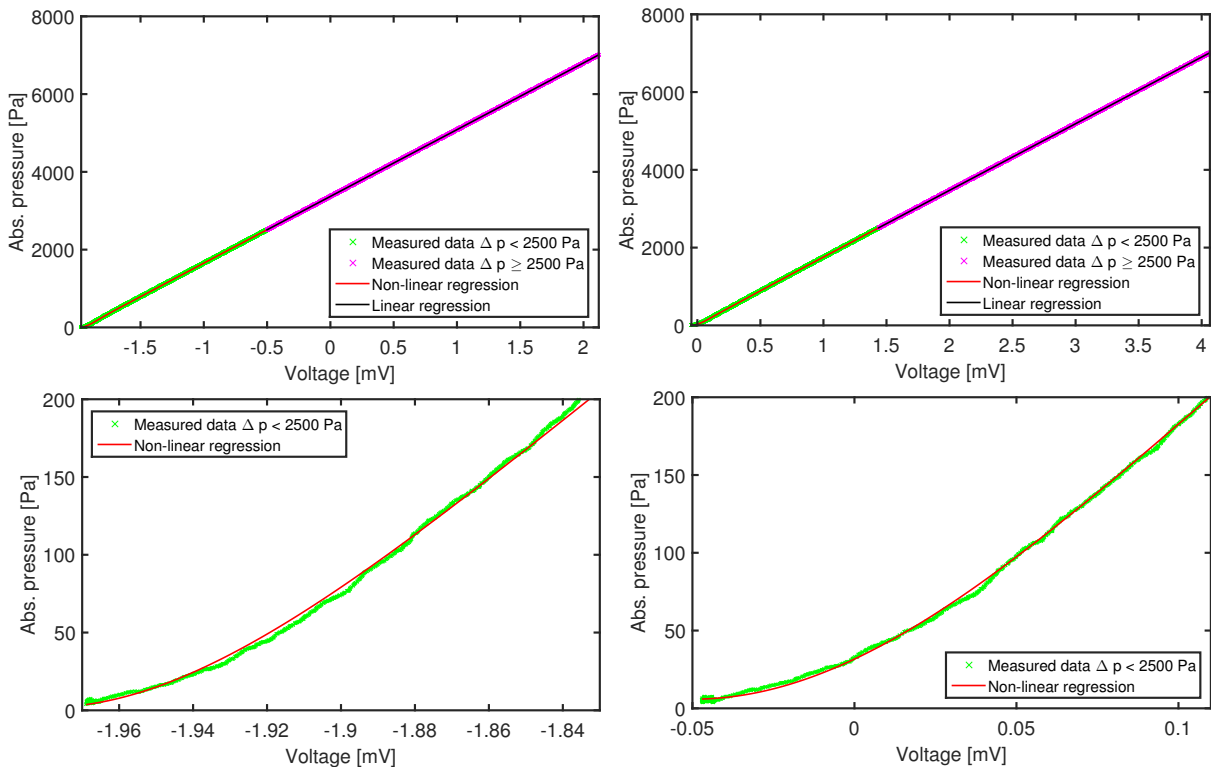
Figure B.4: Detailed view of the individual calibration curves for both absolute pressure sensors (Kulite XCQ-093-abs) mounted in slender lance probes for measurements of free-stream static pressure. Top: Complete calibration curve of primary data, fitted by dedicated nonlinear regression in the range < 2500 Pa and linear regression for amplitudes up to 7000 Pa in the linear range. Bottom: Close-up view of sensor signal non-linearity and voltage offset at very low absolute pressures < 200 Pa.

and henceforth solved for initial condition $\Delta T(x,0) = 0$ and boundary conditions:

$$-k\frac{\partial T(x,t)}{\partial x}\Big|_{x=0} = q_s(t) \tag{B.3}$$

and

$$\Delta T(\infty,t) = 0 \tag{B.4}$$

for convective heat transfer rate $q_s(t)$, temperature rise $\Delta T(x,t)$ and the semi-infinite slab assumption of constant back temperature, respectively. Laplace transformation yields an analytical relation of surface heat flux to temperature:

$$q_s(t) = \sqrt{\frac{\rho c k}{\pi}} \int_0^t \frac{\frac{dT_s(\tau)}{d\tau}}{(t-\tau)^{\frac{1}{2}}}\, d\tau \tag{B.5}$$

where $T_s(t) = \Delta T(0,t)$ is the measured transient surface temperature rise. The analytical solution in Eq. B.5 is, however, inconvenient for data reduction purposes as spurious noise imposed on the transient temperature signal is amplified due to the time derivative. On the contrary, integration by parts yields a more convenient analytical closed-form solution:

$$q_s(t) = \sqrt{\frac{\rho c k}{\pi}}\Big[\frac{T_s(t)}{\sqrt{t}} + \frac{1}{2}\int_0^t \frac{T_s(t) - T_s(\tau)}{(t-\tau)^{\frac{3}{2}}}\, d\tau\Big] \tag{B.6}$$

with initial condition $T(\tau = 0) = 0$. As evaluation of the analytical closed-form solution according to Eq. B.6 will inevitably involve numerical integration of discretized data, several techniques have been proposed to account for the singularity at $t = \tau$. The most commonly employed technique according to Simeonides [147] approximates the discrete surface temperature history by a piecewise linear function and eventually yields the numerically tractable solution as a sum of discrete temperature differences:

$$q_s(t) = 2\sqrt{\frac{\rho c k}{\pi}} \sum_{i=1}^{n} \frac{T_s(t_i) - T_s(t_{i-1})}{(t_n - t_i)^{\frac{1}{2}} + (t_n - t_{i-1})^{\frac{1}{2}}} \tag{B.7}$$

, an approach which is also proposed by Olivier [163]. From Eq. B.7 it is evident that surface heat flux directly scales with the thermal product $\sqrt{\rho c k}\,[W\sqrt{s}/m^2 K]$ of base material thermophysical properties where ρ, c, k denote solid density, thermal heat capacity and thermal conductivity, respectively.

An ideal step function of constant heat flux at the surface yields a square-root rise of surface temperature - or vice versa - which holds certain significance for hypersonic experiments where the test body is subjected to an initial leading shock wave ahead of a quasi-steady test flow. More precisely, the leading head shock wave traverses the flow field with velocity and thus Mach number higher than the test flow following thereafter, such that real experimental data traces often reflect a pronounced and short duration initial peak which can be of physical nature in addition to artifacts of singularities in the data processing scheme. Thereafter heat transfer

drops to an approximately constant plateau for the succeeding quasi-steady test flow. Equation B.7 holds for both types of gauges: coaxial thermocouples and thin-film gauges such that surface heat flux can be readily determined from surface temperature history. In the current work, type-E thermocouples are individually calibrated by the manufacturer via a temperature step function in a reference temperature bath: the thermophysical properties were determined to $\sqrt{\rho ck} = 8700 \pm 40 W \sqrt{s}/m^2 K$.

B.2 CFD Simulation

B.2.1 Governing equations

The conservation equations for mass, momentum and energy for a compressible, viscous flow in a 3-D cartesian coordinate system (x, y, z) with velocity components (u, v, w) are given in differential (non-conservation) form according to Eq. B.8:

$$\frac{\partial W}{\partial t} + \frac{\partial (F(W) - F^v(W))}{\partial x} + \frac{\partial (G(W) - G^v(W))}{\partial y} + \frac{\partial (H(W) - H^v(W))}{\partial z} = S(W) \tag{B.8}$$

where $W = (\rho, \rho u, \rho v, \rho w, \rho E, \rho_s(n_s), \rho_m e_{vibm})^T$ denotes the state vector. Here, ρ_s and n_s denote partial density and number of substance of (atomic and molecular) species s, while ρ_m and e_vib_m denote partial density and vibrational energy of molecular species m. Whereas the source vector S(W) depends on precise thermo-physical and chemical modeling for high-temperature real gas effects and physical modeling for turbulence, described in detail by Leyland et al. [175], the inviscid (convective) flux vectors F(W), G(W), H(W) and viscous flux vectors F^v(W), G^v(W), H^v(W) are given according to Eq. B.9 and B.10:

$$\boldsymbol{F} = \begin{bmatrix} \rho u \\ \rho u^2 + p \\ \rho uv \\ \rho uw \\ u(\rho E + p) \\ \phi u \end{bmatrix}, \boldsymbol{G} = \begin{bmatrix} \rho v \\ \rho uv \\ \rho v^2 + p \\ \rho vw \\ v(\rho E + p) \\ \phi v \end{bmatrix}, \boldsymbol{H} = \begin{bmatrix} \rho w \\ \rho uw \\ \rho vw \\ \rho w^2 + p \\ w(\rho E + p) \\ \phi w \end{bmatrix} \tag{B.9}$$

$$
F^v = \begin{bmatrix} 0 \\ \tau_{xx} \\ \tau_{xy} \\ \tau_{xz} \\ u\tau_{xx} + v\tau_{yx} + w\tau_{zx} + q_x \\ j_x \end{bmatrix}, G^v = \begin{bmatrix} 0 \\ \tau_{yx} \\ \tau_{yy} \\ \tau_{yz} \\ u\tau_{xy} + v\tau_{yy} + w\tau_{zy} + q_y \\ j_y \end{bmatrix},
$$

$$
H^v = \begin{bmatrix} 0 \\ \tau_{zx} \\ \tau_{zy} \\ \tau_{zz} \\ u\tau_{xz} + v\tau_{yz} + w\tau_{zz} + q_z \\ j_z \end{bmatrix}, S = \begin{bmatrix} 0 \\ 0 \\ 0 \\ 0 \\ 0 \\ \dot{\Omega} \end{bmatrix}
\tag{B.10}
$$

where variable ϕ in inviscid flux vectors denotes convective transport of an arbitrary flow property (based on physical, chemical, turbulence modeling) and j_i (i=x, y, z) in viscous flux vectors represents diffusive transport of this quantity. The generalized source term $\dot{\Omega}$ represents generation and destruction of quantity ϕ. E signifies total energy $E = e + 1/2(u^2 + v^2 + w^2)$ and q_i represents heat flux due to temperature gradients in cartesian coordinates (according to Fourier's law) and species diffusion. τ_{ij}(i,j=x, y, z) denotes the viscous shear stress tensor:

$$
\tau_{xx} = \frac{2}{3}\mu(2\frac{\partial u}{\partial x} - \frac{\partial v}{\partial y} - \frac{\partial w}{\partial z})
\tag{B.11}
$$

$$
\tau_{yy} = \frac{2}{3}\mu(-\frac{\partial u}{\partial x} + 2\frac{\partial v}{\partial y} - \frac{\partial w}{\partial z})
\tag{B.12}
$$

$$
\tau_{zz} = \frac{2}{3}\mu(-\frac{\partial u}{\partial x} - \frac{\partial v}{\partial y} + 2\frac{\partial w}{\partial z})
\tag{B.13}
$$

$$
\tau_{xy} = \tau_{yx} = \mu(\frac{\partial v}{\partial x} + \frac{\partial u}{\partial y})
\tag{B.14}
$$

$$
\tau_{xz} = \tau_{zx} = \mu(\frac{\partial w}{\partial x} + \frac{\partial u}{\partial z})
\tag{B.15}
$$

$$
\tau_{yz} = \tau_{zy} = \mu(\frac{\partial v}{\partial z} + \frac{\partial w}{\partial y})
\tag{B.16}
$$

using the Stokes hypothesis where the additional (RANS) terms from turbulence are described by specified RANS turbulence models. NSMB numerically solves the system of partial differential equations by an implicit LU-SGS (Lower-Upper Symmetric Gauss Seidel) scheme, where chemical species and turbulence quantities are solved simultaneously to the mean flow field variables via direct coupling.

B.2.2 Thermo-physical and chemical modeling

In the scope of the present work, three models for high-temperature real gas effects in air - distinguished by NSMB - have been used and are disambiguated in the following:

Thermo-chemical equilibrium

The first high-temperature NSMB model considers equilibrium air chemistry, which is described by a five-species model (N_2, O_2, N, O, NO) that is valid up to ~ 9000 K (before onset of ionization), where equilibrium constants are taken from Park [174]. The gas is considered as a mixture of perfect gas species, neglecting intermolecular particle forces, which is justified in regard of the low densities in expanding hypersonic nozzle flow. Moreover, full thermal equilibrium is assumed, precisely: internal DOF (translation, rotation, vibration) are assumed to have fully equilibrated $T = T_{trans} = T_{rot} = T_{vib}$, assuming relaxation time-scales due to particle collisions to be of magnitudes smaller than characteristic time-scales of the flow and chemistry [185].

The specific enthalpy of the mixture is calculated as the sum of contributions of translational, rotational and vibrational energy modes as well as the heat of formation $h_{f,s}^0$ according to:

$$h = \sum_s y_s c_{p_s} T + \sum_{s=O_2,N_2,NO} y_s e_s^{vib} + \sum_{s=O,N,NO} y_s h_{f,s}^0 \tag{B.17}$$

where y_s denotes species mass fraction. The first term in Eq. B.17 considers contribution of translational and rotational modes, as specific heat capacity (at constant pressure) $c_{p_s} = \kappa/(\kappa - 1)R/M_s$ is calculated with $\kappa = 7/5$ for di-atomic molecules and $\kappa = 5/3$ for mono-atomic species. Vibrational (internal) energy e_s^{vib} is treated separately and calculated from its equilibrium value [130]:

$$e_s^{vib} = \frac{\Theta_{v,s}}{e^{\Theta_{v,s}/T} - 1} \frac{R}{M_s} \tag{B.18}$$

where $\Theta_{v,s}$ denotes vibrational temperature of di-atomic species s= N_2, O_2, NO. Further details are given in [185].

Chemical non-equilibrium

The second high-temperature NSMB model considers non-equilibrium air chemistry, where chemical source terms in Eq. B.10 are described according to the laws of mass action, using finite reaction rates for forward and backward (reversible) reactions [185]. For five chemical species (N_2, O_2, N, O, NO) a total of 17 reactions (15 dissociation reactions due to two-particle collision and two NO-exchange reactions) are considered, where reaction rates are taken from Park [174]. Similar to the former NSMB model, full thermal equilibrium according to Eq. B.17 and B.18 for $T = T_{trans} = T_{rot} = T_{vib}$ is assumed.

Thermo-chemical non-equilibrium

Finally, the third high-temperature NSMB model considers thermal non-equilibrium (by a multi-temperature model) in addition to non-equilibrium air chemistry. Precisely, finite-rate chemistry is described by the same five-species 17-reactions model as in the second NSMB model, where forward and backward reaction rates - similarly taken from Park [174] - are calculated from (translational-rotational) temperature $T = T_{trans} = T_{rot}$. The latter assumes translational and rotational internal DOF to be in equilibrium (for all species, i.e. atoms and molecules alike) and is distinguished from separate vibrational temperatures $T_m^{vib} \neq T$, which describes thermal non-equilibrium of vibrational modes of di-atomic molecules m (N_2, O_2, NO). Atoms, in contrast, do not possess vibrational energy modes. A rigid rotor is assumed.

For thermo-chemical NEQ, the source term $\dot{\Omega}$ reads:

$$\dot{\Omega} = (\dot{\omega}_{ch_s}, \dot{\omega}_{vib_m}^{T-V} + \dot{\omega}_{vib_m}^{V-V} + \dot{\omega}_{vib\,m}^{C-V} + e_{vib\,m}\dot{\omega}_{vib_m})^T \tag{B.19}$$

denoting, species net production rate by chemical reactions, energy exchange (relaxation) due to particle collisions between translational-vibrational (T-V), vibrational (V-V) energy modes and loss/gain in vibrational energy due to coupling with molecular dissociation and recombination [175]. Every species s of the mixture is assumed to behave as a perfect gas, such that pressure and enthalpy are given by:

$$p = \rho R T \sum_s \frac{y_s}{M_s}, \quad h = \sum_s y_s h_s \tag{B.20}$$

where specific enthalpy of each constituent species is calculated according to:

$$h_s = c_{p_s} T + e_s^{vib} + h_{f,s}^0 \tag{B.21}$$

with (translational-rotational) temperature T. For the vibrational term, two cases are distinguished. For molecules m in thermal EQ, e_m^{vib} is (forward-)calculated from the harmonic oscillator model:

$$e_m^{vib} = \frac{\Theta_{v,m}}{e^{\Theta_{v,m}/T} - 1} \frac{R}{M_m} \tag{B.22}$$

based on temperature T (i.e. assuming $T = T_{trans} = T_{rot} = T_m^{vib}$). In contrast, for molecules in thermal NEQ, e_m^{vib} is implicitly obtained from conservation equations, Eq. B.19, while the respective (individual) vibrational temperatures T_m^{vib} of molecules m are calculated in backward-manner from Eq. B.22 - once e_m^{vib} is iteratively determined -, rearranged to:

$$T_m^{vib} = \frac{\Theta_{v,m}}{ln\left(\frac{\Theta_{v,m}}{e_m^{vib}} \frac{R}{M_m} + 1\right)}. \tag{B.23}$$

Specific enthalpy and internal energy are related via:

$$e = \sum_s y_s h_s(T) - \frac{p}{\rho}.$$

(B.24)

The harmonic-oscillator model [167] implies vibrational-vibrational energy exchange to be zero and only contribution from translational-vibrational energy exchange to remain [185]. Further, coupling of chemical dissociation and vibrational relaxation is neglected. The source term in the vibrational energy conservation equations, Eq. B.19, is modeled by the Landau-Teller equation with vibrational relaxation times according to Millikan and White [175]. Characteristic vibrational temperatures of di-atomic molecules and heats of formation employed herein are listed in Table B.1.

Table B.1: Heats of formation and characteristic vibrational temperatures for di-atomic molecules used within NSMB thermo-chemical (non-)equilibrium models and Park's thermo-chemistry model. Data from [185].

Species	NO	N	O
$h_{f,s}^0$ [kJ/g]	2.99	33.541	15.461
Species	NO	N_2	O_2
$\Theta_{v,m}$ [K]	2740	3390	2270

Thermo-physical transport properties

Thermodynamic transport properties for high-temperature multiple species air (viscosity and thermal conductivity) are either obtained for individual species from the Blottner model [176] and by using Wilke's mixing rule; therein constant Prandtl and Lewis number of individual species is assumed. Alternatively, transport properties are directly obtained from polynomial curve fits of NASA 7 and 9 coefficient data bases. Details are given in [185].

Numerical geometry

A list of simulation parameters for numerical geometries is given in Table B.2 where the block orientation and cell distribution is illustrated in Fig. B.5.

B.2.3 Rebuilding results - continued

In Fig. B.6, variation of results from the FS-rebuilding method (w/ static pressure measurement) with three different formulations of the SP tangential velocity gradient, all using the Fay-Riddell-eq. as formulation of the stagnation enthalpy - SP heat flux relation, is quantified. Relative deviation is given relative to data based on the modified Newton definition. Interestingly, both alternative velocity gradient definitions induce consistent over- or underprediction of any stagnation and free-stream quantity. Here, divergence of $\sim$+15% and +55% in stagnation

Table B.2: Parameters of steady state numerical simulations by NSMB.

	Nozzle	Nozzle (w/ test section)	Lance probe	Sphere probes
Blocks	64	64	64	2
Cells	1,465,546	1,740,888	717,600	41,184
Turb.model	1-eq. Spalart-All.	2-eq. k-ϵ	2-eq. k-ω-SST	2-eq. k-ω-SST
Space-scheme	Upwind (AUSM-W)	Upwind (AUSM-W)	Central	Central
Order	1	1	2	2
Time-scheme	Implicit	Implicit	Implicit	Implicit
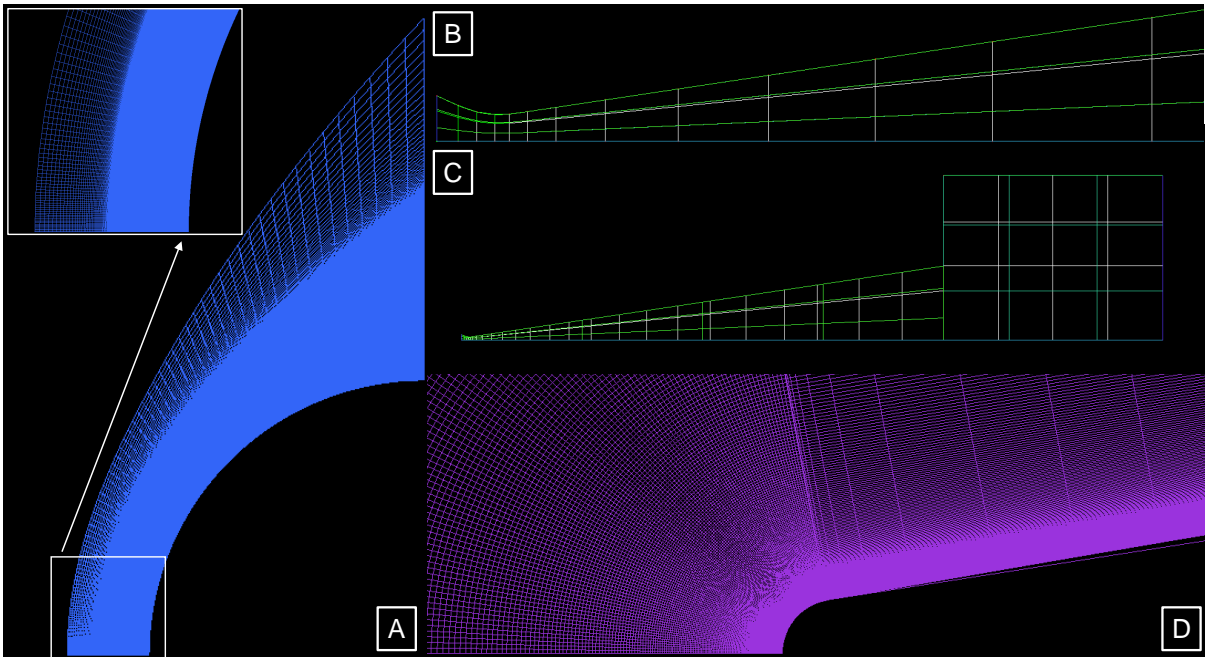
Figure B.5: View of the structured numerical grid, including blocks and cell distribution, for NSMB geometries used within this work. A: Spherical stagnation probe. B: Expansion nozzle (w/o test section). C: Expansion nozzle (w/ test section). D: Slender lance probe.

enthalpy results for the Olivier and Stokes velocity gradient definitions, respectively, particularly towards beginning of the test time. Divergence of similar sign and magnitude is observed for the static temperature. For predicted FS quantities, plotted in Fig. B.7, the largest relative deviation is observed in terms of static density which linearly translates to FS Reynolds number. Both quantities are predicted lower by up to -10% and -35% for the Olivier and Stokes definition, respectively. As such, deviations from the modified Newton reference are generally larger for the Stokes than for the Olivier velocity gradient, up to a factor of 2.

In Fig. B.8, variation of results from the FS-rebuilding method (w/ static pressure measurement) with four alternative formulations of the stagnation enthalpy - SP heat flux relation (according to Fay-Riddell, Verant-Sagnier, Sutton-Graves and Zoby), all based on the modified Newton formulation of the SP tangential velocity gradient, is quantified. Relative deviation is quantified relative to results based on the Fay-Riddell formulation. In contrast to a variation
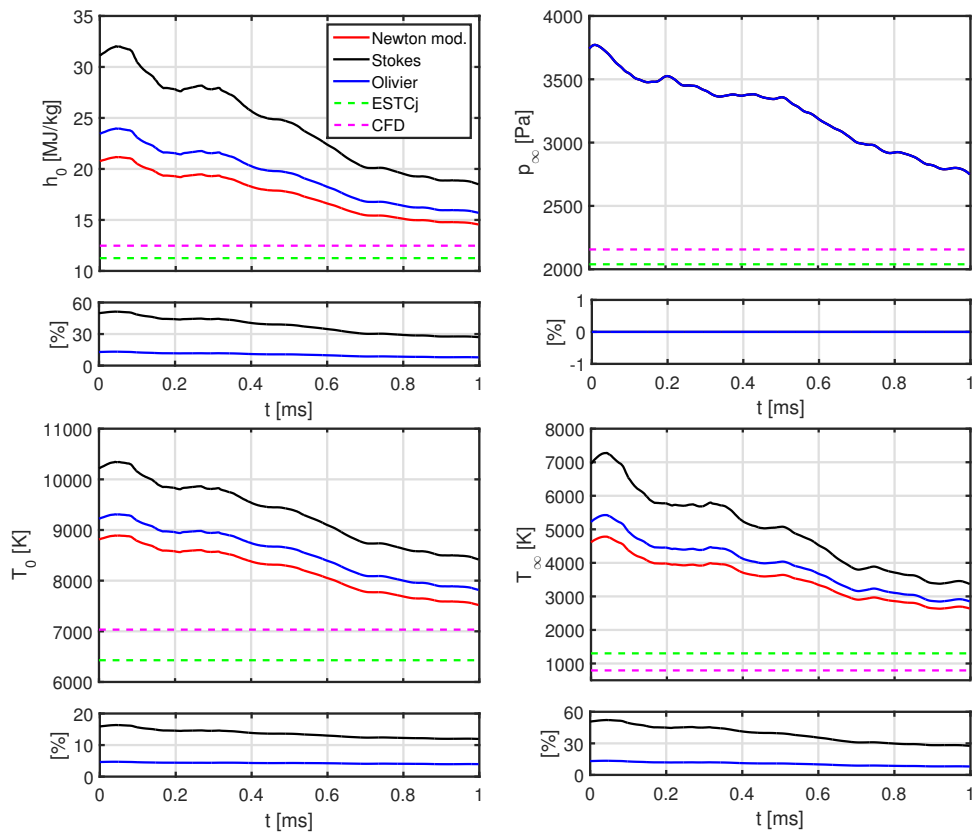
Figure B.6: Variation of free-stream quantities for reference condition RC-1 due to the FS-method (w/ static pressure) and Fay-Riddell-eq. by variation of the tangential velocity gradient.
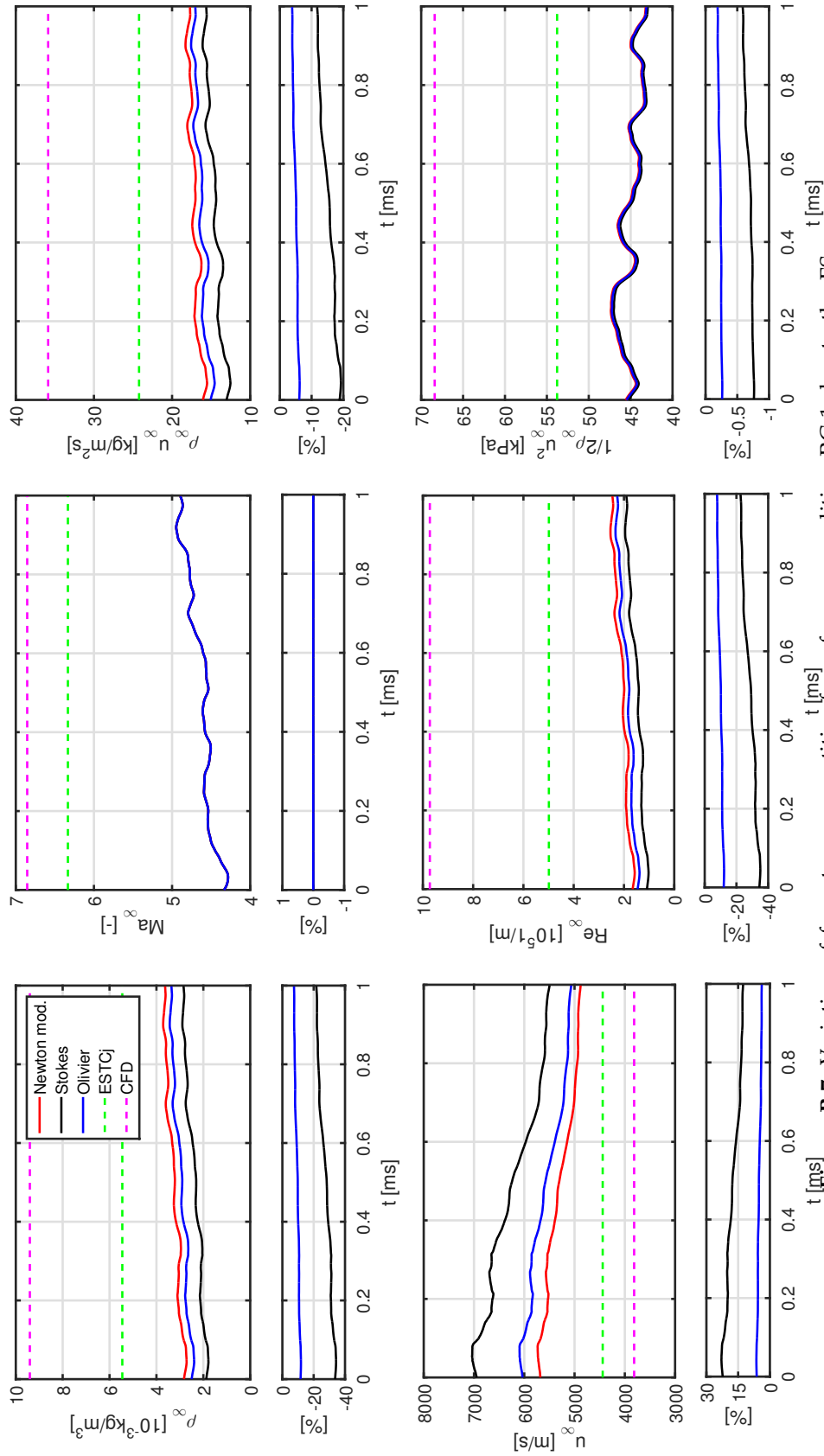
Figure B.7: Variation of free-stream quantities for reference condition RC-1 due to the FS-method (w/ static pressure) and Fay-Riddell-eq. by variation of the tangential velocity gradient.
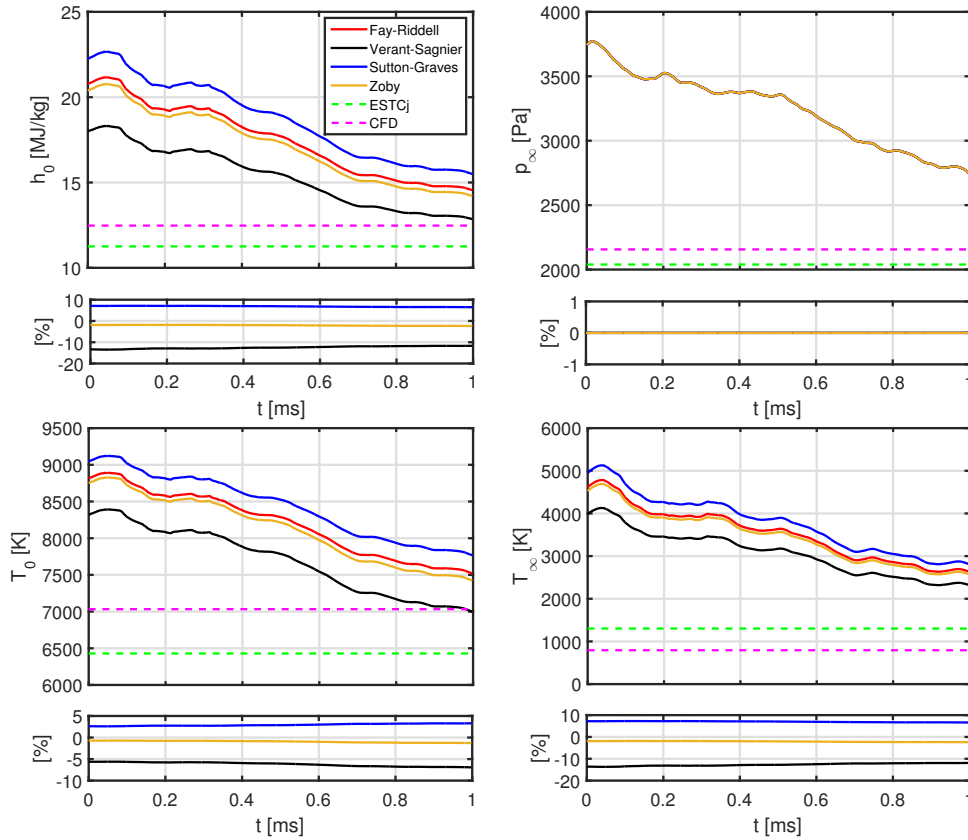
Figure B.8: Variation of free-stream quantities for reference condition RC-1 due to the FS-method (w/ static pressure) and modified Newton velocity gradient by variation of the stagnation point heat-flux-enthalpy-relation.

in the velocity gradient definition, alternative formulations of the enthalpy-heat flux relation result in a positive and negative divergence from Fay-Riddell reference. In terms of stagnation and FS quantities alike, the smallest deviation is generally observed for the Zoby relation, inducing a mere negligible difference of pm2%. Interestingly, the Verant-Sagnier and Sutton-Graves equation each induce differences of near similar magnitude but opposing sign, e.g. Verant-Sagnier underpredicting stagnation enthalpy by $\sim$-12% whereas the latter is overpredicted by Sutton-Graves by $\sim$+9%. In comparison, Eitelberg et al. [154] - imposing constant stagnation enthalpy and calculating expected SP heat flux rates - reported on a consistent over-prediction of SP heat flux by the Sutton-Graves and Verant formulation (of larger magnitude for the Verant-equation), relative to measured heat flux which was found to be in close agreement with predictions by the Fay-Riddell equation. It is thus inferred that the Fay-Riddell formulation will yield a suitable comparison to the current measurements, with Zoby's model representing a useful alternative for a wider range of test gases other than air, which will still yield results of similar magnitude as the established Fay-Riddell formulation.
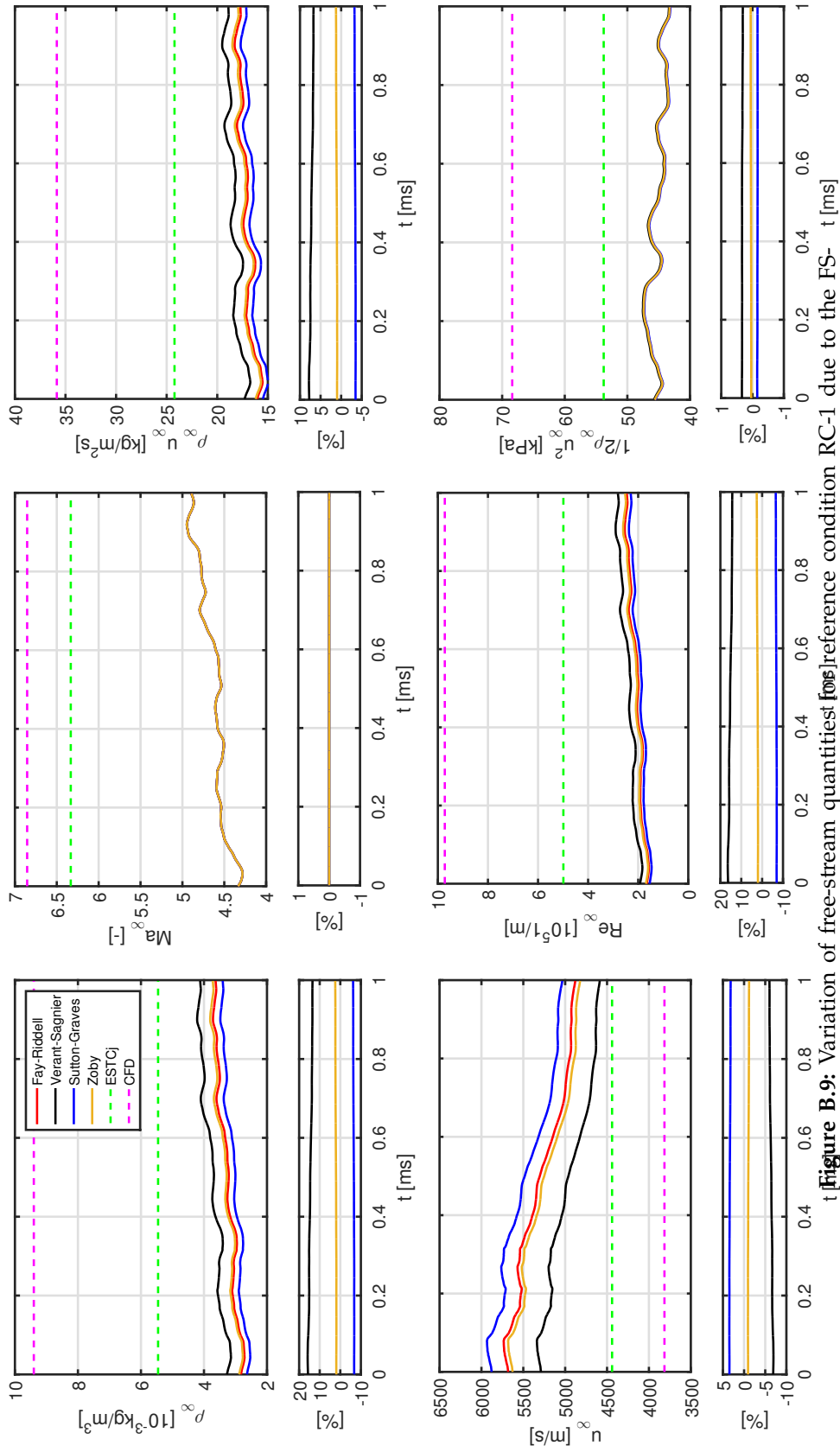
Figure B.9: Variation of free-stream quantities for reference condition RC-1 due to the FS-method (w/ static pressure) and modified Newton velocity gradient by variation of the stagnation point heat-flux-enthalpy-relation.
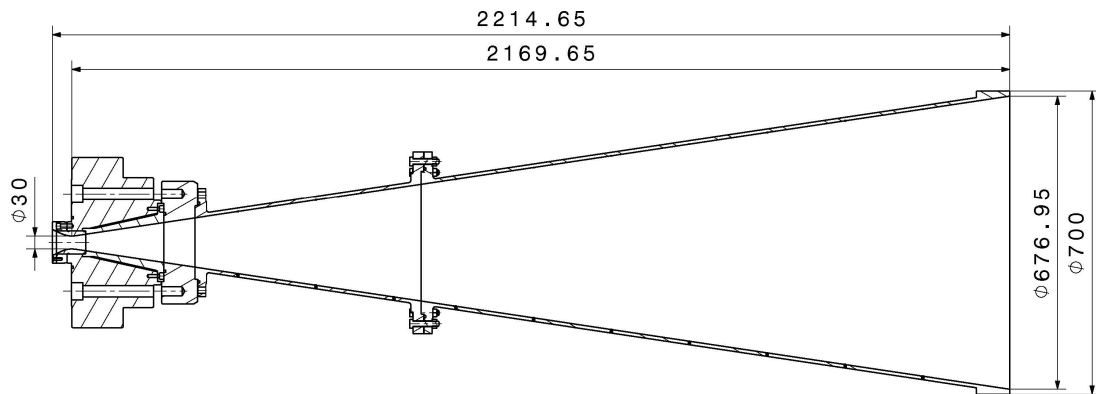
Figure B.10: Technical drawing with geometrical dimensions of the current conical expansion nozzle of the HELM, adopted from Altenhöfer [42].

B.2.4 HELM Expansion nozzle

Geometrical dimensions of the HELM conical expansion nozzle are given in the technical drawing of Fig. B.10.

C Appendix

C.1 Uncertainty analysis

In experimental investigations, measurement uncertainty comprises of accuracy (bias, i.e. systematic offset) and precision (random variation) [186]. According to the principle of error propagation, linearized approximation of a derived quantities' uncertainty is computed from absolute error of measured quantities via their functional relationship, illustrated for a three-parameter model in the following:

$$\delta V = ((\frac{\partial V}{\partial x_1}\delta x_1)^2 + (\frac{\partial V}{\partial x_2}\delta x_2)^2 + (\frac{\partial V}{\partial x_3}\delta x_3)^2)^{0.5} \tag{C.1}$$

where x_1-x_3 denote measured (independent) quantities of absolute measurement error δx and V denotes the derived (dependent) quantity with resultant absolute error δV. In order to assess the impact on acquired data, the measurement error is typically stated relative to the nominal measured quantity. As such, measurement uncertainty can be estimated according to the single samples method proposed by Kline and McClintock [126] and Moffat [127].

C.1.1 Facility measurements

Static pressure

In order to accurately reproduce theoretically predicted tuned FPD and TI operation conditions, static pressures in the buffer vessel (secondary reservoir), CT and ST are measured by (absolute and differential) pressure gauges (WIKA GmbH, type S-20) before initiation of any experiment. Here, a manufacturer stated maximum 0.25% accuracy relative to FS (full scale) values of 100 bar, 1.6 bar and 4.0 bar combines with an 0.05% accuracy of the Siemens Simatic ADC (16-bit amplitude resolution) to a total relative error of 0.3%. Accordingly, nominal values of static pressure in the buffer vessel, CT and ST can be specified to within ± 0.3 bar, ± 4.8 mbar, ± 12 mbar, respectively.

Shock velocity

Absolute velocity of the incident and reflected shock wave within the ST are measurement by difference in time of rising pressure flank arrival at two adjacent piezoelectric, wall-flush

mounted, dynamic pressure gauges (PCB Inc., type 109C11) according to:

$$v_s = \frac{\Delta x}{\Delta t},$$ (C.2)

where Δx denotes the traversed axial distance in time interval Δt. With a nominal relative distance of 300-700 mm between discrete sensors (assumed maximum error of $\delta x = 1$ mm) and a sampling rate of minimum 1 MHz ($\delta t = 0.5 \mu s$), the maximum error of the incident shock velocity - for a nominal value of $v_s \sim 3400$ m/s (Mach 10 in ambient temperature air as test gas) - is computed to absolute ± 22.5 m/s or relative $\pm 0.66\%$. At a sampling rate of 5 MHz this error reduces to absolute ± 6.9 m/s or relative $\pm 0.20\%$. In contrast, if the manufacturer-stated rise time of ≤ 2 μs is used as an alternative measure of time discretization, the error increased to maximum $\pm 2.0\%$ or ± 68.0 m/s.

It is however to be pointed out that such point-discrete measurements of shock velocity via difference in time of arrival are inherently limited to merely yield an average value over a distance specified by adjacent sensor locations and could at best yield an accurate instantaneous value at a discrete location if two sensors were located directly after another. Considering shock wave (velocity) attentuation of $\sim$1-2%/m (as stated by Mirels [45] for turbulent boundary layers in high-pressure ST) due to viscous wall boundary layer displacement and effective cross-section decrease , the effective and significant error of incident shock wave velocity in the nozzle reservoir (i.e. immediately before shock wave endwall-impact and reflection) will be dominated by continuous decrease of shock velocity along the ST. This trend is only unsatisfactorily resolved by averaged or point-discrete measurements but requires non-linear fitting and extrapolation of data from multiple (averaged) values staggered from upstream to downstream along the ST. This procedure will ensure lowest uncertainty and highest accuracy of predicted stagnation quantities in the nozzle reservoir.

Dynamic pressure

Dynamic pressure amplitudes (after the incident and reflected shock wave) within the CT and ST are measured by wall-flush mounted, piezoelectric pressure gauges (PCB Inc., type 109C11), suited for high-pressure, high-temperature measurements behind shock and detonation waves. The sensor diaphragm is thermally insulated from hot measurement environment via a ceramic coating in order to avoid flash temperature effects (i.e. decrease of electric charge and hence voltage readout) on the active piezoelectric crystal and internal charge amplifier. A manufacturer-stated relative error of maximum 1.0% (FS) with respect to a full-range value of 5520 bar yields an absolute error of ± 55.2 bar. This value can be further reduced in the future by dedicated re-calibration (either NIST-traceable by the manufacturer or inhouse, as e.g. suggested in [11]) in the relevant ≤ 1000 bar pressure range. In any case, sensor and calibration-inherent uncertainty is evident to dominate over negligible discretization error (at a minimum 14-bit-depth of the data acquisition ADC) of maximum ± 61 mbar, equivalent to $\pm 0.0061\%$ at 1000 bar nominal pressure.

C.1.2 Free-stream measurements

Static pressure

As for the downstream test section and dump tank, very low static (absolute) pressure amplitudes of <10-100 Pa (0.1-1 mbar) are to be measured after evacuation. Here, highest possible accuracy is imperative in order to ensure accurate quantification of lowest-possible steady absolute pressure (dictated by vacuum pump performance and pressure vessel leakage) which serves as absolute reference (zero-point offset) throughout FS static pressure (slender lance) probe calibration and test flow measurement.

For this purpose, an absolute pressure gauge (WIKA GmbH, type CPT6400) of nominal range 250 mbar is deliberately calibrated (NIST-/DIN EN - traceable) for low absolute pressure (range 0.1-500 Pa) and ± 2 Pa conservative accuracy by the manufacturer. Throughout calibration, the time-average (leakage flow-corrected) pressure level is quantified to be as low as 5.7 Pa which is achieved by tight-sealing the test section with a dedicated lit (using a self-sealing front-end seal) instead of the expansion nozzle (using a radial slide-seal). Static pressure immediately before the experiment ranges around 20-60 Pa due to higher leakage rates.

A differential pressure gauge (Kulite Inc., type XCQ-062) measures the pressure difference between the test section and an evacuated reference volume and is itself accurately calibrated by a dedicated pressure calibrator (GE Inc., DPI 612 pFlex) with two low-amplitude differential pressure modules PM 620 of range 2500 Pa (± 2.5 Pa, $\pm 0.1\%$ FS) and 7000 Pa (± 3.3 Pa, $\pm 0.047\%$ FS), absolute and equivalent relative accuracy, respectively. Eventually, absolute (static) pressure within the free-stream of nominally $\sim$100-4000 Pa is measured to within ± 10 Pa, comprising of combined measurement error and deviation due to the numerical (calibration) fit.

Stagnation temperature and heat flux

Transient wall temperature in the stagnation point of spherical probes is measured by a fast, type E coaxial thermocouple. Conversion of the voltage signal to absolute temperature considers the non-linear relation from voltage to absolute temperature via fitting of NIST-stated reference data via a rational function. Hence, a maximum error of ± 0.1 K or 0.03% with respect to nominal 300 K is deduced. Values of relevant thermo-physical properties $\sqrt{\rho c k}$ are calibrated individually by the manufacturer (SWL at RWTH-Aachen University), see [155]. Due to approximation of instantaneous heat flux by numerical integration of time-discrete data, the error of SP heat flux is deduced to maximum ± 1.0-2.0%.

In contrast, maximum uncertainty of heat flux directly measured by ALTP-sensors (not used herein) is conservatively stated to $\leq$10%, although the factualy error will be lower $\sim$5%.

Pitot pressure

Pitot (stagnation) pressure within the free-stream is measured by two kinds of dynamic pressure sensors: piezoelectric (PCB Inc., type 113B28) and piezoresistive (Kulite Inc., type XCQ-

093). Both gauges are characterized by a manufacturer-stated uncertainty of 1.0% (FS) which yields a maximum error of ± 35 mbar for a nominal value of 3.5 bar. In comparison, contribution of the discretization error from 14- or 16-bit ADC is negligible.

C.1.3 Piston trajectory measurements

On-board accelerometer

Instantaneous acceleration of the compression piston along a full stroke is measured by the on-board accelerometer which consists of the primary piezoelectric MEMS (micro electro mechanical system) sensor (Endevco Inc., type 727-60K-5-120) with $\pm 2.7\%$ relative uncertainty in the 2,000-10,000 g amplitude range as stated by the manufacturer. The full-range value of 10,000 g is approximately equal to the maximum predicted instantaneous acceleration of $\sim 102,240 \, \text{m/s}^2$ exerted by the nominal pressure of 1000 bar on the lightweight aluminum piston used within current experiments. As such, a $<3.0\%$ total uncertainty is assumed, considering contribution of the amplitude discretization error from the 16-bit microcontroller ADC to be negligible.

Inductive proximity sensors

Besides quantitative measurement of instantaneous rigid body acceleration and qualitative trend by the accelerometer, inductive proximity sensors (Baumer GmbH, type IFRP 12P1501/S14) are flush-mounted to the CT wall. Stated relevant signal rise time of $<50\mu s$ yield a corresponding uncertainty of ± 10 mm of instantaneous piston position, in reference to detecting discrete sensor locations. Considering a relative distance of adjacent sensors of minimum 2.5 m, this is found to be equivalent to a maximum relative error of $\pm 0.4\%$.

Due to a high sampling rate of 200 kHz and 700 kHz manufacturer-stated resonance frequency, linearity of amplitude in the relevant frequency-range of ~ 10 kHz for current piston trajectory measurements is considered reasonable. Accordingly, as the resultant piston trajectory is computed from a least-squares fit (no fixed-point interpolation) throught measured data, the factual piston piston position is deduced to be resolved with an error lower than the computed $\pm 0.4\%$.

Similar to shock velocity, time-averaged piston speed is measured from an effective digital signal of rising and falling flanks upon piston passage at a proximity sensor location, due to inductive response of different metals and geometric edges on the piston lateral surface, see Eq. C.2. For the longest available edge-to-edge distance as signal mark, the sensor rise time induces a maximum uncertainty of absolute ± 1.3-11.1 m/s, equivalent to relative ± 1.3-3.7% deviation. Accordingly, lower uncertainty can be achieved in the future by mounting proximity sensors with an even lower signal rise time. Cables of equal length are employed for all proximity sensors used herein to ensure identical electronic transit time.

C.1.4 LIGS Stagnation temperature measurements

In situ LIGS measurements of stagnation temperature within the nozzle reservoir and behind the reflected shock wave are based on calibration of the optical grating geometry (fringe spacing Λ and pump beam intersection angle Θ) at ambient conditions prior to the experiment, with maximum absolute ± 1 K error (relative $\pm 0.33\%$) at 300 K room temperature. Uncertainty of air sound speed of tabulated data by Lemmon et al. [104] is stated as relative 0.2%, entailing an uncertainty of $\pm 1.07\%$ for LIGS grating geometry. Eventually, data processing yields an absolute uncertainty of ± 55 K and ± 50 K for the DFT and curve fit, respectively, which is equivalent to maximum relative $\pm 5.0\%$ and will decrease with measured nominal temperature.

Closing Remarks

„...one opted for the trinity of hex-head, sleeve and nut.“
KEN, undergraduate student

„Hyper, hyper!“
HP Baxter, quotes of world history